Universität Hamburg
DER FORSCHUNG | DER LEHRE | DER BILDUNG

DESY.

Multi-Modal Scanning X-Ray Microscopy for Solar Cell Characterization

Dissertation
zur Erlangung des Doktorgrades
an der Fakultät für Mathematik, Informatik und Naturwissenschaften
Fachbereich Physik
der Universität Hamburg

Vorgelegt von

Christina Sonja Ossig

Hamburg

2022

Gutachter der Dissertation:	Prof. Dr. Christian G. Schroer PD Dr. Tobias Kipp
Zusammensetzung der Prüfungskommission:	Prof. Dr. Christian G. Schroer PD Dr. Tobias Kipp Prof. Dr. Arwen Pearson Prof. Dr. Gabriel Bester Dr. Michael E. Stückelberger
Vorsitzende der Prüfungskommission:	Prof. Dr. Arwen Pearson
Datum der Disputation:	11.11.2022
Vorsitzender des Fach-Promotionsausschusses Physik:	Prof. Dr. Wolfgang J. Parak
Leiter des Fachbereichs Physik:	Prof. Dr. Günter Sigl
Dekan der Fakultät MIN:	Prof. Dr.-Ing. Norbert Ritter

Abstract

Thin-film photovoltaic devices are used to harvest solar energy. To be economically competitive, three aspects are particularly challenging, which we addressed in this work: cost efficiency, defect passivation, and spatial homogeneity. Comprehensive analysis is required to elucidate the underlying mechanisms that limit the conversion efficiency of thin-film solar cells. Traditionally, several probes are sequentially employed to evaluate different properties. Multi-modal hard X-ray scanning microscopy provides an alternative to sequential measurements and is available at micro- and nano-imaging beamlines of synchrotron facilities.

In this work, we extended the range of available scanning X-ray modalities and applied them to two types of thin-film solar cells. Hereby, we utilized the deep penetration depth of hard X-rays to evaluate fully operational solar cells on a point-by-point basis with a sub-micrometer resolution, which allowed us to identify the origin of performance variations.

Specifically, we developed an X-ray excited optical luminescence (XEOL) detection unit to resolve the signal in the spectral and temporal domain with a high signal-to-noise ratio. Combining XEOL with X-ray fluorescence (XRF), we studied wrinkled triple-cation metal-halide perovskite solar cells and directly related the inhomogeneous optical performance to the inhomogeneous absorber composition.

For X-ray beam induced current (XBIC) measurements, we established a guide to using lock-in amplification. By correlating the XBIC with the XRF signal, we found that economically favorable Cu(In,Ga)Se_2 solar cells with a high Ga/In ratio suffer from defect clusters that cannot be sufficiently passivated with the standard Rb post-deposition treatment.

Conflicting requirements pose a challenge for the simultaneous evaluation of multiple modalities. However, we demonstrated that four-fold multi-modal measurements are feasible and provide new insights into the relation between structure, composition, optical performance, and electrical performance, enabling the targeted synthesis of high-efficiency, low-cost solar cells.

Zusammenfassung

Dünnschicht-Photovoltaikgeräte werden zur Gewinnung von Sonnenenergie eingesetzt. Um wirtschaftlich wettbewerbsfähig zu sein, sind drei Aspekte besonders herausfordernd, die wir in dieser Arbeit behandelt haben: Kosteneffizienz, Defektpassivierung und räumliche Homogenität. Um die zugrundeliegenden Mechanismen aufzuklären, die die Umwandlungseffizienz von Dünnschichtsolarzellen begrenzen, sind umfassende Analysen erforderlich. Traditionell werden unterschiedliche Sonden nacheinander eingesetzt, um verschiedene Eigenschaften zu bewerten. Die multimodale harte Röntgen-Rastermikroskopie stellt eine Alternative zu sequenziellen Messungen dar und ist an den Mikro- und Nano-Imaging-Beamlines von Synchrotronanlagen verfügbar.

In dieser Arbeit haben wir die Palette der verfügbaren Röntgenrastermodalitäten erweitert und auf zwei Typen von Dünnschichtsolarzellen angewendet. Dabei nutzten wir die hohe Eindringtiefe der harten Röntgenstrahlung, um voll funktionsfähige Solarzellen Punkt für Punkt mit einer Auflösung von unter einem Mikrometer zu untersuchen, was uns ermöglichte, den Ursprung von Leistungsschwankungen zu identifizieren.

Insbesondere haben wir eine Detektionseinheit für röntgenangeregte optische Lumineszenz (XEOL) entwickelt, um das Signal im spektralen und zeitlichen Raum mit einem hohen Signal-Rausch-Verhältnis aufzulösen. Durch die Kombination von XEOL mit Röntgenfluoreszenz (XRF) untersuchten wir faltige Dreifachkation-Metallhalogenid-Perowskit-Solarzellen und konnten die inhomogene optische Leistung direkt mit der inhomogenen Absorberzusammensetzung in Verbindung bringen.

Für die Messung des röntgenstrahlinduzierten Stroms (XBIC) haben wir eine Anleitung zur Verwendung der Lock-in-Verstärkung erstellt. Durch Korrelation des XBIC mit dem XRF-Signal konnten wir feststellen, dass wirtschaftlich günstige Cu(In,Ga)Se_2-Solarzellen mit einem hohen Ga/In-Verhältnis unter Defektclustern leiden, die mit der Standard-Rb-Nachbehandlung nicht ausreichend passiviert werden können.

Widersprüchliche Anforderungen stellen eine Herausforderung für die gleichzeitige Bewertung mehrerer Modalitäten dar. Wir konnten jedoch zeigen, dass vierfache multimodale Messungen durchführbar sind und neue Einblicke in die Beziehung

zwischen Struktur, Zusammensetzung, optischer Leistung und elektrischer Leistung liefern, was die gezielte Synthese von hocheffizienten, kostengünstigen Solarzellen ermöglicht.

List of own contributions

I took part in several beamtimes at three different synchrotron facilities (ESRF, APS, DESY) and was involved with the data analysis. The following publications were prepared or published during this project with contributions from me.

Peer-reviewed publications as first author:

[1] C. Ossig, T. Nietzold, B. M. West, M. I. Bertoni, G. Falkenberg, C. G. Schroer, and M. E. Stuckelberger, "X-ray beam induced current measurements for multi-modal x-ray microscopy of solar cells", Journal of Visual Experiments, vol. 150, p. e60001, 2019.
doi: 10.3791/60001

[2] C. Ossig, C. Strelow, J. Flügge, A. Kolditz, J. Siebels, J. Garrevoet, K. Spiers, M. Seyrich, D. Brückner, N. Pyrlik, J. Hagemann, F. Seiboth, A. Schropp, R. Carron, G. Falkenberg, A. Mews, C. G. Schroer, T. Kipp, and M. E. Stuckelberger, "Four-fold multi-modal X-ray microscopy measurements of a Cu(In,Ga)Se_2 solar cell", Materials, vol. 14, no. 1, p. 228, 2021.
doi: 10.3390/ma14010228

[3] C. Ossig, N. Pyrlik, R. Carron, G. Fevola, S. Patjens, C. Strelow, J. Flügge, A. Kolditz, J. Siebels, J. Garrevoet, K. M. Spiers, M. Seyrich, D. Brückner, J. Hagemann, F. Seiboth, A. Schropp, G. Falkenberg, A. Mews, C. G. Schroer, T. Kipp, M. E. Stuckelberger, " X-ray vision of Cu(In,Ga)Se_2: from the Ga/In ratio to solar-cell performance", Journal of Physics: Energy, vol. 4, no. 4, p. 045007, 2022.
doi: 10.1088/2515-7655/ac9256

[4] C. Ossig, C. Strelow, J. Flügge, S. Patjens, J. Garrevoet, K. M. Spiers, J. Hagemann, F. Seiboth, E. Aydin, F. H. Isikgor, M. De Bastiani, S. De Wolf, G. Falkenberg, A. Mews, C. G. Schroer, T. Kipp, M. E. Stuckelberger, "Novel

detection scheme for temporal and spectral X-ray optical analysis: Study of triple-cation perovskites," manuscript submitted, 2023.

As first author, I was involved in the data taking, analysis, and writing of the article. These publications are a substantial part of this thesis and will be shown in only slightly altered form to adhere to the reading flow. Chapters based on them will be highlighted at the beginning.

Peer-reviewed publications as co-author:

I am co-author of the following publications and contributed as follows:

[5] M. Stuckelberger, T. Nietzold, B. M. West, T. Walker, C. Ossig, F. Wittwer, J. Deng, J. M. Maser, B. Lai, Z. Cai, V. Rose, A. Ulvestad, M. V. Holt, S. Hruszkewycz, J. J. Dynes, J. Wang, D. Salomon, R. Tucoulou, X. Huang, H. Yan, E. Nazaretski, Y. S. Chu, C. G. Schroer, and M. I. Bertoni, "Challenges and opportunities with highly brilliant X-ray sources for multi-modal in-situ and operando characterization of solar cells," Microscopy and Microanalysis, vol. 24 (Suppl. 2), pp. 434–435, 2018.
doi:10.1017/S1431927618014423

I was part of the team taking data at the ESRF beamline ID16B. I helped in setting up the experiment and contacting the samples. Furthermore, I fitted the X-ray fluorescence (XRF) data and analyzed the X-ray beam induced current (XBIC) data.

[6] A. Schropp, R. Döhrmann, S. Botta, D. Brückner, M. Kahnt, M. Lyubomirskiy, C. Ossig, M. Scholz, M. Seyrich, P. Wiljes, F. Wittwer, M. E. Stuckelberger, J. Garrevoet, G. Falkenberg, Y. Fam, T. L. Sheppard, J.-D. Grunwaldt, and C. G. Schroer, "PtyNAMi: Ptychographic Nano-Analytical Microscope," Journal of Applied Crystallography, vol. 53, no. 4, pp. 957–971, 2020.
doi: 10.1107/S1600576720008420

I was involved in the beamtime at P06 where the data for the measured solar cell was taken.

[7] N. Pyrlik, C. Ossig, C. Ziska, G. Fevola, J. Garrevoet, G. Falkenberg, A. Schropp, and M. E. Stuckelberger, "Image registration in multi-modal scanning microscopy: a solar cell case study," Proc. Photovoltaic Specialist Conference (PVSC), pp. 0913–0920, 2020.

doi: 10.1109/PVSC45281.2020.9300774

I was part of the beamtime at P06, where the data for this work was taken. Furthermore, I have fitted the XRF data and was part of the discussions on the analysis and treatment of the data. Additionally, I was involved in the supervision of Niklas Pyrlik's Bachelor's thesis on which this work is based.

[8] C. Ziska, C. Ossig, N. Pyrlik, R. Carron, E. Avancini, G. Fevola, A. Kolditz, J. Siebels, T. Kipp, Z. Cai, M. V. Holt, and M. E. Stuckelberger, "Quantifying the elemental distribution in solar cells from X-ray fluorescence measurements with multiple detector modules," Proc. Photovoltaic Specialist Conference (PVSC), pp. 1085–1092, 2020.
doi: 10.1109/PVSC45281.2020.9300345

I was involved in the preparation and the conduction of the beamtime at 26-ID-C in Chicago, where this data was taken. Furthermore, I was involved in the supervision of Catharina Ziska's Bachelor's thesis on which this work is based.

[9] G. Falkenberg, J. Hense, J. Barp, C. Ossig, N. Pyrlik, C. Ziska, M. Seyrich, J. Hagemann, M. Lyubomirskiy, F. Seiboth, G. Fevola, S. Patjens, J. Garrevoet, G. Falkenberg, and M. E. Stuckelberger, "Comparison of XBIC and LBIC measurements of a fully encapsulated c-Si solar cell," Proc. Photovoltaic Specialist Conference (PVSC), pp. 1998–2004, 2021.
doi: 10.1109/PVSC43889.2021.9518800

I fitted part of the XRF data. Furthermore, I was involved in the supervision of Gero Falkenberg's Bachelor's thesis on which this work is based.

[10] T. Walker, M. E. Stuckelberger, T. Nietzold, N. Mohan-Kumar, C. Ossig, M. Kahnt, F. Wittwer, B. Lai, D. Salomon, E. Colegrove, and M. I. Bertoni, "The nanoscale distribution of copper and its influence on charge collection in CdTe solar cells," Nano Energy, vol. 91, p. 106595, 2022.
doi: 10.1016/j.nanoen.2021.106595

I was part of the team taking data at the ESRF beamline ID16B. I helped in setting up the experiment and contacting the samples. Furthermore, I fitted the XRF data.

[11] P. Chakrabarti, A. Wildeis, M. Hartmann, R. Brandt, R. Döhrmann, G. Fevola, C. Ossig, M. Stuckelberger, J. Garrevoet, K. Falch, V. Galbierz, G. Falkenberg, and P. Modregger, "X-ray diffraction with micrometer spatial resolution for

highly absorbing samples," arXiv, no. 2201.13264, 2022, doi:10.48550/arXiv.2201.13264

I fitted the XRF data of the measured solar cell.

[12] M. De Bastiani, R. Jalmood, J. Liu, C. Ossig, A. Vlk, K. Vegso, M. Babics, F. H. Isikgor, A. S. Selvin, R. Azmi, E. Ugur, A. J. Mirabelli, E. Aydin, T. G. Allen, A. Ur Rahman, E. Van Kerschaver, P. Siffalovic, M. E. Stuckelberger, M. Ledinsky, S. De Wolf, "Monolithic perovskite/silicon tandems with >28% efficiency: role of silicon-surface texture on perovskite properties", Adv. Funct. Mater. 2023, 33, 2205557.
doi: 10.1002/adfm.202205557

I fitted the XRF data for the measured perovskite solar cells.

Exemplary results of these publications will be shown to introduce the different measurement methods, this will be mentioned at the beginning of the corresponding sections.

In the course of my Ph.D. project, I was partly involved with the supervision of students.

Summer students:

- Rachel Kealy (2018)
- Elizaveta Kamyshova (2018)

Bachelor students:

- Anna Barinskaya (2020)
- Niklas Pyrlik (2020)
- Catharina Ziska (2020)
- Jan Hense (2021)
- Gero Falkenberg (2021)
- Tizian Kaiser (2021)

Master students:

- Jackson Barp (2021)
- Leutrim Pacarizi (2021)

Contents

1 Introduction

Synchrotron radiation was first observed as a by-product of particle accelerators indirectly in 1945 [13] and directly in 1947 [14]. In the nineteen-sixties, the properties of synchrotron radiation started to be recognized as suitable for microscopy and spectroscopy applications. While in the beginning, only a few groups were able to use the light in a 'parasitic' fashion, soon dedicated facilities were built for the generation of synchrotron radiation [15].

Today, there are more than 50 synchrotron facilities around the world [16, 17] and the user group has evolved from dedicated groups to a vast community of scientists. One of these facilities is the Deutsches Elektronen-Synchrotron DESY in Hamburg. Fig. 1.1 shows the dates when the accelerator and storage rings DESY, DORIS, PETRA, HERA, and PETRA III started their respective operations. The establishment of the Hamburger Synchrotronstrahlungslabor HASYLAB in 1980 marks the beginning of dedicated synchrotron radiation experiments in Hamburg where 30% of DORIS beamtime was allocated for synchrotron radiation experiments [15]. With high brilliance, tuneable photon energy, and possible X-ray beam focus on the order of a few nanometers, synchrotrons are superb microscopes. The energy of the produced synchrotron radiation ranges from soft X-rays at below 4 keV to hard X-rays at up to hundreds of keV. This wide energy range allows research in a variety of fields. While synchrotron radiation is suited for fundamental research [28], it also poses great opportunities for the characterization of industry-relevant materials and devices [29–31]. Cultural heritage and life science studies further profit from the highly advanced measurement techniques [28, 32–34].

The advent of fourth-generation synchrotrons, like the ESRF in Grenoble [35] or the planned PETRA IV [36] project in Hamburg, underlines the need to open these state-of-the-art resources for the community outside of academia. One example of a successful application of synchrotron radiation for the immediate benefit of society is the medical screening for possible treatments of Covid-19 [37].

Next to the pandemic, the effects of climate change have been increasingly felt all

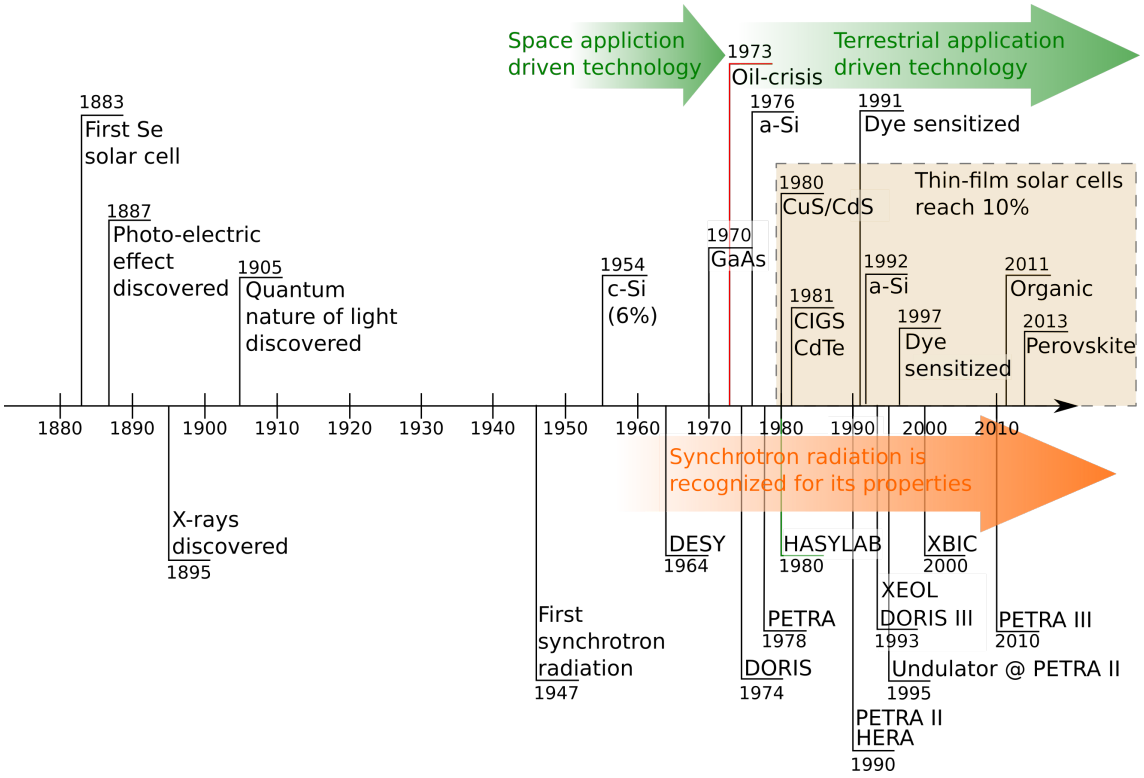

Figure 1.1: Highlights of solar-cell [18–25] (top) and synchrotron radiation [14, 15, 26, 27] (bottom) developments. Dates in the beige box show when a thin-film technology reached 10% efficiency.

around the world and the scientific community is presently strongly discussing future endeavors to handle this global crisis [38–40]. In order to decrease the emission of greenhouse gases and to strengthen the development of renewable energy technologies, synchrotron-based measurements can help to understand i.a. catalytic reactions [41], batteries [42], and solar cells [43].

The latter has undergone rapid development in the last 140 years. Some events are highlighted in Fig. 1.1. The first solar cell based on Se was invented in 1883 by Fritts [18], even before the discovery of the photo-electric effect in 1887 by Hertz [19]. The more commonly known crystalline Si (c-Si) solar cells, which still today hold the major share of the photovoltaic market [44], were first reported in 1954 by Chapin, Fuller, and Pearson [21]. While the photovoltaic (PV) device development was initially focused on space application, after the oil crisis in 1973 it shifted to terrestrial application. As c-Si solar cell absorbers are typically hundreds of micrometers thick [44], alternatives needing less material have emerged. These thinner cells are generally placed under the name of thin-film (TF) solar cells and cover a variety of material systems. The first reported TF solar cell was made from

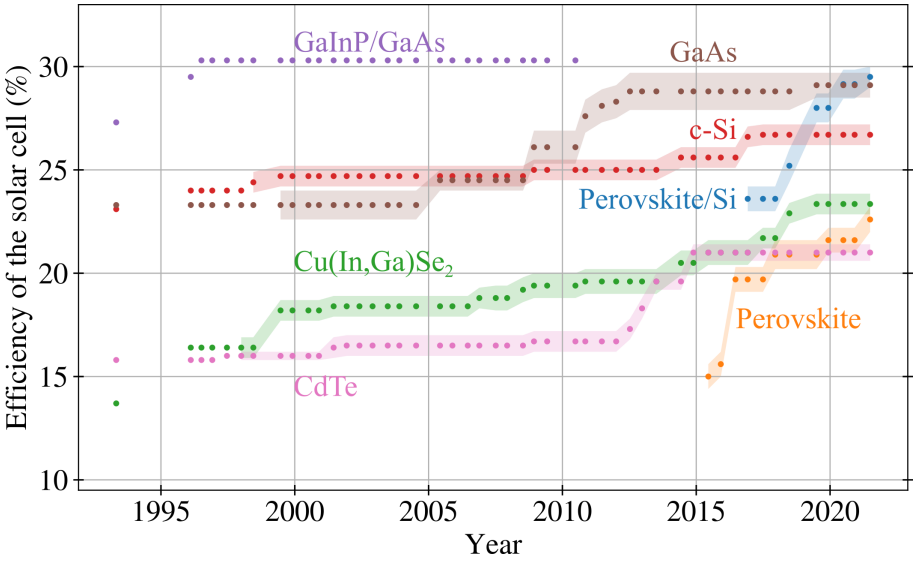

Figure 1.2: Progress in solar cell efficiencies over the years for selected types of cells. The data is taken from the solar efficiency tables by Green et al. from 1991 to 2021 [47]. The dates are the publication dates of the efficiency tables. The colored bands indicate the uncertainties. The cells have a size of at least 1 cm^2 and are measured under the global AM1.5 spectrum (1000 W/m^2) at 25 °C.

amorphous Si (a-Si) in 1976 [23]. From 1980, TF solar cells started to reach the threshold of 10% efficiency [24, 45, 46], as is highlighted in Fig. 1.1 in the beige box.

The emergence of efficient TF solar cells coincides with the growing application of synchrotron radiation. Note that two highlighted measurement modalities, the X-ray excited optical luminescence (XEOL) [26] and the X-ray beam induced current (XBIC) [27], are used to assess the optical and electrical performance of devices and thus are of great interest for solar-cell characterization.

In recent years, the efficiencies of TF solar cells have rapidly improved as can be seen in Fig. 1.2 [47] for selected types. GaAs and c-Si are included here as a comparison to Cu(In,Ga)Se_2 and perovskite solar cells, which will be studied in this work. As can be seen, there is still a gap in efficiencies, but there was rapid improvement in the last seven years. Perovskites and Cu(In,Ga)Se_2 are both of interest for tandem applications [48] where two solar cells are stacked upon each other to complementary harvest the solar light more efficiently. With a perovskite/Cu(In,Ga)Se_2 tandem, efficiencies above 30% are expected to be feasible [49].

Even now, with still lower efficiencies than c-Si and GaAs, TF solar cells have critical advantages in applications. Due to their thinness, they are flexible, opening the field

of applications to curved surfaces, e.g. rooftop tiles, car hoods, or windows, or even clothing.

To further the progress of higher efficiencies for Cu(In,Ga)Se_2 and perovskite solar cells, it is necessary to understand the limiting factors. Both Cu(In,Ga)Se_2 and perovskites are composite materials grown in a grain-like structure. At grain boundaries, the symmetry of the crystals is broken. This can lead to a heightened presence of defect states or in the case of Cu(In,Ga)Se_2 to even voids or crevices in the absorber [50, 51]. Another cause for efficiency loss can be lateral inhomogeneities in the absorber layers, which is especially a problem for some perovskites [52, 53].

To gain a comprehensive picture of the nature of these defects and inhomogeneities, multi-modal measurements are necessary. Synchrotron-based hard X-ray microscopes are able to meet the characterization challenges of TF solar cells: they provide X-ray spot sizes down to the nanometer scale [54–57] and the penetration depth of hard X-rays allows to probe the different device layers [58], including buried absorber layers. With a wealth of different measurement techniques at a scanning X-ray microscope [30, 59], it becomes possible to simultaneously study not just one, but many different aspects of solar cells within multi-modal measurements and to correlate the observed characteristics [60]. For example, XBIC measurements were successfully combined with X-ray fluorescence (XRF) [61–63], XEOL [64, 65], and X-ray diffraction (XRD) [66, 67] to correlate the electrical performance with composition, optical performance, and structure, respectively [43].

The experiments conducted in this work are a firm step further onto the path toward measurements for a wide application of synchrotron-based characterization techniques for TF solar cells. Here, multi-modal scanning X-ray microscopy at synchrotron facilities can offer advantages to studying TF solar cells on a nanometer scale; these advantages are explored and showcased. With the possibilities shown here, we hope that the potential of multi-modal X-ray scanning microscopy characterization measurements will be realized as a standard at fourth-generation synchrotrons and be available for industrial research and development.

The following chapter covers a basic understanding of relevant processes in TF solar cells and their measurement parameters. In Chapter 3 the experimental environment is introduced. This encompasses the comparison of the three synchrotron beamlines and endstations used in this work, the main scanning X-ray microscopy techniques, and finally a discussion of measurement strategies. Chapter 4 covers the methodological development of lock-in amplified X-ray beam induced current

measurements and is based on Ref. [1]. The methods discussed in Chapter 3 and the development presented in Chapter 4 are applied in two science cases in Chapters 5 and 6. Chapter 5 discusses a series of Cu(In,Ga)Se_2 solar cells with varying Ga/In ratio, which is based on Ref. [3]. The impact of Cs on the optical performance of a series of perovskite solar cells is studied in Chapter 6 which is based on Ref. [4]. Finally, an outlook for further development possibilities is given.

2 Solar cells

This chapter will give a brief introduction to the concept of TF solar cells. Starting from the direct to the indirect bandgap of semiconductors, the manipulation of the Fermi-level, recombination processes, and the distribution and occupation of electric states in the solar cell are discussed. Characteristic solar-cell parameters will be introduced and equivalent-circuit models for the solar cell will be presented. For the general working principle of solar cells see Refs. 68, 69.

2.1 Thin-film solar cell design

Semiconductors have an energy range called the bandgap E_g in which no electronic states are allowed. The energy states above the bandgap form the conduction band (CB), while the states below form the valence band (VB). For a semiconductor at the absolute zero of temperature, it is expected that all electrons occupy the states in the VB [70]. While electrons in the VB are highly localized, electrons which have been excited to the CB are able to travel through the material. Analogously, the hole resulting from the excitation of an electron can travel through the material in the VB.

As a crystal is a repetitive structure, it is enough to describe one unit cell. The same is valid in the reciprocal (k-)space where the band structure is described in a single Brillouin zone by Bloch's theorem. It is the description of waves in a periodic medium, which can be solved within a single Brillouin zone and gives the bands their curvature [70]. The curvature of the bands is usually displayed in a form where the bands are plotted from the central point Γ to different positions at the border of the Brillouin zone. There are two types of semiconductors: direct semiconductors where the VB maximum and CB minimum are at the same position of the Brillouin zone, and indirect semiconductors where the VB maximum and CB minimum are offset. The energy diagrams of a direct and indirect bandgap are schematically shown in Fig. 2.1. For the photo-induced transition of an electron from the VB

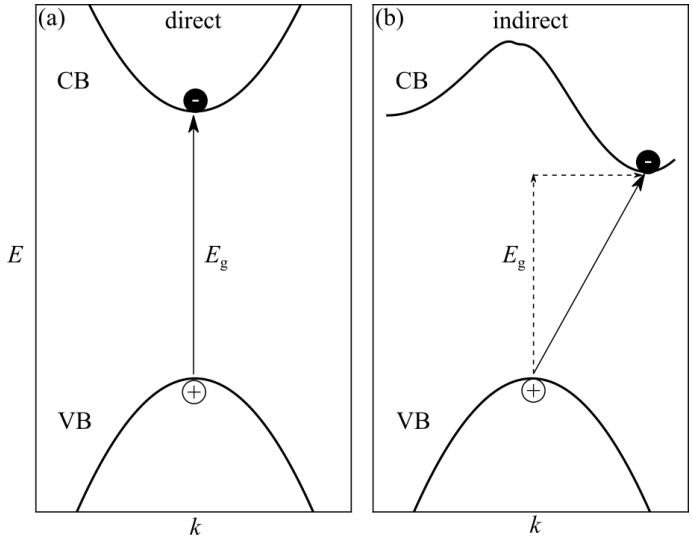

Figure 2.1: Schematic representation of a direct (a) and indirect (b) bandgap. The conduction band (CB) and valence band (VB) as a function of the position in the Brillouin zone (k-space) are shown as black lines. The width of the bandgap is indicated by the length of the vertical arrows.

to the CB, the incoming photon has to have an energy larger than E_g and in the case of an indirect bandgap an additional momentum, in the form of a phonon, is necessary. This additional momentum reduces the absorption cross-section for indirect semiconductors compared to direct semiconductors.

TF solar cells are based on the working principle of p-n junctions [68,69,71]. To create these, they are grown on sub- or superstrates in a layered structure. Simple stacking schemes for exemplary perovskite, Cu(In,Ga)Se_2, and CdTe solar cells is shown in Fig. 2.2. The perovskite solar cell has the thinnest absorber layer with 500 nm, Cu(In,Ga)Se_2 solar-cell absorbers are around 2–3 µm thick, while CdTe is the thickest, here with 5–11 µm. The absorbers in Cu(In,Ga)Se_2 and CdTe cells are p-doped and both have an n-CdS buffer layer. Perovskites are ambipolar semiconductors and can thus be doped to either n- or p-type [76]. A perovskite solar cell has dedicated electron- and hole-transport layers (ETL and HTL), which are here the C_{60} and NiO_x respectively, and with the perovskite as an intrinsic (i) semiconductor they build up a p-i-n structure.

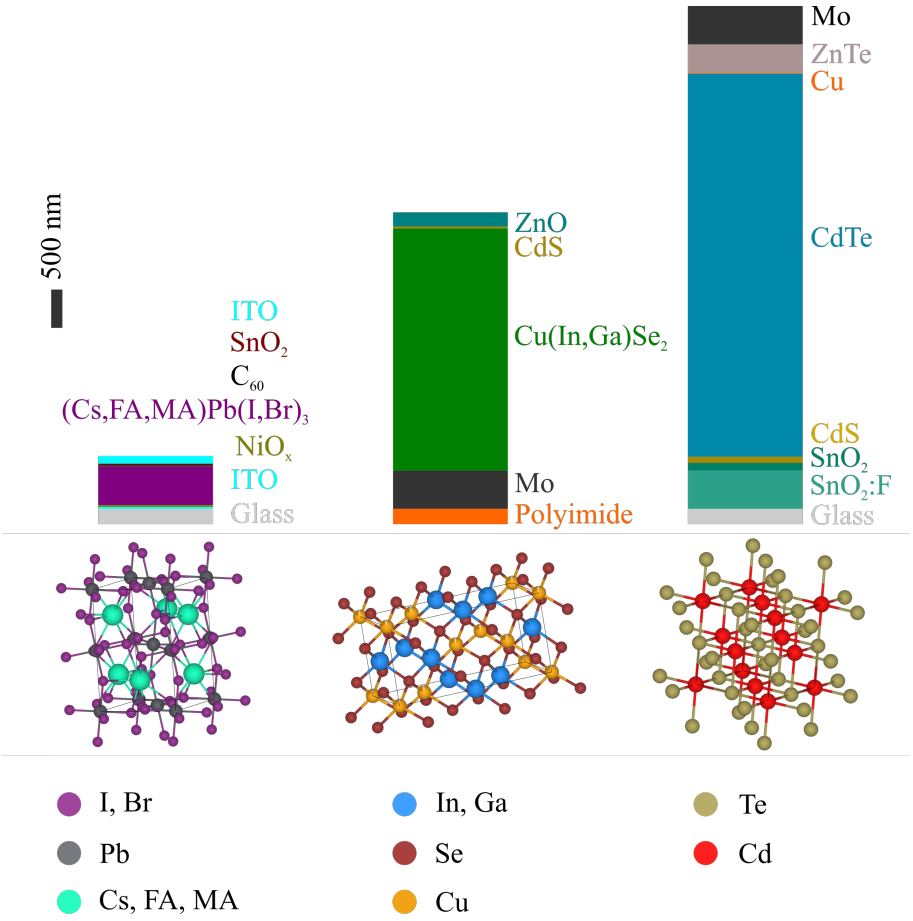

Figure 2.2: Stacking scheme of a perovskite, $Cu(In,Ga)Se_2$, and CdTe solar cell. Typical absorber thicknesses are shown and the other layers are to scale, except for the polyimide and glass layers. The crystallographic structure is made with VESTA [72] and the structures were taken from the open crystallographic database [73–75]. The structures of the perovskite and $Cu(In,Ga)Se_2$ show the composition of $CsPbI_3$ and $CuInSe_2$, respectively. The crystallographic structure of $CsPbI_3$ is a perovskite structure, the $Cu(In,Ga)Se_2$ is a chalcopyrite structure, and the CdTe is a zincblende structure.

2.2 Free charge carriers in thin-film solar cells

As mentioned above, electrons travel only in the CB and holes only in the VB. Therefore, it is of interest to understand the available electronic states and how they are occupied. For the bulk of crystals, the band structure is repetitive; however, as soon as the symmetry is broken additional states or band-bending might occur. Also, variations in the composition of the absorber material affect the band structure and available electronic states. This can be by design in the form of doping or due to the growth process, or unintentionally by the appearance of grain boundaries or

defects.

The following gives a brief summary of electronic states in semiconductors in thermal equilibrium and under illumination, as well as the recombination processes of charge carriers leading back to the equilibrium state.

2.2.1 Fermi levels in semiconductors

The Fermi level in a metal describes the energy level between occupied and unoccupied states [77]. In the case of a non-degenerate semiconductor, the Fermi level lies in the bandgap. The summarized mathematical description of the energy-state occupation presented from hereon will follow Ref. 68.

Semiconductor in thermal equilibrium To determine the number of occupied CB states n in intrinsic semiconductors, the density of states $N(E)$ over all energy levels from the bottom of the CB E_C to the top E_top is multiplied by the occupation density $F(E)$ and then integrated:

$$n = \int_{E_\mathrm{C}}^{E_\mathrm{top}} N(E)F(E)dE. \tag{2.1}$$

The occupation density is the Fermi-Dirac distribution function

$$F(E) = \frac{1}{1+\exp\left\{\frac{E-E_\mathrm{F}}{k_\mathrm{B}T}\right\}} \approx \exp\left\{\frac{E_\mathrm{F}-E}{k_\mathrm{B}T}\right\}, \tag{2.2}$$

with k_B as Boltzmann's constant, T the absolute temperature, and E_F the Fermi energy. The approximation in Eq. 2.2 is valid in the low-temperature regime for energies $E > E_\mathrm{F} + 3k_\mathrm{B}T$, and is called the Boltzmann approximation.

The Fermi energy can be derived from the condition that charge neutrality has to be kept. In the general case, where the Fermi-energy level is several kT below E_C, the Boltzmann approximation is valid, and Eq. 2.1 can be expressed as

$$n = N_\mathrm{C}\exp\left\{-\frac{E_\mathrm{C}-E_\mathrm{F}}{k_\mathrm{B}T}\right\} \tag{2.3}$$

where N_C is an effective density of states in the conduction band. A similar description

can be found for holes in the valence band and is given as

$$p = N_{\mathrm{V}} \exp\left\{-\frac{E_{\mathrm{F}} - E_{\mathrm{V}}}{k_{\mathrm{B}}T}\right\} \tag{2.4}$$

where N_{V} is the effective density of states in the valence band.

In equilibrium, the number of carriers n and p is equal to the square of the intrinsic number of carriers n_{i}

$$np = n_{\mathrm{i}}^2 = N_{\mathrm{C}} N_{\mathrm{V}} \exp\left\{\frac{-E_{\mathrm{g}}}{k_{\mathrm{B}}T}\right\}. \tag{2.5}$$

This is called the equilibrium relation and $E_{\mathrm{g}} = E_{\mathrm{C}} - E_{\mathrm{V}}$.

With the introduction of foreign atoms into the crystal lattice, additional electronic states are created, even in the bandgap region. When donor atoms are incorporated, they 'donate' additional free electrons due to a mismatch in valence bonds with the surrounding material. A schematic highlighting the influence of donor- and acceptor-states inside of the bandgap can be seen in Fig. 2.3. The donor impurities create new electronic states, indicated in orange in Fig. 2.3 (a), and the Fermi level (b) is shifted towards the conduction band. Thus the amount of free electrons is increased (c). In the case of acceptor atoms, they 'accept' electrons, thus creating extra holes. Electronic states close to the valence band (Fig. 2.3 (a), blue) are introduced and the Fermi level is shifted towards the valence band. This creates extra free holes as can be seen in (c). The intentional addition of donors or acceptors to the material is called doping, and the amount of free holes and electrons is carefully manipulated.

As charge neutrality has to be kept, the total negative charges and total positive charges in the semiconductor need to be equal. For example, in the case of donors in the material, the electron density n in the CB is equal to the hole density p in the VB plus the density of ionized donors N_{D}^+

$$n = N_{\mathrm{D}}^+ + p. \tag{2.6}$$

N_{D}^+ is given by

$$N_{\mathrm{D}}^+ = N_{\mathrm{D}} \left[\frac{1}{1 + g \exp\left\{\frac{E_{\mathrm{F}} - E_{\mathrm{D}}}{k_{\mathrm{B}}T}\right\}}\right] \tag{2.7}$$

where E_{D} is the energy of the donor state, and g is the ground-state degeneracy of the donor impurity level (here, $g = 2$: no electron, or one electron of either spin).

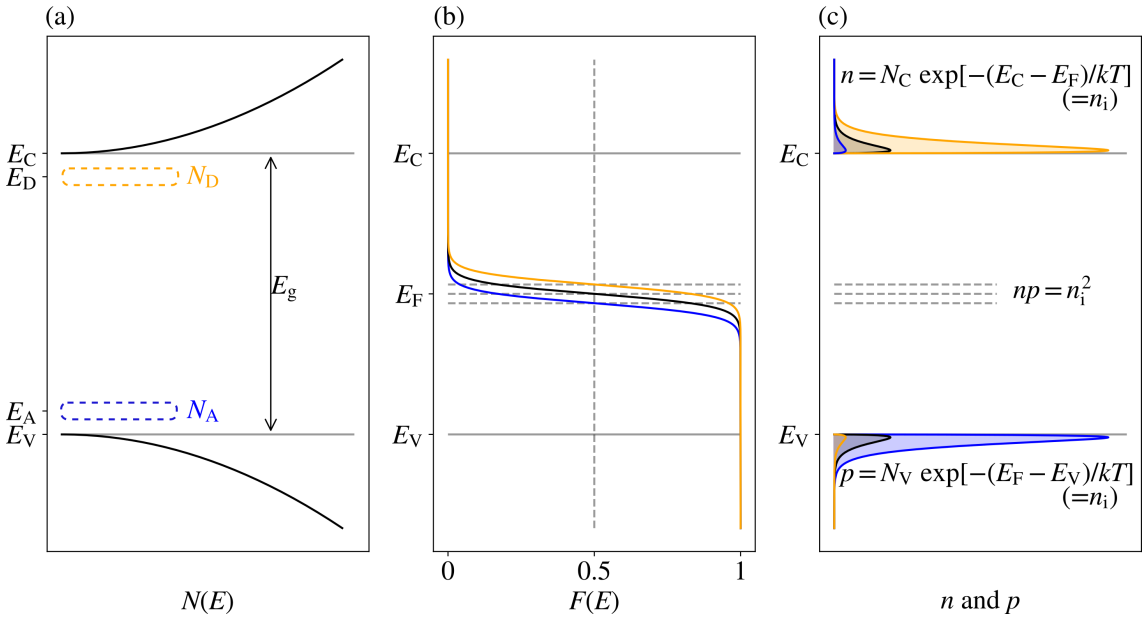

Figure 2.3: Schematic of a semiconductor-state occupation. Three cases are shown: an intrinsic semiconductor in black, a semiconductor with donor atoms in orange, and with acceptor atoms in blue. (a) Density of states $N(E)$ of an intrinsic semiconductor, or with donor (N_D) or acceptor (N_A) states. (b) The Fermi-Dirac distribution with no additional states, additional donor states, or additional acceptor states present (plotted for room temperature, small values were chosen to fit a linear scaling for (c)). (c) The number of occupied states for electrons n and holes p. The position of the Fermi level is dictated by the charge neutrality. For all three cases here $np = n_i^2$ is valid. Figure adapted from Ref. [68].

Analogously, the number of ionized acceptors N_A^- can be expressed as

$$N_A^- = N_A \left[\frac{1}{1 + g \exp\left\{ \frac{E_A - E_F}{k_B T} \right\}} \right], \tag{2.8}$$

with $g = 4$ (no hole, or one hole for one electron of either spin plus double degeneracy due to two degenerate valence bands at $k = 0$). Inserting Eq. 2.7, Eq. 2.3, and Eq. 2.4 into Eq. 2.6 gives

$$N_C \exp\left\{ -\frac{E_C - E_F}{k_B T} \right\} = N_D \left[\frac{1}{1 + 2 \exp\left\{ \frac{E_F - E_D}{k_B T} \right\}} \right] + N_V \exp\left\{ -\frac{E_F - E_V}{k_B T} \right\}, \tag{2.9}$$

which allows for a given set of N_C, N_D, N_V, E_C, E_D, E_V, and T the determination of the Fermi level E_F.

A material with an excess of free electrons is called n-type and a material with an excess of free holes is called p-type. The charge neutrality still holds at equilibrium and at relatively elevated temperatures all donor and acceptor atoms are ionized and Eq. 2.5 can be written as

$$n + N_{\mathrm{A}}^{-} = N_{\mathrm{D}}^{+} + p. \tag{2.10}$$

For an n-type semiconductor, the Fermi level is defined as

$$E_{\mathrm{F}} = E_{\mathrm{i}} + k_{\mathrm{B}}T \ln\left(\frac{n_{\mathrm{no}}}{n_{\mathrm{i}}}\right), \tag{2.11}$$

where n_{no} is the concentration of electrons in an n-type semiconductor at thermal equilibrium and E_{i} is the Fermi level of an intrinsic semiconductor. For a p-type semiconductor, the Fermi level can be defined as

$$E_{\mathrm{F}} = E_{\mathrm{i}} - k_{\mathrm{B}}T \ln\left(\frac{p_{\mathrm{po}}}{n_{\mathrm{i}}}\right), \tag{2.12}$$

where p_{po} is the concentration of holes in a p-type semiconductor at thermal equilibrium.

Semiconductor in non-equilibrium In the case of non-equilibrium conditions, as is the case for a solar cell under illumination, excess carriers are excited and the equilibrium relation holds no longer. Using the Boltzmann relation and introducing so-called *quasi-Fermi levels* for electrons Φ_{n} and holes Φ_{p} respectively, the number of carriers can be expressed as

$$n \equiv n_{\mathrm{i}} \exp\left\{\frac{(\Phi_{\mathrm{n}} - E_{\mathrm{i}})}{k_{\mathrm{B}}T}\right\} \tag{2.13}$$

and

$$p \equiv n_{\mathrm{i}} \exp\left\{\frac{(E_{\mathrm{i}} - \Phi_{\mathrm{p}})}{k_{\mathrm{B}}T}\right\} \tag{2.14}$$

where n_{i} is the intrinsic carrier concentration and E_{i} is the intrinsic Fermi-level. The equations above can be rearranged to give the quasi-Fermi levels

$$\Phi_{\mathrm{n}} = E_{\mathrm{i}} + \frac{k_{\mathrm{B}}T}{q} \ln\left(\frac{n}{n_{\mathrm{i}}}\right), \tag{2.15}$$

$$\Phi_{\mathrm{p}} = E_{\mathrm{i}} - \frac{k_{\mathrm{B}}T}{q} \ln\left(\frac{p}{n_{\mathrm{i}}}\right). \tag{2.16}$$

Excess holes or electrons bring the quasi-Fermi levels closer to the valence and conduction band, respectively. The p-n product can be thus written as

$$pn = n_{\mathrm{i}}^2 \exp\left\{\frac{(\Phi_{\mathrm{n}} - \Phi_{\mathrm{p}})}{k_{\mathrm{B}}T}\right\}. \tag{2.17}$$

With $(\Phi_{\mathrm{n}} - \Phi_{\mathrm{p}})/q = V$ as the electrostatic potential difference across a p-n junction, we can rearrange Eq. 2.17 and get

$$V = \frac{k_{\mathrm{B}}T}{q} \ln\left(\frac{pn}{n_{\mathrm{i}}^2}\right). \tag{2.18}$$

In a perfect solar cell, this potential difference corresponds to the open-circuit voltage V_{OC} [78, 79]. The difference between E_{g} and V_{OC}, denoted the open-circuit-voltage deficit, gives an estimate for the quality of a solar cell: the smaller the deficit, the better the cell.

Recombination processes Besides the desired introduction of impurities into the absorber matrix to tune the Fermi levels, defect sites can severely hinder the charge-collection process. Donor or acceptor states inside the bandgap, depending on their energetic position, can act as traps for holes or electrons, respectively, or as recombination centers. Traps are shallow states where the probability to be re-emitted into the CB for electrons or into the VB for holes is greater than the probability for the charge carriers to recombine [80].

A solar cell in which the charge carriers are not collected, is in the so-called open-circuit state. The excited charge carriers recombine to restore thermal equilibrium after a time. The different recombination pathways the carriers can take are illustrated in Fig. 2.4. Figure 2.4(a) shows the possible capture and emission processes, in the case of an impurity level close to the middle of the bandgap which acts as a recombination center. The impurity state can interact with the charge carriers in four ways: electron capture, electron emission, hole capture, and hole emission [80]. Two of these processes are involved in recombination where first an electron and afterward a hole is captured.

The recombination rate U is given by [71, 81, 82]

$$U = \frac{\sigma_{\mathrm{p}}\sigma_{\mathrm{n}}\nu_{\mathrm{th}}(pn - n_{\mathrm{i}}^2)N_{\mathrm{t}}}{\sigma_{\mathrm{n}}\left[n + n_{\mathrm{i}}\exp\left\{\frac{E_{\mathrm{t}}-E_{\mathrm{i}}}{k_{\mathrm{B}}T}\right\}\right] + \sigma_{\mathrm{p}}\left[p + n_{\mathrm{i}}\exp\left\{-\frac{E_{\mathrm{t}}-E_{\mathrm{i}}}{k_{\mathrm{B}}T}\right\}\right]}, \tag{2.19}$$

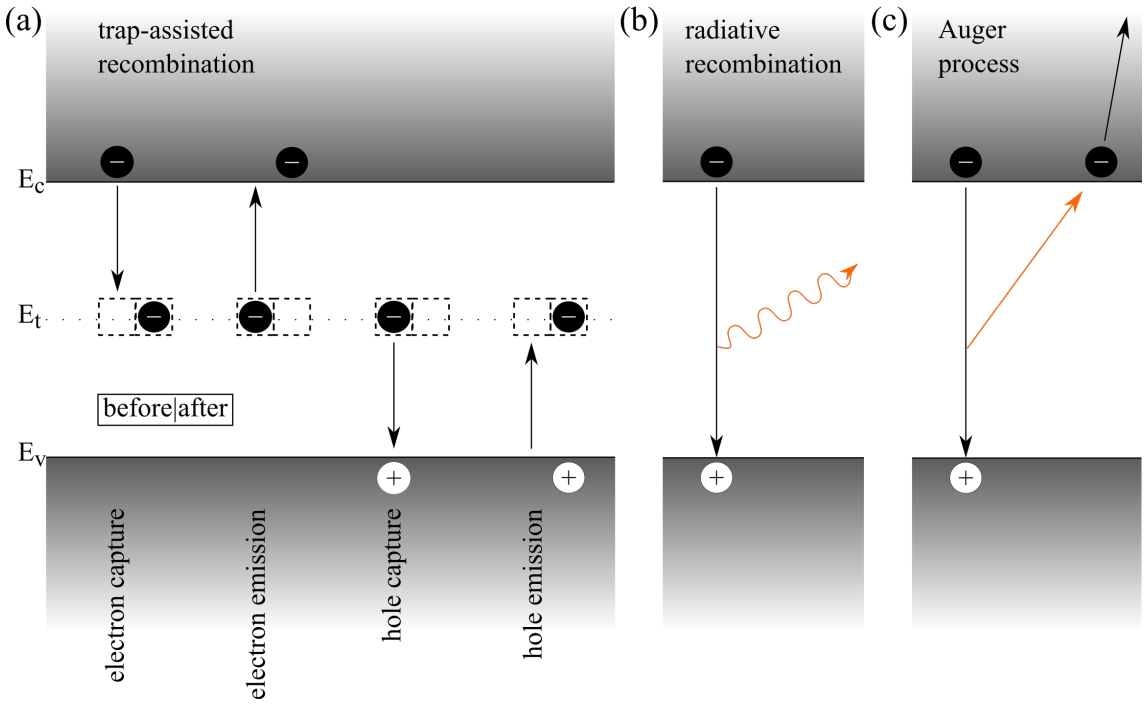

Figure 2.4: Schematics of recombination pathways. (a) Single-trap assisted recombination with electron capture, electron emission, hole capture, and hole emission. For each process, the left side is before and the right side after the event. (b) Radiative band-to-band recombination. (c) Band-to-band recombination with excitation of a second electron - Auger process.

with σ_p and σ_n as the hole- and electron-capture cross sections, ν_{th} the carrier thermal velocity, N_t the trap density, and E_t the trap energy level. If the defect-state energy is close to the intrinsic Fermi level, the trap-assisted recombination rate reaches its maximum. For an intrinsic semiconductor, this would translate to a defect state in the middle of the bandgap. These deep defect sites are usually associated with large lattice distortions. Recombination from those states is more likely to happen via the dissipation of energy into heat and without the emittance of a photon [83]. In the solar-cell community, this recombination via a defect state is broadly referred to as Schockley-Read-Hall (SRH) recombination [84].

At low illumination intensities, the excited charge carriers are very likely to be captured by the available trap states. Furthermore, the recombination rate is dependent on the minority carrier concentration, as the change in majority carriers is comparably small, making this type of recombination a mono-molecular process.

In an ideal solar cell without traps, all carriers would recombine directly from band to band either under the emission of a photon with the energy of the bandgap, called radiative recombination, which is shown in Fig. 2.4 (b), or by exciting another

electron in an Auger process as shown in (c).

When the illumination of the solar cell excites more carriers than defect states are present in the material, radiative recombination becomes the dominant recombination process [84]. In this case, both hole and electron concentrations are limiting the recombination rate, thus making it a second order or bi-molecular process [84, 85].

Besides the SRH and radiative recombination, Auger processes can also occur [68,86]. In that case, the energy from the band-to-band recombination excites another electron in the conduction band to a higher electronic state. At very high illumination and thus high free-carrier concentrations, this Auger process becomes dominant. As two electrons and one hole are involved in this process, it is referred to as a tri-molecular process [85, 87, 88].

The different recombination processes of charge carriers are often expressed in a summarizing and simplified way as

$$-\frac{dn}{dt} = k_1 n + k_2 n^2 + k_3 n^3, \tag{2.20}$$

where n is the charge density and the k_i refers to the mono-, bi-, and tri-molecular recombination rate constants, respectively.

The processes become more complex when more than one trap state is involved and will not be discussed here. An extensive description of the recombination mechanisms is given in the literature, see, e.g., the issues 11–12, volume 21 of Solid-State Electronics from 1978, which cover a wide range of articles on recombination in semiconductors, with the summary article of Mott [89].

Unwanted states in the bandgap can not only be introduced by impurities but at any break in the symmetry of the crystal. This includes individual spots, e.g., due to ionization, or spatial occurrences like grain boundaries or interfaces [90, 91] in the solar-cell stack.

2.3 Performance evaluation of solar cells

For the determination of the overall efficiency of solar cells, a current-voltage measurement (JV-curve) and the external quantum efficiency (EQE) are often evaluated.

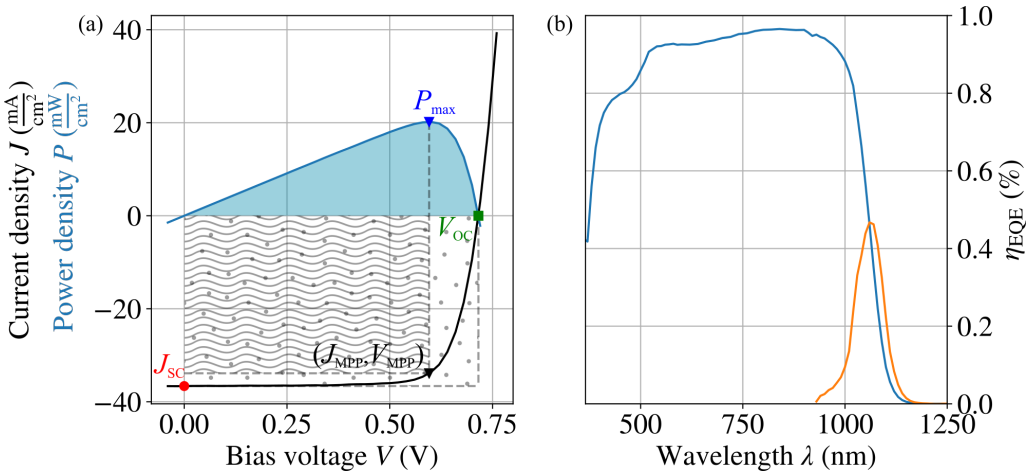

Figure 2.5: (a) Exemplary JV-curve of a Cu(In,Ga)Se_2 solar cell measured with standard AM1.5G-illumination. Highlighted are the open-circuit voltage V_{OC} (green), short-circuit current-density J_{SC}, and the maximum power point (J_{MPP},V_{MPP}) (black), where the highest power P_{max} (blue) is generated. For the fill factor C_{FF} the area spanned by J_{MPP} and V_{MPP} is highlighted with waves and the area spanned by J_{SC} and V_{OC} is highlighted with dots. (b) Exemplary external quantum efficiency (EQE) curve of a similar Cu(In,Ga)Se_2 solar cell as in (a), the gradient is flipped, arbitrarily scaled, and plotted in orange to highlight the inflection point. Data for these curves were kindly provided by EMPA.

2.3.1 JV-curve

In Fig. 2.5 (a), a measured curve of a Cu(In,Ga)Se_2 solar cell is shown. The sample was produced by EMPA (Eidgenössische Materialprüfungs- und Forschungsanstalt), and the measurement data was kindly provided by them. For the JV-curve an irradiance I_{in} corresponding to the AM1.5G-spectrum [92] with 1000 W/m^2 illumination intensity was used. During the measurement the bias voltage applied to the solar cell is varied, and the current is measured. The intersecting points with the axes denote the short-circuit current density (J_{SC}, red dot) and the open-circuit voltage (V_{OC}, green square). From the voltage and the current density, the generated power of the solar cell can be calculated as

$$P = J \times V, \tag{2.21}$$

and is here plotted in blue. The optimal working point of the solar cell is given at (J_{MPP},V_{MPP}) (black triangle), where the power is at the maximum (P_{max}, blue triangle). The fill factor C_{FF} is defined as the ratio of P_{max} to the product of J_{SC}

and V_{OC}

$$C_{\mathrm{FF}} = \frac{P_{\mathrm{max}}}{J_{\mathrm{SC}} V_{\mathrm{OC}}}. \tag{2.22}$$

For an intuitive illustration, the areas represented by both are indicated with waves (P_{max}) and dots ($J_{\mathrm{SC}} V_{\mathrm{OC}}$).

Using the maximum power P_{max}, the conversion efficiency η_{eff} of the solar cell can be calculated as

$$\eta_{\mathrm{eff}} = \frac{P_{\mathrm{max}}}{I_{\mathrm{in}}} = \frac{J_{\mathrm{SC}} V_{\mathrm{OC}} C_{\mathrm{FF}}}{I_{\mathrm{in}}}. \tag{2.23}$$

The efficiency of the cell shown in Fig. 2.5 (a) is thus

$$\eta_{\mathrm{eff}} = \frac{20.19\,\mathrm{mW/cm^2}}{1000\,\mathrm{W/m^2}} = \frac{36.62\,\mathrm{mA/cm^2} \cdot 0.72\,\mathrm{V} \cdot 0.77}{1000\,\mathrm{W/m^2}} = 0.20.$$

2.3.2 External quantum efficiency

Figure 2.5 (b) shows the measurement of the external quantum efficiency (EQE) η_{EQE} of a similar Cu(In,Ga)$\mathrm{Se_2}$ solar cell as in Sec. 2.3.1. The EQE describes the fraction of incident photons, which create electron-hole pairs that are collected. As the plot already shows, η_{EQE} is wavelength dependent and defined as

$$\eta_{\mathrm{EQE}}(\lambda) = \frac{I_{\mathrm{ph}}(\lambda)}{q \Psi_{\mathrm{ph},\lambda}}, \tag{2.24}$$

with I_{ph} as the photo-generated current, q the elemental charge, and $\Psi_{\mathrm{ph},\lambda}$ the spectral photon flow incident on the solar cell.

There are several methods to extract the bandgap of semiconductors as detailed in Ref. [93]. Figure 2.5 (b) illustrates one method where the derivative of the high wavelength EQE edge is used to find the inflection point which corresponds to the bandgap value. The peak wavelength λ_{g} of the derivative can be translated to the bandgap energy via

$$E = h\nu = h\frac{c}{\lambda}, \tag{2.25}$$

where h is Planck's constant and c is the speed of light. The energy for the bandgap obtained by this method here is 1.17 eV.

2.3.3 Equivalent circuit

To express the electrical characteristics of the solar cell mathematically, many models have been developed in the last 70 years [82, 94, 95], starting with equivalent circuit models of transistors [96]. In the following, the three most basic models will be briefly introduced [68, 69]. The net current flowing through a solar cell in the superposition approximation is given by how much current is generated by incident photons, as well as the thermally generated current, and is limited by the recombination current. The net current would thus be described as

$$J(V) = J_{\mathrm{rec}}(V) - J_{\mathrm{gen}}(V) - J_{\mathrm{ph}} = J_0 \left[\exp\left(\frac{qV}{k_B T} \right) - 1 \right] - J_{\mathrm{ph}} \tag{2.26}$$

where J_{rec} is the recombination current density, J_{gen} is the generation current density, J_{ph} is the photo-generated current density, and J_0 is the saturation current density. The solar cell can thus be approximated in an equivalent circuit that considers the contributions to the net current. Figure 2.6 shows the electrical elements used for these models. The p-n junction is commonly described with diodes, while the ideality factor n of the diode considers recombination at the p-n junction. For a factor of $n = 1$, no recombination would take place, thus indicating an ideal diode, while a factor greater than 1 indicates the presence of recombination. The generation of current through the incident photons is described by the circle and the rectangles symbolize resistors.

The simplest model describing Eq. 2.26 only implements one ideal diode and the current source generated by photons, which is drawn in black in Fig. 2.6 and is the ideal solar cell equivalent circuit.

Closer to reality is the extension of the model to include series R_{s} and parallel R_{p} resistances as shown in Fig. 2.6 when black and blue parts are considered. The net current is then described as

$$J = J_0 \left\{ \exp\left[\frac{q(V - J r_{\mathrm{s}})}{k_B T} \right] - 1 \right\} + \frac{V - J r_{\mathrm{s}}}{r_{\mathrm{p}}} - J_{\mathrm{ph}} \tag{2.27}$$

with r_{s} and r_{p} as the specific series and parallel resistance of the unit [$\Omega\mathrm{cm}^2$], respectively. When the parallel resistance decreases, it strongly affects the J_{MPP}, which is reduced. At very low r_{p} the open-circuit voltage is also significantly reduced. An increase in series resistance mainly reduces the V_{MPP}, and at very high resistance the short-circuit current is reduced as well. Thus a high parallel resistance r_{p} and

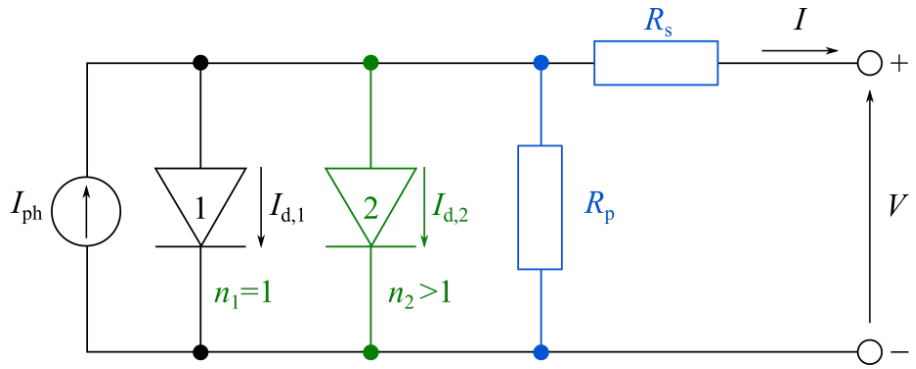

Figure 2.6: Equivalent circuit using the two diode model. The black parts are the basics for the ideal solar cell, adding the blue parts leads to a model for a solar cell with series and parallel resistance, and including the green parts the full two-diode model is shown.

low series resistance r_s are favorable for the solar cell efficiency.

Now, taking further into consideration additional recombination at the p-n junction, a two-diode model is often used. One diode is still assumed to be ideal with an ideality factor of $n = 1$ and the second diode is non-ideal taking recombination into consideration and having an ideality factor of $n > 1$.

Taking all parts of Fig. 2.6 into consideration, it shows the equivalent circuit for the two-diode model, and the J-V characteristics are given by

$$J = J_{0,1}\left\{\exp\left[\frac{q(V - Jr_s)}{n_1 k_B T}\right] - 1\right\} + J_{0,2}\left\{\exp\left[\frac{q(V - Jr_s)}{n_2 k_B T}\right] - 1\right\} + \\ + \frac{V - Jr_s}{r_p} - J_{ph} \tag{2.28}$$

where n_i are the ideality factors of the respective diodes.

These models describe the macroscopic behavior of the solar cell, while many processes and effects that may affect the efficiency of a solar cell are left untouched. One example is leakage-currents, this could be considered by adding another diode to the model [97]. Another example is the capacitance effects of layers other than the absorber, which can be included as a capacitor [98]. Araújo et al. [95] give a detailed overview on the different models and strategies to obtain the JV-parameters and rank the best approaches [99–102].

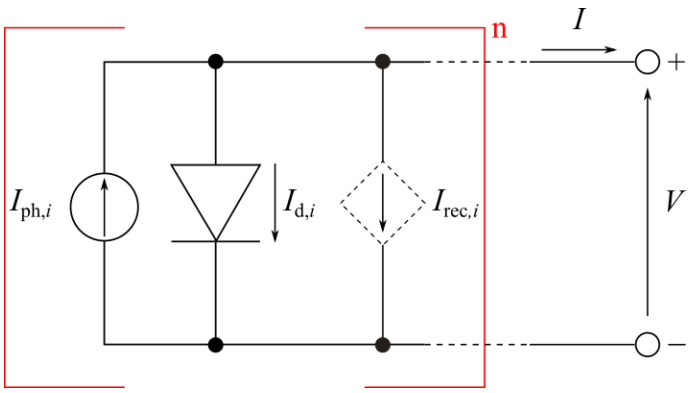

Figure 2.7: Schematic to illustrate a visualization of the equivalent circuit for microscopic measurements of a solar cell.

2.3.4 Microscopical approach

The overall efficiency of the solar cell is limited by its weakest part. To identify these parts a spatially resolved microscopical approach is needed. This is particularly true for TF solar cells which inherently suffer from inhomogeneities due to their polycrystalline and composite nature [61, 103]. The effect of grain boundaries, voids, or crevices on performance is of the highest interest, but their small size and the fact that the absorber is buried in an entire layer stack pose unique characterization challenges. Furthermore, the complex chemistry of multi-component absorber layers with co-existing phases and internal gradients requires advanced characterization methods [104].

The solar cells are typically measured either in the open-circuit state to obtain information about V_{OC}, the Fermi-level splitting and the bandgap, or in the short-circuit state to measure J_{SC}. In a multi-modal microscopy context, where the cell is raster scanned to resolve the electrical performance spatially, only a small part of the solar cell is illuminated and sophisticated modeling is required to understand the complex solar-cell response upon inhomogeneous illumination [105]. Accordingly, conclusions about the absolute efficiency of the solar cell are often not possible from XBIC measurements. Instead, the relative spatial quality of the solar cell is evaluated.

The cause for spatial performance inhomogeneity can, e.g., lie in an inhomogeneous amount of photo-generated current $I_{ph,i}$ due to a variation in absorber thickness, a local variation in the bandstructure, or defects affecting J_0. The simplified model in Fig. 2.7 considers these inhomogeneities by attributing each spot their individual sub-circuit with a photogenerated current $I_{ph,i}$, an ideality factor n_i for the diode

$I_{\mathrm{d},i}$, and a recombination term in form of a load $I_{\mathrm{rec,i}}$. By raster scanning the solar cell, the spots are individually excited and the resulting J_{SC} of the total system is evaluated.

The effect of a varying $I_{\mathrm{ph},i}$ is especially prominent when X-rays are used to raster scan the cell, as only a fraction of the incident photons is absorbed. Therefore, $I_{\mathrm{ph},i}$ scales almost linearly with the thickness of the absorber [43].

3 Experimental environment and methods

Using X-rays instead of visible light or electrons to evaluate solar cells gives some advantages: first, the diffraction limit is far lower, allowing to focus the beam down to sub 100 nm, and second, the penetration depth of hard X-rays is deep enough to measure fully encapsulated devices, and third, by employing a multi-modal approach the composition and structure of the material can be measured simultaneously with the performance [106].

Beamline endstations at synchrotron facilities are highly specialized characterization instruments [35, 36]. The energy range, sample environment, and available detectors are often tailored in a narrow but highly efficient operating field. In this chapter, the beamline endstations tailored for X-ray scanning microscopy that were used in this work will be introduced and the main measurement modalities presented.

3.1 Scanning X-ray microscopes

Synchrotrons all around the world have scanning hard X-ray microscopy beamlines with beam focus sizes in the sub-micrometer range. Figure. 3.1 shows a map of the worlds hard X-ray microscopy beamlines [6, 54–57, 107–114].

The data for this work was taken at different synchrotron light sources in Europe (Germany – Positron-Elektron Tandem-Ringanlage (PETRA III), France – European Synchrotron Radiation Facility (ESRF)) and the USA (Advanced Photon Source (APS)). In the following, the respective beamlines will be introduced. Comprehensive descriptions of each of the beamlines can be found in Refs. [6, 54–56, 115–117]. For an easy comparison, Fig. 3.2 illustrates the beamline setups and Tab. 3.1 shows the energy range, typical beam flux, and focus sizes, as well as available modalities.

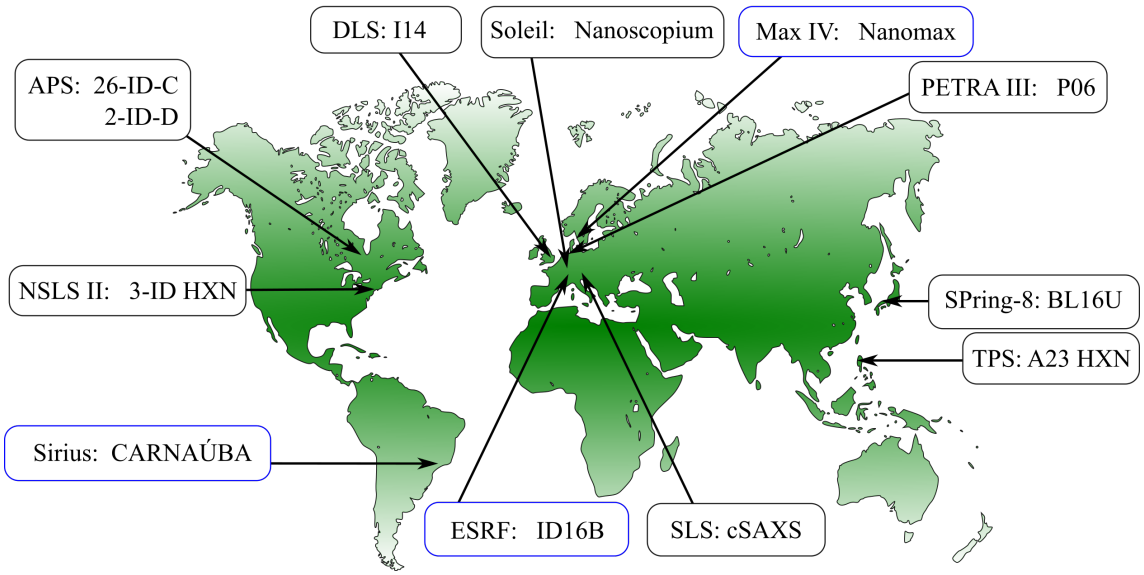

Figure 3.1: World map with hard X-ray microscopy beamlines highlighted. The blue framed beamlines are at a 4$^{\text{th}}$ generation synchrotron source. Information on the beamlines can be found in Refs. [6, 54–57, 107–114].

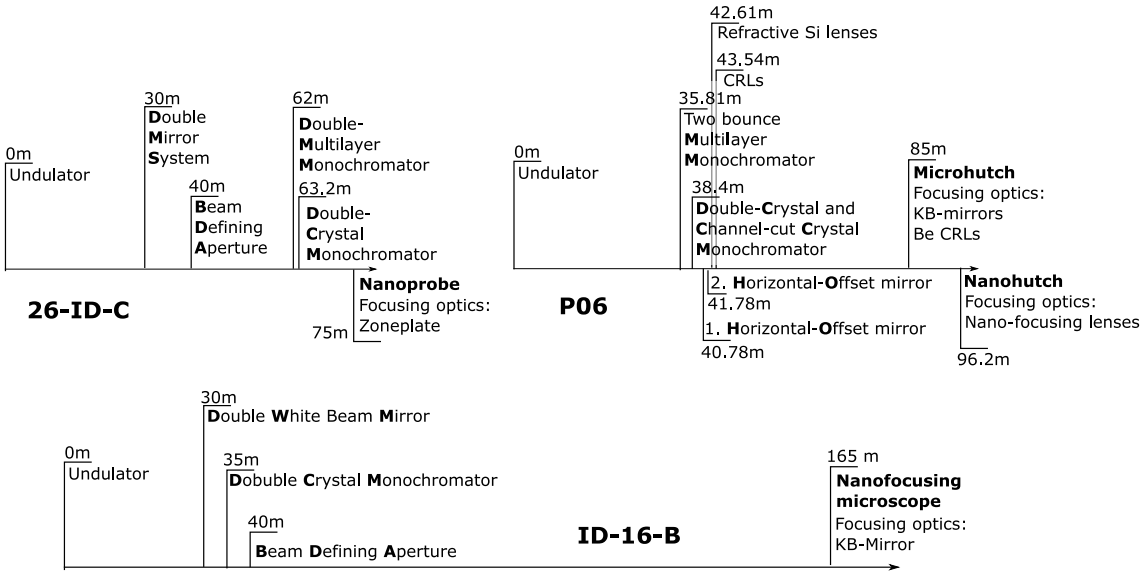

Figure 3.2: Arrangement of the optical beamline components of 26-ID-C, P06 and ID16B [6, 55, 56].

3.1.1 PETRA III — P06 micro-hutch

The beamline P06 of the PETRA III synchrotron ring at DESY has two endstations: the micro-hutch [126] and nano-hutch [6]. The micro-hutch is situated at a distance of 86.05 m to the undulator source. The nano-hutch starts at 96.2 m and allows the placement of an area-detector roughly 8 m downstream of the sample in the micro-

	P06 (micro)	ID16B	26-ID-C
Energy range (keV)	6–35 [54, 118]	5–33 [56, 117]	6–12 [33, 55]
Photon flux (ph/s)	$1 \cdot 10^{10}$ @ 12 keV [119]	$1.4 \cdot 10^{11}$ @ 29.33 keV [120]	$1.8 \cdot 10^{9}$ @ 9.75 keV [55]
Focus size (nm)	100 @ 12 keV [121]	50 @ 17.5 keV,29.6 keV [56]	< 40 @ 9.75 keV [55]
XRF	+ [122]	+ [10]	++ [123]
XBIC	+ [1]	(+) [10]	(+) [43]
XEOL	(+) [2, 4]	+ [124]	-
Ptychography	++ [6]	-	+ [125]
Tomography	++ [126]	+ [127]	+ [128]
XRD	+ [11]	+ [129]	+ [130]
XANES	+ [126]	+ [120]	+ [131]
Time-resolved measurements	+ [4]	+ [124]	++ [132]
Vacuum	+ [122]	-	++ [55, 116]

Table 3.1: Comparison of the three imaging beamlines, P06 (micro-hutch endstation) (PETRA III), ID16B (ESRF), and 26-ID-C (APS). A '+' indicates that the beamline is capable of the measurement of this modality, round brackets indicate user-supplied equipment to be necessary, and '-' indicates that this measurement modality is not accessible.

hutch [6]. The two sample stages in the micro- and nano-hutch are thus roughly 4.66 m apart [6]. The sample stages are built upon granite blocks to minimize vibrations. The micro-hutch has two options for focusing onto the sample, Kirkpatrick-Baez (KB) mirrors [133, 134] or Be-compound refractive lenses (CRLs) [121, 135]. The optics chamber is located directly under a granite bridge that hosts the beamline microscope. In this work, measurements were conducted in the micro-hutch and the Be-CRLs [136] were used. A focus of the coherent part of the X-ray beam down to around 100 nm full-width-half-maximum (FWHM) [2, 4] was achieved. The spacious and open environment allows the users at P06 high flexibility and a large degree of freedom in their options to arrange the necessary detectors and environments around the sample [2, 122, 137]. The normal operational energy range of P06 is between 6 to 35 keV [118] but can potentially go up to 100 keV [54].

3.1.2 ESRF — ID16B

The beamline endstation ID16B at the ESRF is located in a separate building together with the endstation ID16A and specializes in nano-analysis. The hutch is located 165 m from the source. The detectors and sample stages are situated on a granite block, which is further motorized to change between the pink-beam and monochromatic beam [56]. The energy range goes from 6 keV to 33 keV and the beam can be focused with KB-mirrors down to 50–100 nm [56, 117]. The sample stages, possible special sample environments [117, 138–140], as well as the detectors are all arranged on the granite block and built to minimize possible vibrations [56].

3.1.3 APS — 26-ID-C

The nanoprobe endstation of the beamline 26-ID-C at the APS is located 75 m from the source. The energy range is smaller compared to the previously discussed beamlines at 6 keV to 12 keV, although nominally the energy could be tuned from 3–33 keV with the implementation of different zone-plates [55]. While P06 and ID16B both use stages to move the sample, 26-ID-C primarily scans its zone plate to move the beam over the sample. The beam focus size can go down to 30 nm [55]. Furthermore, the sample is situated in a vacuum chamber, which limits the possible arrangement of detector positions. The special timing mode of the APS with dark times in the µs range can be ideally used with a high-frequency vacuum-chopper [132], which allows a pulse frequency as low as 67.8 kHz. With this setup, 26-ID-C is ideally suited for time-resolved measurements [55, 115].

3.1.4 Comparison and future developments

As shown in Tab. 3.1, all three beamlines offer a wide variety of measurement modalities. All of them are perfectly suited for X-ray fluorescence (XRF) measurements, and all are capable of X-ray diffraction (XRD), X-ray beam induced current (XBIC) measurements, and X-ray absorption near edge spectroscopy (XANES). For X-ray excited optical luminescence (XEOL), ID16B is the only one to have a permanently installed detector. As will be introduced later in this chapter, a detection unit for XEOL was developed and used at P06 but is not generally available. While 26-ID-C does not offer XEOL, it has the smallest beam focus of the three and is best suited for time-resolved studies. The energy ranges of P06 and ID16B are comparable,

while the range of 26-ID-C is smaller. The space to arrange the detectors is the greatest at P06, followed by ID16B and lastly 26-ID-C.

The beamline ID16B was already adapted to the ESRF upgrade and profits from an increase of one magnitude in the coherent fraction of the beam, as well as the flux [56, 117]. With the upgrade of PETRA III to PETRA IV [36, 141], and the APS upgrade to APS-U [142], the coherence and flux there will be increased substantially. Techniques, such as ptychography, which rely on the coherence of the beam will not limit the photon-hungry techniques, such as XEOL, anymore. This opens the window to new combinations of measurement modalities which today are only feasible as proof-of-principle work [2]. Multi-modal measurements reaching not only into the 3rd but also 4th dimension will become feasible [60] and allow to gain comprehensive information about a system with the availability of spatial, spectral, and temporal resolution.

3.2 Scanning X-ray microscopy techniques

The way the X-ray beam interacts with the sample can be measured with different methods. Put simply, the intensity of the transmitted X-ray beam through the sample gives information on the optical density of the sample, and with the diffraction pattern in the far-field, the retardation of the phase can be reconstructed with ptychography. The wide angle scattering of the X-ray photons resolves the lattice structure of the crystal via Bragg's law. The absorbed photons excite core electrons and, by filling the core states, X-ray fluorescence is emitted which contains information on the composition of the sample. The excited electron starts a cascading process which generates thermalized electron-hole pairs at the band edge. These electron-hole pairs can either be collected as X-ray beam induced current or their potential can be measured as X-ray beam induced voltage. When they recombine radiatively, the X-ray excited optical luminescence can also be detected and, if measured in a time-resolved fashion, the lifetime of the carriers can be determined. The spectral resolution of the luminescence reveals the energy of the bandgap.

In the following, the different measurement techniques to assess these phenomena and evaluate the material properties will be introduced.

3.2.1 Ptychography

In this section, the basic principles of ptychography are presented. For an in-depth discussion of the principle of ptychography see Ref. [143–148]. Large parts of this section were already published in Ref. 2 and are not explicitly marked.

Ptychography is used to iteratively reconstruct the phase shift of a coherent X-ray beam when passing through material from the distribution of scattered photons measured with an area detector [144, 147].

From the measured scattered photons, only the intensities can be measured, and the reconstruction algorithm for the phase needs an overlap of beam spots to converge.

To describe the propagation of X-rays through a material, a complex refractive index

$$n = 1 - \delta + i\beta, \tag{3.1}$$

can be used, where δ leads to phase shift and β to attenuation. The phase shift is correlated to the material's electron density ρ_e by

$$\delta = \frac{\rho_\mathrm{e} r_\mathrm{e} \lambda^2}{2\pi}, \tag{3.2}$$

where r_e is the classical electron radius and λ is the X-ray wavelength [149, 150].

The phase shift Φ is related to δ from Eq. 3.2 through

$$\Phi = -\frac{2\pi}{\lambda} \int \delta(x) dx \tag{3.3}$$

where λ is the wavelength and x is the direction of X-ray beam propagation [149]. With Eq. 3.2 and the conversion of the electron density to the area electron density via

$$\rho_\mathrm{A}^\mathrm{e} = \int \rho_\mathrm{e}(x) dx, \tag{3.4}$$

the relative phase shift can be converted into the relative area electron density:

$$\Delta\rho_\mathrm{A}^\mathrm{e} = -\frac{\Delta\Phi}{\lambda \cdot r_\mathrm{e}}. \tag{3.5}$$

For the reconstruction of the phase shift in solar cells, an absolute reference for the phase shift is often missing. Therefore, Φ is offset so that the minimal phase shift (maximal value of Φ) is zero; the resulting relative phase shift is denoted $\Delta\Phi$.

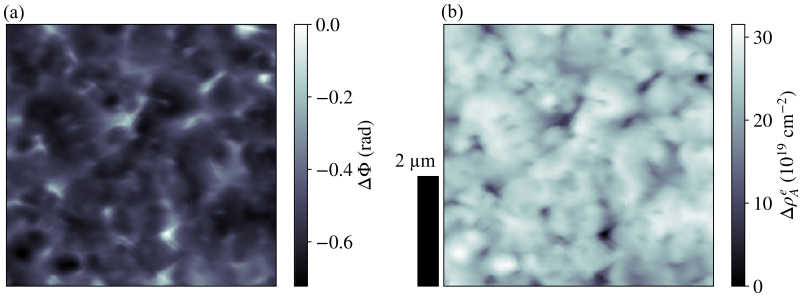

Figure 3.3: (a) Relative phase shift, reconstructed with ptychography and (b) the relative area electron density calculated from (a).

Figure 3.3 (a) shows the reconstructed phase shift of a Cu(In,Ga)Se_2 solar cell measured in the micro hutch of P06. The Cu(In,Ga)Se_2 solar cell substrate was a polyimide film, this allowed the transmission of the X-ray beam.

Figure 3.3 (b) shows the resulting relative area electron density map.

As ptychography deconvolves the probing wavefield and the object, the beam propagation can be reconstructed. This allows to determine the beam caustic as can be exemplarily seen in Fig. 3.4 for the horizontal plane (a), in-focus plane (b), and vertical plane (c). Fig. 3.4 (d–e) show the line profiles through the focus as a horizontal

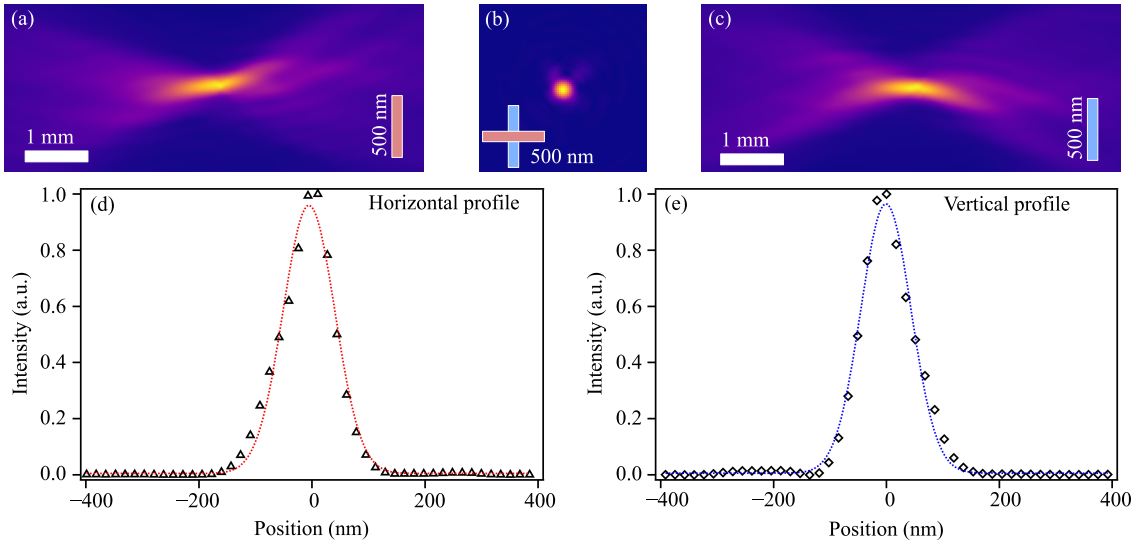

Figure 3.4: Characterization of the nano-focused X-ray beam by ptychography. (a) Beam caustic in the horizontal plane. (b) Beam-intensity distribution in the focus plane. (c) Beam caustic in the vertical plane. Line profiles through the focus for horizontal ((d), points) and vertical ((e), points) planes. The dotted lines are Gaussian fits that yield a FWHM of 108 nm for the horizontal plane and 105 nm for the vertical plane. Image was previously published in Ref. [2]

(h) and vertical (v) profile. The FWHM of the Gaussian fit to the profile gives the coherent focus size of the beam, which was in this case 108 nm (h) × 105 nm (v).

Compared to incoherent X-ray imaging, e.g. through absorption contrast, ptychography offers a greater spatial resolution that is rather limited by the signal captured under the largest scattering angle on the detector than by the spot size of the incident beam [148]. As an example, the resolution in Fig. 3.3 was determined with Fourier-ring-correlation [151] to be on the order of 30 nm, this is significantly lower than the coherent-beam size determined from the reconstructed beam caustic.

3.2.2 X-ray diffraction

For the study of the lattice structure, XRD is a long-established tool, spanning powder diffraction [152–155] and single crystal studies. XRD is based on Bragg's law

$$n\lambda = 2d \cdot \sin(\theta), \tag{3.6}$$

where n is an integer, λ is the wavelength of the incoming photons, d is the distance between lattice planes, and θ is the incoming angle. This technique is ideally suited for multi-modal studies of polycrystalline TF solar cells [66, 67]. The grains in TF solar cells are randomly oriented, leading to singular grains coincidentally fulfilling the Bragg condition. From the variation in the position of the reflection peak on the detector, strain and tilt of single crystals can be derived, as described in Ref. 67. To find the coincidentally correctly oriented grains, an overview scan of the solar cell is performed and the integrated intensity is measured. An example can be seen in Fig. 3.5, where an AgCu(In,Ga)Se_2 solar cell is measured. Figure 3.5 (a) shows the integrated diffraction peaks on the detector which are labeled to the corresponding grains. Figure 3.5 (b) shows the integrated diffraction intensity on the scanned 2D map, while (c) displays the simultaneously taken XRF data of selected elements. From there, a single grain can be selected and measured with greater precision. A common practice is to perform so-called rocking curves over a single grain. There, the sample is tilted slightly around the angle which fulfills the Bragg condition and at each angle, the grain is scanned. Through the angle variation, the tilt and strain of the grain can be deconvoluted [67]. Another approach is to treat all reflecting grains in a statistical way, as was done in Ref. 156.

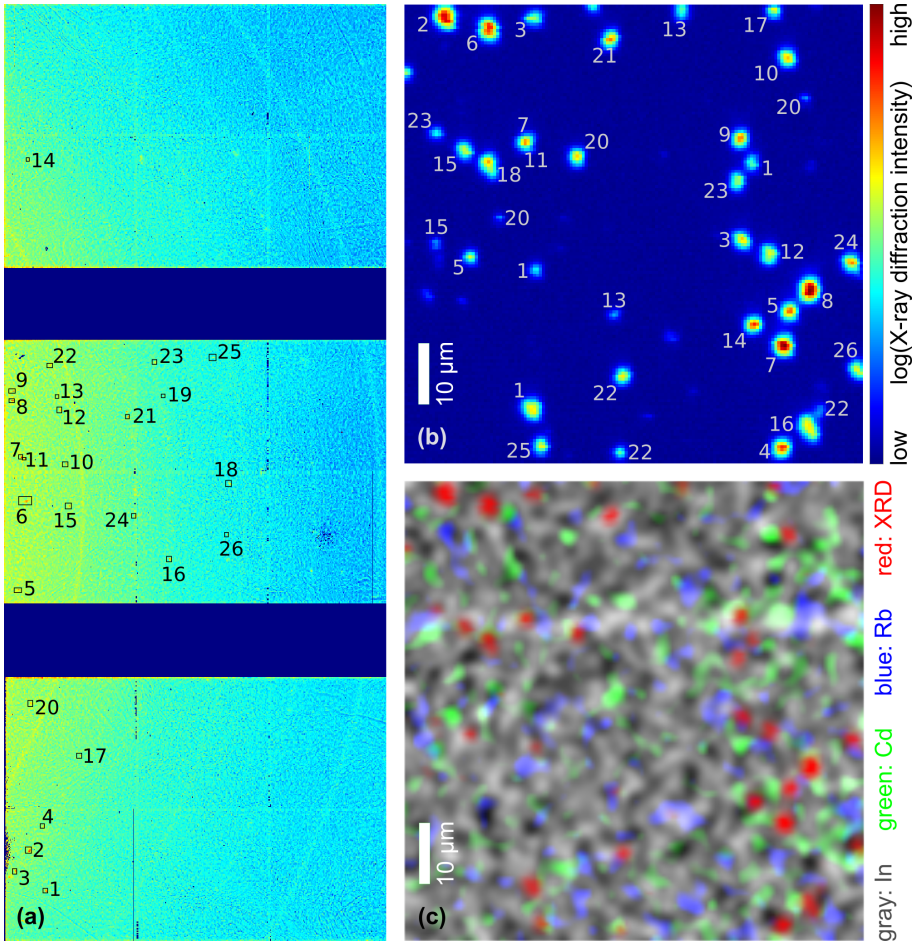

Figure 3.5: X-ray diffraction peaks of an AgCu(In,Ga)Se_2 solar cell. (a) Integrated intensities on the detector with the Bragg peaks numbered to the grains, identified in (b). (c) XRF signal of In (gray), Cd (green), and Rb (blue), and the diffraction peaks in red. Figure from Ref. 11 reprinted with permission from Peter Modregger.

3.2.3 X-ray fluorescence

This section introduces XRF, which is a non-destructive technique to measure the composition of a material. For a comprehensive understanding of the theory behind XRF and its analysis, Refs. [157, 158] are recommended. Here, selected aspects will be highlighted.

The fluorescence spectrum

The very basic principle of XRF can be summarized in four steps: 1. A core electron absorbs an incoming X-ray photon and 2. is excited to a higher energy state. 3. An

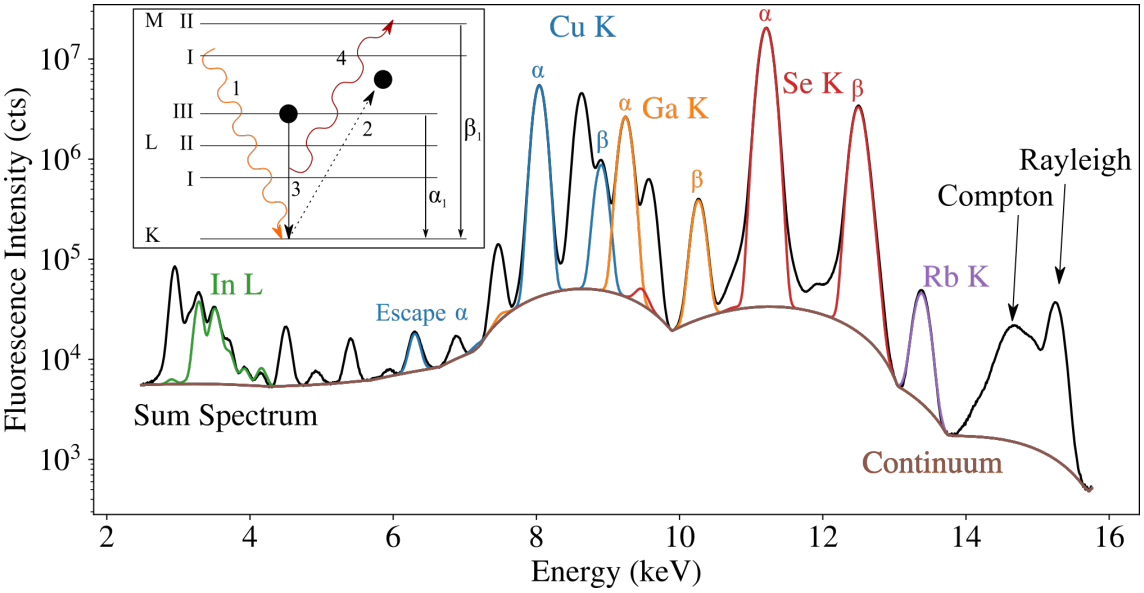

Figure 3.6: Exemplary XRF sum-spectrum of a Cu(In,Ga)Se_2 solar cell. The counts are summed over a map. Elemental peaks are marked and a background estimate is drawn in. Inlay: Scheme of X-ray fluorescence generation in four steps. (1) photon absorption, (2) electron excitation, (3) electron transition to fill the vacancy, and (4) emission of a characteristic photon. As an example, an α transition and one β transition are indicated.

electron from a higher energy level fills the core hole left by the excited electron. 4. As a result of this transition to a lower energy state, an X-ray photon is emitted. The four steps are sketched in the inlay in Fig. 3.6. The photon energy from this transition process is characteristic of each element. The transition is denoted with the letter of the shell where the hole is filled and a Greek letter indicating the strength of the transition (Siegbahn notation). By measuring the photon energy, the elemental species in the sample can be identified, and its concentration can be inferred by the number of counts. The characteristic fluorescence has a Lorentz shape; however, for elements with an atomic number below $Z = 50$, the FWHM of the Gaussian response of the detector with which the fluorescence signal is convoluted is dominant ($FWHM_{Lorentz}$ on the order of 10 eV, $FWHM_{Gauss}$ on the order of 160 eV) [158]. Therefore, it is usually enough to fit fluorescence peaks with a Gaussian function. Figure 3.6 shows an exemplary XRF-spectrum of a Cu(In,Ga)Se_2 solar cell where all counts were summed over a scanned area. The peaks of the absorber elements, as well as the trace element Rb, are highlighted in the spectrum. They are set upon a background denoted 'continuum'. The source of this background is a convolution of factors, part of it are partially detected photons in the detector or Bremsstrahlung of the excited electrons in the material. An exact determination of the background is

difficult and is usually left to the experience of the analyst. The highest energy peak is the Rayleigh peak which contains the energy lost via elastic scattering. The second highest peak belongs to the inelastic scattering and is named Compton peak. The position of the Compton peak is determined by the angular position of the detector to the sample surface. In addition to the characteristic peaks from different transitions within an atom, there are also escape peaks and pile-up peaks. These escape peaks appear when an XRF photon in the detector leads to a secondary XRF event and the secondary XRF photon leaves the detector. The collected energy is then short of this secondary XRF photon, which amounts to 1.75 keV for a Si-detector. In Fig. 3.6 the escape peak of Cu Kα is labeled. Pile-up peaks appear when two photons arrive at the detector simultaneously and their energy is added, this is not highlighted in the spectrum. All counts measured above the excitation energy are due to pile up. The width s of the elemental peaks depends on the electronic contribution to the detector noise W_e and the Fano-factor F_F of the detector as

$$s^2 = \left(\frac{W_\mathrm{e}}{2.3548}\right)^2 + 3.85 \times F_\mathrm{F} \times E_j \tag{3.7}$$

where E_j is the energy (in eV) of the X-ray line [159].

Self-absorption

The detector geometry has a great impact on the detected fluorescence spectrum. Not only is the position of the Compton-peak determined by the angular position of the detector but it also influences the strength of self-absorption effects inside of the sample. At shallow angles, the distance a fluorescence photon has to travel to escape the sample can be several times larger than the thickness of the sample. For example, an XRF photon generated in a sample depth of 500 nm and detected under an angle of 10 ° will travel for almost 3 µm. The chance to be reabsorbed is thus considerably high. The effect is stronger for lower energy photons, as their attenuation length is shorter. The attenuation lengths of an exemplary perovskite mixture, Cu(In,Ga)Se_2 and CdTe are shown in Fig. 3.7. The calculation is based on Lambert-Beer's law and highlights that for photons with an energy on the order of 3–4 keV a travel distance of 3 µm is significant.

The direct effect can be seen in Fig. 3.8 where two scans of a perovskite layer on a textured substrate measured at two different angles are shown. The sample was prepared by King Abdullah University of Science and Technology (KAUST)

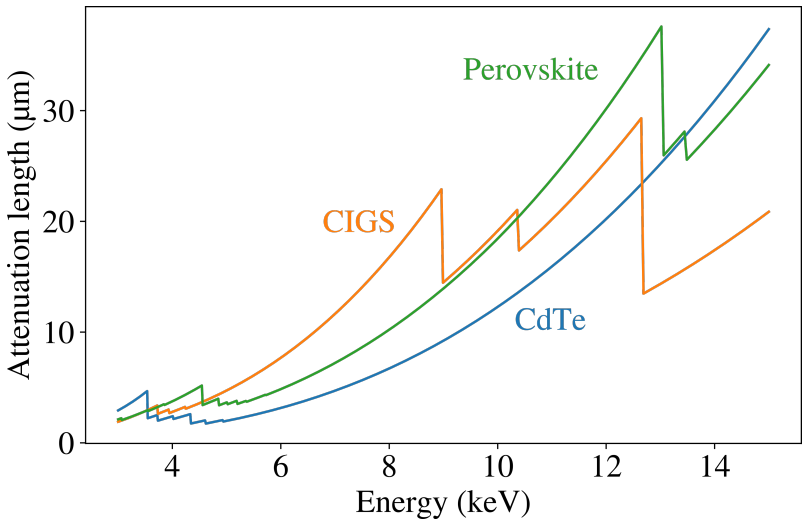

Figure 3.7: Length at which the incoming photon beam is reduced to $1/e$ its intensity in a CdTe, Cu(In,Ga)Se_2 and perovskite compound material. The data was calculated with Ref. [160] at `https://henke.lbl.gov/cgi-bin/atten.pl` accessed 10.04.2022.

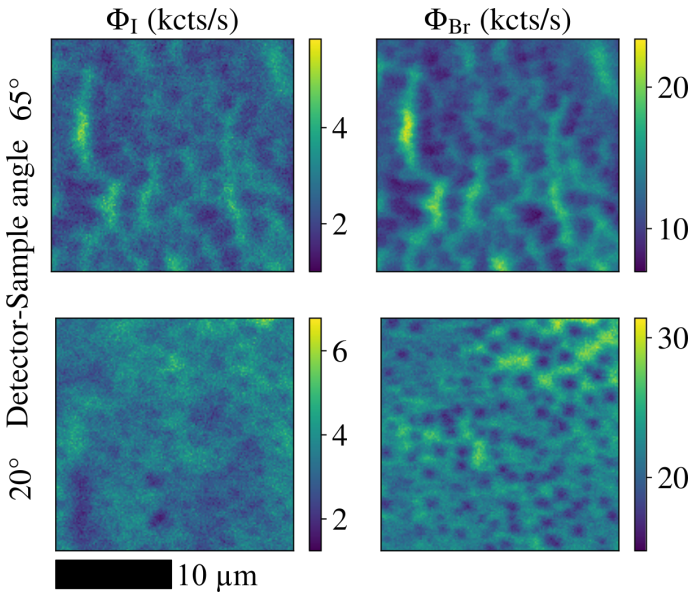

Figure 3.8: XRF-maps of Φ_I and Φ_{Br} of a perovskite layer on a textured surface. *top*: High sample-detector angle of 65° *bottom*: Low sample-detector angle of 20°. The sample was prepared by KAUST and is discussed in Ref. [12].

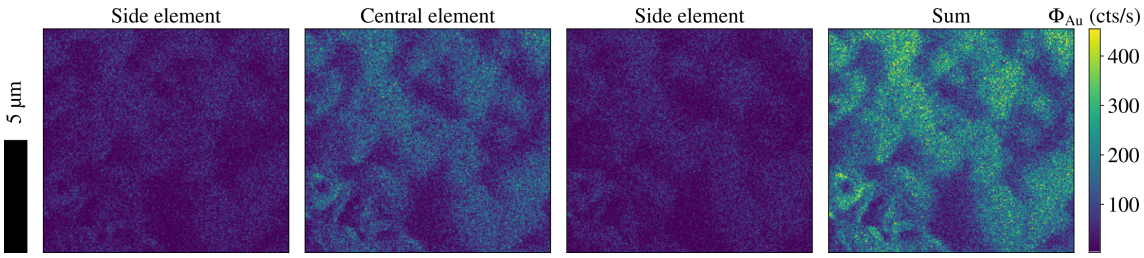

Figure 3.9: Φ_{Au} XRF maps of a layer on top of a CdTe solar cell from three different detector elements and their sum. The solar cell is discussed in [10].

and measured at P06 under an angle of 20° and 65° between the sample and the detector. As the fluorescence energy of the I-L lines has an energy around 4 keV, it is susceptible to self-absorption effects. In comparison with Br-Kα fluorescence (at an energy of 11.9 keV), the influence of self-absorption at shallow angles becomes apparent. At the high detector-sample angle, both Φ_I and Φ_{Br} exhibit clearly the spots associated with the textured substrate. However, at the low detector-sample angle the texture of the substrate is only slightly visible in the Φ_I-map, this is due to the self-absorption effect.

Some detectors have multiple elements, to increase the number of collected photons. However, each of these elements has to be treated as a separate detector with its own energy calibration. Figure 3.9 shows maps of Au fluorescence Φ_{Au} from a layer on a CdTe solar cell measured with a three-element detector at the beamline ID16B (ESRF). The cell is discussed in Ref. [10]. The advantage of summing over the three separate elements becomes clear in the sum map, where the contrasts are enhanced. Additionally to the individual energy calibration, each detector element has a slightly different angle from the sample. This has to be taken into consideration when self-absorption corrections are applied.

An example to highlight this is given in Fig. 3.10 from Ref. [8] where the different effective angles for detector elements are schematically drawn. The implications and chances for analyzing the self-absorption effect were discussed in Ref. [8].

To take these effects into account during the analysis of solar cells, the different absorption cross-sections in the layers of the solar cell have to be considered further as West et al. showed in Ref. [58]. However, in this work, the software PyMca provided by Sole et al. [159] is used to analyze XRF spectra and there the self-absorption correction is based on the fundamental parameter method [161, 162].

In general, it is advised to have a reference specimen, known as fluorescence standard, which contains the elements one is interested in to calibrate the fundamental param-

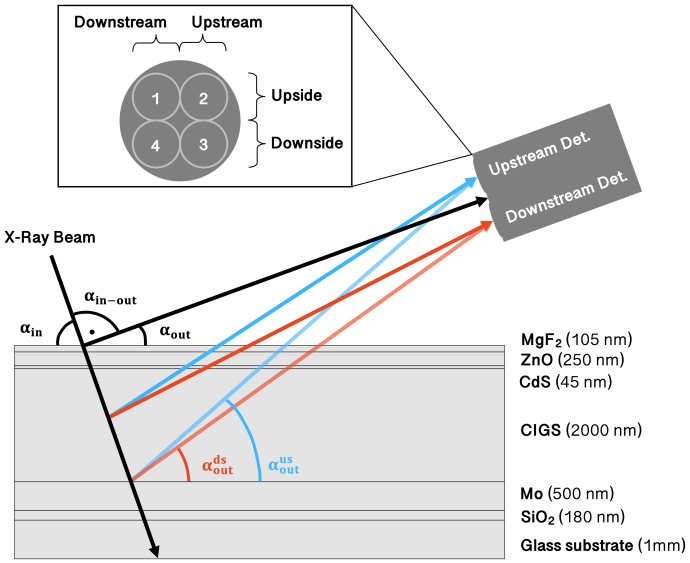

Figure 3.10: Structure of a Cu(In,Ga)Se_2 solar-cell stack with the X-ray fluorescence measurement geometry involving a four-module silicon drift detector. The different effective angles are highlighted in red and blue. Due to the small thickness of the solar-cell layers of interest (≈2 µm) compared to the sample-detector distance (on the order of cm), the angles can be assumed to be independent of the depth in the solar-cell layer stack. Figure reprinted from Ref. [8] with permission from ©2020 IEEE.

eters. However, for complex devices, such as solar cells, this is not always possible. Another approach is to use an element of the absorber matrix as a reference. For Cu(In,Ga)Se_2 solar cells as an example the element Se is often the best fit for the reference role, as it is the most stable in stoichiometric variation. The parameters are thus adapted, such that the expected values for Se are reached. However, this sets as prerequisites for the analysis that the description of the layers in composition and thickness is already known quite well beforehand. If these conditions are met, the area density of the elements can be calculated from the data fitted with PyMca.

Area density calculation from mass-fractions

This subsection is directly taken from the SI of Ref. [2]. Based on the measured fluorescence count rate Φ_i and the unscaled mass fraction w_i^* obtained through PyMca for each element i, the effective molar area density ρ_{A}^i was calculated as follows.

First, the mass fraction was scaled for each element such that the sum equals 1 at

each scanned spot:

$$w_i = \frac{w_i^*}{\sum_j w_j^*}. \tag{3.8}$$

By multiplying the scaled mass fraction w_i with the nominal thickness d_{nom} and mass density $\rho_{\mathrm{nom}}^{\mathrm{mass,tot}}$ of the layer, the nominal mass area density

$$\rho_{\mathrm{A,nom}}^{\mathrm{mass},i} = w_i \cdot d_{\mathrm{nom}} \cdot \rho_{\mathrm{nom}}^{\mathrm{mass,tot}} \tag{3.9}$$

in [g/cm^2] was calculated for each element and converted into the nominal molar area density in [mol/cm^2] with the molar mass M_i:

$$\rho_{\mathrm{A,nom}}^{\mathrm{mol},i} = \frac{\rho_{\mathrm{A,nom}}^{\mathrm{mass},i}}{M_i}. \tag{3.10}$$

To obtain the effective molar area density map for each element i, the count rate Φ_i was scaled to $\rho_{\mathrm{A,nom}}^{\mathrm{mol},i}$ averaged over all scan points:

$$\rho_{\mathrm{A}}^{i} = \frac{\overline{\rho_{\mathrm{A,nom}}^{\mathrm{mol},i}} \cdot \Phi_i}{\overline{\Phi_i}}. \tag{3.11}$$

3.2.4 X-ray beam induced current

This section will introduce XBIC as a measurement technique for solar cell characterization. Most of this section was already published in Ref. 1 and Ref. 2. Here, it was adapted for readability and will not be further marked.

The current induced by the X-ray beam, which we measure, is created by a complex interaction between the beam and the sample. The incident X-ray photons set off particle showers consisting of electrons and photons, resulting in a multitude of excited electron-hole pairs per incident X-ray photon in the semiconducting absorber material. Finally, the electron-hole pairs thermalize to the band edges of the solar cell absorber (simulations of this process are detailed in the supplementary information (SI) of Ref. 163).

Figure 3.11 shows the particle shower and other relaxation pathways of electrons after excitation with an X-ray photon. The figure is adapted from Ref. 26.

The thermalized X-ray excited charge carriers can be treated like charge carriers that are generated by the absorption of photons with energies just above the bandgap during normal solar cell operation, and the resulting current or voltage can be

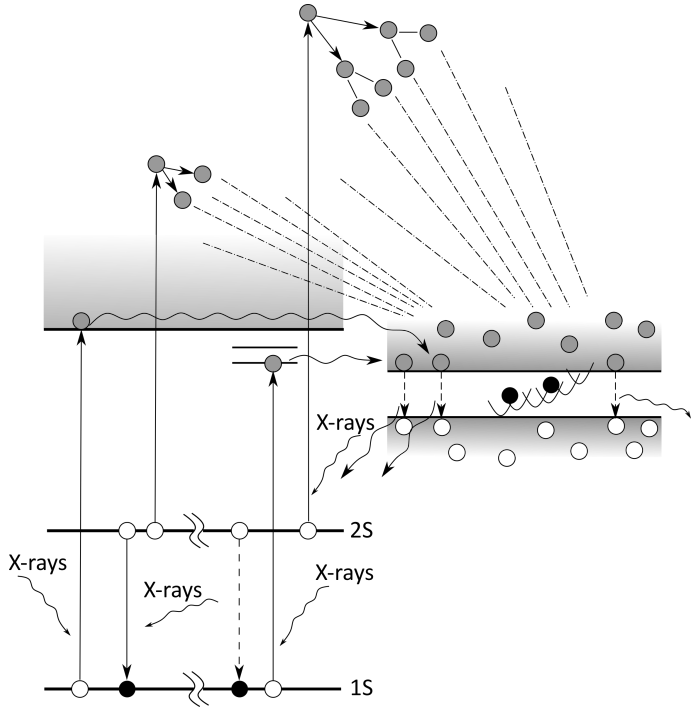

Figure 3.11: Electron cascade and relaxation pathways, after illumination by an X-ray photon. Figure adapted from Ref. 26.

measured as X-ray beam induced current [27, 43, 164] or voltage (XBIV) [62, 165] similar to more common measurements like electron-beam induced current (EBIC) or laser-beam induced current (LBIC).

Note that only electron-hole pairs that are generated in the absorber layer of the device under test (DUT) contribute to the XBIC/XBIV signal. Charge carriers excited in other layers such as the metallic contacts or substrate will immediately recombine, as they have no possibility of being separated by the junction. Therefore, other layers only affect XBIC/XBIV measurements via secondary effects such as parasitic X-ray absorption or the emission of secondary photons and electrons that may be re-absorbed in the absorber layer. In contrast, all layers potentially contribute to the XRF signal.

XBIC vs. LBIC vs. EBIC

A qualitative comparison of XBIC with EBIC and LBIC as measured in electron microscopes or with optical setups is given in Table 3.2.

The electron-hole pair generation by a laser comes closest to the outdoor operation of solar cells. However, the spatial resolution of LBIC is fundamentally limited by

	XBIC	EBIC	LBIC
Multi-modal capability	++	+	+
Spatial resolution	++	++	-
Penetration depth	++	- -	+
Availability	- -	-	+
Sample damage	-	- -	++

Table 3.2: Qualitative assessment of X-ray beam induced current (XBIC), electron beam induced current (EBIC) and laser beam induced current (LBIC). This is adapted from Ossig, C., Nietzold, T., West, B., Bertoni, M., Falkenberg, G., Schroer, C. G., Stuckelberger, M. E. X-ray Beam Induced Current Measurements for Multi-Modal X-ray Microscopy of Solar Cells. J. Vis. Exp. (150), e60001, doi:10.3791/60001 (2019).

the wavelength of the laser. EBIC measurements offer a greater spatial resolution that is typically limited by the interaction radius of the electron beam with the DUT. The main drawback of EBIC measurements is their surface sensitivity, hindering the assessment of the absorber layer performance through the layer stack or even in encapsulated devices. Furthermore, uneven surfaces of the DUT in combination with non-linear secondary-electron emission effects often lead to distorted EBIC results. In contrast, XBIC measurements are more sensitive to the total thickness of the absorber, due to only partial absorption of the beam, than the surface morphology, as the majority of the signal is generated deep in the bulk material and surface-charge effects are mitigated by proper grounding. All three beam-induced techniques have in common that charge injection is highly inhomogeneous, peaking at the beam position. As a consequence, the excess carrier concentration and current density are inhomogeneously distributed. In a simplified picture, the majority of the solar cell operates in dark, and a small spot operates at a high injection level that can reach hundreds of sun equivalents for focused beams. The injection-level distribution depends not only on the beam size and shape, but also on the beam energy, device stack, and time structure of the injection. So far, the X-ray beam has been treated as a continuous beam, which is justified for charge-carrier collection processes that are slower than microseconds. However, synchrotron-sourced X-rays consist of sub-100-ps pulses with intensities and pulse frequency depending on the storage-ring fill pattern. Although no impact of the fill pattern on comparably slow XBIC measurements was noticed here, the short-term injection level does depend on it. In contrast, one can make use of the time structure of X-rays: similar to what was demonstrated for time-resolved XEOL [65], one can imagine time-resolved XBIC or XBIV measurements, or locking the XBIC/XBIV signal into the electron-bunch frequency.

An adequate discussion of the consequences of inhomogeneous injection levels requires a full 3D simulation of all relevant beam and device parameters including the convolution of the time-dependent injection level with the 3D mobility and lifetime in the DUT, which was not conducted for the scope of this work. First simulations were made by Saadaldin et al. in Ref. [105]. However, it is conceptually the same for all beam-induced current and voltage measurements, and the interested reader is referred to the literature discussing the injection-level dependence of EBIC [166] and LBIC [167] measurements.

The negative consequences of local charge injection can experimentally be mitigated by the application of bias light with the intensity of 1 sun equivalent, and beam-induced excitation adding only a negligible amount of excess charge carriers. In practice, this concept is technologically limited by the dynamic reserve of 100–120 dB in state-of-the-art lock-in amplifiers, this corresponds to a signal-to-noise ratio of $1 \cdot 10^5$ to $1 \cdot 10^6$. While this suffices for devices of size comparable to the beam size, it does not allow the application of bias light at relevant levels for macroscopic devices. The obvious solution is to decrease the sample size. Unfortunately, this is often limited by electrical border effects up to several hundred micrometers off the sample border or contact points.

Note also that one can make use of the injection-level dependence of XBIC measurements: similar to EBIC and LBIC, performing injection-level series by varying the X-ray beam intensity can unveil information about dominant recombination mechanisms and charge carrier diffusion [84, 85, 168–171]. In conclusion, the penetration depth of X-rays combined with the high spatial resolution makes XBIC the most fitting technique to study DUT with buried structures such as thin-film solar cells in a correlative microscopy approach. The interaction radius of XBIC measurements is typically smaller than for EBIC, and the spatial resolution is often limited by the diffusion length of the charge carriers. The main drawback of XBIC measurements is the limited availability of X-ray nanoprobes.

Sample contacting and grounding scheme

To minimize possible sources of noise induction a printed circuit board (PCB) can be used to contact the solar cell. An exemplary case is shown in Fig. 3.12. The tools necessary for contacting the solar cell are shown in Fig. 3.12(a). The solar cell is not included there. Depending on the substrate of the cell scissors, the scalpel or a glass cutter is used to cut out a small sample. When using scissors, it is important

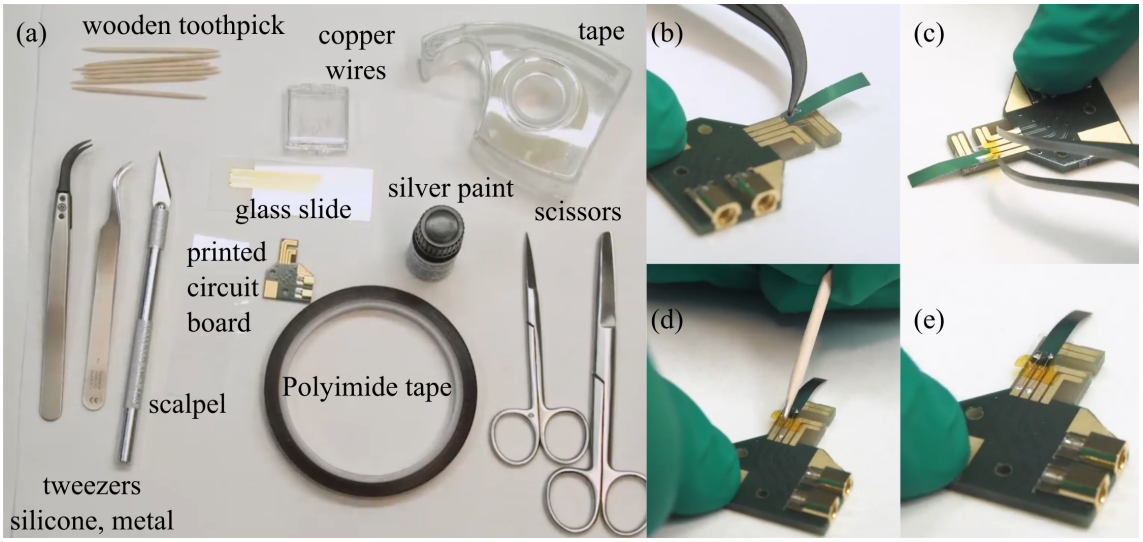

Figure 3.12: Tools used and steps in contacting a thin-film solar cell. (a) Necessary tools. (b) Gluing the thin film solar cell onto the printed circuit board. (c) Fixing and insulating the cell with polyimide tape. (d) Contacting the back and front contact with the respective lane on the circuit board via copper wires with silver paint. (e) The finished contacted device. This is adapted from Ossig, C., Nietzold, T., West, B., Bertoni, M., Falkenberg, G., Schroer, C. G., Stuckelberger, M. E. X-ray Beam Induced Current Measurements for Multi-Modal X-ray Microscopy of Solar Cells. J. Vis. Exp. (150), e60001, doi:10.3791/60001 (2019).

to cut in such a way that the inside of the top shear of the scissor shows towards the piece of solar cell intended to be measured, as that side is cut smoother and less likely to be damaged. When handling the solar cell, caution is advised in using metal tweezers, as these can lead to a short-circuit condition. Therefore, tweezers with a silicone tip are recommended. The sample is glued to the PCB with either nail polish, instant glue, composite glue, or silicone glue, depending on the materials and requirements for later removal. In Fig. 3.12(b) the cell is glued onto the PCB with double-sided tape. Note here that a large part of the cell is shooting over the PCB, which is important for eventual transmission measurements.

Polyimide tape is used to insulate and fixate the cell and the wiring components as can be seen in Fig. 3.12(c). The front and back contact (here, some parts of the cell were scratched off the substrate to reach the back contact) are individually contacted with copper wires. As the energy of the X-ray beam is magnitudes higher than solar light, ionization of the sample has to be taken into consideration. To ensure that the measured current is not simply a replacement current of the ionized surface of the cell, the contact of the side facing upstream of the beam is grounded. To facilitate

the grounding, the upstream facing contact is connected to the shield of the PCB LEMO plug. Later, in the experimental setup, the shield can then be connected to ground with e.g. metal tape. For contacting the copper wires with the sample, a wooden toothpick is used to deliver the silver paint. The softness of the wood ensures that the solar cell is not accidentally scratched and the pointy tip of the toothpick helps to regulate the amount of silver paint used. The contacting can be seen in Fig. 3.12(d) while (e) shows the finished contacted device.

The PCB allows the unshielded cabling in this contacting scheme to be kept to a minimum. Furthermore, in combination with an aluminum sample holder on a kinematic mount, the positioning of the sample in the beam is reproducible.

XBIC measurements with lock-in amplification

As the X-ray beam only illuminates a small part of the solar cell, the resulting currents are similarly small and susceptible to noise. Adding the possibility of bias light or voltage during the measurements, lock-in amplification becomes a very attractive amplification scheme, as it offers the possibility to filter out noise and offsets. The in-depth discussion of lock-in amplification for XBIC measurements will be presented in Chapter 4, here only an overview and the necessary steps will be highlighted. The section follows the protocol part of Ref. [1].

For successful lock-in amplified XBIC measurements, the following hardware is necessary: a nano- or micro- focusing X-ray beamline; an X-ray chopper that absorbs periodically the majority of the X-rays; a pre-amplifier (PA); a lock-in amplifier (LIA); modules for remote control of the chopper, PA, and LIA; a data acquisition (DAQ) system; a DUT.

The kinematic mount holding the PCB with the contacted DUT should be designed to be lightweight but stiff down to the nanometer scale. The contact of the DUT facing upstream of the beam is grounded with e.g. metal-tape to replace any ionization current.

For lock-in amplification modulation of the signal is necessary, thus an optical chopper is installed upstream of the sample, which blocks the beam 50% of the time. The modulation of the X-ray beam will translate to the generated XBIC signal, and allow demodulation to extract the signal from noise.

For very small signals a PA is used and the current signal will be translated into a voltage. If the XBIV should be measured instead of the current, no PA is used.

Otherwise, the measurement scheme follows analogously.

As for all electrical measurements, care has to be taken so that input ranges are not exceeded. Therefore, it is important to eliminate all non-intended light sources which might disturb the measurement.

The parameters of the lock-in amplifier which processes the pre-amplified signal are optimized for scanning speed, chopper frequency, and low-pass filter settings. As a rule of thumb, the selected frequency of the chopper should be as high as possible under the constraints of (a) fast enough response of the DUT, (b) fast enough amplification chain, (c) acceptable level of vibrations induced by the chopper. Furthermore, frequencies that are multiples of common noise frequencies such as 50 Hz, 60 Hz, or 45 kHz should be avoided.

The low-pass filter frequency $f_{\text{cut-off}}$ of the lock-in amplifier should be at least an order of magnitude below the chopping frequency, and an order of magnitude above the sampling rate. Ideally, the $f_{\text{cut-off}}$ is below the utility frequencies of 50 Hz or 60 Hz. The filtered signal is then scaled at the analog output of the LIA to a value well in the range of the acceptance range of the volt-to-frequency (V2F) converters.

The conversion of the measured count rate f_{DAQ} (Hz) to an XBIC signal S_{XBIC} (A) is found by going along the signal chain. The necessary parameters are the pre-amplification factor A_{PA} (V/A), the amplification factor of the LIA A_{LIA} (V/V) at the analog output, and the voltage acceptance range R_{V} (V) of the V2F converter which projects onto the frequency range R_{f} (Hz).

Furthermore, as a lock-in amplifier usually outputs a root-mean-square (RMS) value of the incoming AC signal, a waveform or crest factor C, depending on the shape of the incoming signal is added. For sine-shaped signals, this factor is a $\sqrt{2}$, for square waves it is 1, and for triangular waves a $\sqrt{3}$. Here, it has to be noted that most LIA demodulate with a sine-wave, and therefore if the incoming signal is a square or triangular wave the actual factor will be something in-between these values.

When the parameters are known, a conversion term H_{conv} can be defined to convert the signal

$$S_{\text{XBIC}} = f_{\text{DAQ}} \cdot H_{\text{conv}} \tag{3.12}$$

with

$$H_{\text{conv}} = \frac{2 \cdot C \cdot R_{\text{V}}}{A_{\text{PA}} \cdot A_{\text{LIA}} \cdot R_{\text{f}}}.$$

The factor of 2 in H_{conv} follows as the XBIC signal is not the amplitude of the modulated signal but the peak-to-peak value.

Topological correction

This paragraph was published in Ref. 3. To correct I_{meas} for the difference in absorber thickness for each measurement point, we used XRF data as suggested in Ref. 43 and detailed in Ref. 172. The topologically corrected XBIC signal is referred to as $\widetilde{I}$.

We utilized the Lambert–Beer's law to approximate the attenuation of a photon flux Φ in a material. With Φ_0 being the initial photon flux, α the linear absorption coefficient, and d the penetration depth, Lambert–Beer's law states

$$\Phi(d) = \Phi_0 \cdot \exp\left(-\alpha \cdot d\right). \tag{3.13}$$

Often, the mass attenuation coefficient $\alpha_{\mathrm{m}} = \alpha/\rho$ is used instead of the linear absorption coefficient, where ρ represents the mass density of the material. With ρ_{A} being the area density, Eq. 3.13 is then written as

$$\Phi = \Phi_0 \cdot \exp\left(-\alpha_{\mathrm{m}}\rho_{\mathrm{A}}\right) = \Phi_0 \cdot \exp\left(-\frac{\alpha}{\rho}\rho_{\mathrm{A}}\right). \tag{3.14}$$

X-ray mass attenuation coefficients can be found in [173] for every element j. The corrected XBIC current can then be calculated as

$$\widetilde{I} = \frac{I}{1 - \exp\left(-\sum_j \left(\alpha_{\mathrm{m,j}} \cdot \rho_{A,\,j}\right)\right)}. \tag{3.15}$$

For a Cu(In,Ga)Se_2 solar cell, in order to estimate a thickness correction of the XBIC signal with limited data available from XRF, first the area density $\rho_{A,\,j}$ of an element j in the Cu(In,Ga)Se_2 layer is established as

$$\rho_{A,\,j} = \overline{\rho_{\mathrm{CIGS}}} \cdot \frac{\Phi_j}{\overline{\Phi_j}} \cdot d_{\mathrm{Nom}} \cdot \overline{\omega_j}. \tag{3.16}$$

Here, the XRF count rate Φ_j contains the information about spatial variations in thickness and stoichiometry, the average density of Cu(In,Ga)Se_2 is $\overline{\rho_{\mathrm{CIGS}}} = 5.7\,\mathrm{g/cm^3}$, and the average Cu(In,Ga)Se_2 thickness d_{Nom} is tabulated for each cell in Tab. 5.2 and the mean normalized mass fraction for element j is denoted $\overline{\omega_j}$.

Finally, the thickness-corrected XBIC signal $\widetilde{I}$ of the Cu(In,Ga)Se_2 solar cell is calculated as

$$\widetilde{I} = \frac{I}{1 - \exp\left(-\sum_{j\,\in\,\{\mathrm{Cu,\ In,\ Ga,\ Se}\}} \left(\alpha_j \cdot \rho_{A,\,j}\right)\right)}.$$

Charge collection efficiency

The topologically corrected XBIC signal $\widetilde{I}$ can be seen as an approximation of the charge collection efficiency η_{XCE}. This charge collection efficiency is scaled from 0 to 1 for convenience's sake. However, a more formal definition of η_{XCE} is given as

$$\eta_{\mathrm{XCE}} := \frac{N^{\mathrm{coll}}_{\mathrm{e^-/h^+}}}{N^{\mathrm{gen}}_{\mathrm{e^-/h^+}}} = \frac{\frac{S_{\mathrm{XBIC}}}{q}}{M \cdot N^{\mathrm{in}}_{\mathrm{ph}}} \tag{3.17}$$

where $N^{\mathrm{gen}}_{\mathrm{e^-/h^+}}$ and $N^{\mathrm{coll}}_{\mathrm{e^-/h^+}}$ are the generation and collection rate of electron-hole pairs, $N^{\mathrm{in}}_{\mathrm{ph}}$ is the rate of incident photons, q is the elementary charge, and M is a material constant. The material constant M can be calculated as

$$M := \frac{N^{\mathrm{gen}}_{\mathrm{e^-/h^+}}}{N^{\mathrm{in}}_{\mathrm{ph}}} \approx \frac{E_{\mathrm{abs}}}{\alpha \cdot E_{\mathrm{g}}}, \tag{3.18}$$

where E_{abs} is the energy deposited in the absorber layer per incident X-ray photon, E_{g} is the bandgap of the absorber material and α is a constant. The factor α accounts for the energy efficiency of electron-hole pair generation. It is often approximated as $\alpha \approx 3$ [43, 174, 175].

3.2.5 X-ray excited optical luminescence

This section will introduce XEOL. Large parts of this section are being published in Ref. 4 and are not further marked.

In an analogous way to photo luminescence measurements with laser excitation, XEOL measurements assess the solar-cell performance with respect to radiative recombination of the X-ray excited electron-hole pairs by detection of the emitted photons with an energy corresponding to the bandgap of the solar-cell absorber [26, 106, 176]. Competing non-radiative recombination paths, e.g., through trap states at grain boundaries, may reduce the charge-carrier lifetime, thus decreasing the XEOL intensity.

Portable setup with spectral and time resolution

An XEOL detection unit was developed to study the optical performance of the solar cell. We designed it in a transportable, compact, and modular fashion for easy use and flexibility to adapt to different samples and beamline environments. Therefore,

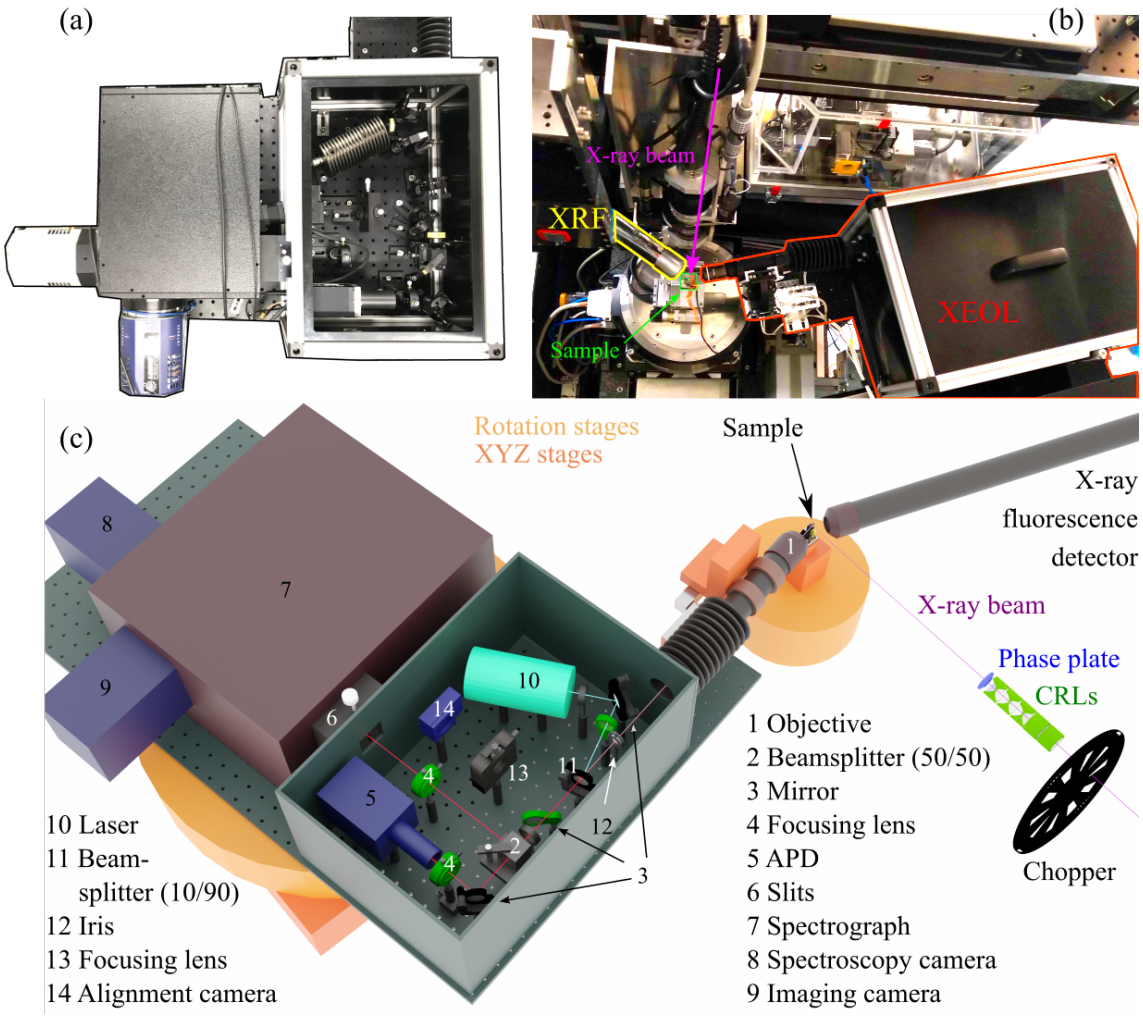

Figure 3.13: (a) Photo top-view of the open optical chamber; (b) photo of the setup implemented at P06 in a multi-modal setting; (c) scheme of the XEOL detection setup with the beam paths indicated: X-ray beam (purple), alignment laser (blue), XEOL photons (red).

the whole setup was built as an optical enclosure upon a breadboard. Figure 3.13(a) shows a top-view image of the setup with the optical chamber open. In (b) the setup is shown integrated into the measurement environment at the P06 micro-hutch where simultaneous XRF measurements are conducted. The detailed scheme of the setup is shown in Fig. 3.13(c) with numbered components and described in the following:

For the coarse alignment with respect to the X-ray beam and the beamline, the breadboard hosting the optical setup was further installed onto a manual rotation stage and xyz-translation stages. An infinity-corrected long working distance objective (Olympus LMPLFLN100X, NA=0.8, (1)), connected to a lens tube was mounted to piezo-motors (PI) for the fine alignment. For the detection of the col-

lected photons, we decided to split the beam into two separate detection units, to obtain simultaneously temporal and spectral resolution (both optimized for high signal-to-noise ratio). Therefore, the collected XEOL photons from the sample were simultaneously focused with lenses (AC254-100-A, with LM1XY, Thorlabs,(4)) onto an avalanche photodiode (APD) (PDM Series, Mirco Photon Devices, (5)) or the entrance slit of a spectrograph. The signals from the APD were fed to a PicoHarp 300 (PicoQuant) for temporal measurements and to the counter of the beamline system. The spectrograph (Acton SpectraPro Series, 2300i Model, Princeton Instruments, (7)) equipped with either a mirror or a 300 gr/mm grating (750 nm blaze) dispersed the light onto one or two of the charged coupled device (CCD) cameras (Andor iDus420 OE, (8): spectroscopy camera, Princeton Instruments ProEM 512, (9): imaging camera) for spectrally resolved measurements. The two cameras were installed for low noise experiments with spectral resolution (iDus420 OE) and fast imaging of the spot emitting the XEOL signal for the proper adjustment (ProEM 512) of the XEOL setup. Both cameras are suitable to operate in the visible spectral range; however, a different camera could easily be mounted here to cover other wavelength regions. A simple imaging camera (webcam with dismounted lense, (14)) and a laser (LDH-P-C-440, Picoquant with PDL 800-D,(10)) were incorporated into the system for initial coarse alignment of the system to the X-ray beam and sample interaction spot. The laser was attenuated by a neutral density filter and filtered by a 450 nm short-pass filter (FES450, Thorlabs). Mirrors (PF10-03-P01, held in KM100, Thorlabs,(3)) guided the beam to a beam splitter (10/90,(11)) directing the beam via an iris (ID12, Thorlabs,(12)) to the entrance aperture of the objective. Using a foldable mirror (PF10-03-P01, in TRF90, Thorlabs,(3)) the collected light from the sample could be either focused on a simple webcam by a lens to inspect the focus of the alignment laser or on the aforementioned CCD and APD detectors. A long pass filter 450 nm (FELH 450, Thorlabs) was placed in front of the 50/50 beamsplitter (KM200B/M, hold with PM4*, Thorlabs) to remove unwanted laser light in case of performing conventional PL experiments.

Both the PicoHarp 300 and CCD cameras were controlled and read out by a PC that was independent of the beamline controls. Synchronization was obtained by trigger signals from the electron bunch clock and scan positions. With additional synchronization of the laser to the bunch clock, pump-probe measurements would in principle be possible. The sideways approach of the objective allowed the X-ray beam to pass undisturbed so that multi-modal measurements, potentially including additional XRD or ptychography, were feasible.

Differences between an XEOL and PL measurement

Regarding the detection unit, the differences between XEOL and PL measurements are small: In the case of a laser excitation source, additional filters which block the reflected laser beam have to be installed.

The greater difference is in the excitement of the charge carriers. The laser energy is usually chosen just above the bandgap and directly creates electron-hole pairs. As described for XBIC, the charge-carriers excited by an X-ray beam are the product of a particle shower, where the particles thermalize to the band edge via Auger [177] and inelastic scattering processes [106]. Thus, a laser photon only creates one electron-hole pair, while a single X-ray photon can create multiple (on the order of hundreds to thousands of) electron-hole pairs. As described in Eq. 3.18 the material constant M gives the amount of generated electron-hole pairs per incident X-ray photon.

With a laser, it is possible to vary the energy of the exciting photon from below the bandgap energy to above. Thus so-called photoluminescence excitation (PLE) spectra are measured which give information about energy states inside of the bandgap [178]. For X-rays the energy can be tuned to be below or above the absorption edges for the element of interest to gauge its influence on the optical performance, this is often done in combination with XANES measurements [106].

Spectrally resolved XEOL

Emitted PL photons are energetically separated by the grating in a spectrograph and collected with a CCD camera. Around the bandgap energy, a mostly Gaussian distribution can be observed which is caused by tail-states reaching into the bandgap on the longer wavelength side and recombinations from higher energetic states — which can be either due to an excess of free carriers, thermal excitation, or local inhomogeneities — on the shorter wavelength side.

From the form of the Gaussian, information about the tail-states and quasi-Fermi level splitting can be gained [85, 179, 180]. However, for these analyses, additional absorption spectra are necessary which are usually not taken in the case of X-ray microscopy measurements. Therefore, the interpretation and correct analysis of the XEOL spectra is still not fully developed, yet.

In this work, the spectra are fitted with a simple Gaussian of the form

$$G(x) = A \cdot \exp\left\{-\frac{1}{2}\frac{(x-x_0)^2}{\sigma^2}\right\} + C, \tag{3.19}$$

where A is the amplitude, x_0 is the central wavelength, σ is the standard deviation and C is an offset, namely the dark counts.

While the amplitude in classical PL measurements gives a good estimate of the goodness of the absorber, in XEOL measurements the goodness of the absorber is further superimposed with the effect of the beam-sample interaction volume. This becomes critical in the face of solar cell absorbers with inhomogeneous thicknesses such as the voids in Cu(In,Ga)Se_2 (see Sec. 3.3) or the appearance of wrinkles in perovskites (see Chapter 6). The central wavelength is associated with the bandgap. However, care has to be taken as photon-recycling effects can red-shift the spectrum [170, 181, 182]. The interpretation of the width of the Gaussian is difficult, as photon-recycling and tail state effects overlap.

If the measurement environment allows it, XEOL should be measured with a detector-to-sample angle close to 90° to avoid shadowing effects from self-absorption in inhomogeneously thick absorbers.

Time-resolved XEOL

For time-resolved measurements, a pulsed excitation source is needed with long dark periods in between. Many synchrotrons have special timing modes where only a few electron bunches are running. At DESY this is the 40-bunch timing mode, with 192 ns between 44 ps long pulses. The APS has an even wider-spaced timing mode where dark periods over a microsecond long are achieved. The brilliant but short pulse excites the material and by recording the emitted XEOL photons the recombination dynamics of the charge carriers can be studied.

The double exponential ansatz is a conventional approach to fit the decay curves in the photoluminescence analysis of perovskites [183, 184] where the fast decay component is attributed to SRH recombination and the slower component to radiative decay. Auger processes are often neglected as the regime for this process needs very high charge-carrier concentrations which are usually not reached. A double-exponential fit to a decay curve is exemplarily shown in Fig. 3.14. The data points are taken from a measurement of a perovskite solar cell, which will be further discussed in Chapter 6. As the measured signal is always a convolution of the actual signal and

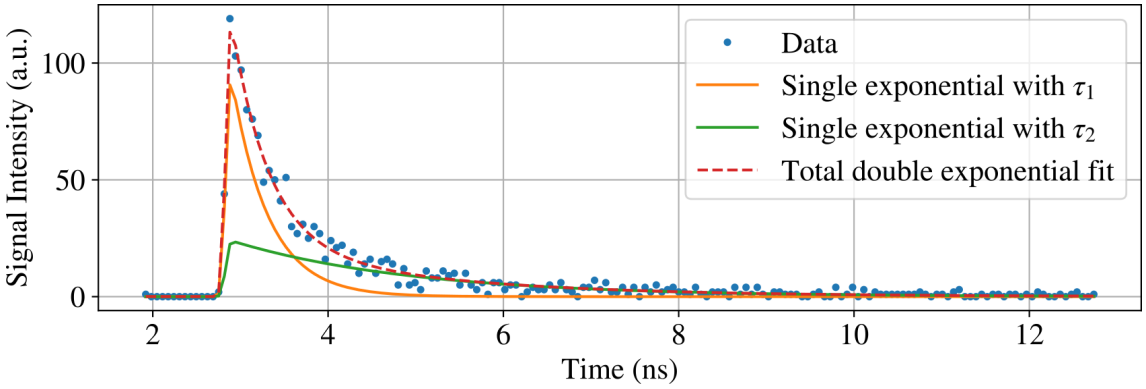

Figure 3.14: Exemplary recorded decay curve (blue dots), with the overlaid double exponential fit.

the instrumental response function (IRF) of the detector, a simple decay function is not sufficient. The IRF is approximated as a Gaussian and convoluted with the exponential decay function. The analytical solution of a convolution between a Gaussian and a single exponential decay is given as

$$S(t) = \frac{A}{2} \exp\left\{-\frac{t}{\tau}\right\} \exp\left\{\frac{\sigma^2}{2\tau^2}\right\} \operatorname{erfc}\left(\frac{\sigma}{\sqrt{2}\tau} - \frac{t}{\sigma\sqrt{2}}\right) \tag{3.20}$$

with A as an amplitude, τ as the decay constant, σ as the sigma of Gaussian width, and $\operatorname{erfc}(x) = 1 - \operatorname{erf}(x)$ begin the complementary error-function with the error-function defined as

$$\operatorname{erf}(x) = \frac{2}{\sqrt{\pi}} \int_0^x \exp\{-t^2\} dt. \tag{3.21}$$

The extension to a double exponential model is trivial as it is a simple summation, leading to the fitting function

$$\begin{aligned} S(t) = &\frac{A_1}{2} \exp\left\{-\frac{t}{\tau_1}\right\} \exp\left\{\frac{\sigma^2}{2\tau_1^2}\right\} \operatorname{erfc}\left(\frac{\sigma}{\sqrt{2}\tau_1} - \frac{t}{\sigma\sqrt{2}}\right) \\ &+ \frac{A_2}{2} \exp\left\{-\frac{t}{\tau_2}\right\} \exp\left\{\frac{\sigma^2}{2\tau_2^2}\right\} \operatorname{erfc}\left(\frac{\sigma}{\sqrt{2}\tau_2} - \frac{t}{\sigma\sqrt{2}}\right) + C \end{aligned} \tag{3.22}$$

where C is an offset.

As all processes depend on the charge-carrier density they are linked to each other and a clear separation of the respective lifetimes is difficult. Therefore, an effective lifetime gained from the amplitudes and decay constants of the individual exponential

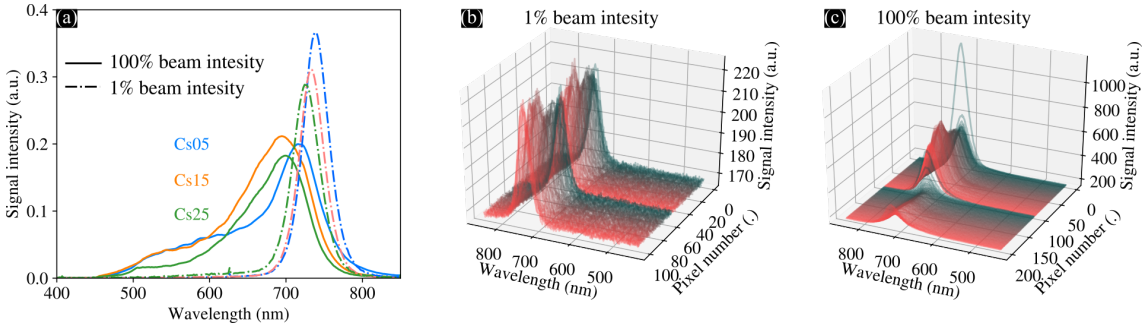

Figure 3.15: (a) Summed spectrally resolved XEOL for the three solar cells, with 100 % (solid line) and 1 % (dashed lines) beam intensity. The individual spectra of the first two rows of a scanned map are shown in (b) at 1 % beam intensity and in (c) at 100 % beam intensity.

decays is calculated as

$$\tau_{\text{eff}} = \frac{\sum_i A_i \tau_i^2}{\sum_i A_i \tau_i}. \tag{3.23}$$

Considerations when measuring XEOL

For XEOL measurements, the topic of beam damage is even more critical than for XBIC measurements. XEOL is in its detection a photon-hungry technique, as only a fraction of the emitted photons is collected and has to be evaluated with respect to time and spectral resolution. Thus, it needs a certain amount of deposited dosage to create a signal of significant statistics. While XBIC measurements have the feasible strategy of 'measure-ahead-of-the-burn' by outrunning the beam damage with a fast measurement speed, this is not applicable for XEOL. The impact beam damage can have on the optical properties of a perovskite solar cell is shown in Fig. 3.15. The three perovskite solar cells (denoted Cs05, Cs15 and Cs25 after their respective Cs content) whose XEOL spectra are shown in Fig. 3.15(a) will be discussed in Chapter 6. The XEOL spectra shown here are summed spectra from maps scanned first at 1 % beam intensity (dashed lines) with a dwell time of 1.1 s and step size of 400 nm and then the same area re-scanned at full beam intensity (solid lines) with a dwell time of 0.3 s and a step size of 200 nm. The high-intensity X-ray beam led to a transformation of the XEOL spectra: A strong blue shift as well as the emergence of a second peak and shoulder at full intensity can be observed. We associated this with the degeneration of the solar cell and the Fermi level reaching into the conduction band, leading to recombination from higher excited states than the conduction band minimum.

Figures 3.15(b) and (c) highlight the effect beam damage has during a scan. In Fig. 3.15 (b) the individual spectra from two lines of the map scanned at 1 % beam intensity are shown. The first pixel is colored in dark green and the gradient to red separates the individual spectra. The first pixel of the second line starts then again with the dark color. The intensity of the XEOL spectra is varying as the absorber is not of homogeneous thickness and quality. However, there is no significant difference between the spectra of line 1 compared to line 2. This is not the case for Fig. 3.15(c) where the same area was re-scanned at full beam intensity. Despite a shorter dwell time than in (b) the effects of beam damage are apparent. First, note the drastic decrease in intensity from the first to the second spectrum, this is again visible in the second line. Second, the second line again has a strong decrease in signal compared to the first, highlighting that the measured area is affected by the measurement of the first line.

Therefore, for these perovskite samples, lower intensity and longer dwell time was the chosen approach to avoid beam damage.

3.3 Measurement strategies

For a comprehensive study of solar cells, one could apply all those measurement techniques just introduced and others to the sample. However, when designing the experiment, it has to be taken into consideration whether these modalities should and could be simultaneously assessed, or if sequential measurements are necessary. In the following, the advantages and disadvantages of multi-modal and sequential measurements will be discussed on the basis of an example. Large parts of this section were already published in Ref. 2 and will not be further highlighted. The XEOL setup used for the work in this section was the first implementation and varies slightly from the setup described in Sec. 3.2.5.

The multi-modal measurement and the subsequent measurements were performed in the course of one beamtime on the same Cu(In,Ga)Se_2 solar cell. Figure 3.16 (b,c) show two representative scanning electron microscopy (SEM) images of the cell surface, exhibiting the granular structure of the absorber layer propagating to the solar-cell surface.

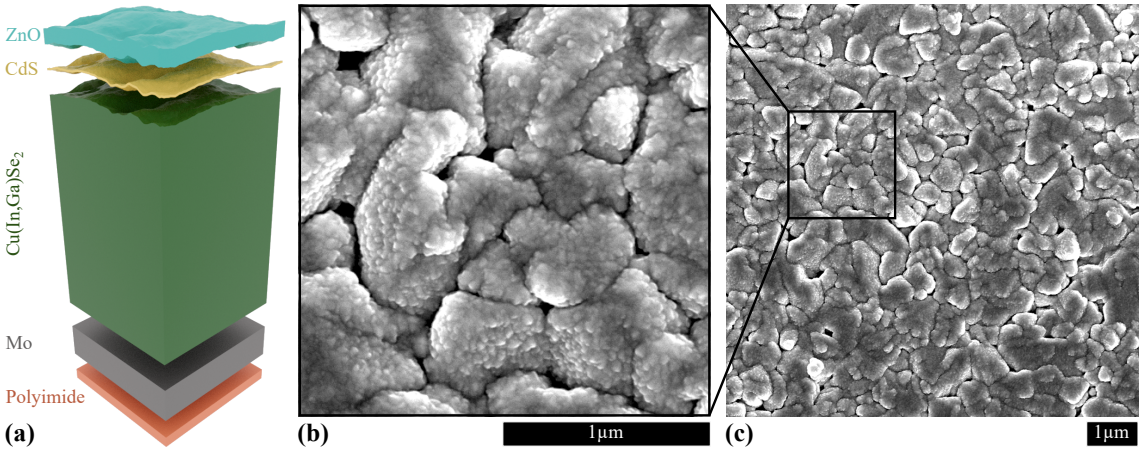

Figure 3.16: (**a**) Scheme of the $Cu(In,Ga)Se_2$ solar cell stack. (**b**–**c**) Scanning electron microscopy image of the solar cell surface (courtesy of A. Jeromin, DESY NanoLab [185]). Figure adapted from Ref. [2].

3.3.1 Sample

The sample was provided by EMPA. The $Cu(In,Ga)Se_2$ solar cell was synthesized on a polyimide foil substrate as described in detail in [51]. The Mo back contact layer (0.5 µm) was deposited by sputtering. The $Cu(In,Ga)Se_2$ absorber layer was deposited by a multistage co-evaporation process around 450 °C substrate temperature and was subjected to an in-situ NaF+RbF post-deposition treatment in Se ambient. The integrated Ga:In composition ratio is 0.41:0.59 and the $Cu(In,Ga)Se_2$ thickness 3.16 µm. The CdS buffer layer (25 nm) was deposited in a chemical bath (CBD), followed by deposition of ZnO (65 nm) and transparent conductive oxide ZnO:Al (120 nm) layers by sputtering. The cell was contacted through an electron-beam evaporated Ni-Al grid and manually isolated by peeling-off surrounding $Cu(In,Ga)Se_2$ material. Manually applied silver paint (far from the region of interest) was used to electrically connect the Ni-Al grid to thin Cu wires and a dedicated PCB from where co-axial wires were used for the connection to the current measurement circuit as detailed in Sec. 3.2.4.

3.3.2 Experimental setup for four-fold multi-modal measurements

The experiment was performed in the micro-hutch of P06 as laid out in Fig. 3.17. Under the constraints of (i) limited space in the experimental hutch, (ii) limited solid angle for the X-ray optics and detectors, and (iii) minimized shielding by detector elements and the sample, the geometry displayed in Fig. 3.17 was found to yield the

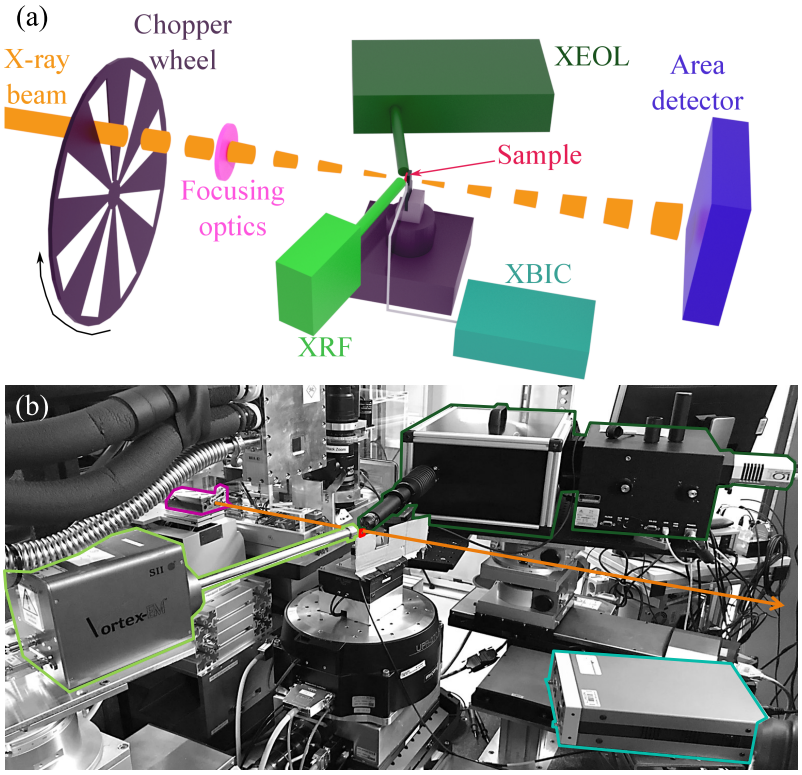

Figure 3.17: Experimental setup. (**a**) Scheme of the multi-modal X-ray microscopy measurement involving X-ray fluorescence (XRF), X-ray beam induced current (XBIC), X-ray excited optical luminescence (XEOL), and ptychography. (**b**) Picture of the actual setup. The area detector for ptychography is located further downstream along the beam path and is not visible here. Figure adapted from Ref. [2]

optimum signal-to-noise ratio for all measurement modalities.

The photon energy was 15.25 keV, just above the Rb_K absorption edge (15.21 keV) for maximum sensitivity to this trace element. Compound refractive lenses (CRL) made of Be, a corrective phase plate [136], and a pinhole were used to focus the beam. The caustic of the nano-focused X-ray beam for the multi-modal measurements was already shown in Figure 3.4 as measured by ptychography. The photon flux was $7 \cdot 10^9$ ph/s, resulting in a dose rate of $1.4 \cdot 10^{13}$ eV/s in the solar-cell absorber.

XRF: For fluorescence measurements, a silicon drift detector (Hitachi, SII Vortex EM) was used with a digital pulse processor (Quantum Detectors, Xspress3). The detector was placed in the plane of the storage ring inboard with an Al collimator; the angle between the sample surface and the detector was 7° and the distance was 2 cm.

XBIC: For lock-in amplified XBIC measurements, the X-ray beam was modulated

with a frequency of 8.015 kHz upstream of the X-ray optics as detailed in Sec. 3.2.4. After pre-amplification (Stanford Research Systems, SR570) with 1 µA/V, the XBIC signal was demodulated by a lock-in amplifier (Zurich Instruments, UHFLI) with a low-pass cutoff frequency of 501.1 Hz (8^{th} order). The front contact of the solar cell was grounded to avoid artifacts from space charge at the cell surface and replacement currents that can be induced by the X-ray beam [43].

XEOL: The XEOL setup was placed in the plane of the storage ring outboard. The angle between the sample surface and the optical axis of the XEOL setup was 10°. The XEOL photons were collected with a 4x objective (Olympus, UPlanSApo) with a numerical aperture of 0.16, and the intensity was measured by a Si CCD camera (Andor, iDus420 OE). A mirror was used instead of a grating in the spectrograph, and only the intensity of the XEOL signal was measured. This was necessitated as the total collected signal was very low.

Ptychography: An area detector (Dectris, Eiger X 4M) was placed 8.05 m downstream of the sample, in the experimental nanoprobe hutch of the beamline P06 [6], to measure the far-field diffraction patterns. The detector was set up in a vacuum ($< 1 \cdot 10^{-3}$ mbar) with a flight tube to minimize the air path between the sample and detector [141].

3.3.3 Multi-modal

For independent XRF, XBIC, XEOL, and ptychography measurements, different sets of measurement parameters would be ideal. Hence, the simultaneous measurement of all modalities requires a compromise between (i) low dose to limit sample degradation, (ii) high dose to maximize signal-to-noise ratio, (iii) high coherence to enable ptychographic reconstruction, and (iv) short dwell time to enhance throughput.

Balanced for the four measurement modalities, a step scan was performed where the fast shutter of the beamline was closed during the position-settling time. An area of 4 µm × 4 µm was mapped with 100 nm × 100 nm step size at a nominal dwell time of 0.5 s per point. The actual dwell time was halved as the chopper fully blocked the beam 50% of the time. The effect of the chopper on the ptychographic reconstruction was deemed marginal in preliminary scans. The sample surface was perpendicular to the incident X-ray beam and the scan motion was executed in the sample-surface plane.

Compared to dedicated scans optimized for each modality separately, the multi-modal

measurement with the parameters specified above led to the following compromise:

XRF: The chopper required for high-sensitivity XBIC measurements blocks 50% of the photons and thus decreases the statistics, this could easily be compensated by doubling the dwell time. In that case, there are no disadvantages of the multi-modal measurement approach compared to XRF-optimized measurements.

XBIC: For XBIC measurements, requirements are relaxed as long as a chopper is used to modulate the X-ray beam. Dedicated XBIC scans could be performed more than two orders of magnitude faster with comparable signal-to-noise; the long dwell time required for the multi-modal measurement would only be a drawback if X-ray beam induced sample damage was present, as is the case e.g. in perovskite solar cells [163, 186].

XEOL: As the most photon-hungry technique used in this experiment, the XEOL measurement determined essentially the minimum dwell time of the multi-modal measurement for satisfying signal-to-noise ratio. Accordingly, the penalty in signal quality by the 50% flux reduction by the chopper is highest in the XEOL signal. In addition, stray light from a multitude of electronic devices present in the X-ray hutch and mechanical vibrations compromised the signal-to-noise.

Ptychography: The high-flux requirement for XRF and XEOL measurements required opening the beam-defining slits in the P06 optics hutch. While this allowed high signal-to-noise XRF and XEOL measurements, it comes at the cost of a reduced spatial coherence of the beam at the location of the X-ray microscope. As a consequence, the image quality in ptychography is reduced in this high-flux operation mode. In the presented measurements, a typical reduction in spatial resolution of less than about a factor of 2 was observed as compared to ptychographic measurements in high-coherence mode, while the focused flux was 10-fold higher. This trade-off between high focused flux and high spatial coherence will be relaxed at fourth-generation storage rings such as PETRA IV [36].

3.3.4 Subsequent/sequential

The subsequent conduction of measurements optimized for each modality respectively gets rid of the need to compromise. However, the sequence in which the measurements are taken still takes the same points (i–iv) into consideration. Depending on the stability of the sample under X-ray illumination, XBIC, XBIV or XEOL measurements should be prioritized. As the composition and structure of most inorganic solar

cells are stable under the X-ray illumination, dedicated XRF measurements are conducted after the performance measurements followed by ptychography. The choice to measure ptychography last is due to the need to close the beam slits further for a more coherent X-ray beam.

In this example four scans were performed and the measured modalities are listed in Table 3.3. The underlined modalities give the optimization required for the respective scan.

For Scan 1–3 the scanned area was 8 µm × 8 µm large while Scan 4 covered a slightly smaller area of 5 µm × 5 µm.

Scan 1 and 2 The first and second scans were optimized for XBIC and XBIV measurements respectively. The dwell time was set to 0.01 s per pixel with a step size of 25 nm × 25 nm in both cases. The scanning speed was thus roughly an order of magnitude larger than in the multi-modal measurement approach. XRF measurements were simultaneously taken, this is helpful for later image registration.

Scan 3 The third scan was optimized for the photon-hungry techniques of XRF and XEOL. As XBIC and XEOL are competing processes, they should optimally not be measured simultaneously. On the other hand, measuring XBIV simultaneously does not have any negative impact, except for the continued use of the chopper which still halves the incoming photon flux. To collect enough statistics, the dwell time was set to 0.5 s per pixel with a step size of 50 nm × 50 nm.

Scan 4 For this last scan, the chopper was taken out effectively doubling the incoming flux, and the slits cutting off incoherent parts of the beam in the horizontal plane were further closed from a gap of 0.2 mm to 0.04 mm thus reducing the flux. The step size was 50 nm × 50 nm with a dwell time of 0.5 s.

Same as for the multi-modal measurements, the images were registered with the EEC transform [187] from the OpenCV library [188]. The Φ_{Se} maps from the XRF

Scan	XBIC	XBIV	XRF	XEOL	Ptycho	Δt_{eff}	Step size	Slit width
1	✓	-	✓	-	-	0.005 s	25 nm	0.2 mm
2	-	✓	✓	-	-	0.005 s	25 nm	0.2 mm
3	-	✓	✓	✓	✓	0.25 s	50 nm	0.2 mm
4	-	-	✓	-	✓	0.5 s	50 nm	0.04 mm

Table 3.3: Measured modalities at the subsequent scans. The respective scan is optimized for the underlined modality. The effective dwell time Δt_{eff}, step size, and width of the slits are further listed for the respective scans.

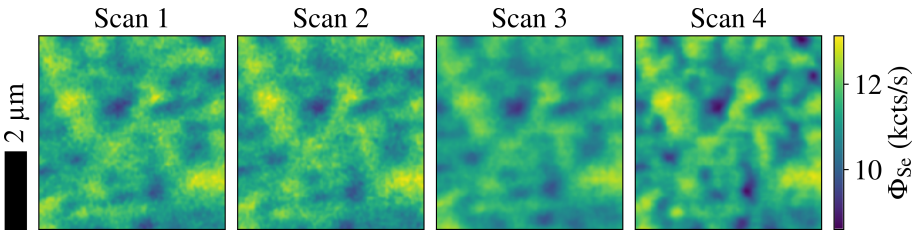

Figure 3.18: XRF maps of Se from all four scans.

measurements, which were taken in all four scans, were used for the registration and can be seen in Fig. 3.18. Only the ptychographic reconstruction from scan 4 was registered cross-modality as it may shift the positions and therefore differ from the simultaneously taken XRF map. The discussion about the registration of sequentially acquired scans can be found in Ref. [7].

3.3.5 Discussion

The full discussion of the four-fold multi-modal scan can be read in Ref. [2]. The in-depth analysis of the sequentially obtained scans will be covered in Ref. [151] (*in preparation*).

Figure 3.19 (a–e) show the maps taken simultaneously of the four modalities, while (f–j) show the sequentially taken maps. The scalebar of 2 µm holds for all maps, and the colorbars are valid for each column of the figure. The numbers in the lower right corner of Fig. 3.19(f–j) indicate the scan during which the data was taken. Resulting from XRF measurements, the area density is shown in Figure 3.19 for Se ($\rho_{\mathrm{A}}^{\mathrm{Se}}$) (a,f) and for Rb ($\rho_{\mathrm{A}}^{\mathrm{Rb}}$) (b,g). The distribution of Se is representative of the main elements in the Cu(In,Ga)Se_2 absorber layer. The distribution of Rb in the absorber layer is of particular interest due to the outstanding role of alkali elements for the Cu(In,Ga)Se_2 solar-cell performance [103, 179]. It is noteworthy that the relative variation of $\rho_{\mathrm{A}}^{\mathrm{Rb}}$ is stronger compared to $\rho_{\mathrm{A}}^{\mathrm{Se}}$, this can only partially be attributed to the smaller signal-to-noise ratio of the Rb quantification (note that $\rho_{\mathrm{A}}^{\mathrm{Rb}} \ll \rho_{\mathrm{A}}^{\mathrm{Se}}$); rather, this indicates a stronger Rb segregation.

The results from XBIC, XEOL, and ptychography measurements are shown in Figure 3.19(c–e) (simultaneous) and (h–j) (sequential) in terms of current (I_{XBIC}), count rate of photons with an energy corresponding to the bandgap of the solar-cell absorber (f_{XEOL}), and relative electron area density ($\Delta\rho_{\mathrm{A}}^{\mathrm{e}}$), respectively.

Comparing the simultaneous and sequentially measured maps, the impact of the

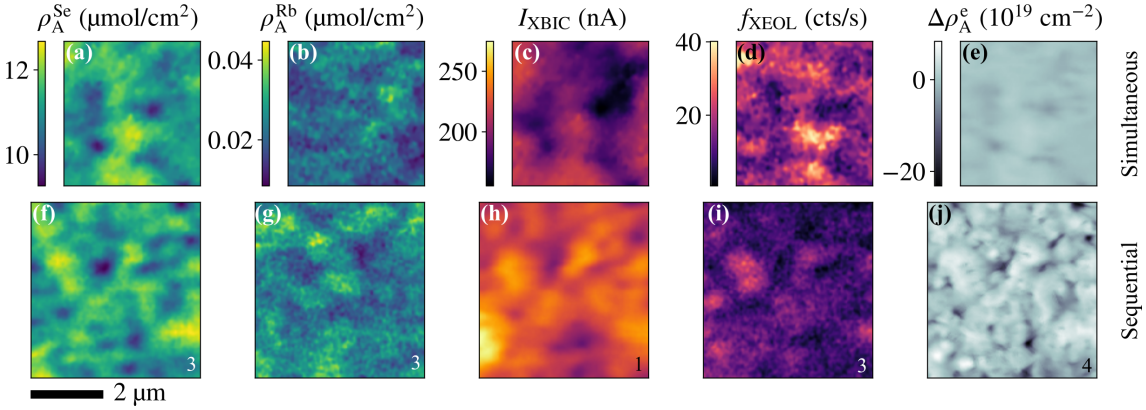

Figure 3.19: (**a–e**) Simultaneously measured maps, (**f–j**) sequentially measured maps. (**a,f**) Area density of Se (ρ_A^{Se}) and (**b,g**) of Rb (ρ_A^{Rb}) from X-ray fluorescence measurements. (**c,h**) X-ray beam induced current (I_{XBIC}) from electrical performance measurements. (**d,i**) Photon count rate (f_{XEOL}) from X-ray excited optical luminescence measurements. (**e,j**) The relative area density of electrons ($\Delta\rho_A^e$) from ptychography measurements, zero was arbitrarily shifted to the mean of the respective map.

compromise necessary for the simultaneous measurement becomes apparent. The clarity of the features in Figure 3.19(f–j) is superior to Figure 3.19(a–e). Note that the contrast in Figure 3.19(e) is not optimally set due to the relative nature of the modality. The strong difference in contrast displayed here is most likely due to some deep-reaching voids in the sequentially measured area, as well as the optimized parameters enabling to resolve the deepest parts of the voids.

Despite the common measurement parameters being sub-optimal for each modality in the simultaneous assessment, Figure 3.19(a–e) demonstrates that a compromise can be found with high measurement quality in all four modalities, as the features displayed in Figure 3.19(a–e) are highly similar in their nature to Figure 3.19(f–j).

Here, it should also be noted that the total measurement time for the multi-modal scan was around 20 min compared to almost 8 h for all the sequential scans together. The time scaling is not directly relatable as the size of the scanned area was different, nevertheless, the order of magnitude in time difference is still clear.

The features, which are similar over the different modalities on a length scale from a few hundred nanometers up to one micrometer, are apparent in all maps of Figure 3.19(a, c–e) and (f,h–j), while the features in the Rb distribution (Figure 3.19(b,g)) follow a different pattern resembling the inverted features of I_{XBIC} (Figure 3.19(c,h)).

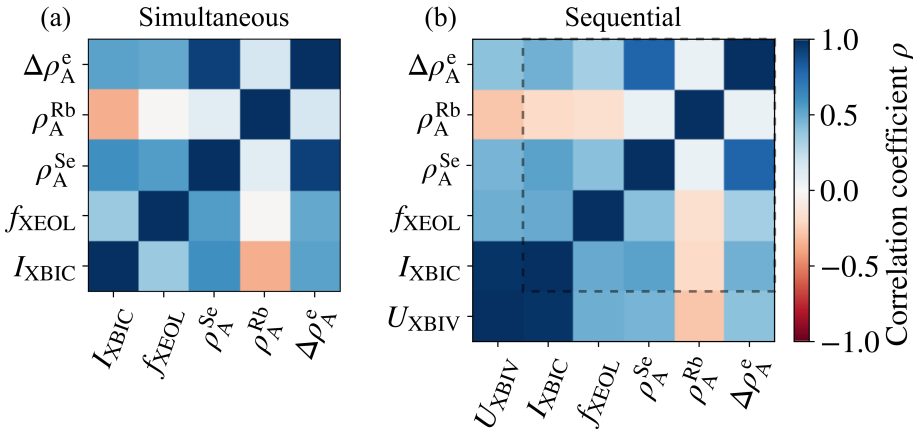

Figure 3.20: (a) Simultaneously measured set, (b) Sequentially measured set. Correlation coefficient ρ for all combinations of the area density of Se (ρ_A^{Se}) and of Rb (ρ_A^{Rb}), of the X-ray beam induced current (I_{XBIC}), of the photon count rate from X-ray excited optical luminescence measurements (f_{XEOL}), and of the relative electron area density ($\Delta\rho_A^e$). In (b) the X-ray beam induced voltage (U_{XBIV}) is additionally included. The black dashed frame highlights the same correlations for (a) and (b).

To compare the correlative analysis of the four-fold multi-modal measurements more in-depth, the statistical correlations between the measurement parameters shown in Figure 3.19 were evaluated. The result is shown in Figure 3.20(a) for the simultaneous and in Figure 3.20(b) for the sequential set, as the matrix of the correlation coefficient ρ, where $\rho = 1$, $\rho = -1$, and $\rho = 0$ describe perfectly correlated, perfectly anti-correlated, and uncorrelated data, respectively [189]. For completeness, the X-ray beam induced voltage (U_{XBIV}) is included in Figure 3.20(b), while the dashed lines outline the shared modalities.

Comparing the correlation coefficients gained through the two measurement strategies, they show similar trends. The biggest difference lies in the correlation of ρ_A^{Rb} with f_{XEOL}. While in Figure 3.20(a) no correlation could be found, in (b) a slight negative correlation is present. The lack of correlation in (a) is most likely caused by the rivalry between the XBIC and XEOL processes. In (b) the negative correlation between ρ_A^{Rb} and all the performance assessing modalities (U_{XBIV}, I_{XBIC}, f_{XEOL}) is apparent. Another difference is in the correlation between ρ_A^{Se} and $\Delta\rho_A^e$. As the optimized ptychography scan enables a higher resolution, the point-by-point correlation with the XRF data is slightly reduced.

Considering the results from the correlative analysis (Figure 3.20) for the interpretation of the maps (Figure 3.19), the following observations can be made even just based on the simultaneously measured set:

Topology: When comparing the two raster-scanned maps in Figure 3.19(a,e), the relative electron area density map shows higher resolution – resulting from the ptychographic reconstruction – than the fluorescence map, enabling finer features in the topology of the absorber layer to be seen.

The similarity of features in the Se area density and relative electron area density maps of Figure 3.19(a,e), and the positive correlation coefficient (Figure 3.20) of $\rho_{\mathrm{A}}^{\mathrm{Se}}$ and $\rho_{\mathrm{A}}^{\mathrm{e}}$ are strong indications that both distributions have the same origin – the topology of the absorber layer. Thus, the claim made in [5] that the ptychographically reconstructed phase shift and the absorber-element distribution represented here by Se are dominated by the absorber topology can be corroborated: the greater the number of atoms in the projected interaction volume of the beam with the absorber layer, the stronger is the fluorescence signal and the electron area density.

Two mechanisms are assumed to be responsible for the structures dominating the topology: first, the area density of the absorber layer tends to be smaller at grain boundaries than at grain cores [61, 190]; second, voids and crevices in the absorber layer are known to be present in this type of solar cell [50], leading to low $\rho_{\mathrm{A}}^{\mathrm{Se}}$ and $\rho_{\mathrm{A}}^{\mathrm{e}}$. The distinction between these two mechanisms would require tomographic measurements which is beyond the scope of this study.

Rubidium segregation: Anti-correlation of $\rho_{\mathrm{A}}^{\mathrm{Rb}}$ and I_{XBIC} is unveiled in direct comparison of the corresponding maps in Figure 3.19(b, c) and in their negative correlation coefficient in Figure 3.20. This indicates that Rb accumulates at recombination-active defect sites (including grain boundaries) where the XBIC signal is weaker. This observation is in accordance with other studies, where Rb was shown to segregate at grain boundaries [191–193] and will be further discussed in Chapter 5.

In the case of the Rb distribution, lacking correlations are also relevant: $\rho_{\mathrm{A}}^{\mathrm{Rb}}$ is not generally correlated with $\rho_{\mathrm{A}}^{\mathrm{Se}}$ or $\rho_{\mathrm{A}}^{\mathrm{e}}$, which indicates that Rb does neither accumulate in voids nor that it is homogeneously distributed in the absorber layer (which would be seen as negative and positive correlations, respectively). This lack of correlation is in accordance with previous findings [194].

Performance: The assessment of the nanoscale performance of a Cu(In,Ga)Se_2 solar cell by two means – electrically by XBIC and optically by XEOL – allows conceptually the discrimination of measurement artifacts based on their different detection path of charge-carrier recombination: while XBIC measurements are affected by the electronic circuit of the entire solar cell, XEOL measurements are affected by the optical performance of the layer stack – a good solar cell is also a good light-emitting

device due to the reciprocity principle [195].

Both performance measurements have in common that they depend, in first approximation linearly, on the X-ray absorptance of the absorber layer. Accordingly, the absorber topology has a strong impact on the XBIC and XEOL signal, this is indicated by the positive correlation between $\rho_{\mathrm{A}}^{\mathrm{Se}}$, $\rho_{\mathrm{A}}^{\mathrm{e}}$, I_{XBIC}, and f_{XEOL}.

For the further improvement of solar cells, it is of particular interest to understand the origin of poor performance in areas that are not limited by topology but by non-radiative recombination, due to the presence of defects. Such areas can be seen in Figure 3.19(a, c–e) as an imperfect match of the maps.

Conclusion

It was shown that it is possible to find a compromise between measurement modalities such that simultaneous multi-modal scanning microscopy yields enough information for correlative analysis. The big advantage of this measurement mode is its time efficiency and point-by-point correlation. Nevertheless, sequentially acquired scans, with optimized parameters, still hold their superiority in resolution and are essential when high precision correlation analysis is needed.

The advent of simultaneous measurements will come with the synchrotron sources of the fourth generation (e.g. PETRA IV) where the coherence and brilliance of the X-ray beam will be boosted by magnitudes [36].

4 Lock-in amplification for XBIC measurements

After the introduction of the measurement modes in the previous chapter, this chapter presents developments for taking X-ray beam induced current measurements for solar cell characterization. It is entirely based on Ref. 1, published in Journal of Visualized Experiments and the text is taken directly from the published article only partially adapted to fit the context of this thesis. The publication gives a protocol to follow for the conduction of XBIC measurements, and the application of lock-in amplification is discussed in regards to the measurement of solar cells. While the principle of lock-in amplification is long known, this specific application case had not yet been discussed extensively before.

Given that the XBIC and XBIV signals can be small (often, variations in the sub-picoampere and nanovolt range are of interest), the signals are easily buried in noise. Therefore, it is suggested to utilize lock-in amplification to extract the XBIC and XBIV signals [5]. For this purpose, the incoming X-ray beam is modulated by an optical chopper as indicated in Fig. 4.1. This modulation carries over to the signal produced by the DUT. Before the signal is fed into the lock-in amplifier (LIA), a pre-amplifier (PA) is typically used to match the raw signal intensity with the range of the analog-to-digital converter at the input of the digital LIA. The LIA mixes the modulated measurement signal with the reference signal. By employing a low-pass filter, only frequencies close to the reference signal are passed through and amplified [196]. This allows for an effective extraction of the XBIC or XBIV signal from a noisy background.

In the following sections the measurement steps for lock-in amplification will be presented. They encompass: signal modulation, pre-amplification, signal mixing in the LIA, low-pass filter frequency of the LIA, and the low-pass filter roll-off of the LIA. Exemplary measurements, partly conducted with a red laser ($\lambda = 620\,\mathrm{nm}$) instead of an X-ray beam and a chopper frequency of $f = 2177.7\,\mathrm{Hz}$, will be discussed

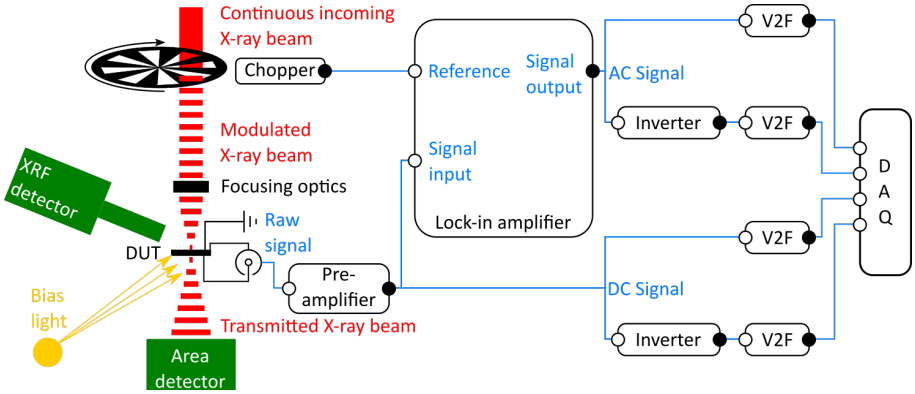

Figure 4.1: Setup for lock-in amplified X-ray beam induced current (XBIC) measurements on a device under test (DUT). The beam path is depicted in red. The green forms indicate optional X-ray fluorescence (XRF) and area detectors for multi-modal measurements, yellow indicates optional bias light. Hardware components for XBIC measurements are colored black, while XBIC signal paths are blue with signal outputs and inputs shown as filled and empty circles, respectively. Before the data acquisition (DAQ), the DC (direct current) and AC (alternating current) signal is converted from a voltage to a frequency (V2F). For alternative signal paths see Sec. 4.3.1. This is adapted from Ossig, C., Nietzold, T., West, B., Bertoni, M., Falkenberg, G., Schroer, C. G., Stuckelberger, M. E. X-ray Beam Induced Current Measurements for Multi-Modal X-ray Microscopy of Solar Cells. J. Vis. Exp. (150), e60001, doi:10.3791/60001 (2019).

to highlight the concepts. Fluorescent tubes served as a source for bias light. The DUT was a thin-film solar cell with a Cu(In,Ga)Se_2 absorber. Although different measurement settings would be chosen for other DUT, the general guidelines described here to find suitable settings are valid for a variety of DUT such as solar cells with different absorber layers or nanowires. The PA was used with an amplification factor of $1 \cdot 10^4$ V/A. The effects discussed here apply equally to other pre-amplifiers. If nothing else is specified, the low-pass filter roll-off of the LIA was 48 dB/oct.

4.1 Process of lock-in amplification

4.1.1 Signal modulation

Figure 4.2 shows the pre-amplified DUT response measured by a scope without (top row) and with (bottom row) bias light turned on. As the PA converts currents to voltages, the displayed signal is in volts. It is negative due to the contacting of the

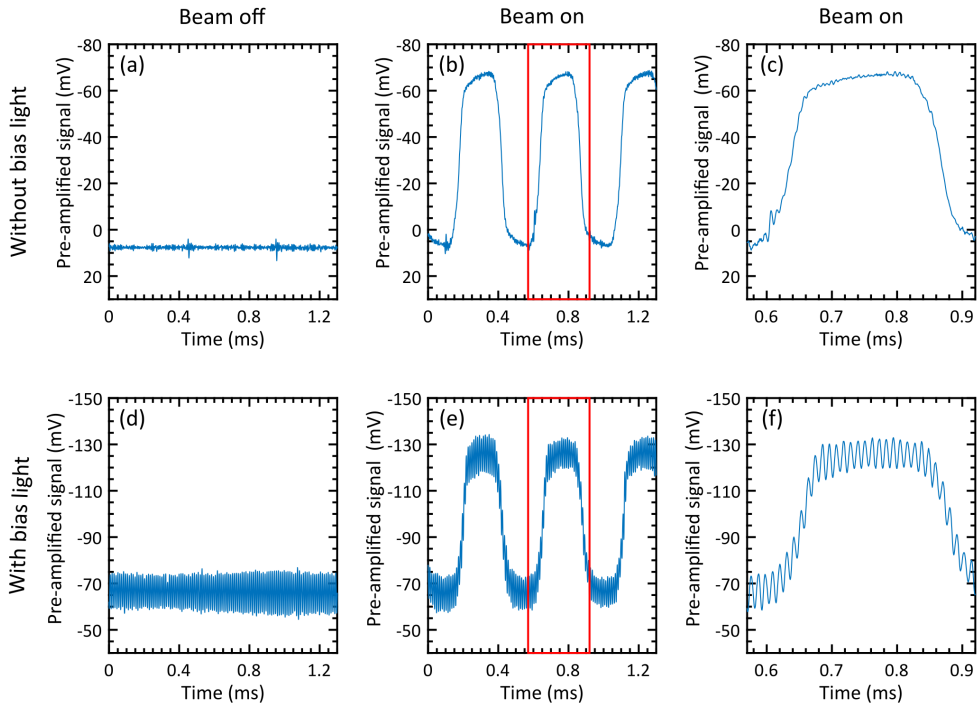

Figure 4.2: Pre-amplified solar cell response upon irradiation with bias light and modulated beam. Top row without bias light, bottom row with bias light: (a) & (d) - beam off; (b) & (e) - beam on; (c) & (f) - zoom into the red rectangle of B & E. This is adapted from Ossig, C., Nietzold, T., West, B., Bertoni, M., Falkenberg, G., Schroer, C. G., Stuckelberger, M. E. X-ray Beam Induced Current Measurements for Multi-Modal X-ray Microscopy of Solar Cells. J. Vis. Exp. (150), e60001, doi:10.3791/60001 (2019).

solar cell, with the p- and n-type contacts connected to the shield and core of the input of the PA, respectively. In XBIC measurements, the solar cell contacting is governed by the necessary grounding of the front contact as discussed in Sec. 3.2.4.

Comparing Fig. 4.2(a) and Fig. 4.2(d), an offset signal on the order of 8 mV that is shifted to −65 mV by turning on the bias light from fluorescence tubes is noted. Furthermore, the signal variation on short timescales is significantly enhanced by the bias light. Such a bias offset of roughly 70 mV can prove problematic, due to limits in the acceptance range of the PA and LIA. To use the full range of the PA, a small offset as in Fig. 4.2(a–c) is preferable. Therefore, all sources of unintentional bias, such as ambient lighting, should be eliminated.

Adding a chopped photon source, as displayed in Fig. 4.2(b,c,e,f), increases the induced signal by the same amount — roughly 66 mV — for both with and without

bias light, when the beam passes through the chopper blade; when the beam is blocked by the blade, the signal remains at the level of the respective offset, as is expected. The frequency of the chopper is distinct in the signal of Fig. 4.2(b) and (e) with a period of $\tau_{\mathrm{mod}} = 1/f_{\mathrm{mod}} = 0.46\,\mathrm{ms}$.

In Fig. 4.2(d–f), an additional modulation at a frequency of 90 kHz is noted. The source of this high-frequency modulation is the electronic ballast of the fluorescent tube, which is driven at 45 kHz. Although lock-in amplification is capable of differentiating the contributions from different modulation frequencies, as will be shown in Fig. 4.5, the reduction of noise signal is paramount for a good measurement. Ambient light is just one possible source, but other electronics can also induce noise, which would then be superimposed onto the signal. Note that bias light is not always unwanted noise, but often bias light is applied on purpose to set the DUT into operating conditions.

Furthermore, in Fig. 4.2(b,c,e,f), it is noted that the response of the DUT upon change of the irradiation intensity is delayed. These rise-time effects will be discussed in greater detail in the next section and originate here from two distinct effects: first, the steep increase and decrease of the DUT response upon the 2177.7 −Hz modulation is delayed by the low-pass filter in the PA. Second, the signal continues to increase/decrease at slower time scales (e.g., visible between 0.68–0.80 ms in Fig. 4.2(c)), which is interpreted here as attributed to the occupation kinetics of defect states in the solar cell.

4.1.2 Pre-amplification

The PA not only amplifies the modulated signal of the DUT but can significantly change its waveform. As detailed above, the contacts of the solar cell are such that a negative voltage is measured upon illumination. No bias light was added for the measurements shown in Fig. 4.3.

The measurements were taken with increasing filter rise times to demonstrate their effects when amplification strength is held constant. In many cases, filter rise times are hardware-coupled to the amplification. The stronger the amplification is, the longer the response time is, and the smaller is the cut-off frequency of the low-pass filter in the PA [197, 198].

With a filter rise time of 10 µs as in the top panel of Fig. 4.3, the signal is barely delayed, spans the nominal peak-to-peak range from roughly 10 mV to −65 mV, and

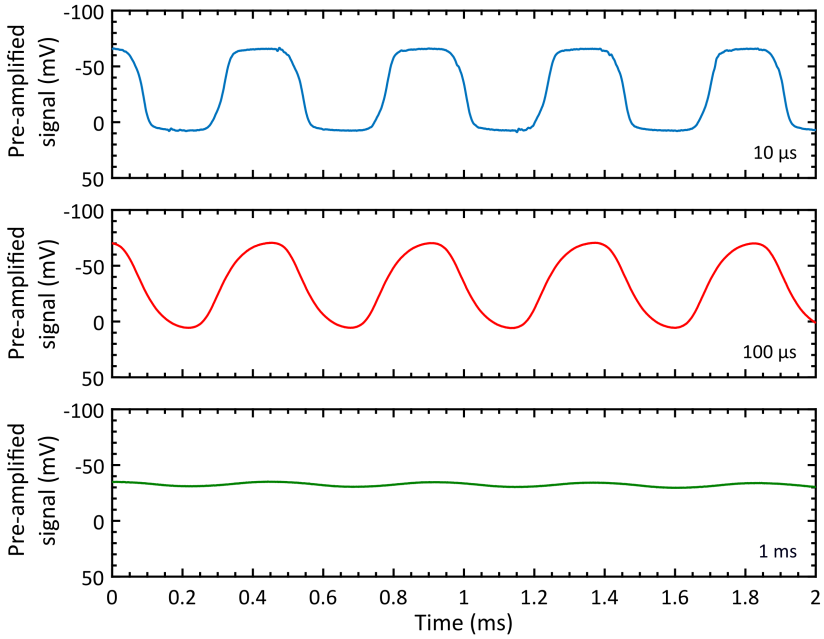

Figure 4.3: Solar cell response after pre-amplification with three different filter rise times (10 µs - blue, 100 µs - red, 1 ms - green) in the pre-amplifier. This is adapted from Ossig, C., Nietzold, T., West, B., Bertoni, M., Falkenberg, G., Schroer, C. G., Stuckelberger, M. E. X-ray Beam Induced Current Measurements for Multi-Modal X-ray Microscopy of Solar Cells. J. Vis. Exp. (150), e60001, doi:10.3791/60001 (2019).

reaches plateaus at the peak values. With 100 µs filter rise time, delay effects are visible in the modulated signal but the modulation is still distinct and the amplitude is in a similar range as for 10 µs. A filter rise time of 1 ms is longer than the period of the modulation (0.46 ms). Therefore, the modulation is suppressed to amplitudes below 10 mV and the shape reflects only the beginning of the rising and falling edge, which is obviously not suited for quantitative XBIC measurements. This connection between gain and filter rise time has to be kept in mind particularly for the combination of fast modulation frequencies, f_{mod}, with strong amplification.

4.1.3 Lock-in amplification

The key difference between standard signal amplification and lock-in amplification is the mixing of the DUT signal with a reference signal and the subsequent suppression of high frequencies by a low-pass filter. The signal path for the mixing is depicted in

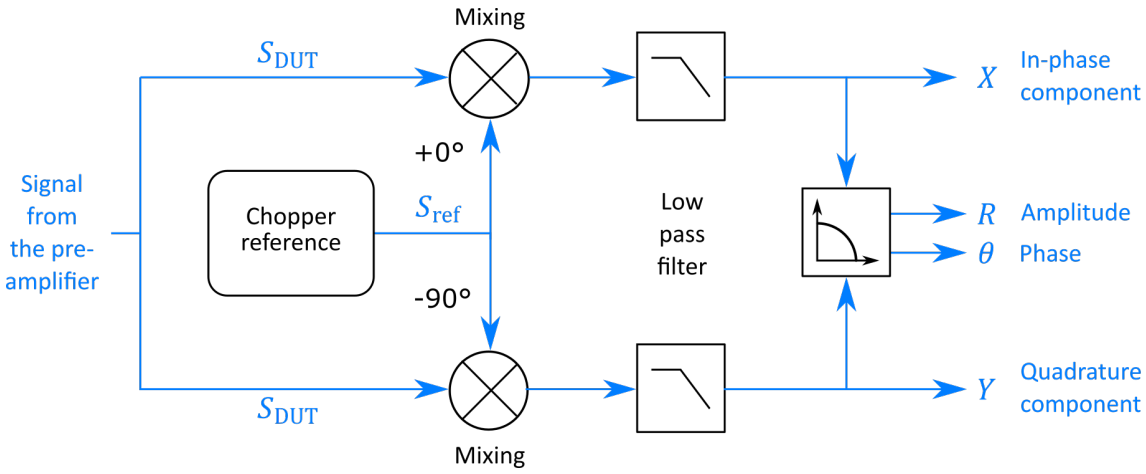

Figure 4.4: Signal processing by the lock-in amplifier31. S_{DUT} is the signal input from the DUT and S_{ref} is the reference signal from the chopper. This is adapted from Ossig, C., Nietzold, T., West, B., Bertoni, M., Falkenberg, G., Schroer, C. G., Stuckelberger, M. E. X-ray Beam Induced Current Measurements for Multi-Modal X-ray Microscopy of Solar Cells. J. Vis. Exp. (150), e60001, doi:10.3791/60001 (2019).

Fig. 4.4. For the discussion of the signal mixing, a few simplifications are made. The reference signal can be described as a sinusoidal signal

$$S_{\mathrm{ref}} = S^0_{\mathrm{ref}} \cdot \cos(2\pi f_1 \cdot t), \tag{4.1}$$

where S^0_{ref} is the amplitude and f_1 is the modulation frequency of the reference signal. The modulated signal of the DUT fed into the LIA can be represented in a similar fashion as

$$S_{\mathrm{DUT}} = S^0_{\mathrm{DUT}} \cdot \cos(2\pi f_2 \cdot t + \Phi), \tag{4.2}$$

where S^0_{DUT} is the amplitude and f_2 is the modulation frequency of the DUT signal, and Φ is a phase offset of the DUT signal to the reference signal.

Following from Eq. 4.1 and Eq. 4.2, the mixed signal is:

$$S_{\mathrm{mixed}} \equiv S_{\mathrm{ref}} \cdot S_{\mathrm{DUT}} = S^0_{\mathrm{ref}} \cdot S^0_{\mathrm{DUT}} \cdot \cos(2\pi f_1 \cdot t) \cdot \cos(2\pi f_2 \cdot t + \Phi). \tag{4.3}$$

The modulation frequency of the DUT is the reference frequency, $f_1 = f_2$. Therefore, the trigonometric principle

$$\cos(a) \cdot \cos(b) = \frac{1}{2}\left[\cos(a+b) + \cos(a-b)\right] \tag{4.4}$$

can be used to rewrite S_{mixed} as the sum of two terms with different frequencies:

$$S_{\text{mixed}} = S_{\text{slow}} + S_{\text{fast}} = S^0_{\text{ref}} \cdot S^0_{\text{DUT}} \cdot \frac{1}{2} \cos(\Phi) + S^0_{\text{ref}} \cdot S^0_{\text{DUT}} \cdot \frac{1}{2} \cos(2 \cdot 2\pi f_1 \cdot t + \Phi). \quad (4.5)$$

The low-pass filter mitigates the fast signal S_{fast} such that the lock-in amplified signal can be approximated [199, 200] as

$$S_{\text{mixed}} \approx S^0_{\text{ref}} \cdot S^0_{\text{DUT}} \cdot \frac{1}{2} \cos(\Phi). \quad (4.6)$$

The DUT signal mixed with the reference signal is called the in-phase component X, and the DUT signal mixed with the 90 ° phase-shifted reference is called the quadrature component Y:

$$X = S^0_{\text{ref}} \cdot S^0_{\text{DUT}} \cdot \frac{1}{2} \cos(\Phi) \quad (4.7)$$

$$Y = S^0_{\text{ref}} \cdot S^0_{\text{DUT}} \cdot \frac{1}{2} \cos(\Phi - 90^\circ) \quad (4.8)$$

From Eq. 4.7 and Eq. 4.8, the amplitude R of the signal vector can be defined as

$$R = \sqrt{X^2 + Y^2}, \quad (4.9)$$

which removes the dependency on the phase shift, between reference and DUT signal. Additionally the phase

$$\Theta = \operatorname{atan} 2(X, Y) \quad (4.10)$$

of the mixed signal can be obtained with the two-argument arcus tangent function. Many LIA have an internal phase adjust to set Φ to zero during measurements.

The actual output of most lock-in amplifiers is the root-mean-square (RMS) value of the incoming signal, which introduces an additional crest factor C. The crest factors for many periodic wave functions are known, e.g. $\sqrt{2}$ for a sine-, 1 for a square-, and $\sqrt{3}$ for a triangular wave.

An in-depth mathematical description of the application of lock-in amplifiers with low pass filtering is given in Ref. [201], by T. Kaiser who finished his Bachelor's thesis in our group.

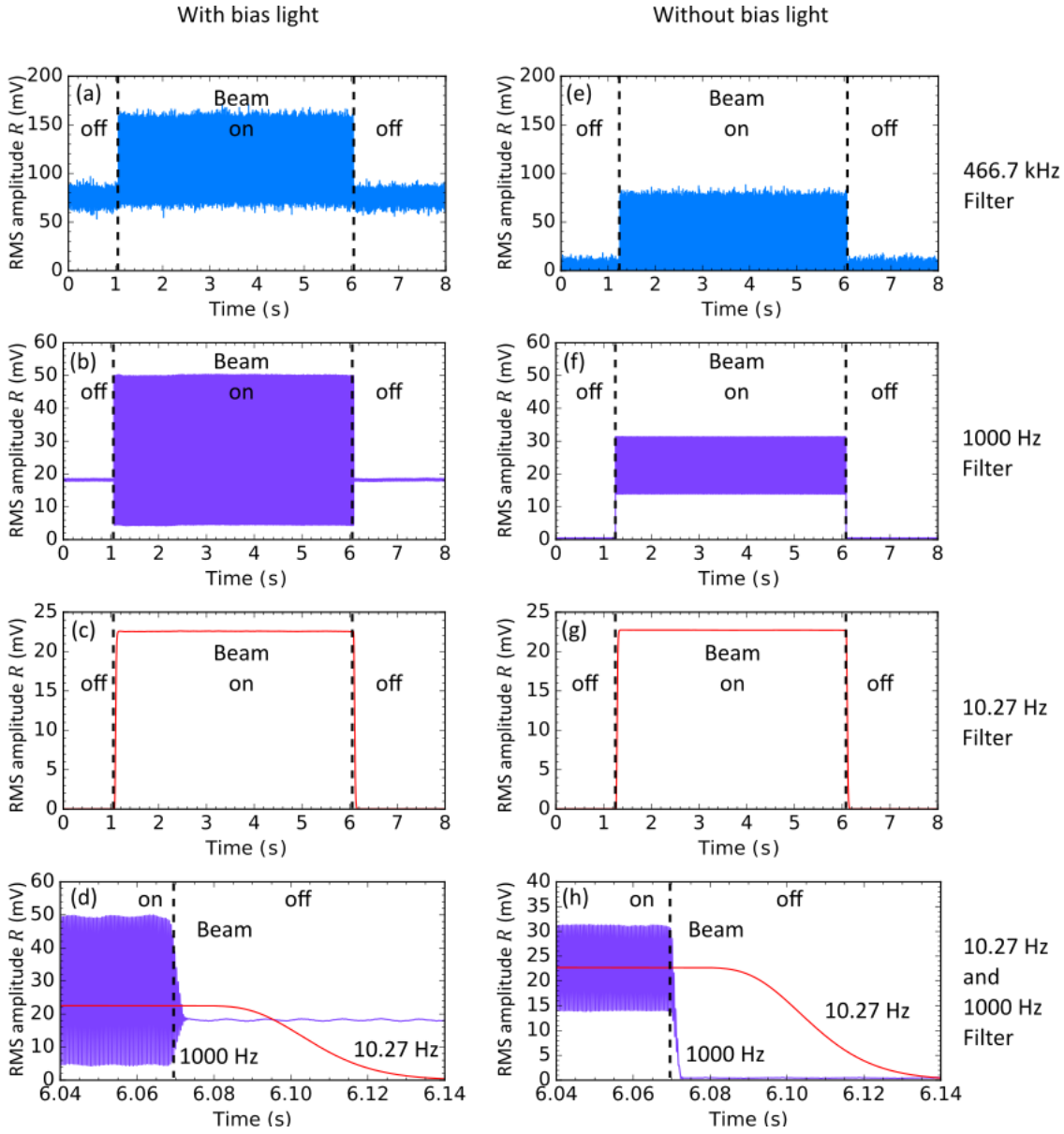

Figure 4.5: Lock-in amplified RMS amplitude R with low-pass filter cut-off frequencies $f_{\text{cut-off}} = 466.7\,\text{kHz}$ (blue), $f_{\text{cut-off}} = 1\,\text{kHz}$ (purple), $f_{\text{cut-off}} = 10.27\,\text{Hz}$ (red), and constant filter roll-off 48 dB/oct. The DUT was a Cu(In,Ga)Se_2 solar cell with (a, b, c, d) and without (e, f, g, h) bias light applied. The times when the chopped photon beam was turned on and off are indicated in the figures as vertical dashed lines. This is adapted from Ossig, C., Nietzold, T., West, B., Bertoni, M., Falkenberg, G., Schroer, C. G., Stuckelberger, M. E. X-ray Beam Induced Current Measurements for Multi-Modal X-ray Microscopy of Solar Cells. J. Vis. Exp. (150), e60001, doi:10.3791/60001 (2019).

4.1.4 Low-pass filter frequency

Figure 4.5 shows the effect of bias light and different low-pass filter settings on the lock-in amplified RMS amplitude, R. A LIA that allowed to record the signal resulting from different filter parameters simultaneously was used.

The cut-off frequency $f_{\text{cut-off}}$ of a low-pass filter defines the frequency, at which the signal is attenuated to 50%. While lower frequencies are transmitted, higher frequencies are suppressed. Figure 4.5(a,e) show the direct signal with $f_{\text{cut-off}} = 466.7\,\text{kHz}$, which effectively does not eliminate noise or lower-frequency modulations but lets them pass with the raw signal. The conversion of the raw pre-amplified signal to the RMS amplitude R leads to an additional factor of $\sqrt{2}$ for frequencies sufficiently below $f_{\text{cut-off}}$. For example, a constant input voltage of $V_{raw} = 1\,\text{V}$ is output as $R = 1.41\,\text{V}$.

Whereas the average offset in Fig. 4.5(e) is negligible without bias light (in average 2 mV), it increases to an average of around 75 mV with bias light (Fig. 4.5(a)). The difference is of comparable strength as between Fig. 4.2(a) and Fig. 4.2(d), but beware that these were separate measurements. In both cases, turning on the chopping source leads to a significant increase in R, and the peak-to-peak variation of R corresponds to the peak-to-peak variation of the raw signal shown in Fig. 4.2(b) and Fig. 4.2(e).

In Fig. 4.5(b,f), the RMS amplitude R is displayed after using a low-pass filter with $f_{\text{cut-off}} = 1000\,\text{Hz}$. Again an offset can be observed in Fig. 4.5(b) due to the bias light, but the offset is smaller with around 18 mV on average. This offset is caused by the 100 Hz modulation of the fluorescent light, whereas the 90 kHz modulation is blocked by the low-pass filter. Furthermore, the noise level of the 'beam on' state is still significant with a peak-to-peak variation around 46 mV, while the average signal value amounts to 32 mV. Without bias light (Fig. 4.5(f)) the peak-to-peak variation amounts to about 17 mV during 'beam on' with an average value of 23.5 mV. The average offset during 'beam off' is smaller than 0.5 mV. These measurements show that the combination of a low-pass filter with $f_{\text{cut-off}} = 1000\,\text{Hz}$ and a chopping frequency of $f_{\text{chopper}} = 2177.7\,\text{Hz}$ is not ideal: the signal carrying the modulation frequency is only partially removed but not entirely suppressed by the low-pass filter. The remaining part leads to significant peak-to-peak variations of R during the 'beam on' state. When bias light is present, the 100 Hz modulation due to net frequency of the fluorescence lamps further increases the peak-to-peak values.

In Fig. 4.5(c,g), the influence of the bias light can be seen as minimal: the 10.27 Hz low-pass filter cuts off most noise and modulation of the fluorescent light, and a clear beam-induced signal can be extracted. Albeit hardly visible here, the offset and spread of noise are still slightly greater with bias light. This can be caused by stray light passing through the chopper wheel onto the DUT. Therefore, it is advisable to implement the chopper far upstream to avoid the modulation of stray light.

Figure 4.5(d,h) are a zoom into the change from 'beam on' to 'beam off' after 6 s in Fig. 4.5(b,c,f,g), respectively. The superimposed modulation at 100 Hz (fluorescence lamps frequency) is visible in Fig. 4.5(d) for the low-pass filter with $f_{\text{cut-off}} = 1000\,\text{Hz}$. Note also the delay in the signal after the filter with $f_{\text{cut-off}} = 10.27\,\text{Hz}$ compared to the signal after the filter with $f_{\text{cut-off}} = 1000\,\text{Hz}$, when the beam is turned off. Similar to the case for slow rise times of the PA, low $f_{\text{cut-off}}$ of the low-pass filter in the LIA cause slower adaptation of R to signal changes.

Altogether, we found that a low-pass filter with $f_{\text{cut-off}} = 10.27\,\text{Hz}$ and a roll-off of 48 dB/oct (see next section) offers in this case the best compromise between fast scanning speed (in favor of high $f_{\text{cut-off}}$ values) and suppression of bias light or noise (in favor of low $f_{\text{cut-off}}$ values, most importantly below the grid frequency of 50 Hz).

4.1.5 Low-pass filter roll-off[1]

As many digital lock-in amplifiers, the model that was used here employs so-called discrete-time RC filters or exponential running average filters whose characteristics are very close to those of an analog resistor-capacitor RC filter [202]. Apart from the filter cut-off frequency that was discussed in the previous section, there is only one free parameter, the filter order n, that defines the slope of the cut-off as $n\cdot$ 6 dB/oct.

Figure 4.6(a) shows the effect of the filter order on the frequency-dependent attenuation for different cut-off frequencies that correspond to time constants $\tau_{\text{C}} = 100\,\text{ms}$ and $\tau_{\text{C}} = 0.1\,\text{ms}$. Time constants between these two extremes are suitable for most XBIC measurements. The filter attenuation was calculated [202] in the frequency domain as the absolute value squared $|H_{\text{n}}(f)|^2$ of the complex transfer function

$$H_{\text{n}}(f) = \frac{1}{(1 + i \cdot 2\pi \cdot f \cdot \tau_{\text{c}})^n}, \tag{4.11}$$

[1] This section is part of Ref. [1] and presented here for completeness. The calculations for this section were conducted by Michael E. Stuckelberger.

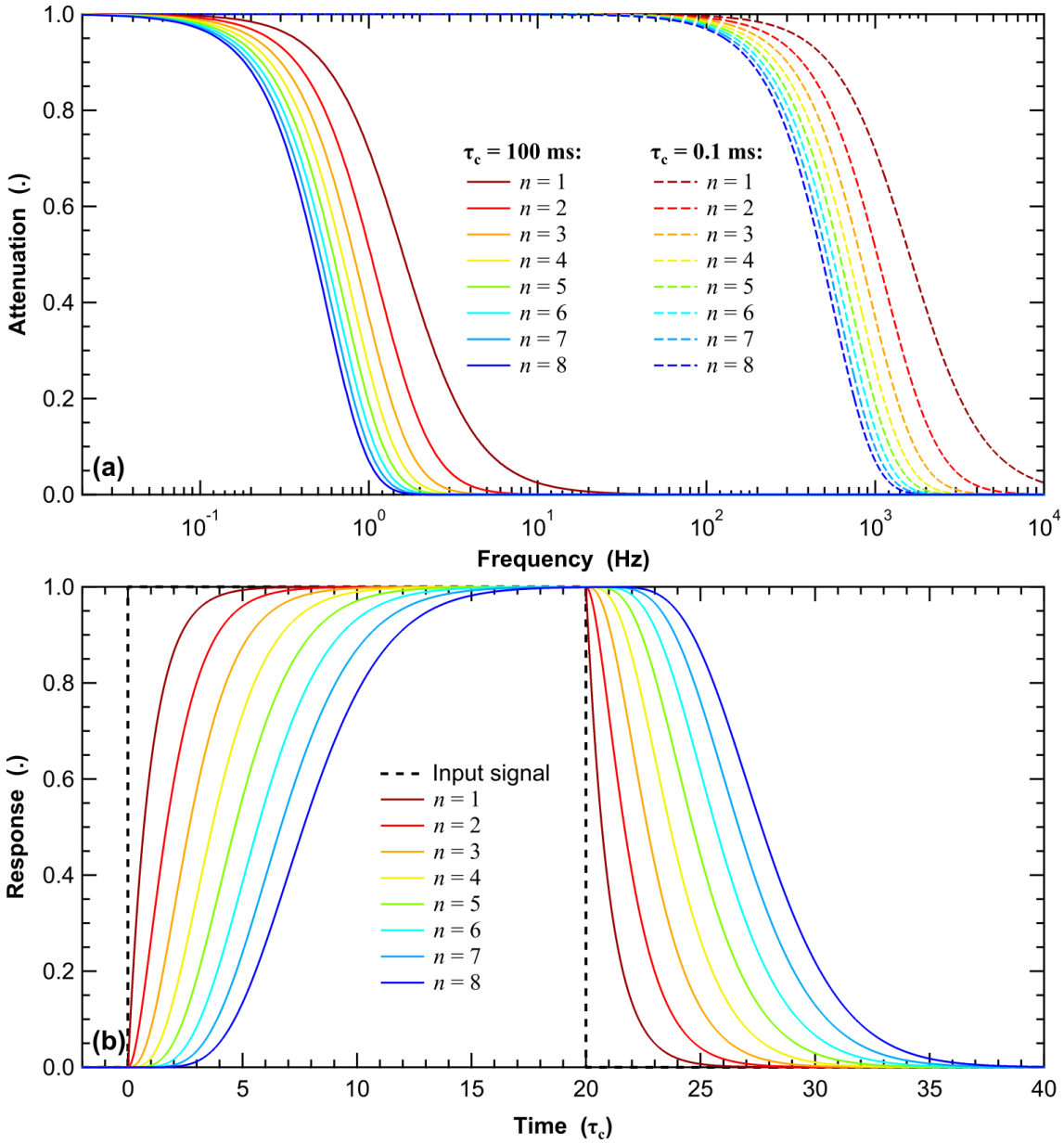

Figure 4.6: Effect of low-pass filter settings in the lock-in amplifier. (a) - Attenuation by the low-pass filter in the frequency domain for two time constants (τ_C = 100 ms and τ_C = 0.1 ms) and for filter orders 1 to 8. (b) - Transmitted signal response of the low-pass filter in the time domain, in units of the time constant τ_C, for filter orders 1 to 8 upon step-like change of the input signal from 0 to 1 at time 0 and from 1 to 0 at time $20 \cdot \tau_C$. This is adapted from Ossig, C., Nietzold, T., West, B., Bertoni, M., Falkenberg, G., Schroer, C. G., Stuckelberger, M. E. X-ray Beam Induced Current Measurements for Multi-Modal X-ray Microscopy of Solar Cells. J. Vis. Exp. (150), e60001, doi:10.3791/60001 (2019). And with courtesy of Michael Stuckelberger.

as a function of the frequency f and a filter of order n with a time constant τ_C. Transfer functions of higher order filters are obtained by multiplication of the transfer functions of the serially connected individual filters. Similar to $f_{\text{cut-off}} := f_{50\%}$, we define $f_{5\%}$ and $f_{95\%}$ as the frequencies, at which the attenuation is 5 % and 95 %, respectively. The product of these frequencies and τ_C is constant and given in Tab. 4.1 for the conversion between the cut-off frequencies and the filter time constant.

In the time domain, the filter response $S_{\text{out}}[i]$ for $n = 1$ is recursively calculated from an input signal $S_{\text{in}}[i]$ that is defined at discrete times $i \cdot \tau_S$, $(i+1) \cdot \tau_S$, $(i+2) \cdot \tau_S$, *etc.*, spaced by the sampling time τ_S:

$$S_{\text{out}}[i] = \exp\left\{-\frac{\tau_S}{\tau_C}\right\} \cdot S_{\text{out}}[i-1] + \left[1 - \exp\left\{-\frac{\tau_S}{\tau_C}\right\}\right] \cdot S_{\text{in}}[i]. \tag{4.12}$$

The response of filters with $n > 1$ is calculated by multiple iteration of Eq. 4.12 with $S_{\text{out}}[i, n]$ calculated from $S_{\text{out}}[i-1, n]$ and $S_{\text{out}}[i, n-1]$. The filter response to an increasing (at time 0) and decreasing step function (at time $20 \cdot \tau_C$) is shown in Fig.4.6 for filter orders 1 to 8, as a function of the time in units of τ_C. Note that the response is delayed with respect to the input signal and that this delay increases with n. The delay is quantified in Tab. 4.1 as the times $\tau_{5\%}$, $\tau_{50\%}$, and $\tau_{95\%}$, within which the transmitted signal reaches 5 %, 50 %, or 95 %, respectively.

The choice of the correct filter roll-off is as critical as of the cut-off frequency when designing the experiment. In the study presented in Sec. 4.2.1, high-quality XBIC measurements were obtained with a chopper frequency of 1177 Hz, dwell time of 100 ms, and cut-off frequency of 40 Hz at filter order 8. With the numbers from Tab. 4.1, this translates into $\tau_C = 0.0479/40\,\text{Hz} = 1.1975\,\text{ms}$, and $\tau_{95\%} = 13.144 \cdot \tau_C = 15.74\,\text{ms}$. This time is considerably shorter than the dwell time such that no delay-artifacts are introduced.

Filter order Roll-off	1 6 dB/oct	2 12 dB/oct	3 18 dB/oct	4 24 dB/oct	5 30 dB/oct	6 36 dB/oct	7 42 dB/oct	8 48 dB/oct
$f_{5\%} \times \tau_C$	0.6938	0.2966	0.2084	0.1681	0.1442	0.1281	0.1163	0.1073
$f_{\text{cut-off}} \times \tau_C$	0.1592	0.1024	0.0811	0.0692	0.0614	0.0557	0.0514	0.0479
$f_{95\%} \times \tau_C$	0.0365	0.0256	0.0209	0.0181	0.0162	0.0147	0.0136	0.0128
$\tau_{5\%}$	0.0503 $\times\tau_C$	0.3539 $\times\tau_C$	0.8157 $\times\tau_C$	1.3638 $\times\tau_C$	1.9671 $\times\tau_C$	2.6095 $\times\tau_C$	3.2813 $\times\tau_C$	3.9763 $\times\tau_C$
	0.0080 / $f_{\text{cut-off}}$	0.0362 / $f_{\text{cut-off}}$	0.0662 / $f_{\text{cut-off}}$	0.0944 / $f_{\text{cut-off}}$	0.1207 / $f_{\text{cut-off}}$	0.1453 / $f_{\text{cut-off}}$	0.1685 / $f_{\text{cut-off}}$	0.1904 / $f_{\text{cut-off}}$
$\tau_{50\%}$	0.6922 $\times\tau_C$	1.6768 $\times\tau_C$	2.6721 $\times\tau_C$	3.6696 $\times\tau_C$	4.6679 $\times\tau_C$	5.6667 $\times\tau_C$	6.6656 $\times\tau_C$	7.6647 $\times\tau_C$
	0.1102 / $f_{\text{cut-off}}$	0.1718 / $f_{\text{cut-off}}$	0.2168 / $f_{\text{cut-off}}$	0.2541 / $f_{\text{cut-off}}$	0.2865 / $f_{\text{cut-off}}$	0.3156 / $f_{\text{cut-off}}$	0.3423 / $f_{\text{cut-off}}$	0.3670 / $f_{\text{cut-off}}$
$\tau_{95\%}$	2.9947 $\times\tau_C$	4.7424 $\times\tau_C$	6.2938 $\times\tau_C$	7.7511 $\times\tau_C$	9.1505 $\times\tau_C$	10.5100 $\times\tau_C$	11.8380 $\times\tau_C$	13.1440 $\times\tau_C$
	0.4766 / $f_{\text{cut-off}}$	0.4858 / $f_{\text{cut-off}}$	0.5107 / $f_{\text{cut-off}}$	0.5366 / $f_{\text{cut-off}}$	0.5616 / $f_{\text{cut-off}}$	0.5854 / $f_{\text{cut-off}}$	0.6079 / $f_{\text{cut-off}}$	0.6294 / $f_{\text{cut-off}}$

Table 4.1: For discrete-time RC filters of orders 1 to 8, the product of the time constant and the frequency, at which the signal is attenuated by 5 %($f_{5\%}$), 50 % ($f_{50\%}$), and 95 % ($f_{95\%}$), is constant and given in the top part. In the lower part, the time delay is given, within which the signal reaches 5 % ($\tau_{5\%}$), 50 % ($\tau_{50\%}$), and 95 % ($\tau_{95\%}$), in units of the time constant τ_C and of the inverse cut-off frequency $1/f_{\text{cut-off}}$. This is adapted from Ossig, C., Nietzold, T., West, B., Bertoni, M., Falkenberg, G., Schroer, C. G., Stuckelberger, M. E. X-ray Beam Induced Current Measurements for Multi-Modal X-ray Microscopy of Solar Cells. J. Vis. Exp. (150), e60001, doi:10.3791/60001 (2019).

4.2 Application of lock-in amplification

4.2.1 XBIC of solar cell with bias voltage and XRF

Figure 4.7(a–b) shows the impact of lock-in amplification on the signal-to-noise ratio in X-ray beam induced current measurements. The noisiness of the direct signal is apparent in Fig. 4.7(a): strong intensity contrasts from line to line are indicative of measurement artifacts, and fine XBIC variations from the DUT get buried in the arbitrarily changing signal. On the other hand, these fine features are clearly visible in Fig. 4.7(b). Note that the noise level in Fig. 4.7(a) is unusually high for unknown reasons despite the optimization of the setup prior to the measurements. In such cases, the signal-to-noise ratio improvement by lock-in amplification is dramatically higher than in cases of already high signal-to-noise ratio with standard amplification, where lock-in amplification would only lead to marginal improvements.

With the PA, forward (Fig. 4.7(c)) and reverse (Fig. 4.7(d)) bias voltages of $-50\,\mathrm{mV}$ and $50\,\mathrm{mV}$, respectively, were applied to the sample and the area of Fig. 4.7(a–b) rescanned. The dominant features visible in Fig. 4.7(b) are still visible in Fig. 4.7(c) and Fig. 4.7(d), but they are less distinct as the maps are noisier. This is because the application of bias voltage or bias light induces a direct current that is often orders of magnitude larger than the modulated XBIC signal. Ultimately, the ratio of direct to modulated signal limits the applicability of lock-in amplification. Despite the poor signal-to-noise ratio, it is worth pointing out that lock-in amplification enables mapping of the solar cell performance at the nanoscale with bias voltage and bias light applied, which would hardly be possible otherwise [5].

As the performance of the $Cu(In,Ga)Se_2$ solar cell is correlated to the absorber layer composition [61, 203], the XRF signal was measured simultaneously with the XBIC. In Fig 4.7(e-f), the concentrations of Ga and In are presented. Both elements are part of the absorber layer and their ratio is deemed to be of great influence to the performance of the solar cell [61]. The statistics of Ga are much greater than for In, which is due to the higher absorption coefficient and less self-absorption at the excitation energy of $10.4\,\mathrm{keV}$ (see Sec. 3.2.3). Due to the low statistics, features in the In map are almost invisible, whereas the Ga concentration is clear enough to be correlated with the electrical performance in Fig. 4.7(b). For a higher In signal, one could either choose longer dwell times or choose an absorption energy with larger In absorption cross section. This illustrates the importance of a sufficiently long dwell time as well as the tailoring of the beam energy to the elements of interest.

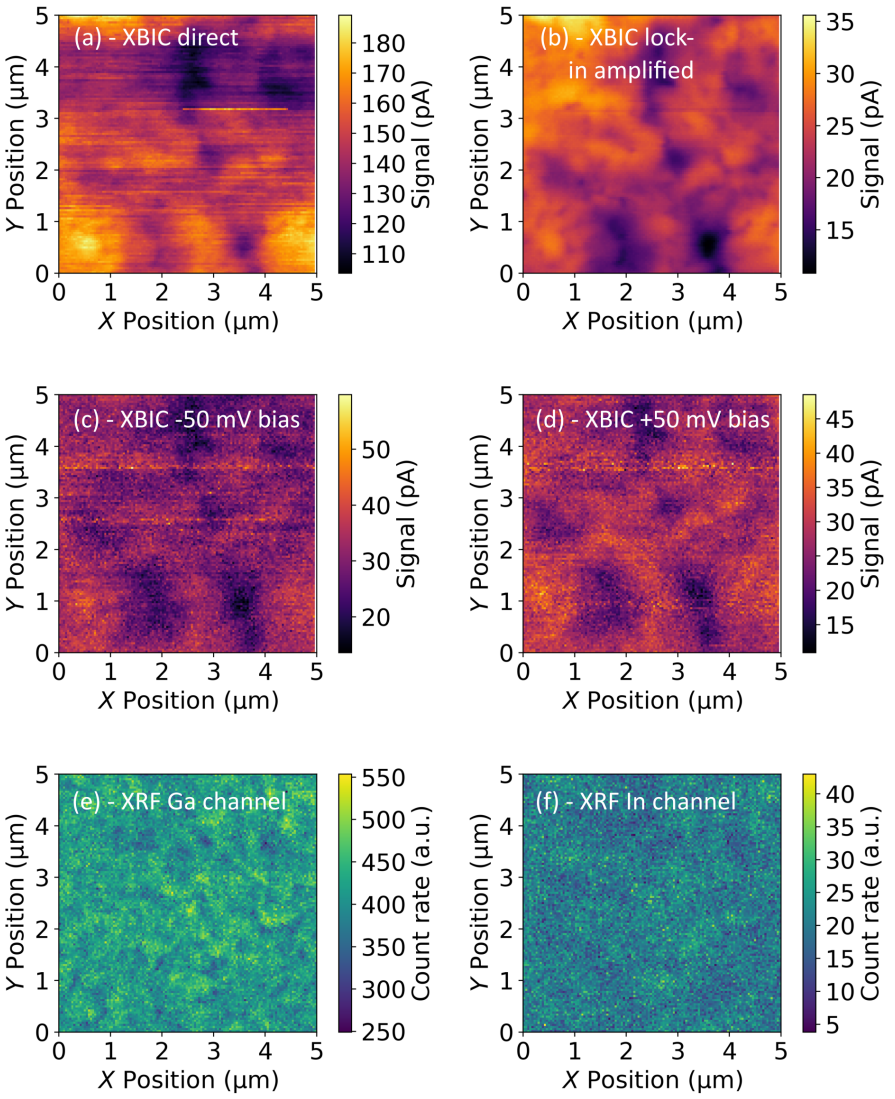

Figure 4.7: X-ray beam induced current (XBIC) and X-ray fluorescence (XRF) measurements of a Cu(In,Ga)Se_2 solar cell, taken at the beamline ID16B at the European Synchrotron Radiation Facility with a focused flux on the order of $1 \cdot 10^8$ ph/s. The PA was used with $A_{\mathrm{PA}} = 5 \cdot 10^6$ V/A, the LIA with $f_{\text{cut-off}} = 40$ Hz (48 db/oct). The beam energy was 10.4 keV, the chopper frequency was 1177 Hz, and the low-pass filter cut off at 40 Hz. The dwell time was 100 ms and the pixel size was 40 nm × 40 nm. The maps (a), (b), (e) and (f) were all taken at the same time; (c) and (d) are retakes after 50 min and 113 min, with 50 mV forward and reverse bias voltage applied, respectively. This is adapted from Ossig, C., Nietzold, T., West, B., Bertoni, M., Falkenberg, G., Schroer, C. G., Stuckelberger, M. E. X-ray Beam Induced Current Measurements for Multi-Modal X-ray Microscopy of Solar Cells. J. Vis. Exp. (150), e60001, doi:10.3791/60001 (2019).

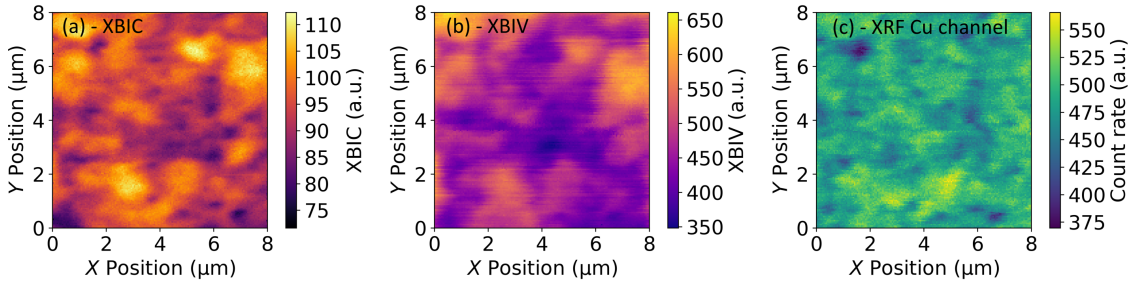

Figure 4.8: Multi-modal measurement of a Cu(In,Ga)Se_2 solar cell, taken at beamline P06 at PETRA III with a focused flux of about $7 \cdot 10^9$ ph/s. The beam energy was 15.25 keV, the chopper frequency was 8015 Hz, and the pixel size 50 nm × 50 nm. (a) - X-ray beam induced current (XBIC) measured with a dwell time of 0.01 s, a PA with $A_{\mathrm{PA}} = 1 \cdot 10^6$ V/A, and a LIA with $f_{\text{cut-off}} = 501.1$ Hz (48 dB/oct); (b) - X-ray beam induced voltage (XBIV) covering the same area as panel (a), measured with a dwell time of 0.5 s and a LIA with $f_{\text{cut-off}} = 10.27$ Hz (48 dB/oct); (c) - Cu count rate from an X-ray fluorescence (XRF) measurement, taken simultaneously with the XBIV measurement. This is adapted from Ossig, C., Nietzold, T., West, B., Bertoni, M., Falkenberg, G., Schroer, C. G., Stuckelberger, M. E. X-ray Beam Induced Current Measurements for Multi-Modal X-ray Microscopy of Solar Cells. J. Vis. Exp. (150), e60001, doi:10.3791/60001 (2019).

With long dwell times and large maps, another point has to be kept in mind: during measurements spanning multiple hours, sample drift can become a critical issue. Thermal fluctuations (particularly after sample change or large motor movements with poor heat dissipation) and the instability of mechanical stage components often lead to sample drift as can be seen by comparing the vertical positions of Fig. 4.7(d) and Fig. 4.7(b). The need for image registration in correlative analysis is thereby shown.

XBIC of a solar cell with XBIV and XRF

Figure 4.8 shows a multi-modal scan of a Cu(In,Ga)Se_2 solar cell, where the cell is operated under short-circuit condition measuring XBIC in Fig. 4.8(a), and under open-circuit condition measuring XBIV in Fig. 4.8(b). The XRF measurement shown in Fig. 4.8(c) was taken simultaneously with the XBIV measurement. To collect enough XRF counts, the dwell time per pixel was 0.5 s for Fig. 4.8(b–c) as compared to 0.01 s in Fig. 4.8(a). Accordingly, a lower cut-off frequency in the low-pass filter for the XBIV measurement could be used compared to the XBIC measurement (10.27 Hz vs. 501.1 Hz, both with roll-off 48 dB/oct). For XBIV measurements alone,

the same dwell time and low-pass filter settings could have been used as for the XBIC measurement with similar signal-to-noise ratio. However, it was overall more time-efficient to combine XBIV with XRF measurements with the XRF measurement governing the dwell time, than performing separate XBIV and XRF measurements.

Comparing Fig. 4.8(a), and Fig. 4.8(b), it is noted that the short-circuit current I_{SC}, measured as XBIC, and the open circuit voltage V_{OC}, measured as XBIV, are correlated: large high- and low-performing areas are visible in both measurement modes. This indicates that local thickness variations and/or recombination dominate the performance here, rather than bandgap variations, which would lead to opposite trends in XBIC and XBIV [165].

Further, taking Fig 4.8(c) into account, one can see that certain areas with low performance such as at $(X, Y) \approx (1.7\,\mu\text{m}, 6.7\,\mu\text{m})$ correlate with low Cu count rate, whereas performance is not correlated with the Cu count rate in other areas.

4.2.2 XBIC and XRF of a nanowire

Beyond solar cells, contacted nanowires [204] or nano-sheets, as well as quantum dots, are other examples of DUT that can profit from lock-in amplified XBIC measurements. For demonstration, Fig. 4.9(a) shows the elemental distribution from XRF measurements, and Fig. 4.9(b) the corresponding XBIC map of a CdS nanowire. The two contacts made of Pt and the CdS wire are clearly distinguishable, and the

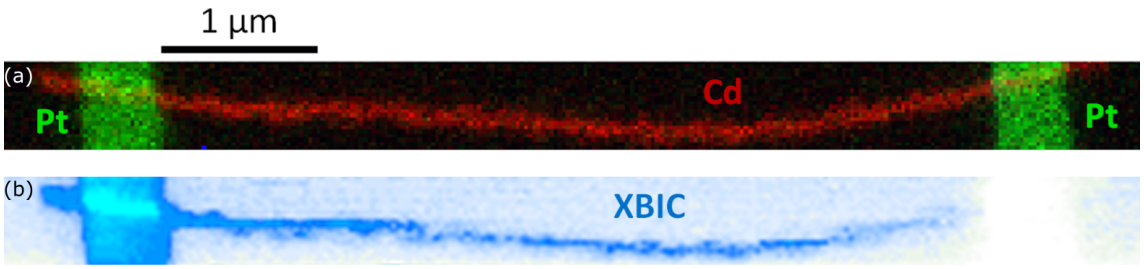

Figure 4.9: Multi-modal measurement of a CdS nanowire with Pt contacts, taken at beamline 26-ID-C of the Advanced Photon Source with a beam energy of 10.6 keV. (a) - Pt and Cd distribution from an X-ray fluorescence measurement. (b) - X-ray beam induced current (XBIC) measurement taken simultaneously with the XRF measurement, without lock-in amplification. This is adapted from Ossig, C., Nietzold, T., West, B., Bertoni, M., Falkenberg, G., Schroer, C. G., Stuckelberger, M. E. X-ray Beam Induced Current Measurements for Multi-Modal X-ray Microscopy of Solar Cells. J. Vis. Exp. (150), e60001, doi:10.3791/60001 (2019).

XBIC signal shows a matching electrical response. Particularly noteworthy is the fact that XBIC can unveil the electrical performance of the nanowire underneath the Pt contact, which is unique to X-ray nanoprobes and attributable to the high penetration depth of hard X-rays. The complementation of material composition and electrical properties of the nanowire exemplary demonstrates the advantages of multi-modal X-ray measurements.

4.3 Considerations when measuring XBIC

4.3.1 Noise and Error

Although lock-in amplification enables a higher signal-to-noise ratio compared to direct amplification, it is critical to avoid the introduction of noise at all levels. For further discussion, the literature discussing the measurement of small electrical signals [205–208] is recommended. Although state-of-the-art lock-in amplifiers are based on digital signal processing today, most strategies to reduce noise using analog lock-in amplifiers still apply.

Summarizing, it should be kept in mind that cables are prone to act as antennae and thus introduce noise into the system. This is particularly true in the environment of X-ray nanoprobes, where strong electro-magnetic fields are often unavoidable, their sources may even remain unknown. As a consequence, cables should be kept as short as possible and oriented such that the induced noise level is minimized. Extra shielding of the signal cables may further reduce the noise level.

The proper contacting of the DUT is equally important for noise minimization. A clean and robust method with small contact points is wire bonding. For TF solar cells, this does not always work due to adhesion issues. Alternatively, conductive tape based on graphite, copper, or aluminum is suited for larger samples. In many cases, the best results are obtained with manual application of silver paint to contact thin copper, gold, or platinum wires to the device (see Sec. 3.2.4). While tape and graphite paste might not give the best contact, silver paint can easily short circuit the device and has to be deposited with utmost care. Polyimide tape can be used to prevent short-circuiting of front and back contact.

Note that the cabling layout from contacting to signal transport needs to be adapted to beamline-specific boundary conditions. For example, the layout depicted in Fig. 4.1 with the pre-amplified signal being split to the LIA and to the V2F converters is risky,

if the V2F converters are located outside of the hutch. In this case, the long cable between pre-amplifier and V2F converter can catch noise that is transferred to the LIA. Therefore, three cases of common signal paths for XBIC or XBIV measurements are distinguished:

Case A: XBIC is measured with a pre-amplifier, and the DC/AC signal is split after the PA as depicted in Fig. 4.1. In this case, a current offset can be applied in the PA such that the signal is always positive, avoiding the need of recording the positive and negative signal via two separate V2F converters. As a drawback, this would reduce the available voltage acceptance range in the LIA and lead to reduced sensitivity.

Case B: Avoiding the splitting of the pre-amplified signal, which is only input to the LIA, an additional demodulator can be used in the LIA with a low-pass filter at the maximum value (i.e. not locking into the modulation frequency) such that the pre-amplified signal can be effectively output to the DAQ unit as demonstrated in Fig. 4.5(a,e). In this case, a voltage offset on the output can be applied to both the AC and DC signal, avoiding the need of recording the positive and negative signal via two separate V2F converters. This has no major drawbacks apart from a reduction of the available frequency range of the V2F, which is rarely limiting.

Case C: XBIV is measured and the DC/AC signal is split between the DUT and the lock-in amplifier. In this case, no voltage offset on the DC signal can be applied without applying an unwanted bias voltage on the DUT, such that always two separate V2F converters are required for the positive and negative signal parts.

In all cases, where the negative and positive parts of a signal are recorded via two different V2F converters, the total XBIC or XBIV signal is obtained as the difference between the positive and negative channel. If a LIA with two or more demodulators is available, typically case B is preferred, as it minimizes the wiring of the raw signal and allows easy switching between XBIC and XBIV measurements.

The error of XBIC measurements highly depends on the equipment and settings used such that no error quantification can be given here. The absolute error is higher than one might expect because of experimental and systematic errors. This is particularly true if the XBIC signal is converted to charge collection efficiency by scaling with a constant as described in the protocol. For example, the empiric relation between bandgap and ionization energy described by α in Eq. 3.18 suffers from significant scatter; photon flux measurements are often not available with absolute errors below 10 %; and the nanoscopic structure of the DUT is poorly known. However, we emphasize that the strength of lock-in amplified XBIC and XBIV measurements lies

in the great relative accuracy within maps or comparable measurements.

4.3.2 Scanning speed

In many measurement modes that are based on photon detection such as XRF or X-ray scattering, the signal intensity increases in first approximation linearly with the acquisition time, with accordingly increased signal-to-noise ratio. This is not true for XBIC measurements, where the window of possible scanning speeds is not dictated by count statistics but by more complex considerations such as carrier dynamics and device structure.

Nevertheless, slow measurements with many periods of modulated signal per pixel typically lead to the best signal-to-noise ratio in lock-in amplified XBIC measurements, and oversampling with smoothing during post-processing (e.g. by binning or applying filters) can further reduce noise levels if measurement time allows. However, apart from throughput considerations, further constraints can set lower limits to the measurement speed, including: (1) X-ray beam induced degradation (see the following section), or environment-induced sample changes during in-situ measurements often reduce the allowable dwell time. (2) Sample drift and reproducibility of stage movements can be limiting, particularly for measurements at the nanoscale. (3) Variations of the electromagnetic noise level may be outrun by faster measurements. (4) Whereas photon-counting measurements can easily be normalized to the incident photon flux, the XBIC signal (and even more so the XBIV signal) is only to some extent linear to the incident photon flux [165]. Therefore, normalization to the photon flux only compensates part of the effects from photon-flux variation, and one should avoid taking XBIC measurements (such as maps or time-series) while the flux is varied. This is particularly an issue when the storage ring is filled during an XBIC map.

If the XBIC measurement speed is not governed by other measurement modes (see Sec. 3.3), XBIC measurements are typically taken with the maximum speed that provides satisfying signal-to-noise ratio. Upper limits to the measurement speed are given by the following constraints: (1) A fundamental upper limit to the measurement speed is the response time of the DUT. Ultimately, the response time is limited by the charge-collection time. For most TF solar cells with charge-carrier lifetimes in the nano- or microsecond range, this is uncritical, but this has to be kept in mind for high-quality crystalline-silicon solar cells with lifetimes of several milliseconds. However, capacitance effects can increase the response time also of TF solar cells such

that it can limit the measurement speed. (2) Rotating chopper blades that are used to modulate the X-ray beam have upper speed limits. Depending on their location in the X-ray beam, the beam size may be up to 1 mm wide, which defines the minimum period of the blade. If the chopper is operated in vacuum, the rotation frequency is rarely limiting, matching in some cases even the electron-bunch frequency. However, the operation of choppers at such speeds in vacuum is challenging, such that most choppers are operated in air. In this case, the rotating speed is limited by mechanical vibrations and ultimately by the speed of the outermost part of the blade that needs to be smaller than the speed of sound. From experience, the chopping frequency is limited often to $\sim 7000\,\mathrm{Hz}$ in air. (3) In many cases, the response time of the PA sets the upper limit of the measurement speed. As shown in Fig. 4.3, fast rise times of the PA are required to translate the signal modulation from the chopper. For large amplification, low-noise current amplifiers are used, which have rise times up to 100 ms. With such rise times, the chopping frequency can be limited to few Hz, which would require dwell times of several seconds. Therefore, the best strategy is often to choose a lower amplification by the PA with a faster response time that matches the chopping frequency. Although this translates into smaller signal-to-noise levels after pre-amplification, lock-in amplification can often still retrieve a high-quality modulated signal.

As an example, the used PA provides a bandwidth of more than 10 kHz for amplification in the µA/V range, even for the low-noise setting [198]. This allows chopping at the kHz range and measurement speeds up to the 100-Hz range with a low-pass filter with a cut-off frequency between the scanning and chopping frequency. These are measurement conditions we often utilize.

To avoid measurement artifacts, it is critically important to analyze the signal along the amplification chain: whereas limitation by the low-pass filter of the LIA can easily be detected as line-artifacts in maps (smearing out of the XBIC signal across several pixels), the system response of the DUT and PA requires inspection of the signal by a scope, which can be integrated in the LIA.

4.3.3 Beam Damage

X-ray beam induced damage is a common issue and has been discussed for many systems, from biological samples to silicon solar cells and detectors [175, 209]. Although inorganic semiconductors are generally more robust against X-ray irradiation compared to organic semiconductors or biological systems, X-ray beam induced dam-

age is common also in TF solar cells. Specifically, we observed X-ray beam induced damage of solar cells with CdTe, Cu(In,Ga)Se_2 [5], perovskite [186], and organic absorber layers. Note that the electronic response of DUT like solar cells is sensitive to defect concentrations below the ppm level, where charge-carrier recombination affects the performance without apparent chemical damage.

Therefore, it is generally required to test the sensitivity of a DUT to beam damage. In practice, the X-ray beam induced degradation of any DUT is evaluated prior to actual XBIC measurements, and conditions that allow measurements to be the least influenced by degradation effects are established.

Different strategies exist to cope with X-ray beam induced damage, but what they all have in common is that they aim to reduce the radiation dosage at a measurement spot prior to the evaluation of the performance there. In other words, the objective is to outrun degradation following the paradigm "measure faster than the DUT degrades". The strategies include: (1) Use short dwell times. (2) Increase the step size, reducing the measurement resolution. (3) Reduce the X-ray beam intensity by attenuation filters. Depending on the beamline and DUT, different approaches may be chosen or a combination thereof. For instance, the lack of fast shutters or fly-scan modes exclude (1), and wide-spread X-ray beam profiles such as those generated by zone plates can lead to significant degradation far away from the central beam position.

Fortunately, most degradation mechanisms only lead to locally enhanced charge carrier recombination. This limits the lateral effect of the degradation to the diffusion length of the charge carriers, and XBIC measurements further away from the degraded areas remain nearly unaffected. If, instead, degradation mechanisms lead to local shunting of the DUT, further XBIC measurements would be seriously hampered. To keep the deposited radiation dosage to a minimum, the critical measurements should be performed first on a fresh spot and then afterwards, photon-hungry methods, like XRF, that are more indifferent to beam damage, may be utilized in the same location.

5 X-ray vision of Cu(In,Ga)Se_2: from the Ga/In ratio to solar-cell performance

Different studies were performed during the time frame of this work, which led to publications. A whole Si-module was studied by Falkenberg et al. in Ref. 9 combining XRF and XBIC, and a CdTe solar cell system was studied by Walker et al. in Ref. 10, which also employed XRF and XBIC measurements.

In this chapter a first author publication will be presented, where we applied multi-modal X-ray scanning microscopy to elucidate relevant aspects of solar cell characterization. The text is slightly adapted for readability, and not further marked as cited from Ref. 3.

This study [3] concerns a Cu(In,Ga)Se_2 solar-cell series which has a shared first authorship with Niklas Pyrlik, who conducted his Bachelor's thesis in our group.

Cost efficiency and defect passivation are the two major challenges that TF solar cells have to overcome for economic competitiveness. For Cu(In,Ga)Se_2 solar cells, the first is addressed by an increase of the Ga/In ratio, which widens the bandgap favorably for tandem applications and reduces the requirement of costly, rare In. The second is addressed by heavy alkali post-deposition treatments. However, the maximum device efficiency is typically achieved with a comparably low Ga/In ratio, which is in contrast to the economic interest of a higher Ga/In ratio and makes it paramount to identify, understand and mitigate the sources of local underperformance in Ga-rich cells. In this work, we investigate a series of Cu(In,Ga)Se_2 cells with varying Ga/In concentration in the absorber, using multi-modal scanning X-ray microscopy. In particular, we analyze differences in chemical composition and electrical performance on the nanoscale, with a focus on the effect of Rb. We find that In-rich cells show, along with a greater overall performance, a more homogeneous distribution of the nanoscale performance compared to the Ga-rich cells. Our analysis of Rb suggests

that this effect is due to more effective passivation of structural defects in the absorbers, i.e. voids and grain boundaries. These results shine a light on the causes of the superiority of Ga-poor/In-rich absorbers and substantiate the trend of higher defect density for Ga-rich absorbers.

5.1 Introduction

As humanity is racing towards a climate and energy crisis, renewable and clean energy sources are key to a sustainable future [38]. TF solar cells offer an interesting perspective due to their low energy pay-back time [210] and material requirements compared to Si solar cells [211]. Furthermore, their compositional nature allows the bandgap to be tuned, which is of particular interest for tandem applications [49, 212, 213]. However, current state-of-the-art TF solar cells still contain scarce elements, namely In in Cu(In,Ga)Se_2 solar cells. Thus, the manufacturing of TF solar cells from more abundant elements is an aspiration. In case of Cu(In,Ga)Se_2 solar cells, a record efficiency was found with a X_{GGI} =[Ga]/([In]+[Ga]) ratio (denoted as 'GGI') of 0.3 [214], corresponding to a bandgap of 1.08 eV [214]. This bandgap matches one of the two efficiency maxima of the Detailed-Balance Limit [78] for single-junction solar cells with AM1.5G spectrum, but solar cells with an absorber bandgap matching the second, wide-bandgap, efficiency maximum at 1.34 eV would be desirable with $X_{\mathrm{GGI}} = 0.5$ [215]. For tandem applications with a Si bottom cell, an even wider bandgap above 1.4 eV would be ideal. Hence, solar cells with lower In concentrations would be desirable, but the efficiency of Cu(In,Ga)Se_2 solar cells with GGI values above 0.3 declines [216].

Lateral inhomogeneities pose another challenge that TF solar cells have to overcome to become competitive on the photovoltaics (PV) market [50, 61, 217]. Bandgap fluctuations induced by inhomogeneities and defects affect the efficiency of the whole cell. Therefore, it is paramount to identify, understand and mitigate the sources of local underperformance [217–219]. The effects of adding alkali elements such as Na, K and Rb in a post-deposition treatment to mitigate defects has been extensively studied before [179, 191, 193, 194, 220–222], and a segregation of the alkali elements to grain boundaries was consistently observed. The diffusion mechanism for alkali metals is assumed to be dominated by Cu vacancies (V_{Cu}) at grain boundaries, and only small alkali metals can move via interstitial positions into grains [223, 224]. This leads to the formation of Rb_{Cu} sites at grain boundaries, while Na diffuses into grains

via interstitial positions, effectively increasing the doping of the material [179, 225]. Inhomogeneities at the sub-micrometer scale include chemical defects and voids; they pose a particular characterization challenge and require imaging techniques on the nanoscale to study them [50]. Synchrotron-based scanning X-ray microscopy offers ideal tools for that purpose and has been used extensively in the last years [1, 2, 43, 59, 66, 67, 191, 226, 227]. Hard X-rays allow to penetrate fully functional solar-cell stacks, and the multitude of available measurement modalities [2, 30, 59] can give complementary information. The combination of XBIC and XRF measurements has been established as a sensitive approach to probe the spatially resolved electrical performance together with the composition [1, 43, 59, 228].

In a previous study by West et al. [61], two cells were measured with $X_{\mathrm{GGI}} = 0.3$ and $X_{\mathrm{GGI}} = 0.6$, respectively. It was highlighted that the latter cell has a steeper local GGI gradient from grain core to grain boundary. To elucidate the underlying cause of the efficiency loss upon GGI increase, we simultaneously assessed XBIC and XRF of four solar cells with different nominal depth-averaged GGI ($X_{\mathrm{GGI}}^{\mathrm{Nom}}$) values between 0.39 and 0.49. Beyond macroscopic comparison, we used point-by-point correlation to link performance and composition for each cell individually. We studied co-evaporated Cu(In,Ga)Se_2 cells that had undergone Rb post-deposition treatment, as the world record efficiency of 22.6% for co-evaporated Cu(In,Ga)Se_2 cells was achieved with this system [103]. Therefore, we evaluated especially the behavior of Rb at identified voids and the impact on the charge-collection efficiency relative to the surrounding absorber matrix. For an inter-cell comparison, we performed a meta-analysis. This is a statistical tool commonly used in medicinal studies to congregate smaller studies into a bigger sample pool [229]; here, the individual voids are treated as sub-studies.

5.2 Experimental setup

5.2.1 Samples

The samples were prepared by EMPA. The Cu(In,Ga)Se_2 solar cells were synthesized on glass substrates with an SiO_x diffusion barrier below the 500 nm Mo back contact deposited by sputtering as described in [230]. The bandgap-graded Cu(In,Ga)Se_2 absorber layers were deposited using a multistage co-evaporation process below 450 °C substrate temperature, and were subjected to an in-situ NaF & RbF post-deposition

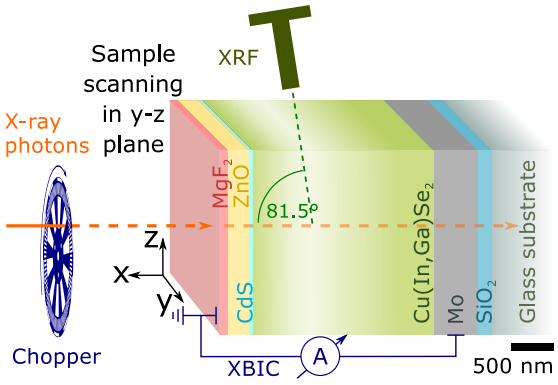

Figure 5.1: Scheme of the experimental setup for multi-modal measurements including XRF and XBIC of a $Cu(In,Ga)Se_2$ solar cell. The color gradient in $Cu(In,Ga)Se_2$ indicates a higher (darker) and lower (brighter) GGI value. The samples were scanned in the $y-z$ plane.

treatment in Se ambient.

The CdS buffer layer (45 nm) was deposited in a chemical bath, followed by sputter deposition of ZnO (250 nm) as transparent conductive oxide, and a MgF_2 layer (105 nm) as anti-reflective coating. An electron-beam evaporated Ni-Al grid was used to contact the cells.

They were manually isolated by peeling off surrounding $Cu(In,Ga)Se_2$ material. The Ni-Al grids were electrically connected to a dedicated printed-circuit board using thin Cu wires and manually applied silver paint (far from the investigated region of interest). Figure 5.1 shows a scheme of the samples and the experimental setup. The wiring for XBIC measurements followed the description in Ref. [43] with the front contact grounded to avoid contributions of the replacement current for ejected electrons to the XBIC signal. The sample preparation was noted before in Ref. [172].

The solar cells were prepared with four different $X_{\mathrm{GGI}}^{\mathrm{Nom}}$ values that are used for referencing the cells in this work. They are listed in Tab. 5.1 along with the bandgap E_{g} from external-quantum-efficiency measurements, the absorber-layer thickness d_{Nom} as well as the open-circuit voltage V_{OC}, V_{OC} deficit $E_{\mathrm{g}}/q - V_{\mathrm{OC}}$, short-circuit current density J_{SC}, fill factor C_{FF}, and the efficiency η from current-voltage measurements of co-processed sister cells using an AM1.5G spectrum with 1000 $\mathrm{W\,m^{-2}}$ illumination intensity. Figure 5.2 shows the J-V curves and the external quantum efficiency (EQE) η_{EQE} of the four evaluated solar cells.

These measurements highlight that high efficiency is associated with high In con-

Table 5.1: Nominal properties and characteristic solar-cell parameters of the four solar cells from current-voltage and external quantum-efficiency measurements, including the nominal absorber-layer thickness d_{Nom}, bandgap E_{g}, open-circuit voltage V_{OC}, V_{OC} deficit $E_{\mathrm{g}}/q - V_{\mathrm{OC}}$, short-circuit current density J_{SC}, fill factor C_{FF}, and the efficiency η. The cells are referred to by their $X_{\mathrm{GGI}}^{\mathrm{Nom}}$ value, and the mean stoichiometric value of Ga $\bar{\nu}_{\mathrm{Ga}}$ from synchrotron XRF measurements is shown for comparison.

$X_{\mathrm{GGI}}^{\mathrm{Nom}}$	$\bar{\nu}_{\mathrm{Ga}}$ (.)	d_{Nom} (µm)	E_{g} (eV)	V_{OC} (V)	$E_{\mathrm{g}}/q - V_{\mathrm{OC}}$ (V)	J_{SC} (mA cm^{-2})	C_{FF} (%)	η (%)
0.39	0.35	1.97	1.166	0.756	0.41	32.4	0.76	18.7
0.42	0.36	2.13	1.175	0.755	0.42	30.8	0.74	17.2
0.46	0.41	2.32	1.197	0.769	0.43	31.2	0.74	17.6
0.49	0.42	2.62	1.203	0.773	0.43	29.7	0.73	16.8

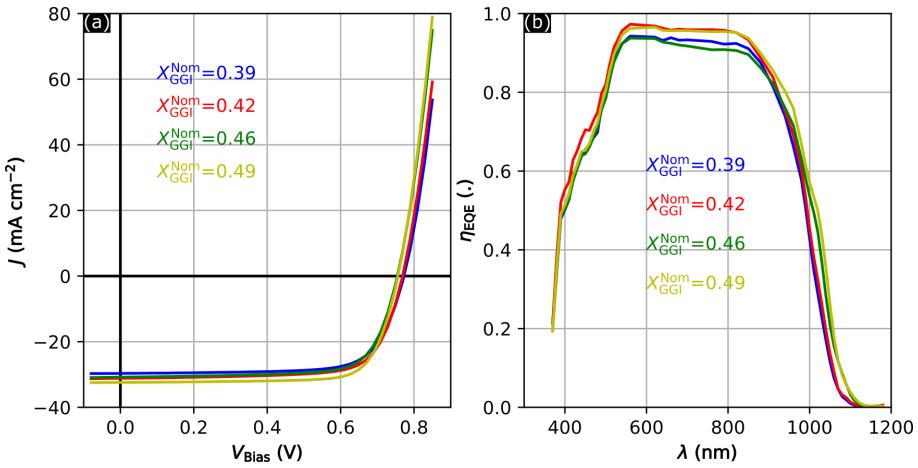

Figure 5.2: (a) J-V curves of the four cells under AM1.5G-spectrum [92] with 1000 W/m^2 illumination. (b) EQE curves of the four cells.

centration (low $X_{\mathrm{GGI}}^{\mathrm{Nom}}$) and low V_{OC} deficit, which means that the voltage remains below expectations for cells with high $X_{\mathrm{GGI}}^{\mathrm{Nom}}$ and is one of the key motivations for this study.

5.2.2 Measurements

The X-ray microscopy measurements were performed by scanning the sample-surface plane ($y-z$) across the focused X-ray beam at the microprobe endstation of the hard X-ray scanning microscopy beamline P06 [54] at PETRA III (Deutsches Elektronen-Synchrotron DESY) in Hamburg, Germany, as shown in Fig. 5.1. The photon energy was set to 15.25 keV and the coherent part of the X-ray beam was focused

by Be compound refractive lenses (CRL) and a correcting phase plate [135] to 108 nm × 105 nm (horizontal × vertical, FWHM). The subsequent XBIC and XRF measurements were optimized for the electrical and compositional assessment. The scans were performed in continuous mode and covered an area of 10 µm × 10 µm with a set scanning speed of 5 µm s^{-1} and 0.5 µm s^{-1} for XBIC and XRF measurements, respectively, assessed every 50 nm.

For maximum signal-to-noise ratio, lock-in amplification was utilized as described in Chapter 4. A chopper (MC2000B, Thorlabs) modulated the incident X-ray beam at 8.015 kHz, and the XBIC signal was demodulated to the chopper frequency using a lock-in amplifier (UHFLI, Zurich Instruments) after the signal underwent amplification by 1 µA V^{-1} through a current pre-amplifier (SR570, Stanford Research Systems). The low-pass filter cut-off frequency of the lock-in amplifier was set to 501.1 Hz (8^{th} order). For the quantitative current evaluation, the XBIC signal was normalized to the incident X-ray photon flux and to the effective pixel dwell time.

XRF photons were detected by a silicon drift detector (SII Vortex EM, Hitachi) that was placed 2 cm from the sample under an angle of 8.25° to the sample surface. The XRF detector was read out by a pulse processor (Xspress3, Quantum Detectors). Fluorescence spectra were fitted using PyMca [159] (V. 5.3.3.) to obtain XRF count rates Φ_{Element} and stoichiometric fractions ν_{Element} (see Sec. 3.2.3) for every element, taking self-absorption, photon flux and dwell time into account. The resulting images from two subsequent scans optimized for XBIC and XRF signal were registered and aligned as described in [7] based on the distribution of Se.

5.3 Results

5.3.1 Performance

Table 5.1 shows that the overall efficiency of the investigated Cu(In,Ga)Se_2 solar cells decreases with a higher $X_{\text{GGI}}^{\text{Nom}}$. To go from a macroscopic to a microscopic evaluation of the performance, its distribution over the scanned maps was therefore measured with XBIC. X-rays with an energy of 15.25 keV have an extinction length of around 100 µm in Cu(In,Ga)Se_2 absorber material [160]. Accordingly, only 9–12 % percent of the incident photons are absorbed in the Cu(In,Ga)Se_2 layer, and the XBIC signal can be assumed to be constituted from electron-hole pairs being homogeneously distributed along the X-ray path (flat generation profile).

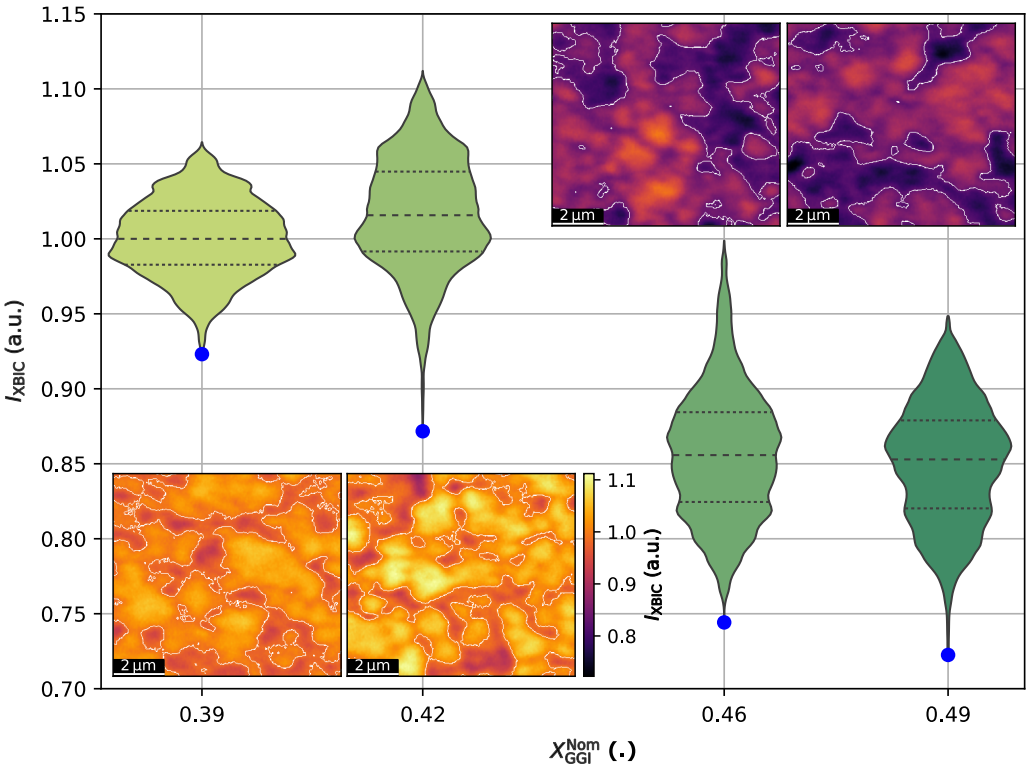

Figure 5.3: Distribution of I_{XBIC} for the four investigated Cu(In,Ga)Se_2 solar cells as 2D maps and violin plots. The dashed lines indicate the 25$^{\mathrm{th}}$, 50$^{\mathrm{th}}$ and 75$^{\mathrm{th}}$ percentile of the distribution. The blue dots highlight the lowest value for each cell. The white lines in the 2D maps are contours indicating the 33 percentiles of low performance. All maps share the same color scale.

To compare the different cells without manipulating their charge-collection efficiency distributions, we have normalized the measured I_{meas}. The scaling of the measured XBIC I_{meas} follows the description in [1, 43]. To estimate the absorptance A of an X-ray beam with 15.25 keV photon energy in Cu(In,Ga)Se_2, we used the nominal thickness d_{Nom} of the absorber layers of the four solar cells and reference [160] accessed at `https://henke.lbl.gov`. The values for the four cells with different X_{GGI} =[Ga]/([In]+[Ga]) ratio are tabulated in Tab. 5.2. The normalization factor representing the number of generated electron-hole pairs per incident photon is calculated as

$$C = \frac{A \cdot 15\,250\,\mathrm{eV}}{3 \cdot E_{\mathrm{g}}}, \tag{5.1}$$

utilizing the rule-of-thumb relation between the bandgap E_{g} and the ionization energy $E_0 \approx 3E_{\mathrm{g}}$ as justified in [43, 175]. The normalized XBIC signal I^*_{XBIC} is thus

$X_{\mathrm{GGI}}^{\mathrm{Nom}}$	d_{Nom} (µm)	Absorptance (.)
0.39	1.97	0.089
0.42	2.13	0.093
0.46	2.32	0.102
0.49	2.62	0.115

Table 5.2: Absorptance along with the nominal absorber thickness d_{Nom} for the four cells with different $X_{\mathrm{GGI}}^{\mathrm{Nom}}$ cells at 15.25 keV photon energy and an absorber density of $5.7\,\mathrm{g/cm^3}$.

calculated as

$$I_{\mathrm{XBIC}}^{*} = \frac{I_{\mathrm{meas}}}{C} \tag{5.2}$$

and finally scaled to the median I_{XBIC}^{*} of the cell with the smallest $X_{\mathrm{GGI}}^{\mathrm{Nom}}$, median $\left(I_{\mathrm{XBIC,0.39}}^{*}\right)$:

$$I_{\mathrm{XBIC}} = \frac{I_{\mathrm{XBIC}}^{*}}{\mathrm{median}\left(I_{\mathrm{XBIC,0.39}}^{*}\right)}. \tag{5.3}$$

The I_{XBIC} maps are shown in Fig. 5.3 along with the corresponding distributions.

In these nanoscale performance measurements, the macroscopically measured superiority of the cells with lower $X_{\mathrm{GGI}}^{\mathrm{Nom}}$ is reflected in higher I_{XBIC} values and narrower distributions. Conversely, broad distributions, as the higher $X_{\mathrm{GGI}}^{\mathrm{Nom}}$ cells display, are typical for poor solar-cell performance [217, 227]. The trend of decreasing performance with increasing $X_{\mathrm{GGI}}^{\mathrm{Nom}}$ is particularly well visible for the points with the lowest performance in each cell that are highlighted with a blue dot. As the underperforming areas limit the overall solar-cell efficiency, the contours of the lowest 33 percentile are indicated with white lines in the 2D maps in Fig. 5.3.

We further note that the spatial granularity of I_{XBIC} seems to decrease with increasing $X_{\mathrm{GGI}}^{\mathrm{Nom}}$ from isolated small areas of underperformance for low-GGI cells to large interconnected areas for high-GGI cells. To elucidate and quantify this trend, we have evaluated for each point the shortest distance d_{min} to an area of the underperforming 33 percentiles. The resulting distance-maps and -distributions are shown as violin plots and inlays in Fig. 5.4. The trend towards locally concentrated, severely underperforming areas with increasing $X_{\mathrm{GGI}}^{\mathrm{Nom}}$ value appears here as a rising median distance and broader distribution as well as larger structures in the 2D maps.

These results offer an explanation for the macroscopically seen lower performance for higher $X_{\mathrm{GGI}}^{\mathrm{Nom}}$: while high $X_{\mathrm{GGI}}^{\mathrm{Nom}}$ values lead to fewer spots of accumulated defects, we hypothesize that these defect areas have a greater negative impact than the more broadly distributed defects in solar cells with a lower $X_{\mathrm{GGI}}^{\mathrm{Nom}}$.

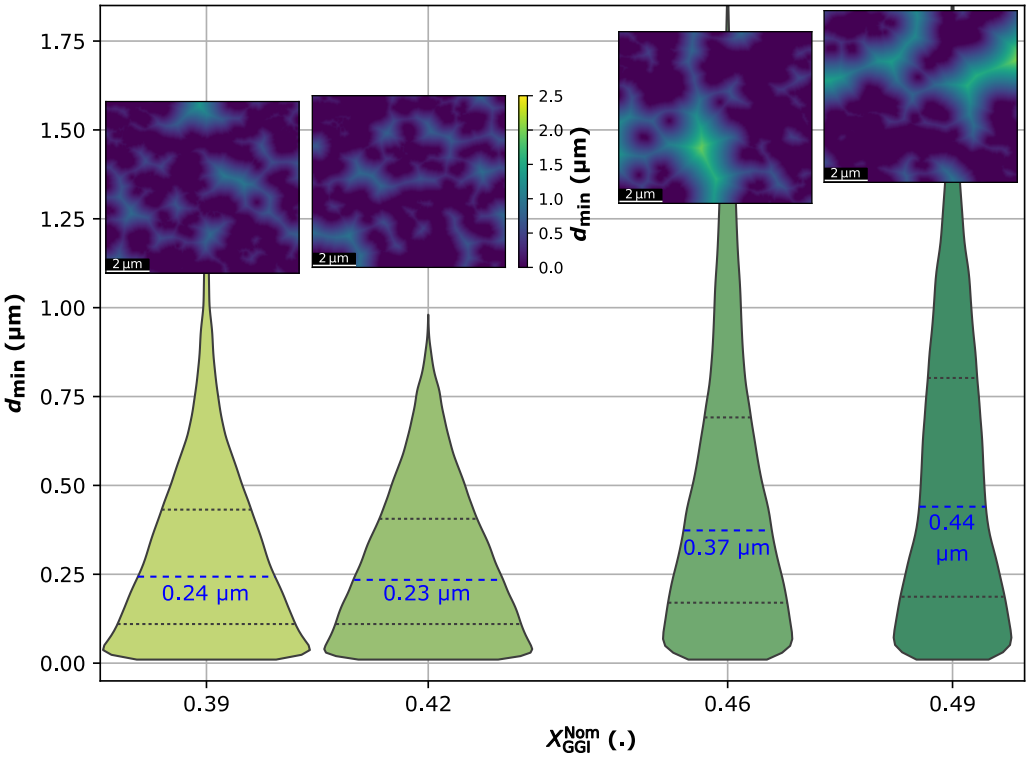

Figure 5.4: Shortest distance d_{min} of each point to an area of the underperforming 33 percentiles of the I_{XBIC} signal shown as violin plots and 2D maps. The dashed lines indicate the 25$^{\mathrm{th}}$, 50$^{\mathrm{th}}$ (with numerical value in blue) and 75$^{\mathrm{th}}$ percentile of the distribution. All maps share the same color scale.

5.3.2 Distribution of Rb

For the type of Cu(In,Ga)Se$_2$ solar cells studied here, voids and crevices tend to appear in the top part of the absorber layer [50], and we used XRF microscopy to localize these material-deficit areas. We chose the excitation energy for our experiment (15.25 keV) just above the absorption edge of Rb (15.2 keV) to be most sensitive to the Rb distribution and evaluate its passivation effect on defects [179, 191, 193, 194, 220–222]. In Cu(In,Ga)Se$_2$ solar cells, the abundance of Cu is sub-stoichiometric to dope the absorber, while Ga and In share a lattice point with intentional spatial grading. Consequently, Se is the most homogeneously distributed absorber-matrix element [231], which allows considering the depth-integrating XRF Se count rate Φ_{Se} as an estimate of the absorber-layer thickness. Accordingly, low Φ_{Se} values are usually associated with grain boundaries [190] or other material deficits such as voids [2] that may–or may not–lead to local underperformance [50].

Figure 5.5 shows the XRF count rates Φ_{Se} (gray) and Φ_{Rb}(red) of Se and Rb for the four cells. These maps clearly unveil the anti-correlation of Rb and Se and

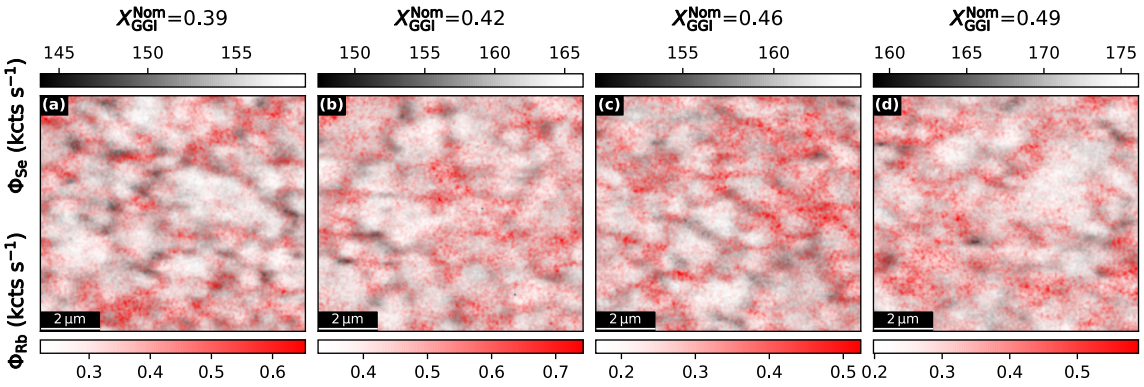

Figure 5.5: (a–d) XRF count rate of Se Φ_{Se} (grayscale) and count rate of Rb Φ_{Rb} (red scale) overlaid. The anti-correlation of Rb and Se illustrates the segregation of Rb towards material-deficit areas such as grain boundaries, voids, and crevices. All color scales cover the entire range of the individual maps.

the segregation of Rb to material-deficient areas (i.e. low Se signal) such as grain boundaries, voids, and crevices. Figure 5.6 shows the XRF signal maps for the absorber elements individually.

5.3.3 Correlation

The statistical correlation between performance, absorber thickness, Rb concentration, and lateral Ga distribution is investigated by Pearson's correlation coefficient ρ and shown in Fig. 5.7; the correlation coefficients of further modalities are shown in Fig. 5.8.

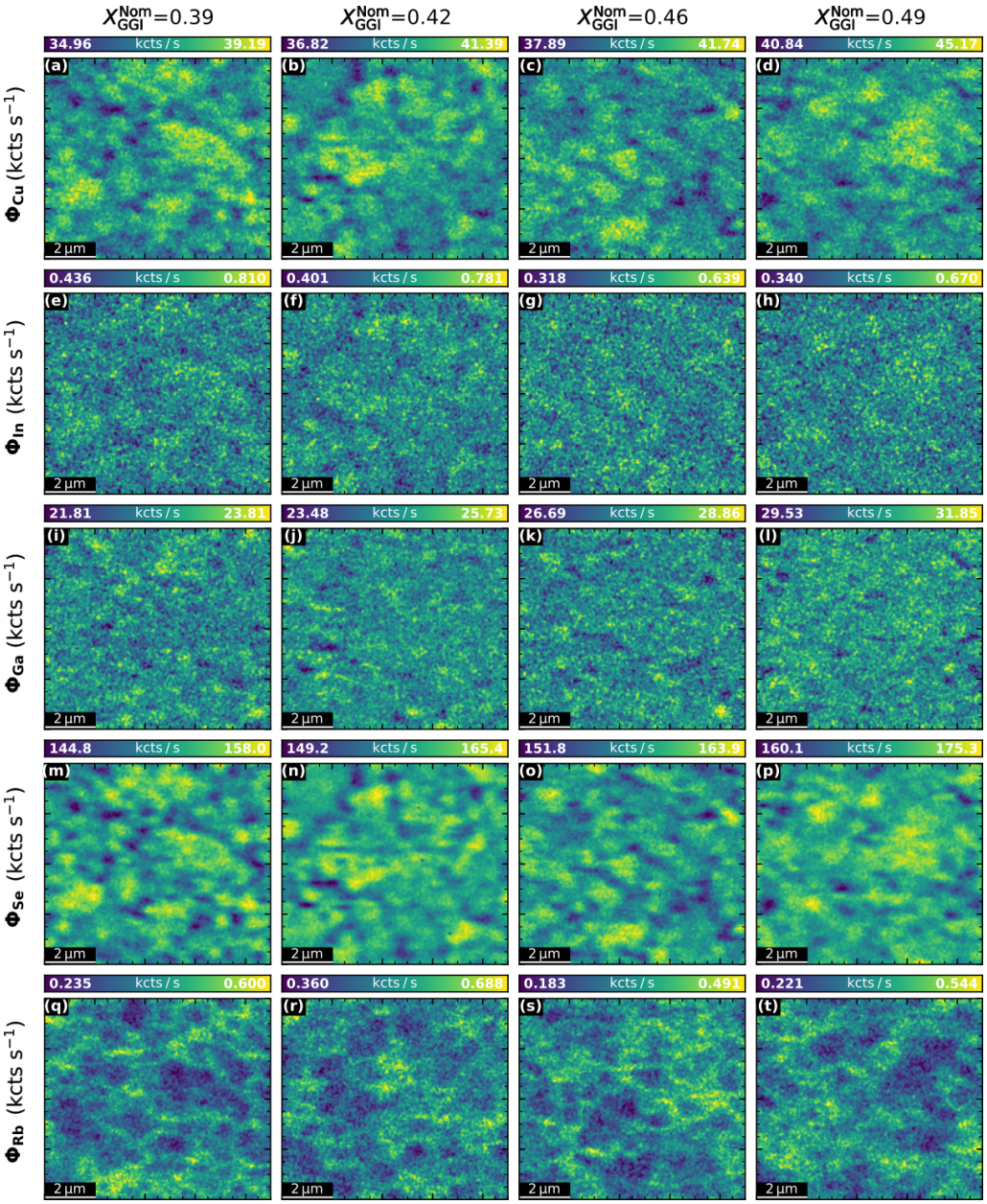

Figure 5.6: Elemental XRF signal maps of Cu, In, Ga, Se, and Rb.

The strong positive correlation of Φ_{Se} and I_{XBIC} (purple squares in Fig. 5.7) is explained by the sample topology dominating the beam/sample interaction volume, which affects the XBIC signal and the fluorescence signal strength in a comparable manner. Interestingly, this correlation decreases with increasing $X_{\mathrm{GGI}}^{\mathrm{Nom}}$, which indicates that other effects than topology—likely defects—gain importance.

For a qualitative assessment of the local performance, we compensated I_{XBIC} for the influence of the beam-sample interaction volume and calculated the charge-collection

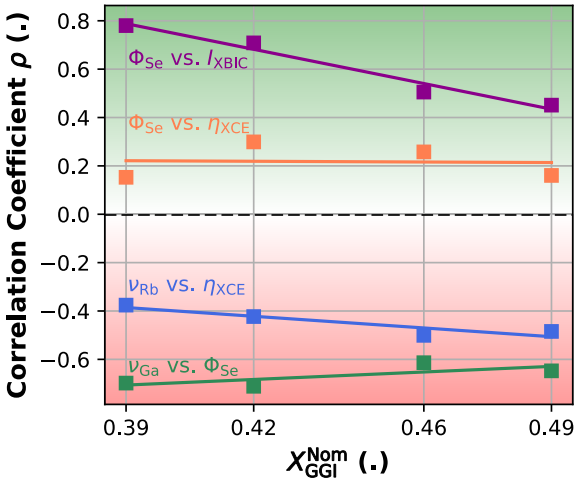

Figure 5.7: Correlation coefficients ρ for selected inter-dependencies: the Se count rate Φ_{Se}, Ga stoichiometric fraction ν_{Ga} and Rb stoichiometric fraction ν_{Rb} from XRF measurements; the X-ray beam induced current I_{XBIC} and the charge-collection efficiency η_{XCE} derived from I_{XBIC}. The lines are linear fits serving as a guide to the eye to illustrate the trend over the solar-cell series. The green and red background colors indicate positive and negative correlations, respectively.

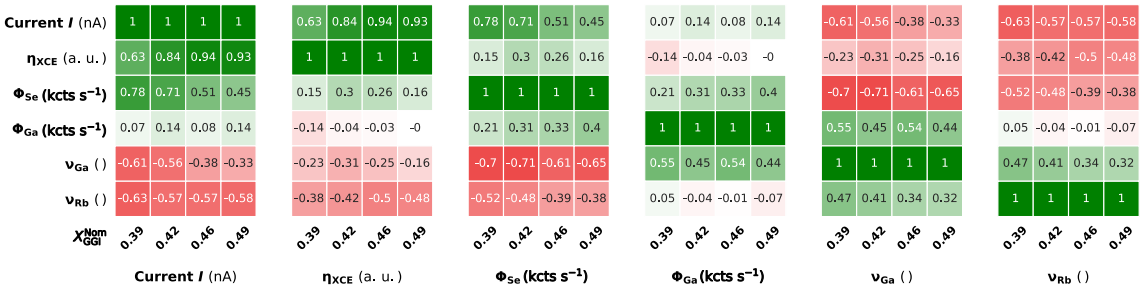

Figure 5.8: Pearson's correlation coefficient for the different modalities.

efficiency η_{XCE} as motivated in [43] and described in the Sec. 3.2.4 and Sec. 3.2.4. Here, we scaled the charge-collection efficiency from 0 to 1 over the complete $\widetilde{I}$ range of all four cells, emphasizing the strength of these measurements being spatial variations rather than absolute values of η_{XCE}:

$$\eta_{\mathrm{XCE}} = \frac{1}{\left(\widetilde{I} - \widetilde{I}_{\mathrm{min,all}}\right)_{\mathrm{max,all}}} \cdot \left(\widetilde{I} - \widetilde{I}_{\mathrm{min,all}}\right). \tag{5.4}$$

The measured XBIC and the charge-collection efficiency are shown in Fig. 5.9. The topology-corrected η_{XCE} is slightly positively correlated with Φ_{Se} for all cells (orange squares in Fig. 5.7), which indicates that areas with material deficit suffer from higher charge-carrier recombination compared to bulk absorber material, which is in

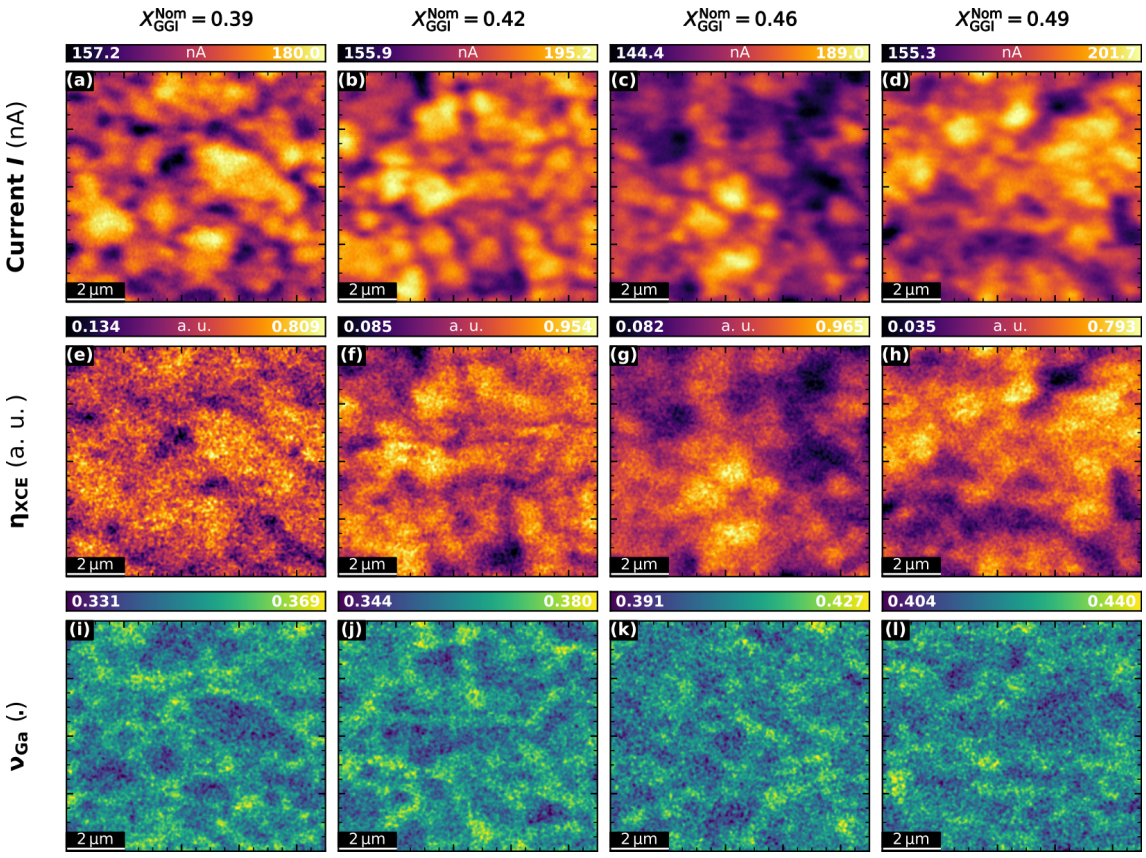

Figure 5.9: XBIC signal I_{XBIC}, charge collection efficiency η_{XCE}.

agreement with earlier findings [191].

The In count rate Φ_{In} is low and strongly influenced by self-absorption artifacts related to the low L-line fluorescence energy [58], which directly translates into uncertainties of $X_{\mathrm{GGI}} = \frac{\Phi_{\mathrm{Ga}}}{\Phi_{\mathrm{Ga}}+\Phi_{\mathrm{In}}}$. Therefore, the spatially resolved X_{GGI} is not considered here. Instead, we used the stoichiometric fraction of Ga, scaled to the stoichiometric fraction of Se, $\nu_{\mathrm{Se}} = 2$, to represent the depth-averaged stoichiometric Ga distribution ν_{Ga} in the absorber matrix. Note that the absolute values of the laterally averaged $\bar{\nu}_{\mathrm{Ga}}$ values listed in Tab. 5.1 are slightly lower than the nominal $X_{\mathrm{GGI}}^{\mathrm{Nom}}$ values, which is probably caused by the effective X_{GGI} differing from $X_{\mathrm{GGI}}^{\mathrm{Nom}}$ and by different experimental setups being used to measure the laboratory-based $X_{\mathrm{GGI}}^{\mathrm{Nom}}$ and the synchrotron-based ν_{Ga} values. Both effects should, however, not affect the observed intra- and inter-cell variation of ν_{Ga}.

Figure 5.7 unveils a strong anti-correlation of ν_{Ga} and the topology-representing Se count rate Φ_{Se}. This indicates a higher X_{GGI} in material-deficit areas compared to areas with a thick absorber layer and is in agreement with reports about increased

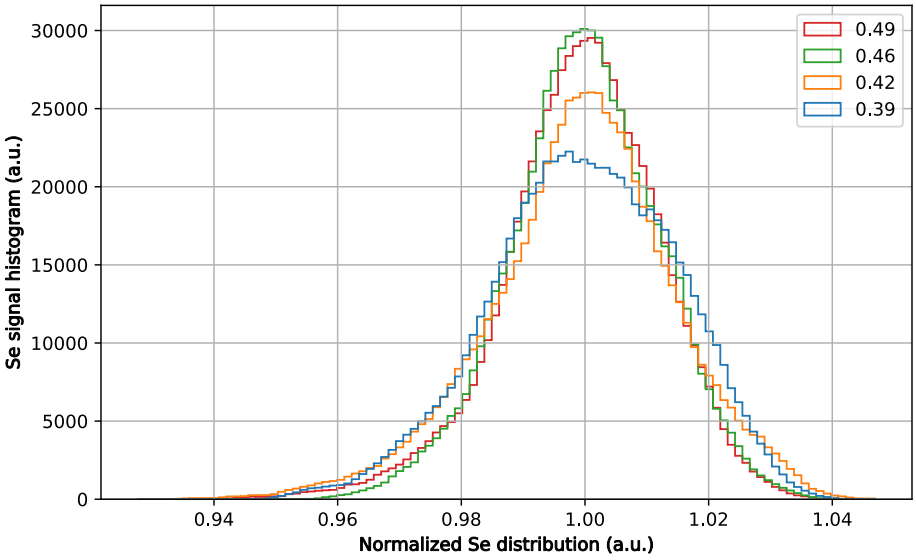

Figure 5.10: Se count-rate distribution for the four cells, normalized to their respective median value.

X_{GGI} at grain boundaries compared to grain cores [50, 61, 191, 232, 233]. The slight decrease in anti-correlation towards higher $X_{\mathrm{GGI}}^{\mathrm{Nom}}$ cells may be caused by statistical effects of increasing absorber thickness, which is consistent with a sharper normalized Se count-rate distribution as seen in Fig. 5.10.

The correlation between the Rb concentration ν_{Rb} and the charge-collection efficiency η_{XCE} shown in Fig. 5.7 is negative as expected from the Rb segregation towards material-deficit absorber areas (see Fig. 5.5). This indicates that the charge-collection efficiency is worse in Rb-rich areas: although Rb has been associated with defect-passivation [191, 221], the defects are apparently not fully mitigated by Rb. Additionally, we observed a slight increase in the anti-correlation for cells with a higher $X_{\mathrm{GGI}}^{\mathrm{Nom}}$. This is compatible with the hypothesis that more severe defects are present in the cells with higher $X_{\mathrm{GGI}}^{\mathrm{Nom}}$ cells and hints toward the selectivity of Rb segregation towards material-deficit areas.

5.3.4 Meta-analysis

From the anti-correlation between ν_{Rb} and η_{XCE} alone, the passivating effect of Rb cannot be corroborated. Therefore, we have segmented those areas with the 4% lowest Φ_{Se} counts and a minimum size of 3 scan pixels ($0.0075\,\mu\mathrm{m}^2$) and declared them as 'voids' for further discussion as compared to 'bulk' for the remaining 96%.

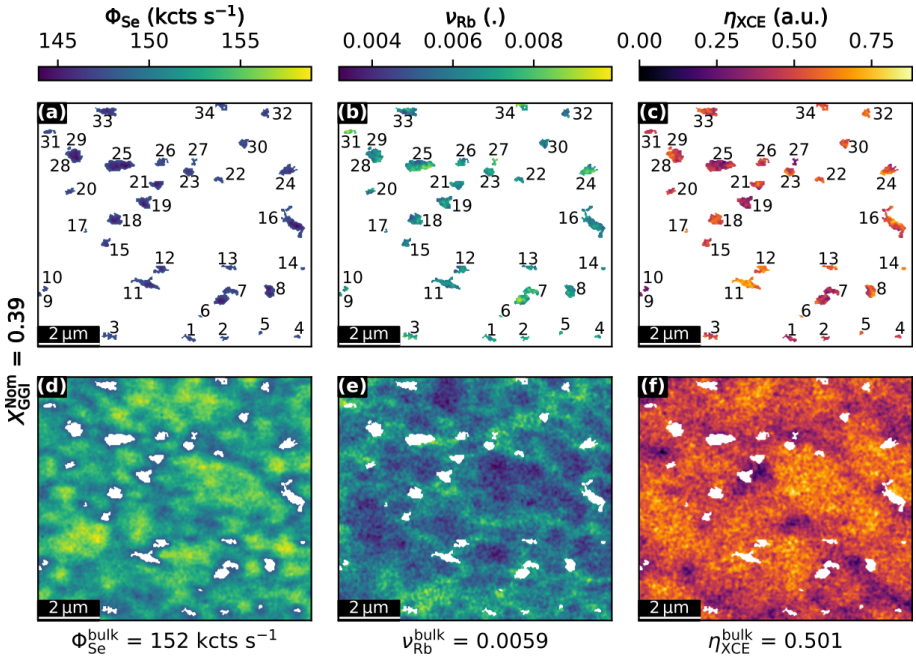

Figure 5.11: Maps of the cell $X_{\mathrm{GGI}}^{\mathrm{Nom}}$=0.39 highlighting the voids in (a) Φ_{Se}, (b) ν_{Rb}, (c) η_{XCE}. (d–f) show the surrounding area, from which the mean value of the bulk is determined as listed below.

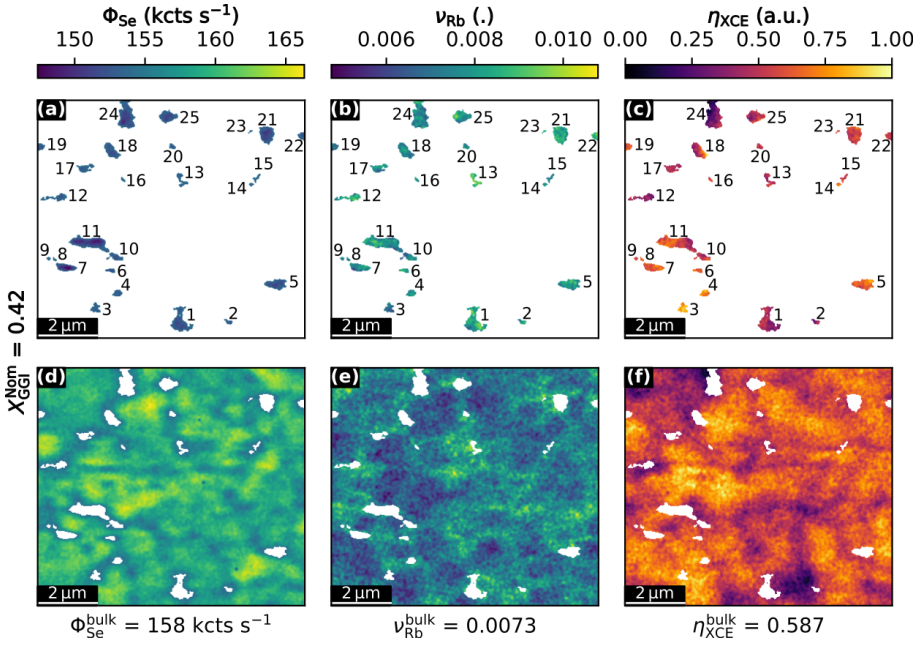

Figure 5.12: Maps of the cell $X_{\mathrm{GGI}}^{\mathrm{Nom}}$=0.42 highlighting the voids in (a) Φ_{Se}, (b) ν_{Rb}, (c) η_{XCE}. (d–f) show the surrounding area, from which the mean value of the bulk is determined as listed below.

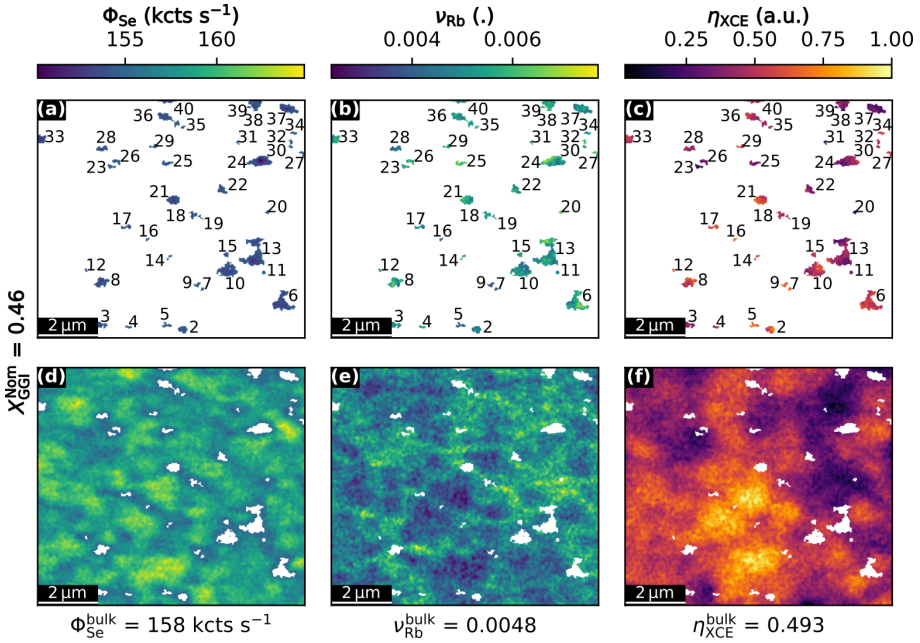

Figure 5.13: Maps of the cell $X_{\mathrm{GGI}}^{\mathrm{Nom}}$=0.46 highlighting the voids in (a) Φ_{Se}, (b) ν_{Rb}, (c) η_{XCE}. (d–f) show the surrounding area, from which the mean value of the bulk is determined as listed below.

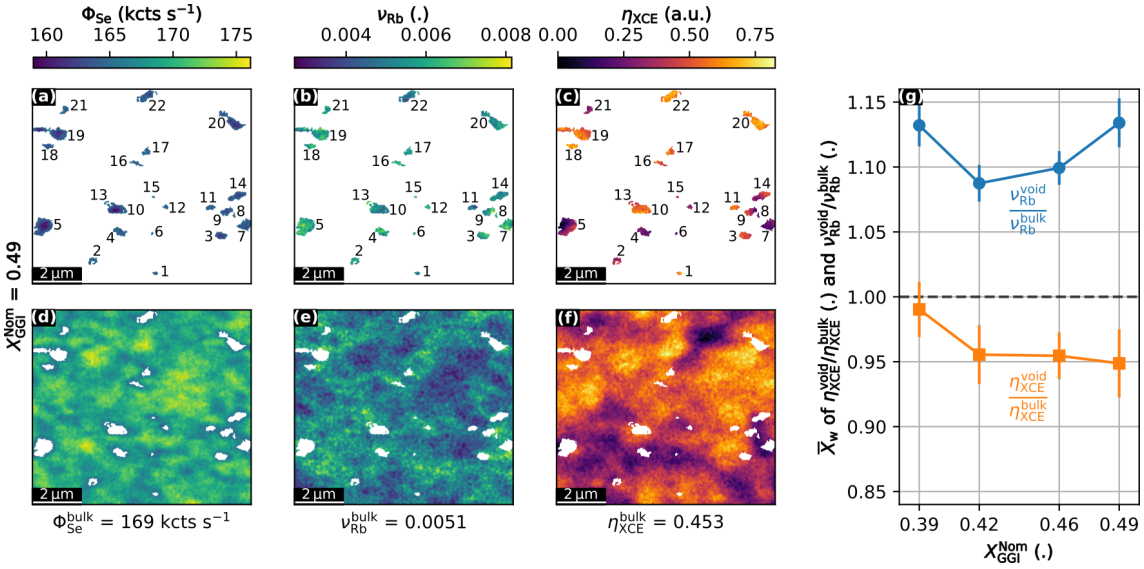

Figure 5.14: Maps of the cell with $X_{\mathrm{GGI}}^{\mathrm{Nom}}$=0.49 highlighting the voids in (a) Φ_{Se}, (b) ν_{Rb}, (c) η_{XCE}. (d–f) show the surrounding area, from which the mean value of the bulk, $\Phi_{\mathrm{Se}}^{\mathrm{bulk}}$ is determined. (g) Effect size for $\nu_{\mathrm{Rb}}^{\mathrm{void}}/\nu_{\mathrm{Rb}}^{\mathrm{bulk}}$ and $\eta_{\mathrm{XCE}}^{\mathrm{void}}/\eta_{\mathrm{XCE}}^{\mathrm{bulk}}$ of the different cells. The dashed line marks the equilibrium between void and bulk values.

Figures 5.11–5.14 show the areas of the voids in the maps of Φ_{Se}, ν_{Rb} and η_{XCE} (a–c) as well as the surrounding area (d–f) from where the average bulk values were extracted, to which we normalized our void values. We used the concept of meta-analysis to obtain a statistically meaningful evaluation of the effect of Rb on the charge-collection efficiency in material-deficient areas. The analysis follows [229] and the most important steps will be introduced shortly in the following. A meta-analysis combines sub-studies into one big study with greater statistical power compared to the individual sub-studies. The sub-studies (groups) in our case are the voids. We were interested in the Rb concentration and the charge-collection efficiency in the voids relative to the bulk. Therefore, we evaluated the effect size $\bar{X}_w$ (that can be understood as a weighted average) of $\nu_{\mathrm{Rb}}^{\mathrm{void}}/\nu_{\mathrm{Rb}}^{\mathrm{bulk}}$ and $\eta_{\mathrm{XCE}}^{\mathrm{void}}/\eta_{\mathrm{XCE}}^{\mathrm{bulk}}$ through $x_i = \nu_{\mathrm{Rb}}^{\mathrm{void\ i}}/\nu_{\mathrm{Rb}}^{\mathrm{bulk}}$ and $x_i = \eta_{\mathrm{XCE}}^{\mathrm{void\ i}}/\eta_{\mathrm{XCE}}^{\mathrm{bulk}}$ considering the mean Rb concentration and charge-collection efficiency in each void. To get the effect size for all groups, x_i of each void was weighted with a factor

$$w_i = \frac{1}{(E(x_i)^2 + \sigma^2)} \tag{5.5}$$

with σ as the standard deviation of the whole population and with the standard error of the respective void calculated as

$$E(x_i) = \frac{\sigma(x_i)}{\sqrt{n}} \tag{5.6}$$

with n as the number of samples (scanned pixels) in the group. The effect size for the whole population is then given by

$$\bar{X}_w = \frac{\sum_{i=1}^{k} w_i x_i}{\sum_{i=1}^{k} w_i} \tag{5.7}$$

with the standard error given as

$$E(\bar{X}_w) = \left[\frac{\sum_{i=1}^{k} (w_i)^2 \mathrm{var}(x_i)}{\left[\sum_{i=1}^{k} w_i \right]^2} \right]^{1/2} . \tag{5.8}$$

Intuitively, the effect size can be understood as a weighted average. Figure 5.15

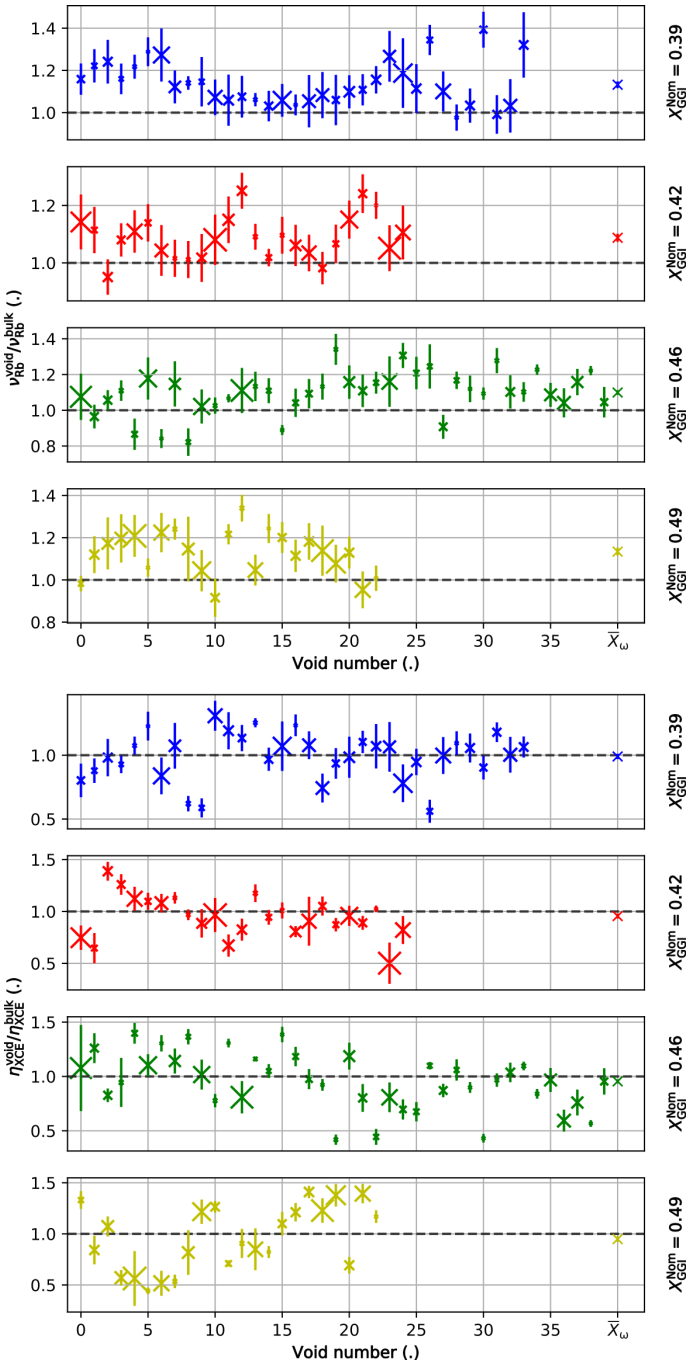

Figure 5.15: The individual mean values x_i of each void are shown for $\nu_{\mathrm{Rb}}^{\mathrm{void}}$ and $\eta_{\mathrm{XCE}}^{\mathrm{void}}$ normalized to the average values of non-void areas ($\nu_{\mathrm{Rb}}^{\mathrm{bulk}}$ and $\eta_{\mathrm{XCE}}^{\mathrm{bulk}}$). The error bar indicates the size of the standard error E, while the marker size indicates the sample size of the group. The last value is the effect size $\bar{X}_w$ resulting from the weighted x_i.

shows the respective mean values x_i of each void, with the marker size indicating the group sample size and the error bar as the standard error E. The last value shows the effect size $\bar{X}_w$ extracted from all voids.

Figure 5.14 (g) shows the effect sizes $\bar{X}_w$ of $\nu_{\mathrm{Rb}}^{\mathrm{void}}/\nu_{\mathrm{Rb}}^{\mathrm{bulk}}$ and $\eta_{\mathrm{XCE}}^{\mathrm{void}}/\eta_{\mathrm{XCE}}^{\mathrm{bulk}}$ for all four cells. It evidences that the Rb concentration is significantly higher in the areas declared as voids compared to the bulk areas, while the charge-collection efficiency is inhibited.

We have established the increased presence of Rb at material-deficit areas before already and can now quantify this increase to be on the order of 10%. Note that there is no systematic trend of the Rb effect size visible. In contrast, the effect size of the charge-collection efficiency decreases with increasing $X_{\mathrm{GGI}}^{\mathrm{Nom}}$. For the cell with the lowest $X_{\mathrm{GGI}}^{\mathrm{Nom}}$, the effect size of the charge-collection efficiency is close to the equilibrium. This means that voids do not significantly underperform, most likely due to the efficient Rb passivation. Towards higher $X_{\mathrm{GGI}}^{\mathrm{Nom}}$, the charge-collection efficiency at voids decreases relative to the surrounding areas despite of comparable total Rb concentration (c.f. Fig. 5.5) and Rb segregation towards voids. This observation further corroborates the hypothesis of higher $X_{\mathrm{GGI}}^{\mathrm{Nom}}$ leading to increased severity of nanoscale defects that cannot be entirely mitigated by Rb passivation and deteriorate the macroscopic solar-cell performance.

5.3.5 Discussion

The experimental evidence for a negative correlation between performance and the GGI ratio is clear–both at the macro- and the microscale. However, we can only hypothesize about the underlying reasons. From literature it is known that Cu(In,Ga)Se_2 solar cells with $X_{\mathrm{GGI}} > 0.5$ form a deep defect in the bandgap [234,235], which merges with the conduction band for smaller GGI values. This state is associated with a Ga_{Cu} defect [234–236]. While the cells in this study were deposited with nominal GGI ratios below the threshold of 0.5, we consider the presence of locally enhanced GGI ratios likely, and the probability of such high-GGI spots should increase with the overall GGI. Accordingly, we expect an enhanced density of deep Ga_{Cu} defects for high-GGI solar cells, whereas shallow V_{Cu} defects dominate for low-GGI cells. The ineffectiveness of Rb to passivate Ga_{Cu} defects explains the observed diminished passivation efficiency of Rb in solar cells with high GGI. The experimental confirmation of this hypothesis would require 3D measurements with great sensitivity to the local GGI, which is beyond the scope of this study.

5.4 Conclusion

The compositional in-plane inhomogeneities of four Cu(In,Ga)Se_2 solar cells with different GGI were measured and correlated with their nanoscale performance. In all samples, we observed lateral inhomogeneities in thickness, Rb concentration, GGI, and charge-collection efficiency. Areas with material deficits corresponding to grain boundaries, crevices, or voids exhibit Rb as well as Ga enrichment along with charge-collection efficiency impairment.

We found that cells with an In-rich absorber outperform cells with a Ga-rich absorber both at the macro- and microscale and could establish distinct defect patterns: for low GGI, defects were comparably homogeneously distributed with limited impact on performance; in contrast, cells with high GGI unveiled concentrated defect clusters with a significantly stronger detrimental impact on the charge-collection efficiency. Investigating further the decreasing charge-collection efficiency with increasing GGI with a meta-analysis, we could corroborate the hypothesis that the Rb passivation of electronically more detrimental nanoscale defects is insufficient for cells with high X_{GGI}. This is in accordance with the evolution of deep $\mathrm{Ga_{Cu}}$ defect states that become more severe for absorber compositions with high GGI.

Altogether, these measurements show a consistent picture linking the macroscopic solar-cell performance to nanoscopic features. Specifically, we could demonstrate that Cu(In,Ga)Se_2 solar cells with a Ga-rich absorber suffer from severe electronic-defect clusters that are related to inefficient passivation of areas with material deficits.

6 X-ray optical analysis of the Cs impact on mixed triple-cation perovskite

This chapter presents a study on a perovskite solar cell (PSC) series, which is covered in Ref. 4. Parts of the manuscript were already presented in Sec. 3 as theoretical background and in Sec. 3.2.5.

Inhomogeneously thick absorber layers can emerge if the mixed-halide perovskites contain Cs on the cation site. For these layers differences in electrical and optical performance have been observed between thick and thin areas. We employed multi-modal scanning X-ray microscopy methods to correlate optical and electrical performance with the composition and topology of the absorber. By correlating the XBIC and the XRF point-by-point, we were able to rule out a compositional cause for electrically under-performing areas. Therefore, we assessed the spatial variation of the optical performance with a new XEOL setup in the temporal- and spectral-domain. We observed segregation of Br to thin absorber areas, which lead to a bandgap widening of roughly 20 meV in these regions. Along with the wider bandgap, we observed a shorter charge-carrier lifetime in areas with a thin absorber, which may indicate either enhanced bulk defect concentrations or surface recombination.

6.1 Introduction

Triple-cation metal-halide perovskites are promising semiconductors for solar cell applications [237] and have significantly improved stability compared to early-stage metal-halide perovskites [238–240]. Density functional theory calculations of Kim et al. [240] revealed that, while mixing Br on the halide side of $FAPbI_3$ (FA: formamidinium) is most effective in the crystallographic stabilization in favor of α-phase perovskite, the bandgap widening diminishes the effectiveness. Therefore, methylammonium

(MA) should be introduced to the cation site to reduce the amount of necessary Br. Adding Cs results in only a minor contribution to stabilizing the α-phase but dramatically increases the chemical stability of $FAPbI_3$ [240]. Furthermore, Hu et al. [241] showed that adding Cs reduces the trap density and charge recombination rates. Promising results were shown by Peng et al. [242] who have created mixed PSCs with an absorber composition of $Cs_{0.05}FA_{0.88}MA_{0.07}PbI_{2.56}Br_{0.44}$ and a record efficiency of 23.17%. However, an increase in Cs can greatly influence the morphology of the resulting TF and leads to the formation of wrinkles [243–246]. We will henceforth refer to thicker absorber areas as "mountains" and thinner absorber areas as "valleys". The underlying reason for the wrinkling is generally associated with a relief of compressive strain [244, 246]. The optical performance of the PSC is usually evaluated with photoluminescence measurements which revealed that the bandgap is not homogeneous throughout the wrinkled layer. It was shown that a bandgap narrowing at mountains [244] or a bandgap widening at mountains [245] is possible. There are three possible causes for this inhomogeneous photoluminescence (PL). First, a compositional inhomogeneity: An absorber with a higher content in Br and Cs would exhibit a wider bandgap. Therefore, if the mountains and valleys would exhibit a different composition the corresponding change in the bandgap could be explained. This has been observed in the work of Bercegol et al. [245] where an increase in Cs has been found in the mountain along with the bandgap widening. Second, lattice strain: Braunger et al. [244] found no compositional variation between mountain and valley, but observed systematically larger grains in the mountains. They associated their observed narrowing of the bandgap at the mountains with findings from D'Innocenzo et al. [247] where higher lattice strain observed in smaller crystals led to a wider bandgap. Third, re-absorption effects: As the mountains are much thicker than the valleys, PL photons have a greater chance to be re-absorbed and emitted. This would shift the peak energy of the spectrally resolved PL spectrum to lower energies and the interpretation of the peak energy as the bandgap energy would be compromised [88, 170, 181, 182].

As the composition [245] as well as the preparation method [244] impact the possible formation of the wrinkles, a large parameter space is given and each system has to be evaluated individually.

The studies mentioned above were challenged by the need to use different probes for the evaluation of the performance (VIS-NIR photons), composition (electrons), and grain structure (X-rays). As electrons are surface sensitive, while the visible or near-infrared laser photons and especially the X-rays have a deeper penetration depth,

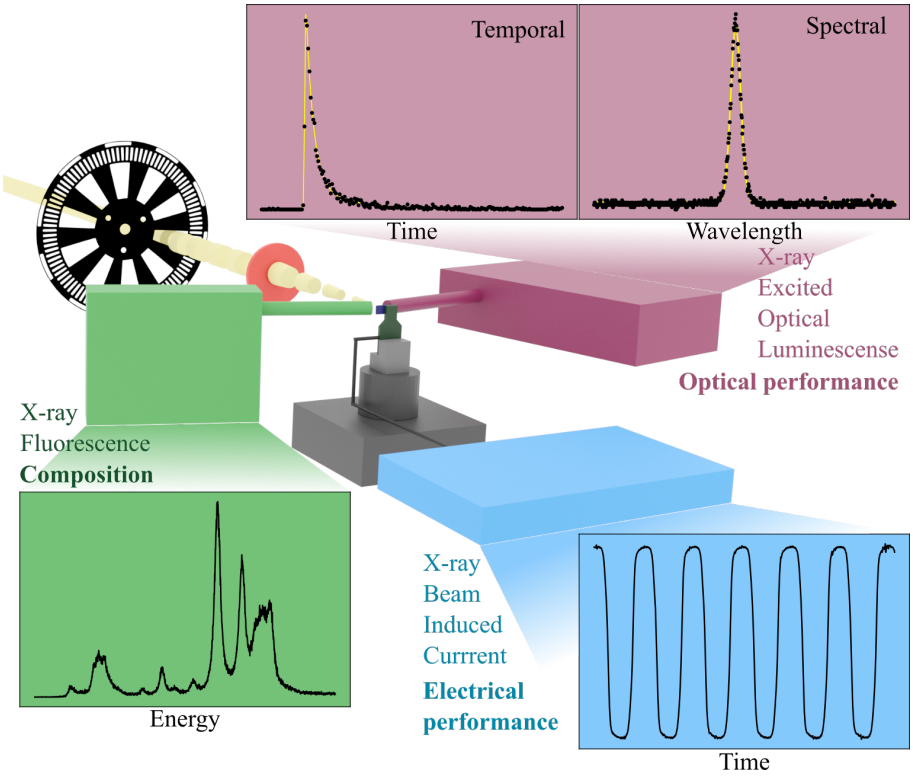

Figure 6.1: Employed modalities in this work: X-ray fluorescence, X-ray beam induced current with lock-in amplification, temporally and spectrally resolved X-ray excited optical luminescence.

their respective beam-sample interaction volumes are not comparable. Therefore, a direct link between local optical performance and composition or grain structure could not yet be established.

Here, we combined for the first time X-ray-based measurement techniques to elucidate the local relation between topology (mountain vs. valley), composition, and performance of PSCs. For the composition evaluation, we used XRF instead of electron dispersive spectroscopy (EDS). The advantage of XRF over electron or ion-based methods is the ability to measure the full depth of the solar cell in a non-destructive fashion. The electrical performance of the solar cell was evaluated with lock-in amplified XBIC measurements [1, 27, 43] instead of a laser-based LBIC measurements. For the evaluation of the local optical performance, we implemented for the first time the novel XEOL detection unit, introduced in Sec. 3.2.5, to directly resolve the XEOL [2, 26, 106] in the spectral and the temporal domain, instead of using classical PL measurements. An illustration of the measurement setup is shown in Fig. 6.1.

By using high-energy X-rays, we were able to penetrate a full solar-cell stack and

map the sample response to the modalities with sub-micrometer resolution. The tuneable X-ray beam energy at synchrotron beamlines allowed us to choose the excitation energy so that we were highly sensitive to the elements of interest.

The problem of degradation of the sample between and during measurements can be mitigated with this simultaneous assessment, where the modalities evaluate the sample in the same state and environment. The same probe for all modalities further ensures that the sampled spot is identical, and we can directly link composition and performance on a point-by-point basis.

6.2 Experimental setup

6.2.1 Samples

The samples were provided by KAUST and processed as follows: For PSC fabrication, indium tin oxide (ITO)-covered glass (15 Ω/sq, XinYan Technologies) substrates were sonicated in water-acetone-IPA (isopropyl alcohol) baths, prior to a 10-minute UV-Ozone treatment to clean the surface. The NiO_x hole transport layer (HTL) (20 nm) was deposited via RF magnetron sputtering following a well-established procedure [248]. The perovskite layer (ca. 500 nm) was deposited under nitrogen atmosphere via spin-coating of perovskite solutions of $Cs_xMA_{0.15}FA_{0.85\text{-}x}Pb(I_{0.8},Br_{0.2})_3$ (1 M) in a co-solvent of dimethyl formamide (DMF)/dimethyl sulfoxide (DMSO) (4/1:v/v). Here, a two-step spin-coating process with 2000 rpm for 10 s and 5000 rpm for 30 s was used. During the second step on the 10^{th} second, 300 µL of chlorobenzene were dropped as an antisolvent. The films were subsequently annealed at 100 °C for 25 min. The C_{60} electron transport layer (ETL) (20 nm, nano-C), 5 nm of bathocuproine (BCP, Sigma-Aldrich), and 100 nm silver contacts were deposited via thermal evaporation (Angstrom Engineering) within the same deposition chamber, as reported previously [249].

6.2.2 Experimental settings

The measurements were conducted at the micro-imaging beamline P06 at DESY, Germany. A removable optical chopper (Thorlabs), for lock-in amplification (UHFLI, Zurich Instruments), running at 813 Hz was installed upstream of the focusing optics (Be-CRLs (compound refractive lenses) [136], a phase plate and a 400 µm pinhole).

The beam energy was set to 13.5 keV and the coherent part of the beam was focused down to a FWHM of 100 nm×96 nm. The sample surface was oriented perpendicular to the beam path to minimize the footprint. The XEOL detector was angled to the sample at 10° without blocking the beam. A fluorescence detector (VortexME4) was situated opposite the XEOL detector with an angle of 47.6° to the sample surface. The sample was mounted and contacted on a printed circuit board, fastened to a kinematic mount (Thorlabs), as described in Sec. 3.2.4.

6.2.3 Measurement settings

For the XBIC and XEOL measurements, the beam was attenuated to only 1% of the full beam, while XRF measurements were conducted at full beam intensity. All overview maps were measured in 1 µm steps, with a dwell time of 25 ms. The XEOL maps were measured in 400 nm steps with a dwell time of 1.1 s. The XRF maps were measured in 200 nm steps with a dwell time of 0.3 s.

6.2.4 XRF analysis

The XRF fitting was done with PyMca [159]. The channels of the VortexME4 were fitted individually and summed after the fitting.

6.3 Results and discussion

6.3.1 Impact of Cs on the wrinkling periodicity

To study the impact of Cs, we prepared three samples with varying Cs content. The perovskite mixture of the samples was $Cs_xMA_{0.15}FA_{0.85-x}Pb(I_{0.8},Br_{0.2})_3$, with x being 0.05, 0.15, and 0.25. We henceforth refer to the three samples as Cs05, Cs15, and Cs25, respectively.

For an overview of the samples, we first assessed the composition and electrical performance with XRF and XBIC measurements, respectively. The beam energy was chosen as 13.5 keV, which is slightly above the Pb_{L3} edge (13.04 keV). Thus, we were very sensitive to the Pb XRF count rate Φ_{Pb}. As most of the X-rays pass through the sample, only a fraction is absorbed. Here, by using Lambert–Beer's law, a perovskite layer of 500 nm absorbs only 2% of a beam with an energy of 13.5 keV, while this

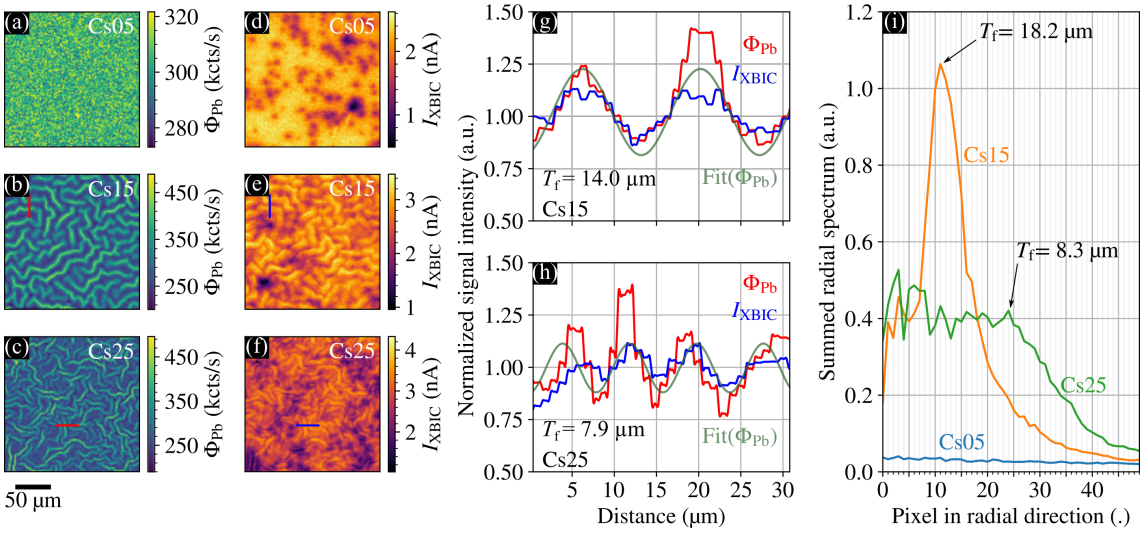

Figure 6.2: XRF signal of Pb Φ_{Pb} of (a) Cs05, (b) Cs15, (c) Cs25. XBIC signal I_{XBIC} of (d) Cs05, (e) Cs15, (f) Cs25. (g) Line plots of Cs15 as indicated in (b) (red line) and (e) (blue line) with a sine fit of Φ_{Pb} (green). (h) Line plots of Cs25 as indicated in (c) (red line) and (f) (blue line) with a sine fit of Φ_{Pb} (green). The line plots are normalized to their respective median value. (i) Radial profiles of the fast Fourier transformed of (a–c).

value is around 2.8% for a 700 nm thick perovskite. [160]. For low absorption values, a linear approximation between sample thickness and absorbed photons is justifiable, which is in accordance with the TF approximation [250]. As Pb is not directly contesting with other elements for its lattice space, the Φ_{Pb} count rate gives thus a good measure of the absorber topology. Figure 6.2 shows the distribution of Φ_{Pb} (a–c) together with the electrical performance as XBIC signal I_{XBIC} (d–f). The wrinkle structures of Cs15 and Cs25 are visible in the Φ_{Pb} distribution as well as in the I_{XBIC} signal. Areas of drastically lower performance are present in the I_{XBIC} maps (Fig. 6.2(d–f)). However, we could not find corresponding variations in the XRF signals of the absorber elements, as can be seen in Fig. 6.3–Fig. 6.5, which show the respective elemental distribution maps.

Thus, we speculate that pinholes of the size of only a few nanometers are responsible for the underperforming areas instead of spatially extended inorganic inhomogeneities in the absorber layer.

The overall XBIC signal shows the same wrinkling structure as the Φ_{Pb} count rate, as it is inherently dependent on the beam-sample interaction volume. For XBIC, a linear relationship between the number of absorbed photons and the XBIC signal strength is usually assumed [186]. Therefore, we would have expected the XBIC

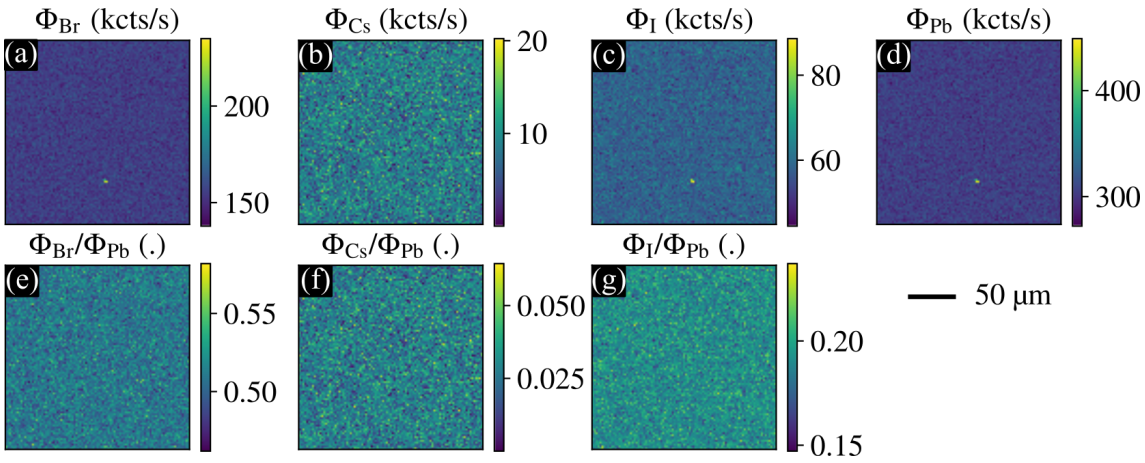

Figure 6.3: XRF signal maps and ratios of absorber elements of Cs05.

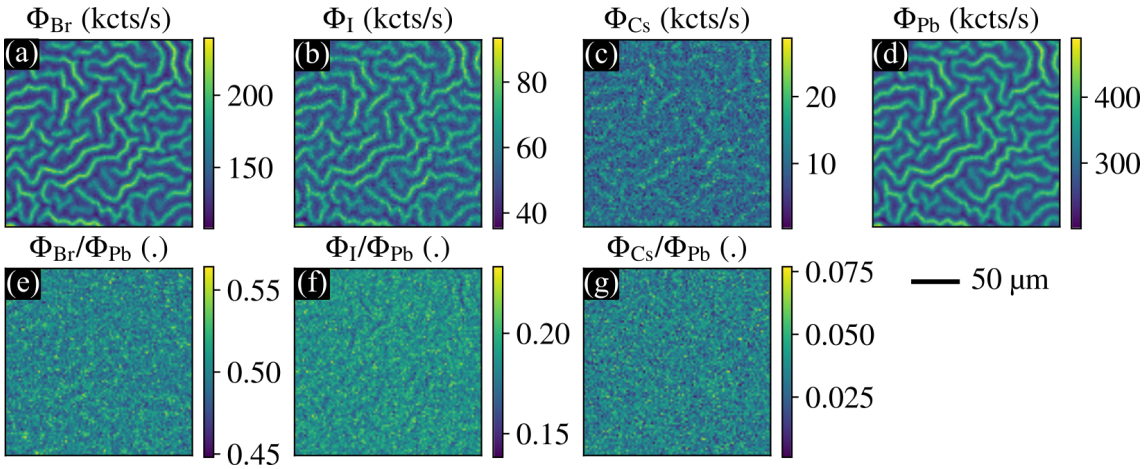

Figure 6.4: XRF signal maps and ratios of absorber elements of Cs15.

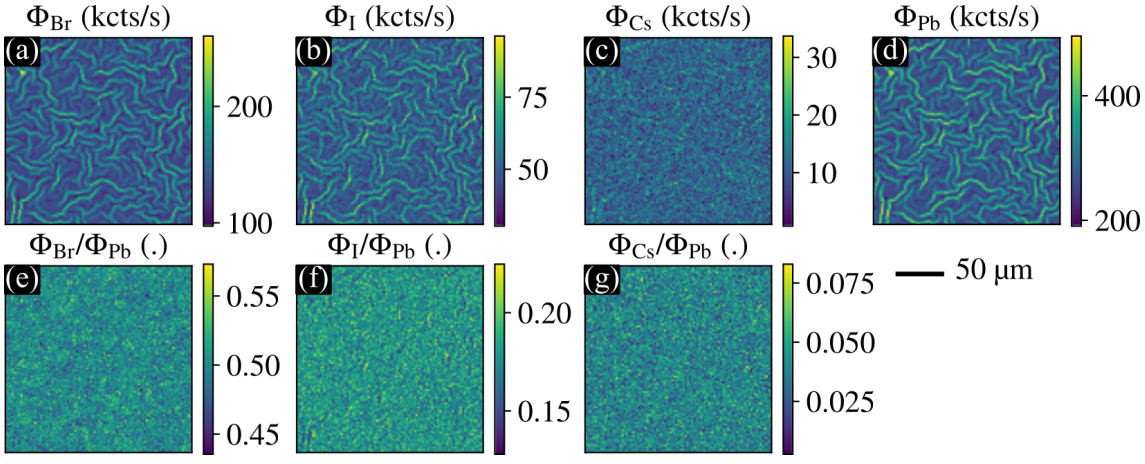

Figure 6.5: XRF signal maps and ratios of absorber elements of Cs25.

signal amplitude to relatively scale in the same way as the Φ_{Pb} count rate. However, we observed systematic non-linearity between I_{XBIC} and Φ_{Pb} comparing the maps (b,c) and (e,f) in Fig. 6.2 and the lineplots in panels (g,h). While the periodicity T_{f} of I_{XBIC} and Φ_{Pb} match, the modulation amplitude is smaller for I_{XBIC} than for Φ_{Pb}. We speculated, that this non-linearity is due to the larger beam-interaction volume for XBIC than XRF. As the $\mathrm{Pb}_{\mathrm{L3}}$ edge is close to the excitation energy, secondary excitation is unlikely which limits the generation of the Φ_{Pb} XRF signal to the direct beam-sample interaction volume. On the other hand, XBIC measures the thermalized charge carriers, which are generated after a cascading process of the initially excited high-energy electrons [106, 175]. This process increases the effective beam-sample interaction volume [163]. Additionally, XBIC is influenced by long carrier-diffusion lengths, which have been observed for similar systems on a micrometer scale [251]. Therefore, the XBIC measured at the peak would also encompass areas of the slope around it, which translates as a dampening of the amplitude in the line plot. Comparing the behavior of XBIC in Fig. 6.2(g) and (h), we noted that the delta between peak and valley of I_{XBIC} in (h) is smaller than in (g). Following the assumption of a carrier-diffusion length on the micrometer scale, we considered the influence of a different frequency of the wrinkled structure. As a first estimate, we fitted the Φ_{Pb} line plots with a sine to extract the periodicity. For Cs15, this amounted to a period T_{f} of 14 µm and for Cs25 to a T_{f} of 7.9 µm. Due to the smaller periods, the spots at the bottom of the valley and at the peak were heavily influenced by the surrounding slopes and the weight of their respectively lesser or greater beam-interaction-volume was mitigated.

To analyze the periodicity of the wrinkles over the whole map, it was quantified in Fig. 6.2(i) through the azimuthally integrated radial profile of the fast-Fourier transform of the Φ_{Pb} maps. As expected, we did not see a prominent frequency in Cs05 as the mapped area had no distinct features. For Cs15 this analysis unveiled a characteristic frequency with a wrinkle period of $T_{\mathrm{f}} = 18.2$ µm. While Cs15 had a clear peak frequency, Cs25 had rather a threshold of prominent frequencies where the smallest was highlighted in Fig. 6.2(i) with a T_{f} of 8.3 µm. This was close to the frequency obtained through the line plot fit in Fig. 6.2(h). The frequencies belonging to larger periods can be explained when two parallel running wrinkles were interpreted as one unit.

The evaluation of the electrical performance showed that drastically underperforming areas were not linked to compositional inhomogeneities nor that the underperformance in localized areas was a direct cause of the wrinkles.

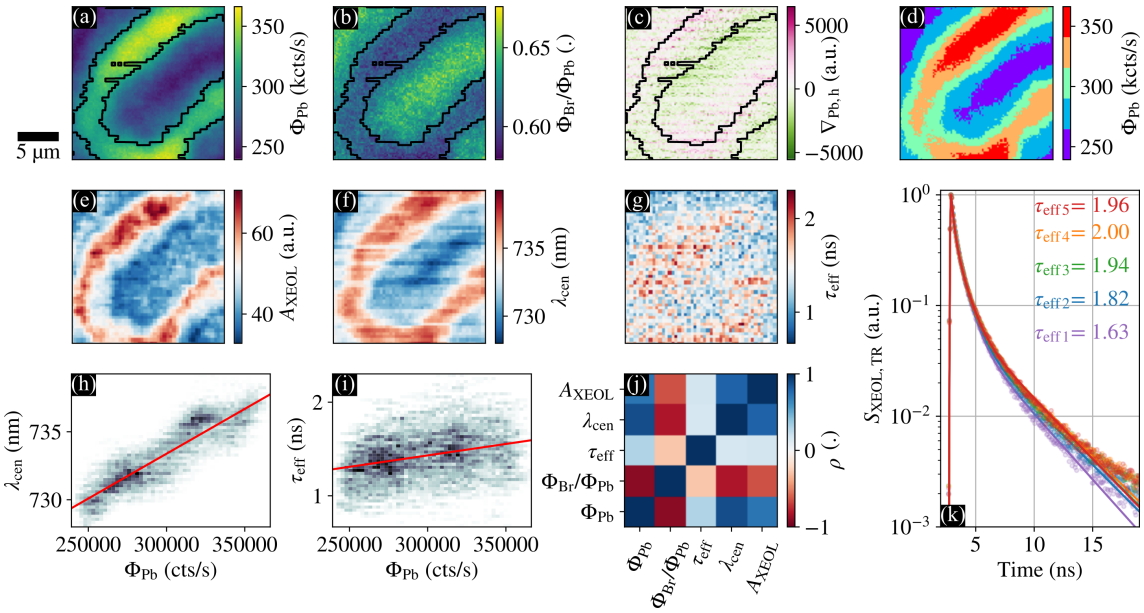

Figure 6.6: XRF and XEOL analysis of Cs15. (a) XRF Φ_{Pb} signal. (b) XRF Φ_{Br} to Φ_{Pb} ratio. (c) Horizontal gradient $\nabla_{Pb,h}$ of the Φ_{Pb} map. (d) XRF Φ_{Pb} signal with different colormap from (a) to indicate the binned areas. (e) Amplitude A_{XEOL} of the spectrally resolved XEOL. (f) Central wavelength λ_{cen} of the spectrally resolved XEOL. (g) Effective lifetime τ_{eff} from a double exponential fit. (h) 2D histogram of λ_{cen} over Φ_{Pb} with a linear fit (red line). (i) 2D histogram of τ_{eff} over Φ_{Pb} with a linear fit (red line). (j) Pearson's correlation coefficients ρ. (k) Triple exponential fits of summed decay curves from the respective areas highlighted in (d).

6.3.2 Nanoscale inhomogeneities in perovskite solar cells

The overall impact of Cs on the optical performance of PSCs was observed in previous studies in the temporal and spectral domain. In temporally-resolved PL measurements, PSCs with higher Cs content exhibited longer PL lifetimes [245], which was linked to a defect passivating role of Cs [238, 241]. In spectrally-resolved PL measurements, a general blue shift of the peak wavelength was observed, which corresponds to a bandgap widening [238, 252–254]. In the following, we will discuss the spatially-resolved optical performance of Cs15.

In Fig. 6.6(a) Φ_{Pb} distribution is shown, which reflects the thickness of the absorber. A horseshoe-like wrinkle structure is visible. The ratio of the XRF Br count rate Φ_{Br} to Φ_{Pb} is shown in Fig. 6.6(b) and exhibits the same horseshoe-like feature with an opposite trend. If the absorber matrix was homogeneous over the raster scanned area, the ratio of Φ_{Br} to Φ_{Pb} should not have shown any features. Furthermore, as both the Pb_{L3} absorption edge and Br_K absorption edges are above 10 keV, self-absorption

effects are not strong enough to explain these variations in their ratio. Therefore, we concluded that we indeed have a Br-richer area in the valleys, while the mountains should have a higher I content. This demixing of Br and I is a known phenomenon for perovskites [251, 255]. With our raster scanned XEOL maps — the amplitude A_{XEOL} shown in Fig. 6.6 (e), the central wavelength λ_{cen} shown in (f) — we see that the central wavelength of PL spectra is red-shifted at the mountains compared to the valleys. In Fig. 6.6(f) we observed a difference of 10 nm in λ_{cen} over the scanned area indicating a bandgap narrowing of ∼20 meV from valley to mountain. This is similar to the results by Braunger et al. [244], however, here we could directly link the red-shift with the segregation of Br and I, observed in (b), while they found no compositional change. To verify our statement we have overlaid a contour of $\lambda_{\mathrm{cen}} =$ 734 nm from (f) to (a–c). The contour clearly places the red-shifted signal in the thicker absorber area (a) and the blue-shifted signal in the Br-poor region (b). We excluded photon recycling by re-absorption as the driving force behind the red shift in this study, as one would observe a stronger red shift at the side of the mountain facing away from the XEOL detector. To illustrate the orientation of the absorber surface to the detector that approaches from the left side, Fig. 6.6(c) highlights the gradient of (a) in the horizontal direction, where positive values indicate that the slope is facing toward the detector, and negative values indicate an away facing slope. Comparing the contour with the positive and negative gradient it became apparent that the away-facing areas did not have a significantly higher red shift in XEOL. The clear correlation between λ_{cen} and the absorber composition and topology is highlighted and further corroborated in Fig. 6.6(h), where λ_{cen} and Φ_{Pb} are plotted.

While the spectral shift, in this case, was not significantly disturbed by the geometrical arrangement of the detector to the sample surface, it did have an effect on the number of XEOL photons collected as can be seen in Fig. 6.6(e). Despite the objective having a large aperture, thus a large solid angle to collect photons, the amount of photons that can be collected is diminished in the case that the solid angle of emission is oriented in a different direction thus reducing the overlap. Therefore, the expected increased signal due to a larger beam-sample interaction volume at regions of high Φ_{Pb}, is not the only influence on the XEOL amplitude A_{XEOL}. If these geometrical and topological influences were perfectly accounted for, the XEOL amplitude A_{XEOL} would be a good indicator for the electronic quality of the cell, as a good solar cell is also a good emitter [195], due to fewer trap-states promoting non-radiative recombination being present.

An overview of the correlations is shown in Figure 6.6(j) as Pearson's correlation coefficient ρ. Here, 1 stands for perfectly positively correlated, 0 for uncorrelated and -1 for perfectly anti-correlated. The strong anti-correlation between the central wavelength λ_{cen} and the Φ_{Br} to Φ_{Pb} ratio is evident, while the slightly weaker correlation of the amplitude A_{XEOL} is explained by geometrical concerns.

The effective lifetime, as defined by Eq. 3.23, τ_{eff} shown in Fig. 6.6(g) was determined from double-exponential fits. We saw a longer effective lifetime for thicker areas of the absorber. As the map is quite noisy we have binned thicker and thinner areas into five equally distributed parts (Fig. 6.6(d)) and fitted the averaged and normalized decay curves with a triple-exponential fit, which is shown in Fig. 6.6(k). The effective lifetimes from these fits, corroborated the impression of longer lifetimes for thicker absorber areas as highlighted in Fig. 6.6(i) where τ_{eff} and Φ_{Pb} are plotted and (j) where τ_{eff} shows a positive correlation with Φ_{Pb}.

This increase in the effective lifetime might be due to a diffusion of charge carriers to the narrower bandgap at the mountains. Thus, when we probe the valley area, carriers would diffuse out of our detection spot, which reduces the measured lifetime. Consequently, carriers that had been excited at the mountainsides could first diffuse away and later be drawn back to the narrow bandgap, thus increasing the measured lifetime. Carrier funneling effects in perovskites have already been observed by Frohna et al. [251]. On the other hand, a reduced number of defects in the mountains, due to the passivating effect of Cs [241, 245] could also be a cause for an increase in lifetime. This would be in accordance with previous findings [244–246].

Comparing the three PSCs in their optical performance we could corroborate the trends of an increase in the effective lifetime and blue shift of the spectrum with higher Cs content. In Fig. 6.7(a) the effective lifetimes are plotted as violin plots. The width of the violin is a histogram of the lifetimes (τ_{eff}, vertical axis). We observed a clear increase in the effective lifetime from Cs05 to Cs15 by comparing the distributions of the three cells, while the distribution of effective lifetimes for Cs25 was broader and no obvious trend can be observed. Fig. 6.7(b) similarly displays violin plots of histograms of the distributions of the central wavelengths (λ_{cen}) of the spectrally resolved XEOL. We clearly observed the blue-shifting effect of Cs as well as an increasing spread in the distribution. The average peak-position of the Gaussian fit over the whole map was 739 nm for Cs05, 733 nm for Cs15 and 722 nm for Cs25, showing the same trend of roughly 10 nm in blue-shift per 10% of Cs as noted in the literature [238, 252–254]. The red-side end of the distribution only

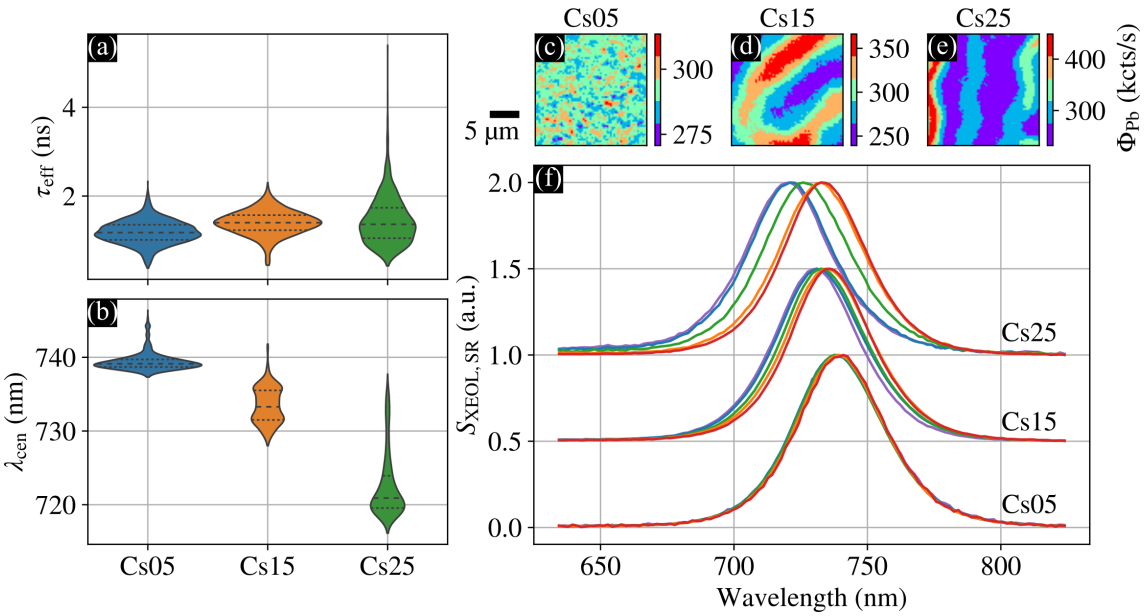

Figure 6.7: Comparing the optical performance of the three PSCs Cs05, Cs15, and Cs25. (a) Distribution of the effective lifetimes as violin plots, the dashed lines indicate the 25th, 50th, and 75th percentile. (b) Distribution of the central wavelength as violin plots, the dashed lines indicate the 25th, 50th, and 75th percentile. (c) Φ_{Pb} count rate of Cs05. (d) Φ_{Pb} count rate of Cs15. (e) Φ_{Pb} count rate of Cs25. (f) Area averaged XEOL spectra corresponding to the colored areas in (c–e) respectively.

shifts less than 10 nm while the bulk of the distribution shifts almost 20 nm. The spectral shift in correlation to the thickness of the absorber is further highlighted in Fig. 6.7(c–f). The maps indicate the respectively binned areas based on the Φ_{Pb} maps and Fig. 6.7(f) shows the corresponding averaged spectra. Here, it seemed that the red-side edge was almost not shifted at all, while the blue side was shifting stronger for higher Cs containing PSCs. This non-intuitive 'pinning' of the red side could be explained as the increase in I inside of the wrinkle countering the blue shift induced by higher Cs content. Additionally, the valley areas had a cumulative effect of increased Cs and Br content, both of which are responsible for blue-shifting the spectrum [256].

6.4 Conclusion

We spatially resolved the wrinkled structure of PSCs containing higher amounts of Cs (Cs15, Cs25) using our multi-modal hard X-ray scanning microscopy setup. The increased frequency of the wrinkles in Cs25 compared to Cs15 was assumed

to have a mitigating effect on the variation of the local electrical performance, as the diffusion length of the carriers seemed to be large. Regarding the analysis of areas demonstrating drastic electrical underperformance, we speculate on pinholes instead of compositional inhomogeneities in the perovskite absorber as the cause of the underperformance. The XEOL analysis of the three cells allowed us to confirm the overall blue-shifting effect of Cs. Our multi-modal approach allowed us to identify the segregation of I and Br to thick and thin absorber areas respectively, which we identified as the primary cause for the bandgap narrowing in the mountains and bandgap widening in the valleys.

With these findings, a major advantage of XEOL over classical PL was demonstrated, namely that by performing multi-modal, simultaneous XEOL and XRF measurements, the optical performance was directly linked with the composition, eliminating the disadvantages of separate measurements.

Conducting XEOL instead of classical PL measurements, gave rise to new constraints and considerations. We were generally limited by low count rates, due to our small beam-sample interaction volume, low absorption cross-section, and considerations to beam damage. Therefore, our setup was designed to have an objective with a large numerical aperture to collect as many photons as possible while not interfering with the other detectors. Additionally, the detection units for the temporal and spatial resolution were implemented separately to get the highest signal-to-noise ratio possible. Other raster scanning XEOL setups operating with nanoscale resolution, such as at the hard X-ray nanoprobe 23A in Taiwan [112], or at ID16B at the ESRF [124], use a fiber-coupled system and streak cameras to measure spectrally and temporally resolved XEOL simultaneously. While these setups allow a convenient measurement, their indirect beam path and lower-EQE detectors lead to a worse signal-to-noise ratio than our setup.

We can envision further experiments encompassing more modalities by demonstrating the multi-modal compatibility of our setup in this study. A first logical extension would be the inclusion of X-ray diffraction, to verify the impact of inhomogeneous lattice spacing on the optical performance. However, the randomly oriented nature of the grains in the absorber will only allow the measurement of those few grains which coincidentally fulfill the Bragg condition. With the introduction of 4^{th} generation synchrotrons, ptychography appears as a feasible addition to our multi-modal suite as the demand for a coherent beam would no longer limit the photon flux.

7 Conclusions & outlook

7.1 Conclusions

Using synchrotron-based hard X-ray multi-modal scanning microscopy, we were able to characterize full stacks of Cu(In,Ga)Se_2 [2, 3] and perovskite [4] TF solar cells.

For the characterization, we showcased how to apply lock-in amplification to XBIC measurements, to extract small current signals from the noisy background and when the cell is electrically biased [1]. Furthermore, we expanded the measurement environment at P06 by designing an XEOL detection unit [2, 4] that allowed us to measure temporally and spectrally resolved XEOL. In a proof-of-principle measurement, we were able to combine the four modalities XBIC, XRF, XEOL, and ptychography for the characterization of a Cu(In,Ga)Se_2 solar cell. The advantages of simultaneous (sample in the same state, direct correlation, time efficient) and sequential (optimal scanning parameters) measurements were discussed and compared. In-depth studies were conducted on two solar cell series.

We studied the impact of different Ga to In ratios on Cu(In,Ga)Se_2 solar cells by analyzing a series with XRF and XBIC. Additionally, we adapted the concept of a meta-analysis to elucidate the role of Rb as a defect-mitigating agent and discovered that cells with higher Ga content were prone to more severe defect sites where the passivating effect of Rb is reduced [3].

PSCs were studied in regards to their tendency to exhibit a wrinkling structure when Cs is added at the cation site. We were able to elucidate their inhomogeneous performance, electrically via XBIC and optically via XEOL. By correlating their local performance with the composition from XRF measurements, we were able to rule out a compositional cause for electrically sub-performing areas, but we could directly link segregation of Br and I rich areas to variations of the optical performance [4].

With the hard X-ray beam being able to fully penetrate a solar cell stack and exploiting the multitude of measurement modalities, we were able to gain a more

comprehensive picture of the devices. All in all, this work shows the feasibility and advantages of synchrotron-based multi-modal X-ray scanning microscopy measurements for solar cell characterization.

7.2 Outlook

The advantages of multi-modal X-ray scanning microscopy measurements are evident and can further be seen in the high number of already existing beamlines [6, 54–57, 107–113]. These beamlines are steadily improved and adapted to research needs [2, 6, 116, 117, 122]. With the upgrade of the synchrotron sources to the fourth generation, new measurement schemes will become feasible opening not only the door to routinely conducted 3D but even 4D measurements [60]. The higher brilliance and pulsed structure of fourth-generation synchrotron sources [35, 36] will allow high throughput with spatial and temporal resolution.

For the analysis of solar cells, the works of Fevola et al. [151, 257] illuminate the necessity of 3D measurements to fully elucidate the absorber topology. Uncertainties concerning the cause of the inhomogeneous optical performance of perovskites [240, 244, 245] are a prime example, where a five-fold multi-modal measurement would be of great interest. The simultaneous assessment of composition, crystallographic properties, electronic density, as well as electrical and optical performance in a 3D fashion would be able to pinpoint the contributions of the individual variations to the performance. This "Dream Experiment" is illustrated in Fig. 7.1 and would only be possible at fourth-generation synchrotrons, as they have the capability to offer a highly coherent and brilliant beam so that we would not be flux-limited. Taking it even a step further, the inclusion of heating [258] or cooling environments [117] would open the door to in-situ studies.

7.2.1 XEOL setup

The XEOL setup presented in Sec. 3.2.5 is further under development and the integration of an IR-CCD camera (Princeton, Nirvana 640) is one of the improvements. Currently, it is used with a laser excitation source but due to its portable nature, nothing prevents its application in new X-ray beamtime experiments. Experiments based on pump-probe schemes using this setup are one further aspect that is interesting for future endeavors and would extend the measurement modality in another

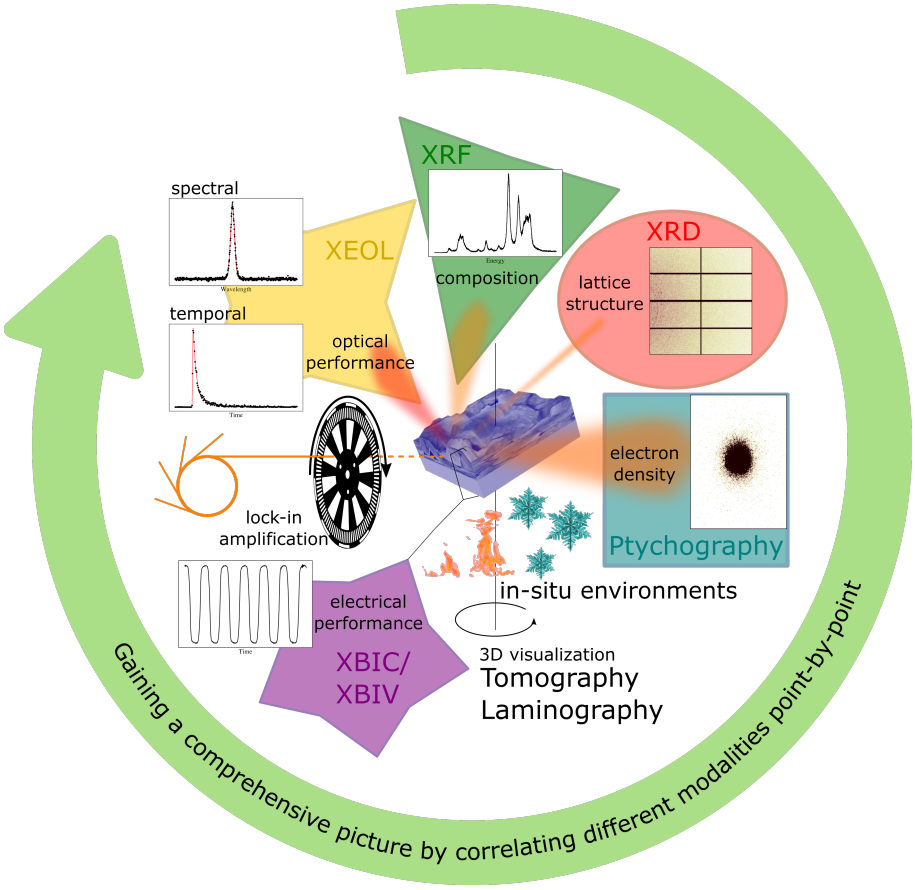

Figure 7.1: A dream experiment, where the optoelectronic performance, the composition, the lattice structure, and the electron density can be simultaneously assessed in 3D with the option to set the sample in a heating or cooling environment. When all these can be assessed together, a comprehensive picture of the sample can be gained.

dimension.

7.2.2 Scanning laser microscope

In analogy to the XEOL setup presented in Sec. 3.2.5, we have started to develop a scanning laser microscope (SLM) which is the focus of the Ph.D. thesis of Jackson Barp. The setup utilizes two vertically stacked layers: the laser source in the lower layer and the detection unit on the top layer. Figure 7.2 schematically shows the beam and signal path of the SLM setup (a) and a CAD drawing of the setup with the box (b). The microscope is situated in a black box to eliminate light pollution. The setup will encompass temporally and spectrally resolved PL detection units as well as lock-in amplification for LBIC measurements. This allows the characterization of

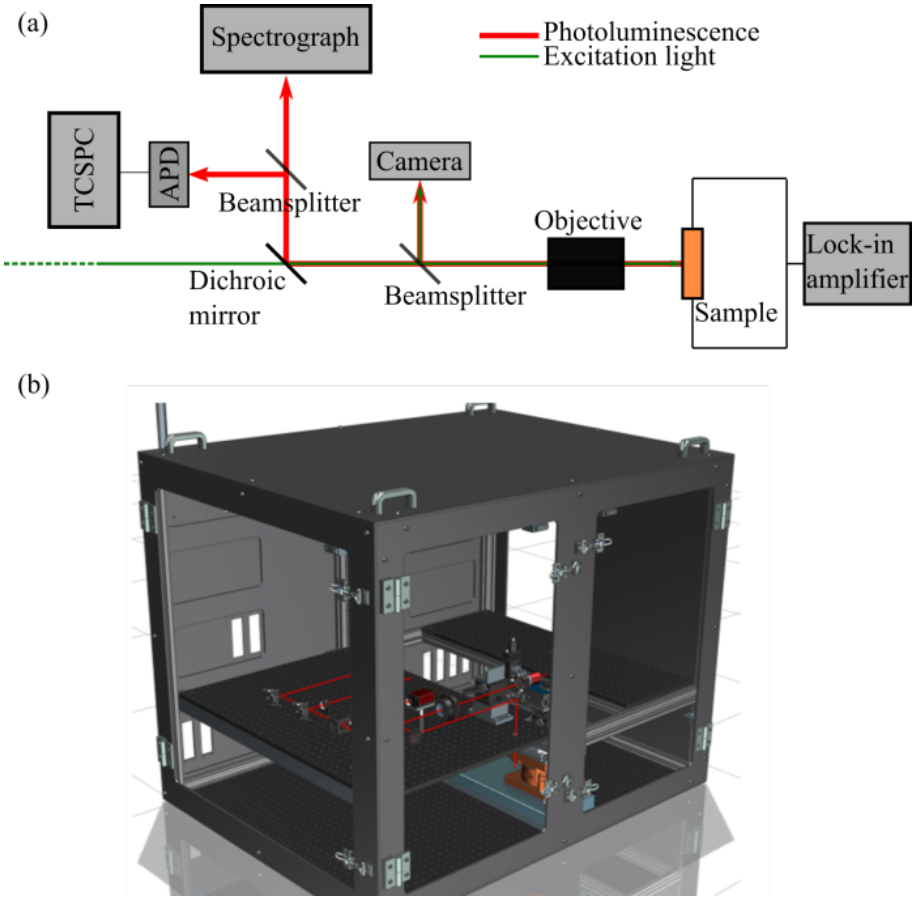

Figure 7.2: (a) Scheme of the signal pathway of the scanning laser microscope. (b) CAD drawing of the scanning laser microscope, courtesy of FS-Petra-Engineering.

solar cells before and after a beamtime for an optimization of the characterization scheme. Furthermore, it offers a testbed to experiment with setup geometries and settings to optimize XEOL and XBIC/XBIV measurements for the requirements at the beamline.

7.2.3 Laboratory-based XBIC for industrial samples

With a laboratory-based X-ray source (Viscom-XT9160-TED, Mo target), an optical chopper (Thorlabs), a lock-in amplifier (Zurich Instruments, UHFLI/MFLI), and a focusing capillary (XOS, Polycapillary), it is planned to transfer XBIC measurements from synchrotron-based X-ray sources to a laboratory source for XBIC measurements targeted at industrial solar cells. First characterizations with the setup are part of the Master's thesis of Kathrin Raeker.

Bibliography

[1] C. Ossig, T. Nietzold, B. M. West, M. I. Bertoni, G. Falkenberg *et al.*, "X-ray beam induced current measurements for multi-modal x-ray microscopy of solar cells," *Journal of Visual Experiments*, vol. 150, p. e60001, 2019. doi:10.3791/60001

[2] C. Ossig, C. Strelow, J. Flügge, A. Kolditz, J. Siebels *et al.*, "Four-fold multi-modal X-ray microscopy measurements of a Cu(In,Ga)Se_2 solar cell," *Materials*, vol. 14, no. 1, p. 228, 2021. doi:10.3390/ma14010228

[3] C. Ossig, N. Pyrlik, R. Carron, G. Fevola, S. Patjens *et al.*, "X-ray vision of Cu(In,Ga)Se_2: from the Ga/In ratio to solar-cell performance," *Journal of Physics: Energy*, vol. 4, no. 4, p. 045007, oct 2022. doi:10.1088/2515-7655/ac9256

[4] C. Ossig, C. Strelow, J. Flügge, S. Patjens, J. Garrevoet *et al.*, "Novel detection scheme for temporal and spectral X-ray optical analysis: Study of triple-cation perovskites," *manuscript submitted*, 2023.

[5] M. Stuckelberger, T. Nietzold, B. M. West, T. Walker, C. Ossig *et al.*, "Challenges and opportunities with highly brilliant X-ray sources for multi-modal in-situ and operando characterization of solar cells," *Microscopy and Microanalysis*, vol. 24 (Suppl. 2), pp. 434–435, 2018. doi:10.1017/S1431927618014423

[6] A. Schropp, R. Döhrmann, S. Botta, D. Brückner, M. Kahnt *et al.*, "PtyNAMi: Ptychographic Nano-Analytical Microscope," *Journal of Applied Crystallography*, vol. 53, no. 4, pp. 957–971, 2020. doi:10.1107/S1600576720008420

[7] N. Pyrlik, C. Ossig, C. Ziska, G. Fevola, J. Garrevoet *et al.*, "Image registration in multi-modal scanning microscopy: a solar cell case study," *Proc. Photovoltaic Specialist Conference (PVSC)*, pp. 0913–0920, 2020. doi:10.1109/PVSC45281.2020.9300774

[8] C. Ziska, C. Ossig, N. Pyrlik, R. Carron, E. Avancini *et al.*, "Quantifying the elemental distribution in solar cells from X-ray fluorescence measurements with

multiple detector modules," *Proc. Photovoltaic Specialist Conference (PVSC)*, pp. 1085–1092, 2020. doi:10.1109/PVSC45281.2020.9300345

[9] G. Falkenberg, J. Hense, J. Barp, C. Ossig, N. Pyrlik *et al.*, "Comparison of XBIC and LBIC measurements of a fully encapsulated c-Si solar cell," *Proc. Photovoltaic Specialist Conference (PVSC)*, pp. 1998–2004, 2021. doi:10.1109/PVSC43889.2021.9518800

[10] T. Walker, M. E. Stuckelberger, T. Nietzold, N. Mohan-Kumar, C. Ossig *et al.*, "The nanoscale distribution of copper and its influence on charge collection in CdTe solar cells," *Nano Energy*, vol. 91, p. 106595, 2022. doi:10.1016/j.nanoen.2021.106595

[11] P. Chakrabarti, A. Wildeis, M. Hartmann, R. Brandt, R. Döhrmann *et al.*, "X-ray diffraction with micrometer spatial resolution for highly absorbing samples," *arXiv*, no. 2201.13264, 2022. doi:10.48550/arXiv.2201.13264

[12] M. De Bastiani, R. Jalmood, J. Liu, C. Ossig, A. Vlk *et al.*, "Monolithic perovskite/silicon tandems with >28% efficiency: role of silicon-surface texture on perovskite properties," *Advanced Functional Materials*, p. 2205557, 2022. doi:https://doi.org/10.1002/adfm.202205557

[13] J. P. Blewett, "Radiation losses in the induction electron accelerator," *Phys. Rev.*, vol. 69, pp. 87–95, Feb 1946. [Online]. Available: https://link.aps.org/doi/10.1103/PhysRev.69.87. doi:10.1103/PhysRev.69.87

[14] F. R. Elder, A. M. Gurewitsch, R. V. Langmuir, and H. C. Pollock, "Radiation from electrons in a synchrotron," *Phys. Rev.*, vol. 71, pp. 829–830, Jun 1947. [Online]. Available: https://link.aps.org/doi/10.1103/PhysRev.71.829.5. doi:10.1103/PhysRev.71.829.5

[15] E. Lohrmann and P. Söding, *Von schnellen Teilchen und hellem Licht: 50 Jahre Deutsches Elektronen-Synchrotron DESY*, 2nd ed., 2013.

[16] Https://lightsources.org/lightsources-of-the-world/.

[17] D. H. Bilderback, P. Elleaume, and E. Weckert, "Review of third and next generation synchrotron light sources," *Journal of Physics B: Atomic, Molecular and Optical Physics*, vol. 38, no. 9, pp. S773–S797, apr 2005. [Online]. Available: https://doi.org/10.1088/0953-4075/38/9/022. doi:10.1088/0953-4075/38/9/022

[18] C. E. Fritts, "On a new form of selenium cell, and some electrical discoveries made by its use," *American Journal of Science*, vol. s3-26, no. 156, pp. 465–472,

1883. doi:10.2475/ajs.s3-26.156.465

[19] H. Hertz, "Ueber einen einfluss des ultravioletten lichtes auf die electrische entladung," *Annalen der Physik*, vol. 267, no. 8, pp. 983–1000, 1887.

[20] A. Einstein, "Über einem die erzeugung und verwandlung des lichtes betreffenden heuristischen gesichtspunkt," *Annalen der physik*, vol. 4, 1905.

[21] D. M. Chapin, C. S. Fuller, and G. L. Pearson, "A new silicon p-n junction photocell for converting solar radiation into electrical power," *Journal of applied physics*, vol. 25, no. 5, pp. 676–677, 1954.

[22] Z. I. Alferov, V. M. Andreev, M. B. Kagan, I. I. Protasov, and V. G. Trofim, "Solar-energy converters based on p-n AlxGal-x As-GaAs heterojunctions," *Sov. Phys. - Semicond. (Engl. Transl.); (United States)*, vol. 4:12, 6 1971. [Online]. Available: https://www.osti.gov/biblio/5083845

[23] D. E. Carlson and C. R. Wronski, "Amorphous silicon solar cell," *Applied Physics Letters*, vol. 28, no. 11, pp. 671–673, 1976.

[24] National Renewable Energy Laboratory, "Champion photovoltaic module efficiency chart," https://www.nrel.gov/pv/module-efficiency.html, accessed: 2019-10-26.

[25] B. O'regan and M. Grätzel, "A low-cost, high-efficiency solar cell based on dye-sensitized colloidal TiO_2 films," *nature*, vol. 353, no. 6346, pp. 737–740, 1991.

[26] S. Emura, T. Moriga, J. Takizawa, M. Nomura, K. R. Bauchspiess *et al.*, "Optical-luminescence yield spectra produced by x-ray excitation," *Physical Review B*, vol. 47, no. 12, pp. 6918–6930, 1993.

[27] H. Hieslmair, A. A. Istratov, R. Sachdeva, and E. R. Weber, "New synchrotron-radiation based technique to study localized defects in silicon: "EBIC" with X-ray excitation," *10^{th} Workshop on Crystalline Silicon Solar Cell Materials and Processes*, pp. 162–165, 2000.

[28] E. Lombi and J. Susini, "Synchrotron-based techniques for plant and soil science: opportunities, challenges and future perspectives," *Plant Soil*, vol. 320, pp. 1–35, 2009. doi:10.1007/s11104-008-9876-x

[29] C. Lamberti, "The use of synchrotron radiation techniques in the characterization of strained semiconductor heterostructures and thin films," *Surface Science Reports*, vol. 53, no. 1, pp. 1–197, 2004.

doi:https://doi.org/10.1016/j.surfrep.2003.12.001

[30] L. Mino, E. Borfecchia, J. Segura-Ruiz, C. Giannini, G. Martinez-Criado *et al.*, "Materials characterization by synchrotron x-ray microprobes and nanoprobes," *Rev. Mod. Phys.*, vol. 90, no. 2, p. 025007, 2018. doi:10.1103/RevModPhys.90.025007

[31] Y. Zhou, H. Zhou, J. Deng, W. Cha, and Z. Cai, "Decisive structural and functional characterization of halide perovskites with synchrotron," *Matter*, vol. 2, no. 2, pp. 360–377, 2020. doi:https://doi.org/10.1016/j.matt.2019.12.027

[32] K. Janssens, M. Alfeld, G. Van der Snickt, W. De Nolf, F. Vanmeert *et al.*, "The use of synchrotron radiation for the characterization of artists' pigments and paintings," *Annual Review of Analytical Chemistry*, vol. 6, no. 1, pp. 399–425, 2013. doi:10.1146/annurev-anchem-062012-092702

[33] M. Cotte, A. Genty-Vincent, K. Janssens, and J. Susini, "Applications of synchrotron x-ray nano-probes in the field of cultural heritage," *Comptes Rendus Physique*, vol. 19, no. 7, pp. 575–588, 2018, physics and arts / Physique et arts. doi:https://doi.org/10.1016/j.crhy.2018.07.002

[34] K. Janssens and M. Cotte, *Using Synchrotron Radiation for Characterization of Cultural Heritage Materials*. Cham: Springer International Publishing, 2020, pp. 2457–2483.

[35] D. Andrault, R. Barrett, S. Bayat, P. Berkvens, J.-C. Biasci *et al.*, "The orange Book: ESRF UPGRADE PROGRAMME PHASE II (2015 - 2022)," 2019. [Online]. Available: https://doi.esrf.fr/10.15151/ESRF-DC-186715732. doi:10.15151/ESRF-DC-186715732

[36] C. G. Schroer, I. Agapov, W. Brefeld, R. Brinkmann, Y.-C. Chae *et al.*, "PETRA IV: the ultralow-emittance source project at desy," *Journal of Synchrotron Radiation*, vol. 25, no. 5, pp. 1277–1290, 2018. doi:10.1107/S1600577518008858

[37] S. Günther, P. Y. A. Reinke, Y. Fernández-García, J. Lieske, T. J. Lane *et al.*, "X-ray screening identifies active site and allosteric inhibitors of sars-cov-2 main protease," *Science*, vol. 372, no. 6542, pp. 642–646, 2021. doi:10.1126/science.abf7945

[38] International Energy Agency, "World energy outlook 2021," 2021, https://www.iea.org/reports/world-energy-outlook-2021, last accessed October 20, 2021.

[39] REN21, "Renewables 2022 global status report," 2022.

[40] International Energy Agency, "Net zero by 2050," 2021, https://www.iea.org/reports/net-zero-by-2050, last accessed July 18, 2022.

[41] S. Alizadehfanaloo, J. Garrevoet, M. Seyrich, V. Murzin, J. Becher *et al.*, "Tracking dynamic structural changes in catalysis by rapid 2D-XANES microscopy," *Journal of Synchrotron Radiation*, vol. 28, no. 5, pp. 1518–1527, Sep 2021. doi:10.1107/S1600577521007074

[42] S.-M. Bak, Z. Shadike, R. Lin, X. Yu, and X.-Q. Yang, "In situ/operando synchrotron-based x-ray techniques for lithium-ion battery research," *NPG Asia Materials*, vol. 10, pp. 563–580, 2018. doi:10.1038/s41427-018-0056-z

[43] M. Stuckelberger, B. West, T. Nietzold, B. Lai, J. M. Maser *et al.*, "Review: Engineering solar cells based on correlative X-ray microscopy," *Journal of Materials Research*, vol. 32, no. 10, pp. 1825–1854, 2017. doi:10.1557/jmr.2017.108

[44] S. Philipps and W. Warmuth, "Fraunhofer ISE: Photovoltaics report, updated: June 30, 2021," https://www.ise.fraunhofer.de/content/dam/ise/de/documents/publications/studies/Photovoltaics-Report.pdf, last accessed July 14, 2021.

[45] J. Leong and S. Deb, "Advances in the SERI/DOE program on CdS/Cu/sub 2/S and CdS/Cu-ternary photovolaic cells," *15. IEEE PV specialists conference*, 5 1981. [Online]. Available: https://www.osti.gov/biblio/6466553

[46] Y.-S. Tyan and E. A. Perez-Alburne, "Efficient thin-film CdS/CdTe solar cells," *Conf. Rec. IEEE Photovoltaic Spec. Conf.; (United States)*, 9 1982. [Online]. Available: https://www.osti.gov/biblio/5460623

[47] M. A. Green, E. D. Dunlop, J. Hohl-Ebinger, M. Yoshita, N. Kopidakis *et al.*, "Solar cell efficiency tables (version 58)," *Progress in Photovoltaics: Research and Applications*, vol. 29, pp. 657–667, 2021. doi:10.1002/pip.3444

[48] M. Jošt, L. Kegelmann, L. Korte, and S. Albrecht, "Monolithic perovskite tandem solar cells: A review of the present status and advanced characterization methods toward 30% efficiency," *Advanced Energy Materials*, vol. 10, no. 26, p. 1904102, 2020. doi:https://doi.org/10.1002/aenm.201904102

[49] M. Jošt, E. Köhnen, A. Al-Ashouri, T. Bertram, S. Tomšič *et al.*, "Perovskite/CIGS Tandem Solar Cells: From Certified 24.2% toward 30% and Beyond," *ACS Energy Letters*, vol. 7, no. XXX, pp. 1298–1307, 2022. doi:10.1021/acsenergylett.2c00274

[50] E. Avancini, D. Keller, R. Carron, Y. Arroyo-Rojas Dasilva, R. Erni *et al.*, "Voids and compositional inhomogeneities in Cu(In,Ga)Se_2 thin films: evolution during growth and impact on solar cell performance," *Science and Technology of Advanced Materials*, vol. 19, pp. 871–882, 2018.

[51] R. Carron, S. Nishiwaki, T. Feurer, R. Hertwig, E. Avancini *et al.*, "Advanced Alkali Treatments for High-Efficient Cu(In,Ga)Se_2 Solar Cells on Flexible Substrates," *Advanced Energy Materials*, vol. 9, no. 1900408, pp. 1–8, 2019.

[52] C. G. Bischak, A. B. Wong, E. Lin, D. T. Limmer, P. Yang *et al.*, "Tunable polaron distortions control the extent of halide demixing in lead halide perovskites," *The Journal of Physical Chemistry Letters*, vol. 9, no. 14, pp. 3998–4005, 2018. doi:10.1021/acs.jpclett.8b01512

[53] S. J. Yoon, M. Kuno, and P. V. Kamat, "Shift Happens. How Halide Ion Defects Influence Photoinduced Segregation in Mixed Halide Perovskites," *ACS Energy Letters*, vol. 2, no. 7, pp. 1507–1514, 2017. doi:10.1021/acsenergylett.7b00357

[54] C. G. Schroer, P. Boye, J. M. Feldkamp, J. Patommel, D. Samberg *et al.*, "Hard X-ray nanoprobe at beamline P06 at PETRA III," *Nuclear Instruments and Methods in Physics Research A*, vol. 616, pp. 93–96, 2010. doi:10.1016/j.nima.2009.10.094

[55] R. P. Winarski, M. V. Holt, V. Rose, P. Fuesz, D. Carbaugh *et al.*, "A hard x-ray nanoprobe beamline for nanoscale microscopy," *Journal of Synchrotron Radiation*, vol. 19, no. 6, pp. 1056–1060, 2012.

[56] G. Martínez-Criado, J. Villanova, R. Tucoulou, D. Salomon, J.-P. Suuronen *et al.*, "ID16B: a hard X-ray nanoprobe beamline at the ESRF for nano-analysis," *Journal of Synchrotron Radiation*, vol. 23, pp. 344–352, 2016.

[57] E. Nazaretski, H. Yan, K. Lauer, N. Bouet, X. Huang *et al.*, "Design and performance of an X-ray scanning microscope at the Hard X-ray Nanoprobe beamline of NSLS-II," *Journal of Synchrotron Radiation*, vol. 24, no. 6, pp. 1113–1119, 2017.

[58] B. West, M. Stuckelberger, A. Jeffries, S. Gangam, B. Lai *et al.*, "X-ray fluorescence at nanoscale resolution for multicomponent layered structures: a solar cell case study," *Journal of Synchrotron Radiation*, vol. 24, pp. 288–295, 2017. doi:10.1107/S1600577516015721

[59] M. Kodur, R. E. Kumar, Y. Luo, D. N. Cakan, X. Li *et al.*, "X-ray microscopy

of halide perovskites: Techniques, applications, and prospects," *Advanced Energy Materials*, p. 1903170, 2020. doi:10.1002/aenm.201903170

[60] M. E. Stuckelberger, "Multimodal scanning x-ray microscopy at nanoprobe endstations of fourth-generation synchrotrons," *Spectroscopy*, vol. 34, no. 7, pp. 42–44, 2019. doi:10.3204/PUBDB-2019-02971

[61] B. West, M. Stuckelberger, H. Guthrey, L. Chen, B. Lai *et al.*, "Grain engineering: How nanoscale inhomogeneities can control charge collection in solar cells," *Nano Energy*, vol. 32, pp. 488–493, 2017. doi:10.1016/j.nanoen.2016.12.011

[62] M. Stuckelberger, T. Nietzold, B. M. West, R. Farshchi, D. Poplavskyy *et al.*, "How does CIGS performance depend on temperature at the microscale?" *Proc. Photovoltaic Specialist Conference (PVSC)*, 2017.

[63] L. Chayanun, S. Hammarberg, H. Dierks, G. Otnes, A. Björling *et al.*, "Combining nanofocused x-rays with electrical measurements at the NanoMAX beamline," *Crystals*, vol. 9, no. 432, pp. 1–11, 2019.

[64] G. Martínez-Criado, A. Homs, B. Alén, J. A. Sans, J. Segura-Ruiz *et al.*, "Probing quantum confinement within single core–multishell nanowires," *Nano Letters*, vol. 12, no. 11, pp. 5829–5834, 2012. doi:10.1021/nl303178u

[65] G. Martínez-Criado, J. Segura-Ruiz, B. Alén, J. Eymery, A. Rogalev *et al.*, "Exploring single semiconductor nanowires with a multimodal hard x-ray nanoprobe," *Advanced Materials*, vol. 26, pp. 7873–7879, 2014.

[66] A. Ulvestad, S. O. Hruszkewycz, M. V. Holt, M. O. Hill, I. Calvo-Almazán *et al.*, "Multimodal x-ray imaging of grain-level properties and performance in a polycrystalline solar cell," *Journal of Synchrotron Radiation*, vol. 26, no. 4, pp. 1316–1321, Jul 2019. doi:10.1107/S1600577519003606

[67] I. Calvo-Almazán, A. P. Ulvestad, E. Colegrove, T. Ablekim, M. V. Holt *et al.*, "Strain mapping of CdTe grains in photovoltaic devices," *IEEE Journal of Photovoltaics*, vol. 9, no. 6, pp. 1790–1799, 2019. doi:10.1109/JPHOTOV.2019.2942487

[68] S. M. Sze and K. K. Ng, *Physics of semiconductor devices*. Wiley, 2007.

[69] A. Smets, K. Jäger, O. Isabella, R. Van Swaaij, and M. Zeman, *Solar Energy: The physics and engineering of photovoltaic conversion, technologies and systems*. UIT Cambridge Ltd., 2016.

[70] W. Harrison, *Solid State Theory*, ser. Dover Books on Physics. Dover

Publications, 1980. [Online]. Available: https://books.google.de/books?id=5Y_Z4F95cacC

[71] W. Shockley and W. T. Read, "Statistics of the recombinations of holes and electrons," *Physical Review*, vol. 87, no. 5, pp. 835–842, 1952.

[72] K. Momma and F. Izumi, "Vesta 3 for three-dimensional visualization of crystal, volumetric and morphology data," *Journal of Applied Crystallography*, vol. 44, no. 6, pp. 1272–1276, 2011.

[73] D. B. Straus, S. Guo, and R. J. Cava, "Kinetically Stable Single Crystals of Perovskite-Phase $CsPbI_3$," *Journal of the American Chemical Society*, vol. 141, no. 29, pp. 11 435–11 439, 2019. doi:10.1021/jacs.9b06055

[74] W. H. Zachariasen, "Die kristallstruktur der telluride von zink, cadmium und quecksilber," *Norsk Geologisk Tidsskrift*, vol. 8, pp. 302–306, 1926.

[75] L. Kaplan, G. Leitus, V. Lyakhovitskaya, F. Frolow, H. Hallak *et al.*, "Synchrotron X-ray Diffraction Evidence for Native Defects in the Photovoltaic Semiconductor $CuInSe_2$," *Advanced Materials*, vol. 12, no. 5, pp. 366–370, 2000. doi:https://doi.org/10.1002/(SICI)1521-4095(200003)12:5¡366::AID-ADMA366¿3.0.CO;2-9

[76] C. Zuo, H. J. Bolink, H. Han, J. Huang, D. Cahen *et al.*, "Advances in perovskite solar cells," *Advanced Science*, vol. 3, no. 7, p. 1500324, 2016. doi:https://doi.org/10.1002/advs.201500324

[77] A. Kahn, "Fermi level, work function and vacuum level," *Mater. Horiz.*, vol. 3, pp. 7–10, 2016. doi:10.1039/C5MH00160A

[78] W. Shockley and H. J. Queisser, "Detailed balance limit of efficiency of p-n junction solar cells," *Journal of Applied Physics*, vol. 32, no. 3, pp. 510–519, 1961. doi:10.1063/1.1736034

[79] U. Rau, B. Blank, T. C. M. Müller, and T. Kirchartz, "Efficiency potential of photovoltaic materials and devices unveiled by detailed-balance analysis," *Phys. Rev. Applied*, vol. 7, p. 044016, Apr 2017. [Online]. Available: https://link.aps.org/doi/10.1103/PhysRevApplied.7.044016. doi:10.1103/PhysRevApplied.7.044016

[80] J. G. Simmons and G. W. Taylor, "Nonequilibrium steady-state statistics and associated effects for insulators and semiconductors containing an arbitrary distribution of traps," *Phys. Rev. B*, vol. 4, pp. 502–511, Jul

1971. [Online]. Available: https://link.aps.org/doi/10.1103/PhysRevB.4.502. doi:10.1103/PhysRevB.4.502

[81] R. N. Hall, "Electron-hole recombination in germanium," *Phys. Rev.*, vol. 87, pp. 387–387, Jul 1952. [Online]. Available: http://link.aps.org/doi/10.1103/PhysRev.87.387. doi:10.1103/PhysRev.87.387

[82] C.-T. Sah, R. N. Noyce, and W. Shockley, "Carrier generation and recombination in p-n junctions and p-n junction characteristics," *Proceedings of the IRE*, vol. 45, no. 9, pp. 1228–1243, Sept 1957. doi:10.1109/JRPROC.1957.278528

[83] J. S. Park, S. Kim, Z. Xie, and A. Walsh, "Point defect engineering in thin-film solar cells," *Nat Rev Mater*, vol. 3, pp. 194–210, 2018. doi:https://doi.org/10.1038/s41578-018-0026-7

[84] S. D. Stranks, V. M. Burlakov, T. Leijtens, J. M. Ball, A. Goriely *et al.*, "Recombination Kinetics in Organic-Inorganic Perovskites: Excitons, Free Charge, and Subgap States," *Phys. Rev. Appl.*, vol. 2, p. 034007, 2014. doi:10.1103/PhysRevApplied.2.034007

[85] T. Kirchartz, J. A. Márquez, M. Stolterfoht, and T. Unold, "Photoluminescence-based characterization of halide perovskites for photovoltaics," *Advanced Energy Materials*, vol. 10, p. 1904134, 2020. doi:10.1002/aenm.201904134

[86] G. Smestad and H. Ries, "Luminescence and current-voltage characteristics of solar cells and optoelectronic devices," *Solar Energy Materials and Solar Cells*, vol. 25, no. 1, pp. 51–71, 1992. [Online]. Available: https://www.sciencedirect.com/science/article/pii/092702489290016I. doi:https://doi.org/10.1016/0927-0248(92)90016-I

[87] S. D. Stranks, "Nonradiative Losses in Metal Halide Perovskites," *ACS Energy Lett.*, vol. 2, no. 7, pp. 1515–1525, 2017. doi:10.1021/acsenergylett.7b00239

[88] F. Staub, U. Rau, and T. Kirchartz, "Statistics of the auger recombination of electrons and holes via defect levels in the band gap—application to lead-halide perovskites," *ACS Omega*, vol. 3, no. 7, pp. 8009–8016, 2018. doi:10.1021/acsomega.8b00962

[89] N. Mott, "Recombination; a survey," *Solid-State Electronics*, vol. 21, no. 11, pp. 1275–1280, 1978. doi:https://doi.org/10.1016/0038-1101(78)90192-2

[90] M. Turcu and U. Rau, "Compositional trends of defect energies, band alignments, and recombination mechanisms in the Cu(In,Ga)(Se,S)$_2$ alloy

system," *Thin Solid Films*, vol. 431-432, pp. 158–162, 2003, proceedings of Symposium B, Thin Film Chalcogenide Photovoltaic Materials, E-MRS Spring Meeting. [Online]. Available: https://www.sciencedirect.com/science/article/pii/S0040609003002256. doi:https://doi.org/10.1016/S0040-6090(03)00225-6

[91] W. Tress, "Perovskite solar cells on the way to their radiative efficiency limit – insights into a success story of high open-circuit voltage and low recombination," *Advanced Energy Materials*, vol. 7, no. 14, p. 1602358, 2017. doi:https://doi.org/10.1002/aenm.201602358

[92] IEC, "IEC (International Electrotechnical Commission) 61646 Ed.2: Thin-film terrestrial photovoltaic (PV) modules - Design qualification and type approval," 2008.

[93] R. Carron, C. Andres, E. Avancini, T. Feurer, S. Nishiwaki *et al.*, "Bandgap of thin film solar cell absorbers: A comparison of various determination methods," *Thin Solid Films*, vol. 669, pp. 482–486, 2019. [Online]. Available: https://www.sciencedirect.com/science/article/pii/S0040609018307582. doi:https://doi.org/10.1016/j.tsf.2018.11.017

[94] P. Landsberg and Y. Wang, "Equivalent circuits for recombination-generation processes in semiconductors: A unified approach," *Solid-State Electronics*, vol. 32, no. 7, pp. 525–534, 1989. [Online]. Available: https://www.sciencedirect.com/science/article/pii/0038110189901081. doi:https://doi.org/10.1016/0038-1101(89)90108-1

[95] N. Araújo, F. Sousa, and F. Costa, "Equivalent models for photovoltaic cell–a review," *Revista de Engenharia Térmica*, vol. 19, no. 2, pp. 77–98, 2020.

[96] W. Shockley, "The theory of p-n junctions in semiconductors and p-n junction transistors," *Bell System Technical Journal*, vol. 28, no. 3, pp. 435–489, 1949.

[97] K. Nishioka, N. Sakitani, Y. Uraoka, and T. Fuyuki, "Analysis of multicrystalline silicon solar cells by modified 3-diode equivalent circuit model taking leakage current through periphery into consideration," *Solar Energy Materials and Solar Cells*, vol. 91, no. 13, pp. 1222–1227, 2007. [Online]. Available: https://www.sciencedirect.com/science/article/pii/S0927024807001493. doi:https://doi.org/10.1016/j.solmat.2007.04.009

[98] K. Tvingstedt, L. Gil-Escrig, C. Momblona, P. Rieder, D. Kiermasch *et al.*, "Removing leakage and surface recombination in planar perovskite solar cells," *ACS energy letters*, vol. 2, pp. 424–430, 2017.

[99] N. Boutana, A. Mellit, S. Haddad, A. Rabhi, and A. M. Pavan, "An explicit I-V model for photovoltaic module technologies," *Energy Conversion and Management*, vol. 138, pp. 400–412, 2017. [Online]. Available: https://www.sciencedirect.com/science/article/pii/S0196890417301243. doi:https://doi.org/10.1016/j.enconman.2017.02.016

[100] A. Orioli and A. Di Gangi, "A procedure to calculate the five-parameter model of crystalline silicon photovoltaic modules on the basis of the tabular performance data," *Applied Energy*, vol. 102, pp. 1160–1177, 2013. [Online]. Available: https://www.sciencedirect.com/science/article/pii/S0306261912004813. doi:https://doi.org/10.1016/j.apenergy.2012.06.036

[101] Y. A. Mahmoud, W. Xiao, and H. H. Zeineldin, "A Parameterization Approach for Enhancing PV Model Accuracy," *IEEE Transactions on Industrial Electronics*, vol. 60, no. 12, pp. 5708–5716, 2013. doi:10.1109/TIE.2012.2230606

[102] K. Ishaque, Z. Salam, and H. Taheri, "Simple, fast and accurate two-diode model for photovoltaic modules," *Solar Energy Materials and Solar Cells*, vol. 95, no. 2, pp. 586–594, 2011. [Online]. Available: https://www.sciencedirect.com/science/article/pii/S0927024810005477. doi:https://doi.org/10.1016/j.solmat.2010.09.023

[103] P. Jackson, R. Wuerz, D. Hariskos, E. Lotter, W. Witte *et al.*, "Effects of heavy alkali elements in Cu(In,Ga)Se_2 solar cells with efficiencies up to 22.6%," *Phys. Status Solidi RRL*, vol. 10, no. 8, pp. 583–586, 2016. doi:10.1002/pssr.201600199

[104] D. Abou-Ras, T. Kirchartz, and U. Rau, *Advanced characterization techniques for thin film solar cells*. John Wiley & Sons, 2016.

[105] A. Saadaldin, A. M. Slyamov, M. E. Stuckelberger, P. S. Jørgensen, C. Rein *et al.*, "Multi-modal characterization of kesterite thin-film solar cells: experimental results and numerical interpretation," *Faraday Discussions*, 2022. doi:10.1039/d2fd00044j

[106] T.-K. Sham and R. A. Rosenberg, "Time-resolved synchrotron radiation excited optical luminescence: Light-emission properties of silicon-based nanostructures," *ChemPhysChem*, vol. 8, no. 18, pp. 2557–2567, 2007. doi:https://doi.org/10.1002/cphc.200700226

[107] B. Lai, D. Capatina, C. Roehrig, O. Antipova, Z. Cai *et al.*, "APS 2-ID Microprobes: Status and Future Plans," *Microscopy and Microanalysis*, vol. 24, no. S2, pp. 330–331, 2018. doi:10.1017/S1431927618013971

[108] H. C. N. Tolentino, R. R. Geraldes, G. B. Z. L. Moreno, C. S. B. Dias, C. A. Pérez *et al.*, "TARUMÃ station for the CARNAÚBA beamline at SIRIUS/LNLS," in *X-Ray Nanoimaging: Instruments and Methods IV*, B. Lai and A. Somogyi, Eds., vol. 11112, International Society for Optics and Photonics. SPIE, 2019, pp. 8 – 19.

[109] A. Somogyi, K. Medjoubi, G. Baranton, V. Le Roux, M. Ribbens *et al.*, "Optical design and multi-length-scale scanning spectro-microscopy possibilities at the Nanoscopium beamline of Synchrotron Soleil," *Journal of Synchrotron Radiation*, vol. 22, no. 4, pp. 1118–1129, Jul 2015. doi:10.1107/S1600577515009364

[110] U. Johansson, D. Carbone, S. Kalbfleisch, A. Björling, M. Kahnt *et al.*, "NanoMAX: the hard X-ray nanoprobe beamline at the MAX IV Laboratory," *Journal of Synchrotron Radiation*, vol. 28, no. 6, pp. 1935–1947, Nov 2021. doi:10.1107/S1600577521008213

[111] G.-C. Yin, S.-H. Chang, B.-Y. Chen, H.-Y. Chen, B.-H. Lin *et al.*, "Multimodal hard x-ray nanoprobe facility by nested montel mirrors aimed for 40nm resolution at taiwan photon source," *AIP Conference Proceedings*, vol. 1696, no. 1, p. 020026, 2016. doi:10.1063/1.4937520

[112] B.-H. Lin, Y.-H. Wu, X.-Y. Li, H.-C. Hsu, Y.-C. Chiu *et al.*, "Capabilities of time-resolved X-ray excited optical luminescence of the Taiwan Photon Source 23A X-ray nanoprobe beamline," *Journal of Synchrotron Radiation*, vol. 27, no. 1, pp. 217–221, Jan 2020. doi:10.1107/S1600577519013675

[113] M. Holler, J. Raabe, A. Diaz, M. Guizar-Sicairos, R. Wepf *et al.*, "Omny—a tomography nano cryo stage," *Review of Scientific Instruments*, vol. 89, no. 4, p. 043706, 2018. doi:10.1063/1.5020247

[114] P. D. Quinn, L. Alianelli, M. Gomez-Gonzalez, D. Mahoney, F. Cacho-Nerin *et al.*, "The Hard X-ray Nanoprobe beamline at Diamond Light Source," *Journal of Synchrotron Radiation*, vol. 28, no. 3, pp. 1006–1013, May 2021. doi:10.1107/S1600577521002502

[115] M. I. Bertoni, D. P. Fenning, V. Rose, M. Holt, J. Maser *et al.*, "Synchrotron-based characterization of solar cell nanodefects," in *2011 37th IEEE Photovoltaic Specialists Conference*, 2011, pp. 000 154–000 156.

[116] S. Bean, P. Amann, M. Bartlein, Z. Cai, T. Graber *et al.*, "A Novel Vacuum Chamber Design for the APS Upgrade of the 26-ID Nanoprobe," *JACoW*, vol. MEDSI2020, p. WEPB15, 2021. doi:10.18429/JACoW-MEDSI2020-WEPB15

[117] R. G. Steinmann, G. Martinez-Criado, D. Salomon, H. Vitoux, R. Tucoulou *et al.*, "A helium mini-cryostat for the nanoprobe beamline ID16B at ESRF: characteristics and performance," *Journal of Synchrotron Radiation*, vol. 27, no. 4, pp. 1074–1079, 2020. doi:10.1107/S1600577520007110

[118] G. Falkenberg, F. Seiboth, F. Koch, K. V. Falch, A. Schropp *et al.*, "CRL optics and silicon drift detector for p06 microprobe experiments at 35 keV," *Powder Diffraction*, vol. 35, no. S1, pp. S34–S37, 2020.

[119] G. Falkenberg, G. Fleissner, D. Neumann, G. Wellenreuther, P. Alraun *et al.*, "Moonlight receptor of the "1-h-midge" clunio marinus studied by micro-xrf," *J. Phys.: Conf. Ser.*, vol. 463, no. 012016, 2013. doi:10.1088/1742-6596/463/1/012016

[120] A. Johannes, D. Salomon, G. Martinez-Criado, M. Glaser, A. Lugstein *et al.*, "In operando x-ray imaging of nanoscale devices: Composition, valence, and internal electrical fields," *Science Advances*, vol. 3, no. 12, p. eaao4044, 2017. [Online]. Available: https://www.science.org/doi/abs/10.1126/sciadv.aao4044. doi:10.1126/sciadv.aao4044

[121] A. Schropp, D. Brückner, J. Bulda, G. Falkenberg, J. Garrevoet *et al.*, "Scanning Hard X-Ray Microscopy Based on Be CRLs," *Microscopy and Microanalysis*, vol. 24, no. S2, pp. 186–187, 2018. doi:10.1017/S1431927618013284

[122] C. Rumancev, T. Vöpel, S. Stuhr, A. von Gundlach, T. Senkbeil *et al.*, "Micro x-ray fluorescence analysis of trace element distribution in frozen hydrated HeLa cells at the P06 beamline at Petra III," *Biointerphases*, vol. 16, no. 1, p. 011004, 2021. doi:10.1116/6.0000593

[123] T. Nietzold, B. M. West, M. Stuckelberger, B. Lai, S. Vogt *et al.*, "Quantifying X-ray fluorescence data using MAPS," *Journal of Visual Experiments*, vol. 132, no. e56042, 2018. doi:10.3791/56042

[124] J. Segura-Ruiz, D. Salomon, A. Rogalev, J. Eymery, B. Alén *et al.*, "Spatially and Time-Resolved Carrier Dynamics in Core–Shell InGaN/GaN Multiple-Quantum Wells on GaN Wire," *Nano Letters*, vol. 21, no. 22, pp. 9494–9501, 2021. doi:10.1021/acs.nanolett.1c02760

[125] S. O. Hruszkewycz, M. Allain, M. V. Holt, C. E. Murray, J. R. Holt *et al.*, "High-resolution three-dimensional structural microscopy by single-angle bragg ptychography," *Nat Mater*, vol. 16, no. 2, pp. 244–251, 02 2017. [Online]. Available: http://dx.doi.org/10.1038/nmat4798

[126] U. Boesenberg, C. G. Ryan, R. Kirkham, D. P. Siddons, M. Alfeld *et al.*, "Fast X-ray microfluorescence imaging with submicrometer-resolution integrating a Maia detector at beamline P06 at PETRA III," *Journal of Synchrotron Radiation*, vol. 23, no. 6, pp. 1550–1560, 2016. [Online]. Available: https://onlinelibrary.wiley.com/doi/abs/10.1107/S1600577516015289. doi:https://doi.org/10.1107/S1600577516015289

[127] G. Requena, P. Barriobero-Vila, K. Bugelnig, J. Haubrich, J. Gussone *et al.*, "High Resolution 3D and 4D Characterization of Microstructure Formation in Novel Ti Alloys for Additive Manufacturing," *Microscopy and Microanalysis*, vol. 25, no. S2, pp. 384–385, 2019. doi:10.1017/S1431927619002654

[128] C. E. Shuck, M. Frazee, A. Gillman, M. T. Beason, I. E. Gunduz *et al.*, "X-ray nanotomography and focused-ion-beam sectioning for quantitative three-dimensional analysis of nanocomposites," *Journal of Synchrotron Radiation*, vol. 23, no. 4, pp. 990–996, Jul 2016. doi:10.1107/S1600577516007992

[129] U. Urdiroz, E. Navarro, M. Sánchez-Agudo, F. Cebollada, F. J. Palomares *et al.*, "Local coercivity at x-ray nanobeam irradiated regions in amorphous $fe_{80}b_{20}$ stripes," *AIP Advances*, vol. 11, no. 1, p. 015318, 2021. doi:10.1063/9.0000090

[130] G. W. P. Adhyaksa, S. Brittman, H. Āboliņš, A. Lof, X. Li *et al.*, "Understanding detrimental and beneficial grain boundary effects in halide perovskites," *Advanced Materials*, vol. 30, no. 52, p. 1804792, 2018. doi:https://doi.org/10.1002/adma.201804792

[131] J. R. Poindexter, M. A. Jensen, A. E. Morishige, E. E. Looney, A. Youssef *et al.*, "Distribution and charge state of iron impurities in intentionally contaminated lead halide perovskites," *IEEE Journal of Photovoltaics*, vol. 8, no. 1, pp. 156–161, 2018. doi:10.1109/JPHOTOV.2017.2775156

[132] H. Chang, M. Cummings, N. Shirato, B. Stripe, D. Rosenmann *et al.*, "Ultra-high vacuum compatible optical chopper system for synchrotron x-ray scanning tunneling microscopy," *AIP Conference Proceedings*, vol. 1696, no. 1, p. 020001, 2016. doi:10.1063/1.4937495

[133] P. Kirkpatrick and A. V. Baez, "Formation of optical images by x-rays," *JOSA*, vol. 38, no. 9, pp. 766–774, 1948.

[134] H. Mimura, H. Yumoto, S. Matsuyama, Y. Sano, K. Yamamura *et al.*, "Efficient focusing of hard x rays to 25 nm by a total reflection mirror," *Applied Physics Letters*, vol. 90, no. 5, p. 051903, 2007. doi:10.1063/1.2436469

[135] F. Seiboth, A. Schropp, M. Scholz, F. Wittwer, C. Rödel *et al.*, "Perfect x-ray focusing via fitting corrective glasses to aberrated optics," *Nat. Comm.*, vol. 8, p. 14623, 2017. doi:10.1038/ncomms14623

[136] F. Seiboth, F. Wittwer, M. Scholz, M. Kahnt, M. Seyrich *et al.*, "Nanofocusing with aberration-corrected rotationally parabolic refractive x-ray lenses," *Journal of Synchrotron Radiation*, vol. 25, no. 1, pp. 108–115, Jan 2018. doi:10.1107/S1600577517015272

[137] W. H. Schroeder, B. De Samber, T. Claußen, E. Vergucht, J. Garrevoet *et al.*, "A Cryogenic Sample Environment for the Analysis of Frozen Hydrated Biological Tissue at the Hard X-ray Micro/Nano-Probe Beamline P06 at PETRA III," 2014.

[138] J. Villanova, R. Daudin, P. Lhuissier, D. Jauffrès, S. Lou *et al.*, "Fast in situ 3D nanoimaging: a new tool for dynamic characterization in materials science," *Materials Today*, vol. 20, no. 7, pp. 354–359, 2017. [Online]. Available: https://www.sciencedirect.com/science/article/pii/S1369702117301025. doi:https://doi.org/10.1016/j.mattod.2017.06.001

[139] R. Kumar, J. Villanova, P. Lhuissier, and L. Salvo, "In situ nanotomography study of creep cavities in Al-3.6-Cu alloy," *Acta Materialia*, vol. 166, pp. 18–27, 2019. [Online]. Available: https://www.sciencedirect.com/science/article/pii/S1359645418309625. doi:https://doi.org/10.1016/j.actamat.2018.12.020

[140] V. Vanpeene, J. Villanova, A. King, B. Lestriez, E. Maire *et al.*, "Dynamics of the Morphological Degradation of Si-Based Anodes for Li-Ion Batteries Characterized by In Situ Synchrotron X-Ray Tomography," *Advanced Energy Materials*, vol. 9, no. 18, p. 1803947, 2019. [Online]. Available: https://onlinelibrary.wiley.com/doi/abs/10.1002/aenm.201803947. doi:https://doi.org/10.1002/aenm.201803947

[141] C. G. Schroer, M. Seyrich, A. Schropp, R. Döhrmann, S. Botta *et al.*, "Ptychographic Nano-Analytical Microscope (PtyNAMi) at PETRA III: signal-to-background optimization for imaging with high sensitivity," vol. 11112, pp. 42 – 50, 2019. doi:10.1117/12.2529096

[142] T. E. Fornek, "Advanced photon source upgrade project final design report," 5 2019. [Online]. Available: https://www.osti.gov/biblio/1543138. doi:10.2172/1543138

[143] M. Seyrich, "High-resolution and in-solution hard x-ray ptychography at the

ptychographic nano-analytical microscope ptynami," Ph.D. dissertation, Universität Hamburg, 2020.

[144] J. M. Rodenburg, "Ptychography and Related Diffractive Imaging Methods," *Advances in Imaging and Electron Physics*, vol. 150, pp. 87–184, 2008.

[145] J. M. Rodenburg and H. M. L. Faulkner, "A phase retrieval algorithm for shifting illumination," *Applied Physics Letters*, vol. 85, no. 20, pp. 4795–4797, 2004. doi:10.1063/1.1823034

[146] P. Thibault, M. Dierolf, O. Bunk, A. Menzel, and F. Pfeiffer, "Probe retrieval in ptychographic coherent diffractive imaging," *Ultramicroscopy*, vol. 109, no. 4, pp. 338–343, 2009. doi:https://doi.org/10.1016/j.ultramic.2008.12.011

[147] F. Pfeiffer, "X-ray ptychography," *Nature Photonics*, vol. 12, pp. 9–17, 2018.

[148] A. Schropp, R. Hoppe, J. Patommel, D. Samberg, F. Seiboth *et al.*, "Hard x-ray scanning microscopy with coherent radiation: Beyond the resolution of conventional x-ray microscopes," *Applied Physics Letters*, vol. 100, no. 25, p. 253112, 2012. doi:10.1063/1.4729942

[149] A. Diaz, P. Trtik, M. Guizar-Sicairos, A. Menzel, P. Thibault *et al.*, "Quantitative x-ray phase nanotomography," *Physical Review B*, vol. 85, p. 020104(R), 2012. doi:10.1103/PhysRevB.85.020104

[150] G. H. Chen, J. Zambelli, N. Bevins, Z. Qi, and K. Li, "X-ray phase sensitive imaging methods: basic physical principles and potential medical applications," *Current medical imaging reviews*, vol. 6, no. 2, pp. 90–99, 2010. doi:10.2174/157340510791268533

[151] G. Fevola et al., 2023, Mansucript in preparation.

[152] A. Slobodskyy, T. Slobodskyy, T. Ulyanenkova, S. Doyle, M. Powalla *et al.*, "In-depth analysis of the $CuIn_{1-x}Ga_xSe_2$ film for solar cells, structural and optical characterization," *Applied Physics Letters*, vol. 97, no. 25, p. 251911, 2010.

[153] R. Mainz and R. Klenk, "In situ analysis of elemental depth distributions in thin films by combined evaluation of synchrotron x-ray fluorescence and diffraction," *Journal of Applied Physics*, vol. 109, no. 12, p. 123515, 2011. doi:10.1063/1.3592288

[154] Y.-I. Kim, K.-B. Kim, and M. Kim, "Characterization of lattice parameters gradient of $Cu(In_{1-x}Ga_x)Se_2$ absorbing layer in thin-film solar cell by glancing incidence X-ray diffraction technique," *Journal of Materials Science &*

Technology, vol. 51, pp. 193–201, 2020.

[155] C. Iatosti, M. Moret, A. Tiberj, and O. Briot, "Analysis of the gallium gradient in $Cu(In_{1-x}Ga_x)Se_2$ absorbers by X-ray diffraction," *Solar Energy Materials and Solar Cells*, vol. 220, p. 110847, 2021.

[156] N. Pyrlik et al., 2022, manuscript in preparation.

[157] R. Tertian and F. Claisse, *Principles of Quantitative X-ray Fluorescence Analysis*. Heydon & Son Ltd, 1982.

[158] R. E. Van Grieken and A. A. Markowicz, *Handbook of X-ray Spectrometry*, 2nd ed. Marcel Dekker, Inc., 2001.

[159] V. Solé, E. Papillon, M. Cotte, P. Walter, and J. Susini, "A multiplatform code for the analysis of energy-dispersive X-ray fluorescence spectra," *Spectrochim. Acta Part B*, vol. 62, pp. 63–68, 2007. doi:10.1016/j.sab.2006.12.002

[160] B. Henke, E. Gullikson, and J. Davis, "X-ray interactions: photoabsorption, scattering, transmission, and reflection at e=50-30000 ev, z=1-92," *Atomic Data and Nuclear Data Tables*, vol. 54, no. 2, pp. 181–342, 1993. doi:10.1006/adnd.1993.1013

[161] D. K. G. de Boer, "Calculation of x-ray fluorescence intensities from bulk and multilayer samples," *X-ray Spectrometry*, vol. 19, pp. 145–154, 1990.

[162] A. Heginbotham and V. A. Solé, "CHARMed PyMca, Part I: A Protocol for Improved Interlaboratory Reproducibility in the Quantitative EDXRF Analysis of Copper Alloys," *Archaeometry*, vol. 49, pp. 714–730, 2017. doi:10.1111/arcm.12282

[163] M. E. Stuckelberger, T. Nietzold, B. M. West, Y. Luo, X. Li *et al.*, "Effects of X-rays on perovskite solar cells," *The Journal of Physical Chemistry C*, vol. 124, no. 33, pp. 17 949–17 956, 2020. doi:10.1021/acs.jpcc.0c04645

[164] O. F. Vyvenko, T. Buonassisi, A. A. Istratov, H. Hieslmair, A. C. Thompson *et al.*, "X-ray beam induced current–a synchrotron radiation based technique for the in situ analysis of recombination properties and chemical nature of metal clusters in silicon," *Journal of Applied Physics*, vol. 91, no. 6, pp. 3614–3617, 2002.

[165] M. Stuckelberger, T. Nietzold, B. M. West, B. Lai, J. Maser *et al.*, "X-ray beam induced voltage: A novel technique for electrical nanocharacterization of solar cells," *Proc. Photovoltaic Specialist Conference (PVSC)*, pp. 2179–2184,

2017. doi:10.1109/PVSC.2017.8366368

[166] D. Cavalcoli and A. Cavallini, "Evaluation of diffusion length at different excess carrier concentrations," *Materials Science and Engineering*, no. B24, pp. 98–100, 1994.

[167] G. Micard, G. Hahn, and B. Terheiden, "Injection in light beam induced current systems: An analytical model," *physica status solidi (a)*, vol. 213, no. 5, pp. 1329–1339, 2016. [Online]. Available: https://onlinelibrary.wiley.com/doi/abs/10.1002/pssa.201532680. doi:https://doi.org/10.1002/pssa.201532680

[168] O. Marcelot and P. Magnan, "From EBIC images to qualitative minority carrier diffusion length maps," *Ultramicroscopy*, vol. 197, pp. 23–27, 2019. [Online]. Available: https://www.sciencedirect.com/science/article/pii/S0304399118302225. doi:https://doi.org/10.1016/j.ultramic.2018.11.005

[169] J. Wallentin, M. Osterhoff, R. N. Wilke, K.-M. Persson, L.-E. Wernersson *et al.*, "Hard x-ray detection using a single 100 nm diameter nanowire," *Nano Letters*, vol. 14, no. 12, pp. 7071–7076, 2014, pMID: 25419623. doi:10.1021/nl5040545

[170] J. M. Richter, M. Abdi-Jalebi, A. Sadhanala, M. Tabchnyk, J. P. Rivett *et al.*, "Enhancing photoluminescece yields in lead halide perovskites by photon recycling and light out-coupling," *Nature Communications*, vol. 7, p. 13941, 2016. doi:10.1038/ncomms13941

[171] C. Wehrenfennig, G. E. Eperon, M. B. Johnston, H. J. Snaith, and L. M. Herz, "High charge carrier mobilities and lifetimes in organolead trihalide perovskites," *Adv. Mater.*, vol. 26, pp. 1584–1589, 2014.

[172] N. Pyrlik, "The effect of stoichiometric variations on performance in CIGS solar cells measured using X-ray microscopy," 2020, Bachelor's Thesis at Universität Hamburg.

[173] J. H. Hubbell and S. M. Seltzer, "Tables of X-ray mass attenuation coefficients and mass energy-absorption coefficients 1 keV to 20 MeV for elements Z=1 to 92 and 48 additional substances of dosimetric interest," *National Inst. of Standards and Technology*, 1995.

[174] C. A. Klein, "Bandgap dependence and related features of radiation ionization energies in semiconductors," *Journal of Applied Physics*, vol. 39, no. 4, pp. 2029–2038, 1968. [Online]. Available: https://doi.org/10.1063/1.1656484. doi:10.1063/1.1656484

[175] J. Cazaux, "A physical approach to the radiation damage mechanisms induced by X-rays in X-ray microscopy related techniques," *Journal of Microscopy*, vol. 188, no. 2, pp. 106–124, 1997.

[176] R. Taylor, A. Finch, J. Mosselmans, and P. Quinn, "The development of a XEOL and TR XEOL detection system for the I18 microfocus beamline Diamond light source," *Journal of Luminescence*, vol. 134, pp. 49–58, 2013.

[177] Cazaux, Jacques, "The role of the auger mechanism in the radiation damage of insulators," *Microsc. Microanal. Microstruct.*, vol. 6, no. 3, pp. 345–362, 1995. [Online]. Available: https://doi.org/10.1051/mmm:1995125. doi:10.1051/mmm:1995125

[178] B. Monemar, "Fundamental energy gap of gan from photoluminescence excitation spectra," *Phys. Rev. B*, vol. 10, pp. 676–681, Jul 1974. [Online]. Available: https://link.aps.org/doi/10.1103/PhysRevB.10.676. doi:10.1103/PhysRevB.10.676

[179] S. Siebentritt, E. Avancini, M. Bär, J. Bombsch, E. Bourgeois *et al.*, "Heavy alkali treatment of Cu(In,Ga)Se_2 solar cells: Surface versus bulk effects," *Advanced Energy Materials*, vol. 10, no. 8, p. 1903752, 2020. doi:10.1002/aenm.201903752

[180] J. K. Katahara and H. W. Hillhouse, "Quasi-fermi level splitting and sub-bandgap absorptivity from semiconductor photoluminescence," *Journal of Applied Physics*, vol. 116, no. 17, p. 173504, 2014. doi:10.1063/1.4898346

[181] M. Wang, K. Wang, Y. Gao, J. I. Khan, W. Yang *et al.*, "Impact of photoluminescence reabsorption in metal-halide perovskite solar cells," *Solar RRL*, vol. 5, no. 5, p. 2100029, 2021. doi:https://doi.org/10.1002/solr.202100029

[182] P. Fassl, V. Lami, F. J. Berger, L. M. Falk, J. Zaumseil *et al.*, "Revealing the internal luminescence quantum efficiency of perovskite films via accurate quantification of photon recycling," *Matter*, vol. 4, no. 4, pp. 1391–1412, 2021. [Online]. Available: https://www.sciencedirect.com/science/article/pii/S2590238521000199. doi:https://doi.org/10.1016/j.matt.2021.01.019

[183] Z.-Y. Zhang, H.-Y. Wang, Y.-W. Hao, C. Sun, Y. Zhang *et al.*, "The Role of Trap-assisted Recombination in Luminescent Properties of Organometal Halide $CH_3NH_3PbBr_3$ Perovskite Films andQuantum Dots," *Scientific Reports*, vol. 6, p. 27286, 2016. doi:10.1038/srep27286

[184] E. V. Péan, S. Dimitrov, C. S. De Castro, and M. L. Davies, "Interpreting time-resolved photoluminescence of perovskite materials," *Phys. Chem. Chem. Phys.*, vol. 22, pp. 28 345–28 358, 2020.

[185] A. Stierle, T. F. Keller, H. Noei, V. Vonk, and R. Roehlsberger, "Desy nanolab," *J. Large-Scale Res. Facil. JLSRF*, vol. 2, p. A76, 2016. doi:http://dx.doi.org/10.17815/jlsrf-2-140

[186] M. Stuckelberger, T. Nietzold, G. N. Hall, B. West, J. Werner *et al.*, "Charge collection in hybrid perovskite solar cells: relation to the nanoscale elemental distribution," *IEEE Journal of Photovoltaics*, vol. 7, no. 2, pp. 590–597, 2017. doi:10.1109/JPHOTOV.2016.2633801

[187] G. D. Evangelidis and E. Z. Psarakis, "Parametric image alignment using enhanced correlation coefficient maximization," *IEEE Computer Society*, vol. 30, pp. 1–8, 2008.

[188] OpenCV, "Open source computer vision library," 2015, available at: https://opencv.org, (accessed June 19, 2020).

[189] R. J. Barlow, *Statistics: A Guide to the Use of Statistical Methods in the Physical Sciences (The Manchester Physics Series).* John Wiley & Sons, 2008.

[190] O. Cojocaru-Mirédin, P.-P. Choi, D. Abou-Ras, S. S. Schmidt, R. Caballero *et al.*, "Characterization of grain boundaries in Cu(In,Ga)Se_2 films using atom-probe tomography," *IEEE Journal of Photovoltaics*, vol. 1, no. 2, pp. 207–212, 2011. doi:10.1109/JPHOTOV.2011.2170447

[191] P. Schöppe, S. Schönherr, R. Wuerz, W. Wisniewski, G. Martínez-Criado *et al.*, "Rubidium segregation at random grain boundaries in Cu(In,Ga)Se_2 absorbers," *Nano Energy*, vol. 42, pp. 307–313, 2017. doi:10.1016/j.nanoen.2017.10.063

[192] A. Vilalta-Clemente, M. Raghuwanshi, S. Duguay, C. Castro, E. Cadel *et al.*, "Rubidium distribution at atomic scale in high efficient Cu(In,Ga)Se_2 thin-film solar cells," *Applied Physics Letters*, vol. 112, no. 10, p. 103105, 2018. doi:10.1063/1.5020805

[193] C. T. Plass, M. Ritzer, P. Schöppe, S. Schönherr, M. Zapf *et al.*, "In-operando nanoscale x-ray analysis revealing the local electrical properties of rubidium-enriched grain boundaries in Cu(In,Ga)Se_2 solar cells," *ACS Applied Materials & Interfaces*, vol. 12, no. 51, pp. 57 117–57 123, 2020. doi:10.1021/acsami.0c17849

[194] R. Wuerz, W. Hempel, and P. Jackson, "Diffusion of Rb in polycristalline Cu(In,Ga)Se_2 layers and effect of Rb on solar cell parameters of Cu(In,Ga)Se_2 thin-film solar cells," *Journal of Applied Physics*, vol. 124, p. 165305, 2018. doi:10.1063/1.5044629

[195] M. A. Green, "Radiative efficiency of state-of-the-art photovoltaic cells," *Progress in Photovoltaics: Research and Applications*, vol. 20, pp. 472–476, 2012. doi:https://doi.org/10.1002/pip.1147

[196] Z. Instrument, *Principles of lock-in detection and the state of the art*, 11 2016, https://www.zhinst.com/others/en/resources/principles-of-lock-in-detection, last accessed June 15, 2023.

[197] *Model 486 Picoammeter Model 487 Picoammeter/Voltage Source Instruction Manual*. Keithley Instruments Inc., 2000, no. 486-901-01 Rev. D.

[198] *MODEL SR570 Low-Noise Current Preamplifier*. SRS Standford Research Systems, 2015.

[199] J. H. Scofield, "Frequency-domain description of a lock-in amplifier," *American Journal of Physics*, vol. 62, no. 2, pp. 129–133, 1994. [Online]. Available: https://doi.org/10.1119/1.17629. doi:10.1119/1.17629

[200] T.-C. Poon, *Encyclopedia of Modern Optics - Heterodyning*, 1st ed. Elsevier Ltd. 373, 2005.

[201] T. Kaiser, "Lock-in amplification for laser and x-ray beam induced current measurements of solar cells," 2021, Bachelor's Thesis at Universität Hamburg.

[202] Z. Instruments, *UHF User Manual*, 2018.

[203] W. Witte, D. Abou-Ras, K. Albe, G. H. Bauer, F. Bertram *et al.*, "Gallium gradients in Cu(In,Ga)Se_2 thin-film solar cells," *Progress in Photovoltaics: Research and Applications*, vol. 23, no. 6, pp. 717–733, 2015.

[204] L. Chayanun, V. Dagytė, A. Troian, D. Salomon, M. Borgström *et al.*, "Spectrally resolved x-ray beam induced current in a single InGaP nanowire," *Nanotechnology*, vol. 29, no. 45, p. 454001, 2018. [Online]. Available: https://doi.org/10.1088/1361-6528/aadc76. doi:10.1088/1361-6528/aadc76

[205] P. J. Fish, *Electronic Noise and Low Noise Design*. The Macmillan Press LTD., 1993.

[206] Keithley A Tektronix Company, *Precision DC Current, Voltage and Resistance*

Measurements, ser. Low Level Measurements Handbook - 7th Edition, 2013.

[207] S. Letzter and N. Webster, "Noise in amplifiers," *IEEE Spectrum*, vol. 7, no. 8, pp. 67–75, 1970. doi:10.1109/MSPEC.1970.5213514

[208] M. L. Meade, *Lock-in amplifiers: principles and applications*. Peter Peregrinus Ltd., 1983.

[209] S. M. Polvino, C. E. Murray, Ö. Kalenci, I. Noyan, B. Lai *et al.*, "Synchrotron microbeam x-ray radiation damage in semiconductor layers," *Applied Physics Letters*, vol. 92, no. 22, p. 224105, 2008.

[210] M. J. de Wild-Scholten, "Energy payback time and carbon footprint of commercial photovoltaic systems," *Solar Energy Materials & Solar Cells*, vol. 119, pp. 296–305, 2013.

[211] M. Powalla, S. Paetel, D. Hariskos, R. Wuerz, F. Kessler *et al.*, "Advances in cost-efficient thin-film photovoltaics based on Cu(In,Ga)Se_2," *Engineering*, vol. 3, pp. 445–451, 2017. doi:10.1016/J.ENG.2017.04.015

[212] T. Feurer, P. Reinhard, E. Avancini, B. Bissig, J. Löckinger *et al.*, "Progress in thin film CIGS photovoltaics–research and development, manufacturing, and applications," *Progress in Photovoltaics: Research and Applications*, vol. 25, no. 7, pp. 645–667, 2017. doi:10.1002/pip.2811

[213] M. Langenhorst, B. Sautter, R. Schmager, J. Lehr, E. Ahlswede *et al.*, "Energy yield of all thin-film perovskite/cigs tandem solar modules," *Progress in Photovoltaics: Research and Applications*, vol. 27, no. 4, pp. 290–298, 2019. doi:https://doi.org/10.1002/pip.3091

[214] M. Nakamura, K. Yamaguchi, Y. Kimoto, Y. Yasaki, T. Kato *et al.*, "Cd-Free Cu(In,Ga)(Se,S)$_2$ Thin-Film Solar Cell With Record Efficiency of 23.35%," *IEEE Journal of Photovoltaics*, vol. 9, no. 6, pp. 1863–1867, 2019. doi:10.1109/JPHOTOV.2019.2937218

[215] J. Keller, P. Pearson, N. Shariati Nilsson, O. Stolt, L. Stolt *et al.*, "Performance Limitations of Wide-Gap (Ag,Cu)(In,Ga)Se_2 Thin-Film Solar Cells," *Solar RRL*, vol. 5, no. 9, p. 2100403, 2021. doi:https://doi.org/10.1002/solr.202100403

[216] M. A. Contreras, L. M. Mansfield, B. Egaas, J. Li, M. Romero *et al.*, "Improved energy conversion efficiency in wide bandgap Cu(In,Ga)Se_2 solar cells," *Proc. Photovoltaic Specialist Conference (PVSC)*, pp. 000 026–000 031, 2011.

[217] S. Siebentritt, "What limits the efficiency of chalcopyrite solar cells?"

Solar Energy Materials & Solar Cells, vol. 95, pp. 1471–1476, 2011. doi:10.1016/j.solmat.2010.12.014

[218] U. Rau and J. Werner, "Radiative efficiency limits of solar cells with lateral band-gap fluctuations," *Applied Physics Letters*, vol. 84, p. 3735, 2004. doi:10.1063/1.1737071

[219] P. O. Grabitz, U. Rau, B. Wille, G. Bilger, and J. H. Werner, "Spatial inhomogeneities in Cu(In,Ga)Se_2 solar cells analyzed by an electron beam induced voltage technique," *Journal of Applied Physics*, vol. 100, no. 12, p. 124501, 2006.

[220] H. Aboulfadl, K. V. Sopiha, J. Keller, J. K. Larsen, J. J. Scragg *et al.*, "Alkali dispersion in (Ag,Cu)(In,Ga)Se_2 thin film solar cells – insight from theory and experiment," *ACS Applied Materials & Interfaces*, vol. 13, pp. 7188–7199, 2021. doi:10.1021/acsami.0c20539

[221] H. Tangara, S. Zahedi-Azad, J. Not, J. Schick, A. Lafuente-Sampietro *et al.*, "Study of defect properties and recombination mechanism in rubidium treated Cu(In,Ga)Se_2 solar cells," *Journal of Applied Physics*, vol. 129, p. 183108, 2021. doi:10.1063/5.0046098

[222] N. Nicoara, R. Manaligod, P. Jackson, D. Hariskos, W. Witte *et al.*, "Direct evidence for grain boundary passivation in Cu(In,Ga)Se_2 solar cells through alkali-fluoride post-deposition treatments," *Nature Communications*, vol. 10, p. 3980, 2019. doi:10.1038/s41467-019-11996-y

[223] R. Fonoll-Rubio, S. Paetel, E. Grau-Luque, I. Becerril-Romero, R. Mayer *et al.*, "Insights into the Effects of RbF-Post-Deposition Treatments on the Absorber Surface of High Efficiency Cu(In,Ga)Se_2 Solar Cells and Development of Analytical and Machine Learning Process Monitoring Methodologies Based on Combinatorial Analysis," *Advanced Energy Materials*, vol. 12, no. 8, p. 2103163, 2022. doi:https://doi.org/10.1002/aenm.202103163

[224] M. Malitckaya, H.-P. Komsa, V. Havu, and M. J. Puska, "Effect of Alkali Metal Atom Doping on the $CuInSe_2$-Based Solar Cell Absorber," *The Journal of Physical Chemistry C*, vol. 121, no. 29, pp. 15 516–15 528, 2017. doi:10.1021/acs.jpcc.7b03083

[225] T. Kodalle, M. D. Heinemann, D. Greiner, H. A. Yetkin, M. Klupsch *et al.*, "Elucidating the Mechanism of an RbF Post Deposition Treatment in CIGS Thin Film Solar Cells," *Solar RRL*, vol. 2, no. 9, p. 1800156, 2018.

doi:https://doi.org/10.1002/solr.201800156

[226] P. Schöppe, C. S. Schnohr, M. Oertel, A. Kusch, A. Johannes *et al.*, "Improved Ga grading of sequentially produced Cu(In,Ga)Se_2 solar cells studied by high resolution X-ray fluorescence," *Applied Physics Letters*, vol. 106, p. 013909, 2015. doi:http://dx.doi.org/10.1063/1.4905347

[227] M. E. Stuckelberger, T. Nietzold, B. M. West, R. Farshchi, D. Poplavskyy *et al.*, "Defect activation and annihilation in CIGS solar cells: an operando x-ray microscopy study," *Journal of Physics: Energy*, vol. 2, no. 2, p. 025001, 2020. doi:10.1088/2515-7655/ab5fa6

[228] T. Buonassisi, A. A. Istratov, S. Peters, C. Ballif, J. Isenberg *et al.*, "Impact of metal silicide precipitate dissolution during rapid thermal processing of multicrystalline silicon solar cells," *Applied Physics Letters*, vol. 87, no. 12, p. 121918, 2005. doi:10.1063/1.2048819

[229] T. J. Cleophas and A. H. Zwinderman, *Modern Meta-Analysis*, 1st ed. Springer, Cham, 2017.

[230] E. Avancini, R. Carron, B. Bissig, P. Reinhard, R. Menozzi *et al.*, "Impact of compositional grading and overall Cu deficiency on the near-infrared response in Cu(In,Ga)Se_2 solar cells," *Progress in Photovoltaics: Research and Applications*, vol. 25, no. 3, pp. 233–241, 2017.

[231] B. M. West, M. Stuckelberger, B. Lai, J. Maser, and M. I. Bertoni, "Nanoscale growth kinetics of Cu(In,Ga)Se_2 absorbers," *The Journal of Physical Chemistry C*, vol. 122, no. 40, pp. 22 897–22 902, 2018. doi:10.1021/acs.jpcc.8b05062

[232] M. Raghuwanshi, B. Thöner, P. Soni, M. Wuttig, R. Wuerz *et al.*, "Evidence of Enhanced Carrier Collection in Cu(In,Ga)Se_2 Grain Boundaries: Correlation with Microstructure," *ACS Applied Materials & Interfaces*, vol. 10, pp. 14 759–14 766, 2018.

[233] P. Schöppe, S. Schönherr, M. Chugh, H. Mirhosseini, P. Jackson *et al.*, "Revealing the origin of the beneficial effect of cesium in highly efficient Cu(In,Ga)Se_2 solar cells," *Nano Energy*, vol. 71, p. 104622, 2020. doi:10.1016/j.nanoen.2020.104622

[234] C. Spindler, F. Babbe, M. H. Wolter, F. Ehré, K. Santhosh *et al.*, "Electronic defects in Cu(In, Ga)Se_2: Towards a comprehensive model," *Phys. Rev. Materials*, vol. 3, p. 090302, Sep 2019. doi:10.1103/PhysRevMaterials.3.090302

[235] J. Keller, H. Aboulfadl, L. Stolt, O. Donzel-Gargand, and M. Edoff, "Rubidium Fluoride Absorber Treatment for Wide-Gap (Ag,Cu)(In,Ga)Se_2 Solar Cells," *Solar RRL*, vol. 6, no. 6, p. 2200044, 2022. doi:https://doi.org/10.1002/solr.202200044

[236] B. Huang, S. Chen, H.-X. Deng, L.-W. Wang, M. A. Contreras *et al.*, "Origin of Reduced Efficiency in Cu(In,Ga)Se_2 Solar Cells With High Ga Concentration: Alloy Solubility Versus Intrinsic Defects," *IEEE Journal of Photovoltaics*, vol. 4, no. 1, pp. 477–482, 2014. doi:10.1109/JPHOTOV.2013.2285617

[237] M. M. Byranvand, C. Otero-Martínez, J. Ye, W. Zuo, L. Manna *et al.*, "Recent progress in mixed a-site cation halide perovskite thin-films and nanocrystals for solar cells and light-emitting diodes," *Advanced Optical Materials*, vol. 10, no. 14, p. 2200423, 2022. doi:https://doi.org/10.1002/adom.202200423

[238] M. Saliba, T. Matsui, J.-Y. Seo, K. Domanski, J.-P. Correa-Baena *et al.*, "Cesium-containing triple cation perovskite solar cells: improved stability, reproducibility and high efficiency," *Energy & Environmental Science*, vol. 9, pp. 1989–1997, 2016. doi:10.1039/cSee03874j

[239] M. Salado, M. A. Fernández, J. P. Holgado, S. Kazim, M. K. Nazeeruddin *et al.*, "Towards extending solar cell lifetimes: Addition of a fluorous cation to triple cation-based perovskite films," *ChemSusChem*, vol. 10, no. 19, pp. 3846–3853, 2017. doi:https://doi.org/10.1002/cssc.201700797

[240] S. Kim, T. Eom, Y.-S. Ha, K.-H. Hong, and H. Kim, "Thermodynamics of multicomponent perovskites: A guide to highly efficient and stable solar cell materials," *Chemistry of Materials*, vol. 32, no. 10, pp. 4265–4272, 2020. doi:10.1021/acs.chemmater.0c00893

[241] Y. Hu, E. M. Hutter, P. Rieder, I. Grill, J. Hanisch *et al.*, "Understanding the role of cesium and rubidium additives in perovskite solar cells: Trap states, charge transport, and recombination," *Advanced Energy Materials*, vol. 8, no. 16, p. 1703057, 2018. doi:https://doi.org/10.1002/aenm.201703057

[242] J. Peng, D. Walter, Y. Ren, M. Tebyetekerwa, Y. Wu *et al.*, "Nanoscale localized contacts for high fill factors in polymer-passivated perovskite solar cells," *Science*, vol. 371, no. 6527, pp. 390–395, 2021. doi:10.1126/science.abb8687

[243] K. Sveinbjörnsson, K. Aitola, J. Zhang, M. B. Johansson, X. Zhang *et al.*, "Ambient air-processed mixed-ion perovskites for high-efficiency solar cells," *J. Mater. Chem. A*, vol. 4, pp. 16 536–16 545, 2016. doi:10.1039/c6ta06912f

[244] S. Braunger, L. E. Mundt, C. M. Wolff, M. Mews, C. Rehermann *et al.*, "$Cs_xFA_{1-x}Pb(I_{1-y}Br_y)_3$ Perovskite Compositions: the Appearance of Wrinkled Morphology and its Impact on Solar Cell Performance," *The Journal of Physical Chemistry C*, vol. 122, pp. 17 123–17 135, 2018.

[245] A. Bercegol, F. J. Ramos, A. Rebai, T. Guillemot, J.-B. Puel *et al.*, "Spatial inhomogeneity analysis of cesium-rich wrinkles in triple-cation perovskite," *The Journal of Physical Chemistry C*, vol. 122, pp. 23 345–33 351, 2018. doi:10.1021/acs.jpcc.8b07436

[246] S.-G. Kim, J.-H. Kim, P. Ramming, Y. Zhong, K. Schötz *et al.*, "How antisolvent miscibility affects perovskite film wrinkling and photovoltaic properties," *Nat Commun*, vol. 12, 2021. doi:10.1038/s41467-021-21803-2

[247] V. D'Innocenzo, A. R. S. Kandada, M. De Bastiani, M. Gandini, and A. Petrozza, "Tuning the Light Emission Properties by Band Gap Engineering in Hybrid Lead Halide Perovskite," *J. Am. Chem. Soc.*, vol. 136, pp. 17 730–17 733, 2014. doi:10.1021/ja511198f

[248] E. Aydin, J. Troughton, M. De Bastiani, E. Ugur, M. Sajjad *et al.*, "Room-temperature-sputtered nanocrystalline nickel oxide as hole transport layer for p–i–n perovskite solar cells," *ACS Applied Energy Materials*, vol. 1, no. 11, pp. 6227–6233, 2018. doi:10.1021/acsaem.8b01263

[249] R. Azmi, E. Ugur, A. Seitkhan, F. Aljamaan, A. S. Subbiah *et al.*, "Damp heat-stable perovskite solar cells with tailored-dimensionality 2d/3d heterojunctions," *Science*, vol. 376, no. 6588, pp. 73–76, 2022. doi:10.1126/science.abm5784

[250] V. Thomsen, "Basic fundamental parameters in x-ray fluorescence," *Spectroscopy*, vol. 22, no. 5, 2007.

[251] K. Frohna, M. Anaya, S. Macpherson, J. Sung, T. A. S. Doherty *et al.*, "Nanoscale chemical heterogeneity dominates the optoelectronic response of alloyed perovskite solar cells," *Nature Nanotechnology*, vol. 17, pp. 190–196, 2022. doi:10.1038/s41565-021-01019-7

[252] X. Yu, T. Liu, Q. Wei, C. Liang, K. Wang *et al.*, "Tailoring the surface morphology and phase distribution for efficient perovskite electroluminescence," *J. Phys. Chem. Lett.*, vol. 11, pp. 5877–5887, 2020.

[253] S. Ašmontas, A. Čerškus, J. Gradauskas, A. Grigucevičienė, K. Leinartas *et al.*, "Cesium-containing triple cation perovskite solar cells," *Coatings*, vol. 11, p.

279, 2021. doi:https:// doi.org/10.3390/coatings11030279

[254] C. Wang, Z. Song, Y. Yu, D. Zhao, R. A. Awni *et al.*, "Synergistic effects of thiocyanate additive and cesium cations on improving the performance and initial illumination stability of efficient perovskite solar cells," *Sustainable Energy & Fuels*, vol. 2, p. 2435, 2018. doi:10.1039/c8se00200b

[255] Y. Wang, X. Quintana, J. Kim, X. Guan, L. Hu *et al.*, "Phase segregation in inorganic mixed-halide perovskites: from phenomena to mechanisms," *Photon. Res.*, vol. 8, no. 11, pp. A56–A71, Nov 2020. doi:10.1364/PRJ.402411

[256] K. A. Bush, K. Frohna, R. Prasanna, R. E. Beal, T. Leijtens *et al.*, "Compositional engineering for efficient wide band gap perovskites with improved stability to photoinduced phase segregation," *ACS Energy Lett.*, vol. 3, no. 2, pp. 428–435, 2018. doi:10.1021/acsenergylett.7b01255

[257] G. Fevola, P. S. Jørgensen, M. Verezhak, A. Slyamov, A. Crovetto *et al.*, "Resonant x-ray ptychographic nanotomography of kesterite solar cells," *Physical Review Research*, vol. 2, no. 1, p. 013378, mar 2020. [Online]. Available: https://link.aps.org/doi/10.1103/PhysRevResearch.2.013378. doi:10.1103/PhysRevResearch.2.013378

[258] M. Stuckelberger, T. Nietzold, B. M. West, R. Farshchi, D. Poplavskyy *et al.*, "How does CIGS performance depend on temperature at the microscale?" *IEEE Journal of Photovoltaics*, vol. 8, no. 1, pp. 278–287, Jan 2018. doi:10.1109/JPHOTOV.2017.2762584

Danksagung

In den letzten viereinhalb Jahren ist neben der Entstehung dieser Arbeit einiges passiert. Umso mehr möchte ich den Leuten danken, die mich in dieser Zeit begleitet und unterstützt haben.

Zuerst möchte ich mich bei Christian Schroer bedanken, dafür, dass ich meine Arbeit in seiner Arbeitsgruppe schreiben durfte. Besonders möchte ich mich dafür bedanken, dass Du mir immer den Rücken frei gehalten hast und dass Du die Arbeitsgruppe in solch einer herzlichen und warmen Atmosphäre führst.

Ich danke Tobias Kipp für die Übernahme des Zweitgutachtens dieser Arbeit und allen anderen Mitgliedern der Prüfungskommission, Arwen Pearson, Gabriel Bester und Michael Stückelberger, für die Beurteilung meiner Disputation.

Mein besonderer Dank gilt Michael Stückelberger. Als die Arbeit anfing, waren wir die einzigen, die sich mit Solarzellen in FS-PETRA beschäftigt haben, und ich habe die enge Zusammenarbeit sehr geschätzt. Michael ist nicht nur ein Vorbild, was gute Wissenschaft angeht, sondern auch als Betreuer außerordentlich engagiert. Ich konnte mit jedem Problem zu Dir kommen und fühlte ich mich nach den Diskussionen mit Dir jedes mal bestärkt. Vielen Dank für die gesamte Unterstützung während und außerhalb dieser Arbeit.

Wir haben sehr früh eine Kooperation mit der Arbeitsgruppe von Alf Mews der Universität Hamburg angefangen, ohne die der XEOL Aufbau so niemals existiert hätte. Ganz besonders möchte ich dort Christian Strelow, Tobias Kipp, Jan Flügge, Jan Siebels, Andreas Kolditz und Svenja Patjens danken. Ob auf der Messzeit in Chicago oder Hamburg, Messungen in den Laboren der Uni oder beim Diskutieren der Daten, es war immer eine Freude mit Euch zusammen Arbeiten zu dürfen. Ich bedanke mich daher ganz herzlich, für die gesamte Unterstützung, die ich durch Euch erfahren durfte.

Auch möchte ich mich in dem Zuge bei der gesamten Gruppe FS-PETRA bedanken. Egal worum es ging, es gab immer jemanden, der mit Rat und Tat zur Seite stand.

Speziellen Dank hier an Johannes Hagemann, Jackson Barp und Giovanni Fevola als sehr coole Büro-Mitbewohner. Danke auch an Martin Seyrich für die Unterstützung mit PetraPy und als Erfahrungsquelle, was die regularien der Doktorarbeit angeht. Auch möchte ich allen Studenten unserer Solar-SubGroup danken, es hat Spaß gemacht mit Euch zu Arbeiten. Besonderer Dank an Niklas Pyrlik, mit dem ich mir die Erst-Autorenschaft für das CIGS Paper teile.

Ein Danke geht an die Crew von P06, für ihre rund-um-die-Uhr Unterstützung während der Strahlzeit. Auch in der Vor- und Nachbereitung der Messungen wart Ihr eine große Hilfe.

Auch möchte ich allen Herstellern, KAUST und EMPA, deren Solarzellen wir im Zuge dieser Arbeit vermessen haben, danken. Besonderer Dank hierbei an Romain Carron, für sein ausführliches Feedback und tiefgreifende Diskussionen. Ebenso möchte ich mich sehr herzlich bei Ramis Hertwig für den angenehmen Aufenthalt in Zürich und die Besichtigung des Labors bedanken.

Danke an alle meine Co-Autoren für ihre Unterstützung.

Ein Danke an all meine Kommilitonen, die sich ebenfalls dazu entschlossen haben eine Doktorarbeit anzufertigen, es war immer wieder schön sich austauschen zu können. Besonderer Dank hier an Lukas, ohne den ich nicht zu FS-PETRA gekommen wäre.

Weiterhin möchte ich der TaiChi-Gruppe, Ute Krell, Hella Hummerjohann, Steffi Killough, und Carsten Muhl danken. Es war immer eine seelische Wohltat mit Euch Tee zu trinken und durch die TaiChi-Form zu gehen. Vielen Dank, dass ich Eurer Gruppe beitreten durfte, Ihr wart ein Ruhepol in dieser turbulenten Zeit.

Ebenso ein besonderes Dankeschön an meine D&D Party, Kaja, Matz und Fridtjof. Ich möchte mit niemandem lieber Riesen-kloppen gehen als mit euch und nicht nur in Zeiten der Pandemie war unser Sonntags Abenteuer eine willkommene Reise in eine andere Welt.

Danke auch an meine Laufpartner, es tut gut jemanden zu haben, mit dem man gemeinsam Sport machen kann.

Ich danke all meinen Korrekturlesern, besonders Michael, Giovanni, Jackson, Matz, Fridtjof und Tante Andrea.

Ein riesengroßes Dankeschön gehört Alex. Ohne Dich wäre ich wahrscheinlich halb wahnsinning geworden in den letzten Jahren. Das beste Essen, die größten Abenteuer, die engsten Umarmungen, und so viel mehr gehen auf Dein Konto. Du bist mein

Fels in der Brandung und mein sicherer Hafen, dafür danke ich Dir.

Danke besonders an Caro, die beste Schwester, die man sich wünschen kann. Die Woche in Düsseldorf war Gold wert.

Zum Schluss möchte ich mich bei meinen Eltern bedanken, die mich immer in meinen Vorhaben unterstützt haben. Ihr habt immer ein offenes Ohr für mich und bietet mir einen Ort, an den ich mich zurück ziehen kann. Gleichzeitig gebt ihr mir genug Rückenwind, um unbeschwert in die Welt ziehen zu können. Danke!

Eidesstattliche Versicherung

Hiermit versichere ich an Eides statt, die vorliegende Dissertationsschrift selbst verfasst und keine anderen als die angegebenen Hilfsmittel und Quellen benutzt zu haben.

Ort, Datum

Christina Sonja Ossig